THE UNIVERSITY *of* EDINBURGH

Multiscale modelling of trabecular bone

From micro to macroscale

THE UNIVERSITY *of* EDINBURGH

Francesc Levrero Florencio

School of Engineering

The University of Edinburgh

This dissertation is submitted for the degree of

Doctor of Philosophy

2016

Declaration

I hereby declare that except where specific reference is made to the work of others, the contents of this thesis are original and have not been submitted in whole or in part for consideration for any other degree or qualification in this, or any other university. This thesis is my own work and contains nothing which is the outcome of work done in collaboration with others, except as specified in the text and acknowledgements. I am an author of the publications which are included in the appendices.

Francesc Levrero Florencio
2016

Lay abstract

Trabecular bone has a complex and porous microstructure. This study develops approaches to determine the mechanical behaviour of this material at the macroscopic level by developing models of its microstructure and computationally subjecting them to mechanical loading. This study provides an assessment of how the mechanical behaviour of trabecular bone at the macroscale, i.e. organ level, is affected by the mechanical behaviour at lower scales. It is expected that this study can be employed to provide further information to enhance current clinical prediction tools, and improve bone strength and implant stability predictions.

The main tool used to simulate the mechanical behaviour of trabecular bone is the micro-finite element method, which is basically the finite element method applied to geometries obtained through micro-computed tomography scans. These simulations were carried out using cutting edge high performance computing platforms, i.e. supercomputers, which are essentially a large number of very powerful "normal" computers linked together through a high speed network.

Results show that changing the microscopic yield characteristics only has a small effect on the macroscopic behaviour. The overall shape of the macroscopic yield surface was also investigated. The results show that yielding defined in terms of strain is largely isotropic, permitting use of relatively simple models. In load cases with shear, different yield strains for clockwise and counter-clockwise shear may arise. The macroscopic post-yield behaviour of trabecular bone was also investigated by including both plasticity (i.e. permanent deformations) and damage (i.e. reduction in the elastic properties) at the microscopic level. Results show that the reduction in elastic properties is not isotropic, which is contrary to what has been assumed in the literature; additionally, hardening and damage were seen to evolve differently in tension, compression and shear.

Abstract

Trabecular bone has a complex and porous microstructure. This study develops approaches to determine the mechanical behaviour of this material at the macroscopic level through the use of homogenisation-based multiscale methods using micro-finite element simulations. In homogenisation-based finite element methods, a simulation involving a representative volume element of the microstructure of the considered material is performed with a specific set of boundary conditions. The macroscopic stresses and strains are retrieved as averaged quantities defined over this domain. Most of the homogenisation-based work on trabecular bone has been performed to study its macroscopic elastic regime, and therefore define its constant macroscopic stiffness tensor.

The rod and plate-shaped microstructure of trabecular bone can be precisely identified with advanced scanning tools, such as micro-computed tomography devices. Taking into account the size requirements to achieve a certain independence of boundary conditions for trabecular bone in a homogenisation-based multiscale setting, the resulting stack of images can have around ten million solid voxels after binarisation. Although a completely linear finite element simulation with such a large system may be feasible with commercial packages (with the proper time and memory requirements), it is not possible to perform a nonlinear simulation for such a mesh in a reasonable time frame, and the amount of required memory may not be available. A highly scalable parallel driver program which solves finite strain elastoplastic systems was developed within the framework of the existing parallel code ParaFEM. This code was used throughout this study to evaluate the yield and post-yield properties of trabecular bone. It was run on cutting edge high performance computing platforms (BlueGene/Q at the Hartree Centre, Science and Technology Facilities Council; and ARCHER, UK National Supercomputing Service, at Edinburgh Parallel Computing Centre).

Micro-finite element simulations require definition of properties at the microscopic scale and it is unclear how these properties affect the macroscopic response. This study examines the effect of compressive hydrostatic yield at the microscopic scale on the macroscopic behaviour. Two different microscopic yield criteria, one permitting yielding at compressive hydrostatic stresses and the other not, were considered. A

large number of load cases were examined. It was found that these two microscopic yield criteria only influence macroscopic yield behaviour in load scenarios which are compression-dominated; for other load cases, macroscopic response is insensitive to the choice of the microscopic yield criterion, provided it has an appropriate strength asymmetry. Also, in compression-dominated load cases, high density bone is much more sensitive as it is more like a *continuum*, resulting in the microscopic properties being more directly upscaled.

Only a few previous studies have employed homogenisation to evaluate the macroscopic yield criterion of trabecular bone. However, they either used a simplified microscopic yield surface or examined only a small number of load cases. A thorough multiaxial evaluation of the macroscopic yield surface was performed by applying a wide range of loading scenarios (160 load cases) on trabecular bone samples. Closed-form yield surfaces with different symmetries (isotropy, orthotropy and full anisotropy) were fitted to the numerically obtained macroscopic yield points in strain space, and the fitting errors were evaluated in detail for different subsets of load cases. Although orthotropy and full anisotropy showed the smallest fitting errors, they were not significantly superior to the isotropic fit. Thus, isotropy in strain space presents itself as the most suitable option due to the simplicity of its implementation. The study showed that fitting errors do depend on the chosen set of load cases and that shear load cases are extremely important as it was found that even for these highly aligned samples, trabecular bone presents some degree of shear asymmetry, i.e. different strength in clockwise and counter-clockwise shear directions.

There have been no previous attempts to evaluate the post-yield behaviour of trabecular bone through homogenisation-based studies on detailed micro-finite element trabecular bone meshes. A damage and plasticity constitutive law for the microscale based on existing data in the literature was considered. A homogenisation-based multiscale approach was used to evaluate the hardening and stiffness reduction at the macroscale when uniaxial load scenarios are applied to trabecular bone samples, for a small range of plastic strain Euclidean norms. Results show that damage progression at the macroscale for trabecular bone is not isotropic, which is contrary to what has been assumed previously, and that both the evolution of the yield surface and damage are different for tension, compression and shear. Nonetheless, they can be correlated with plastic strain Euclidean norms by using linear relationships. It was also observed that macroscopic damage in a specific load case affects differently the on-axis orthotropic stiffness and the off-axis orthotropic stiffness components.

The findings of this study will permit the use of a more rigorous definition of the post-elastic macroscopic behaviour of trabecular bone in finite element settings.

I dedicate this thesis to my family and to 莫沁穎

Acknowledgements

Many people contributed to this thesis. Besides the individuals mentioned below, I would like to specially mention all of my friends, who are too numerous to individually name. However, a special mention goes to Samuel Martin as he has been very supportive for the whole thesis and for being my best friend.

I would like to start by thanking my first supervisor Dr Pankaj Pankaj for his supervision and unconditional support in every aspect concerning my PhD. I do hope future bosses are at least half as nice as he has been for these three years and I also hope that we can keep contact and maybe even establish future collaborations.

Although he is officially not one of my PhD supervisors, I would like to thank Dr Lee Margetts from University of Manchester for his continuous collaboration and support in high performance computing, without which my thesis would have not been possible.

Most of my work would have not been possible without the assistance of other people in the research group. Special thanks go to Dr Erika Sales for being a friend and sharing her expertise in medical image acquisition and processing; Dr Robert Wallace for helping in using the medical equipment located in the Royal Infirmary of Edinburgh; Dr Krishnagoud Manda for helping with my computational work and providing valuable insight on my scientific output; Dr Noel Conlisk for doing some "bits and pieces", which included helping me with the writing and formalities of this thesis, and finally Dr Shane Burns for proofreading my thesis and my cover letters for job applications.

These three years in Edinburgh would have been far less eventful if it had not been for my friends, flatmates and office mates and thus I would like to thank them all. I would like to specifically mention Dr John Paul Morrissey for his grumpiness and his "special" diet; Utibe Umoh for being my gym buddy . . . from time to time; Luis Fernando Montaño for disappointing me as he did not usually wear a Mexican sombrero, which I expected; Dr Shane Burns (again) for being the (ironically) only Irish I know who drinks alcohol; Yuki Wang for being a Chinese girl with a Japanese name; Lorenzo Conti for making me believe that the stereotypes about Italian people might be sometimes true; and Dr Alisdair McLeod because we share the same birthday.

Final, but not less important, special thanks go to my beloved family. Particular thanks go to my parents and sister for their moral and economic support, and for being a constant source of inspiration, and also to my partner, 莫沁穎, for her love and patience with this third member of our relationship, and without whom my thesis writing would have been even more exhausting.

Table of contents

List of figures

List of tables

Nomenclature

Symbols

A	Area
$\mathbf{A}$	Generic set of thermodynamical forces
$\mathbb{A}$	Consistent material tangent operator
$\mathscr{A}$	Assembly operator in a FE setting
$\mathbf{B}$	Discrete symmetric gradient operator or left Cauchy-Green strain tensor
$\mathbb{C}$	Consistent spatial tangent operator
d	Distance to a yield point in strain space
$\mathbf{d}$	Newton update direction
D	Damage scalar variable
D_c	First damage parameter
$\mathbb{D}^e$	Elastic stiffness tensor
$\mathbb{D}^e_{0\,dam}$	Damaged macroscopic elastic stiffness tensor
$\mathbb{D}^{ep}$	Consistent tangent operator
e_{ij}	Ith and jth orthotropic coefficient of the macroscopic elastic stiffness tensor in matrix form
E	Young's Modulus
$\mathbf{e}_i$	Ith eigenvector of a second-order tensor
$\mathbf{E}_i$	Ith eigentensor of a second-order tensor
$Error_{FIT}$	Fitting error
$Error_{ORT}$	Orthotropic error
f	Yield surface in stress space
$\mathbf{f}^{ext}$	External force vector
$\mathbf{f}^{int}$	Internal force vector
$\bar{\mathbf{f}}^{ext}$	Total external force vector
F_0	Constant defining the shape and eccentricity of an isotropic yield surface in stress space

F^D	Damage dissipation potential
$\mathbf{F}$	Second-order tensor defining the offset from the origin of a quadric in stress space or deformation gradient
$\mathbf{F}_\Delta$	Incremental deformation gradient
$\mathbb{F}$	Fourth-order tensor defining the shape and orientation of a quadric in stress space
$\mathscr{F}_y$	Microscopic constitutive functional
g	Yield surface in strain space
g_0	First constant defining the shape and eccentricity of an isotropic yield surface in strain space
G	Shear modulus
G_0	Second constant defining the shape and eccentricity of an isotropic yield surface in strain space
$\mathbf{G}$	Second-order tensor defining the offset from the origin of a quadric in strain space or discrete spatial gradient operator
$\mathbb{G}$	Fourth-order tensor defining the shape and orientation of a quadric in strain space
H	Conjugate thermodynamical force associate with a scalar internal variable
$\overline{H}_{dam}$	Constant associated with damage evolution
$\overline{H}_{iso}$	Hardening modulus associated with a scalar internal variable
$\mathbf{H}$	Generic set of hardening modulus
$\mathbf{I}$	Second-order unit tensor
$\mathbb{I}$	Fourth-order unit tensor ($\delta_{ik}\,\delta_{jl}$)
$\mathbb{I}_{sym}$	Fourth-order symmetric identity tensor $\left(\frac{1}{2}[\delta_{ik}\,\delta_{jl}+\delta_{il}\,\delta_{jk}]\right)$
$\mathbf{J}$	Jacobian of the transformation between the continuum and the standard integration domain
$\mathbf{J}_{CPPM}$	Jacobian of a Closest-Point Projection Method
k_p	Second damage parameter
K	Bulk modulus
K_{dam}	Damaged stiffness
$\mathbf{K}$	Global stiffness matrix
$\mathscr{K}$	Set of kinematically admissible displacements
l	Characteristic length of the continuum
l_μ	Characteristic length of the RVE
$\mathscr{L}$	Lagrangian function
m_i	Ith eigenvalue of the fabric tensor
$\mathbf{m}_i$	Ith eigenvector of the fabric tensor

M	Continuous descent function of a line search procedure
$\hat{M}$	Merit function of a line search procedure
$\mathbf{M}_i$	Ith eigentensor of the fabric tensor
$\mathbb{M}$	Structural tensor
n_{CPPM}	Maximum number of allowed Closest-Point Projection Method iterations
n_{dim}	Number of physical dimensions
n_{el}	Number of elements in a FE mesh
n_{gauss}	Number of integration points in a FE element
n_{ls}	Maximum number of allowed line search iterations
n_{max}	Cardinality of a set
n_{Newton}	Maximum number of allowed Newton-Raphson iterations
n_{nod}	Number of nodes in a FE mesh
$\mathbf{n}$	Unit normal vector to the boundary of the RVE
N_i^{el}	Shape function defined in an element and associated with node i
$\mathbf{N}$	Flow tensor or interpolation matrix
Obj	Objective function to be minimised for orthotropic stiffness
Orth^3	Set of second-order orthogonal tensors in three dimensions
$\mathbf{P}$	First Piola-Kirchhoff stress tensor
q	Thermodynamical force associated with a scalar internal variable
$\mathbf{Q}$	Orthogonal tensor
R^2	Coefficient of determination of a regression
R^2_{adj}	Adjusted coefficient of determination of a regression
$\mathbf{R}_{(\cdot)}$	Residual of $(\cdot)$
$\mathbb{R}$	Set of real numbers
$\mathbb{R}^{(\cdot)}$	Vector space of dimension $(\cdot)$ over the set of real numbers
SOrth^3	Subset of the set of second-order orthogonal tensors in three dimensions
Sym^6	Space of 6×6 symmetric matrices
t	(Pseudo-) Time
tol	Tolerance for stopping an iterative numerical scheme
$\mathbf{t}^{ext}$	External traction field
$\mathbf{u}_\mu$	Microscopic displacement
$\mathbf{u}_0$	Mean of the microscopic displacement
$\tilde{\mathbf{u}}_\mu$	Fluctuation of the microscopic displacement
$\bar{\mathbf{u}}$	Prescribed displacement
$\mathscr{U}$	Vector space of dimension equal to the number oh physical dimensions
V	Volume
$\mathbf{V}$	Left stretch tensor

$\mathscr{V}$	Space of virtual displacements
w_i	Weight of the ith Gaussian integration point
$\mathbf{x}$	Deformed (spatial) coordinates in the continuum or solution vector
$\mathbf{X}$	Undeformed (material) coordinates in the continuum
Y	Thermodynamic force associated with a scalar damage variable
$\mathbf{y}$	Coordinates within the RVE
α	Line search parameter
$\boldsymbol{\alpha}$	Generic set of internal variables
$\overline{\boldsymbol{\alpha}}$	Internal variable incremental constitutive function
β	First constant of a line search procedure involving a quadratic fit
γ_{ij}	Shear yield strain in the $\mathbf{e}_i\,\mathbf{e}_j$ plane
$\dot{\gamma}$	Plastic multiplier
$\boldsymbol{\delta}$	Kronecker Delta
ε_h	Trial strain parameter
ε_{ii}^{+}	Tensile yield strain in the ith orthotropic direction
ε_{ii}^{-}	Compressive yield strain in the ith orthotropic direction
ε_{ij}^{+}	Clockwise shear yield strain in the $\mathbf{e}_i\mathbf{e}_j$ plane
ε_{ij}^{-}	Counter-clockwise shear yield strain in the $\mathbf{e}_i\mathbf{e}_j$ plane
ε_0^{+}	Tensile yield strain of an isotropic quadric in stress space
ε_0^{-}	Compressive yield strain of an isotropic quadric in stress space
$\overline{\varepsilon}^p$	Accumulated plastic strain
$\boldsymbol{\varepsilon}$	Strain tensor
$\tilde{\boldsymbol{\varepsilon}}_\mu$	Microscopic strain tensor fluctuation
ζ_0	Parameter which controls the shape of a quadric in stress space
η	Second constant of a line search procedure involving a quadratic fit
$\boldsymbol{\eta}$	Virtual displacement
$\overline{\kappa}$	Scalar internal variable
λ	First Lamé constant or load factor
μ	Second Lamé constant
ν	Poisson's ratio
ξ_{ij}	Strain interaction coefficients between the ith and the jth orthotropic directions
ξ_0	Parameter which controls the shape of a quadric in strain space
ρ	Density or bone volume over total volume fraction
σ_{ii}^{+}	Tensile yield stress in the ith orthotropic direction
σ_{ii}^{-}	Compressive yield stress in the ith orthotropic direction
σ_0^{+}	Tensile yield stress of an isotropic quadric in stress space

σ_0^-	Compressive yield stress of an isotropic quadric in stress space
$\boldsymbol{\sigma}$	Generic stress tensor
$\boldsymbol{\sigma}^{proj}$	Stress solution of the closest-point projection method equations without considering hardening and damage
$\overline{\boldsymbol{\sigma}}$	Stress incremental constitutive function
τ_{ij}	Shear yield stress in the $\mathbf{e}_i\,\mathbf{e}_j$ plane
$\boldsymbol{\tau}$	Kirchhoff stress tensor
φ	Scalar function to be minimised in a Closest-Point Projection Method context
$\boldsymbol{\varphi}$	Deformation map
χ	Complementary energy function
χ_{ij}	Stress interaction coefficients between the ith and the jth orthotropic directions
Ξ	Dissipation potential
ψ	Free energy function
ψ^e	Elastic contribution to the free energy function
ψ^p	Plastic contribution to the free energy function
Ω	Domain of a generic body
Ω_μ	Domain of the RVE
$\partial\Omega_t$	Boundary of the RVE where tractions are prescribed
$\partial\Omega_u$	Boundary of the RVE where displacements are prescribed
$\partial\Omega_\mu$	Boundary of the RVE

Abbreviations

BiCGStab	Stabilised bi-conjugate gradient
BiCGStab(l)	Stabilised hybrid bi-conjugate gradient
BMD	Bone mineral density
BV/TV	Bone volume over total volume ratio
Conn	Connectivity
CPPM	Closest-point projection method
CPU	Central processing unit
CT	Computed tomography
DOA	Degree of anisotropy
DOF	Degrees of freedom
DVC	Digital Volume Correlation
DXA	Dual energy X-ray absortiometry

FE	Finite element
FEM	Finite element method
GMRES	Generalised minimum residual
GPU	Graphical processing unit
HPC	High performance computing
KUBC	Kinematic uniform boundary conditions
MIL	Mean intercept length
MINRES	Minimum residual method
MPI	Message passing interface
PBC	Periodic boundary conditions
PCG	Preconditioned conjugate gradient
PDE	Partial differential equation
RVE	Representative volume element
SMI	Structure model index
SRμCT	Synchrotron radiation micro-computed tomography
SUBC	Static uniform boundary conditions
Tb.Th	Trabecular thickness
TMD	Tissue mineral density
VE	Volume element
μCT	Micro-computed tomography
μFE	Micro-finite element

Other symbols and operators

$\mathrm{d}(\cdot)$	Differential of $(\cdot)$
$\det(\cdot)$	Determinant of $(\cdot)$
$\mathrm{div}(\cdot)$	Divergence of $(\cdot)$
$\mathrm{div}_{\mathbf{X}}(\cdot)$	Material divergence of $(\cdot)$
$\mathrm{div}_{\mathbf{x}}(\cdot)$	Spatial divergence of $(\cdot)$
$\mathrm{e}^{(\cdot)}$	Exponential of $(\cdot)$
$\ln(\cdot)$	Natural logarithm of $(\cdot)$
$\Delta(\cdot)$	Increment of $(\cdot)$, typically associated with a time, or pseudo-time, increment
$\delta(\cdot)$	Iterative increment of $(\cdot)$, typically associated with an iteration of a numerical scheme
$\nabla(\cdot)$	Gradient of $(\cdot)$
$\nabla^{sym}(\cdot)$	Symmetric gradient of $(\cdot)$

$\nabla_{\mathbf{X}}(\cdot)$	Material gradient of $(\cdot)$
$\nabla_{\mathbf{x}}(\cdot)$	Spatial gradient of $(\cdot)$
$\partial(\cdot)$	Boundary of the domain $(\cdot)$
$\frac{\partial}{\partial a}(\cdot)$	Derivative of $(\cdot)$ with respect to a
$\dot{(\cdot)}$	Time derivative of $(\cdot)$
$(\cdot)^{\mathrm{T}}$	Transpose of $(\cdot)$
$\mathbf{a}\cdot\mathbf{b}$	Single contraction of two vectors ($a_i\,b_i$)
$\mathbf{a}\cdot\mathbf{B}$	Single contraction of a vector $\mathbf{a}$ and a second-order tensor $\mathbf{B}$ ($a_i\,B_{ij}$)
$\mathbf{A}\mathbf{b}$	Single contraction of a second-order tensor $\mathbf{A}$ and a vector $\mathbf{b}$ ($A_{ij}\,b_j$)
$\mathbf{A}\mathbf{B}$	Single contraction of two second-order tensors ($A_{ik}\,B_{kj}$)
$\mathbf{A}:\mathbf{B}$	Double contraction of two second-order tensors ($A_{ij}\,B_{ij}$)
$\mathbb{A}:\mathbf{B}$	Double contraction of a fourth-order tensor $\mathbb{A}$ and a second-order tensor $\mathbf{B}$ ($\mathbb{A}_{ijkl}\,B_{kl}$)
$\mathbf{A}:\mathbb{B}$	Double contraction of a second-order tensor $\mathbf{A}$ and a fourth-order tensor $\mathbb{B}$ ($A_{ij}\,\mathbb{B}_{ijkl}$)
$\mathbb{A}:\mathbb{B}$	Double contraction of two fourth-order tensors ($\mathbb{A}_{ijmn}\,\mathbb{B}_{mnkl}$)
$\mathbf{a}\otimes\mathbf{b}$	Tensor product of two vectors ($a_i\,b_j$)
$\mathbf{a}\otimes^{sym}\mathbf{b}$	Symmetric tensor product of two vectors $\left(\frac{1}{2}(a_i\,b_j+b_i\,a_j)\right)$
$\mathbf{A}\otimes\mathbf{B}$	Tensor product of two second-order tensors ($A_{ij}\,B_{kl}$)
$\mathbf{A}\,\overline{\otimes}\,\mathbf{B}$	Symmetric tensor product of two second-order tensors $\left(\frac{1}{2}(A_{ik}\,B_{jl}+A_{il}\,B_{jk})\right)$
$\mathbf{A}\odot\mathbf{B}$	Alternate tensor product of two second-order tensors ($A_{il}B_{jk}$)
$\boldsymbol{\alpha}*\boldsymbol{\beta}$	Appropriate product between two entities, $\boldsymbol{\alpha}$ and $\boldsymbol{\beta}$, in a specific context
$\|\mathbf{a}\|$	Euclidean norm of a vector ($\|\mathbf{a}\|=\sqrt{\mathbf{a}\cdot\mathbf{a}}$)
$\|\mathbf{A}\|$	Euclidean norm of a second order tensor ($\|\mathbf{A}\|=\sqrt{\mathbf{A}:\mathbf{A}}$)
$A\in B$	A is an element of B
$\forall(\cdot)$	The statement preceding $\forall$ is true for all values of $(\cdot)$
$\int_{x_{min}}^{x_{max}}(\cdot)\,\mathrm{d}x$	Definite integral of $(\cdot)$ over x from x_{min} to x_{max}
$\bigcup_{i=1}^{n_{max}}(\cdot)_i$	Union of sets $(\cdot)$, from $i=1$ to $i=n_{max}$
$\sum_{i=1}^{n_{max}}(\cdot)_i$	Summation of elements $(\cdot)$, from $i=1$ to $i=n_{max}$

Indicial notation

Italic subscripts (i, j, k, l ...) are used for Cartesian components, and they range over the number of dimensions considered, which is three throughout this study. When an index appears twice in the same product, summation over the repeated index is implied as per the Einstein notation. However, an important exception occurs when a summation symbol ($\sum$) including the product appears, which in this case implies no summation

over repeated indices, and these indices are not Cartesian components any more but rather elements of a set.

It is also important to point out that subscripts are not exclusively used for indicial notation, as explained in the next section. The meaning of the subscript will be made clear from the context where it appears.

Subscripts and superscripts

$(\cdot)_0$	The variable is related to the macroscale in a multiscale setting. Important exceptions are: σ_0^+, σ_0^-, ε_0^+, ε_0^-, ζ_0 and ξ_0 which denote tensile and compressive yield stresses and strains and the corresponding shape parameters for an isotropic quadric in the corresponding space
$(\cdot)_\mu$	The variable is related to the microscale in a multiscale setting
$(\cdot)_{n+1}$	The variable is in the time increment $n+1$
$(\cdot)_{(k)}$	The variable is in the iteration k within an iterative numerical scheme
$(\cdot)^e$	The variable is related to the elastic regime
$(\cdot)^p$	The variable is related to the plastic regime
$(\cdot)^{trial}$	The variable is in the trial predictor stage of an operator split scheme
$(\cdot)^+$	The variable is related to the positive boundary of an RVE or with a tensile load case
$(\cdot)^-$	The variable is related to the negative boundary of an RVE or with a compressive load case
$(\cdot)^{ext}$	The variable is related to an external boundary of an RVE. An important exception is $\mathbf{f}^{ext}$ which denotes the external force vector in an FE setting
$(\cdot)^{int}$	The variable related to an internal boundary of an RVE. An important exception is $\mathbf{f}^{int}$ which denotes the internal force vector in an FE setting
$(\cdot)^s$	The variable is related to the solid phase of an RVE
$(\cdot)^v$	The variable is related to the void phase of an RVE
$(\cdot)^t$	The variable denotes the history of the corresponding quantity up to instant t
$(\cdot)^{ip}$	The variable is a field which is interpolated from the field $(\cdot)$
$(\cdot)^g$	The variable is a global quantity in an FE setting
$(\cdot)^{(k)}$	The variable is in the iteration k within an iterative numerical scheme

Brackets

Parentheses ( )	They are used to indicate priority in the order in which mathematical operations are performed. However, they are sometimes used to express the dependency of some physical quantity on another, such as $\boldsymbol{\sigma}(t)$, which indicates time dependency of the stress tensor.
Square brackets [ ]	They are used in conjunction with parentheses to indicate priority in the order of mathematical operations. An important exception occurs when they are used to represent a matrix projection of a fourth-order tensor or of four-dimensional tuples, such as $[\mathbb{A}]$ or $[\mathbf{K}]$.
Curly brackets { }	They are used to represent a vector projection of second-order tensors or of two-dimensional tuples, such as $\{\boldsymbol{\sigma}\}$ or $\{\mathbf{f}^{int}\}$.
Double square brackets ⟦ ⟧	They are used to indicate the jump equation of what is within the brackets.
Vertical bars |	They are used in conjunction with a subscript, for example $\|_{(\cdot)}$ to indicate that the expression preceding the vertical bar is evaluated at $(\cdot)$.

Character fonts

- *Italic letters A, a, B, b, C, c* ...: Scalars and scalar-valued functions.
- *Greek characters* α, β, γ ...: Scalars and scalar-valued functions. An important exception is Ω which denotes the region of Euclidean space occupied by a generic body.
- *Bold lower case letters* **a, b, c** ...: Vectors and vector-valued functions. An important exception is **d** which denotes the Newton update direction.
- *Bold upper case letters* **C, D, E** ...: Second-order tensors and second-order tensor-valued functions. Important exceptions are **A**, which denotes the generic set of thermodynamical forces, **B** which denotes the discrete symmetric gradient operator, **G** which denotes the discrete spatial gradient operator, **H** which denotes the generic set of hardening modulus, **J** which denotes the Jacobian of the Closest-Point Projection Method, **N** which denotes the interpolation matrix in a FE context, and **K** which denotes the global stiffness matrix of a FE system.

- *Greek bold characters* $\boldsymbol{\alpha}$, $\boldsymbol{\beta}$, $\boldsymbol{\gamma}$ ...: Second-order tensors and second-order tensor-valued functions. An important exception is $\boldsymbol{\alpha}$ which denotes the generic set of internal variables.

- *Double-barred upper case letters* $\mathbb{A}$, $\mathbb{B}$, $\mathbb{C}$ ...: Fourth-order tensors. An important exception is $\mathbb{R}$ which denotes the set of real numbers.

- *Calligraphic upper case letters* $\mathscr{A}$, $\mathscr{B}$, $\mathscr{C}$ ...: Spaces or sets. Important exceptions are $\mathscr{F}_y$, which denotes the microscopic constitutive functional, $\mathscr{A}$, which denotes the assembly operator in a FE setting, and $\mathscr{L}$, which denotes a Lagrangian function.

Chapter 1

Introduction

The exponential growth of the older population around the world in general, and in developed countries in particular, implies that problems associated with deteriorated mechanical properties of bone are increasing at an alarming rate, with osteoporosis being the most common cause for bone fracture in elderly population. Osteoporosis is three times more common in women than in men, especially after menopause. An increase in life expectancy means that women now live more than a third of their lives after menopause, and this number is increasing (World Health Organisation, 2003).

World Health Organisation (2003) states that Osteoporosis affects more than 75 million people in Europe, Japan and USA, and that it causes more than 2.3 million fractures annually in Europe and USA alone. Hip, vertebral and forearm fractures were estimated to potentially affect 40% of the population at some point in their lifetime, a percentage similar to coronary heart diseases. Hip fractures are the most severe type as they are associated with a high degree of morbidity and a significant mortality (Sambrook and Cooper, 2006; World Health Organisation, 2003). Osteoporosis is not only affecting life quality but also results in significant economic burden. For instance, in England and Wales, the cost was estimated at £942 million each year (Torgerson and Cooper, 1998). In USA, direct medical expenses on fracture were estimated to be around $14 billion in 1995 (Ray et al., 1997). These costs are mainly attributed to classic osteoporotic fractures (Johnell, 1997).

As mentioned in the previous paragraph, bone fractures are most common in anatomic sites with a large proportion of trabecular bone. Bone fractures can be predicted through a proper assessment of bone strength. The current bone strength assessment gold standard for low radiation methods is dual energy X-ray absortiometry (DXA) (Dall'Ara et al., 2012), because of its low cost, high reliability and ease of use (Bergot et al., 2001). It measures areal bone mineral density (aBMD). Some experimental studies have shown that the strength of bone is affected by bone mineral

density (BMD) (Siris et al., 2004), which remains as the prime predictor, by the quality of bone (Ammann and Rizzoli, 2003; McDonnell et al., 2007), by its micro-architecture (Ciarelli et al., 2000; Homminga et al., 2004), by possible accumulations of existing micro-damage (Bouxsein, 2003; Wenzel et al., 1996), and by the properties of the solid phase of trabecular bone (Boivin et al., 2000).

Implants are in a constant development and are nowadays expected to work in problematic environments, such as extremely debilitated osteoporotic trabecular bone or under more extreme loading conditions, such as those derived from more active lifestyles. Implants are also expected to last longer due to the increase in the life expectancy of people. Therefore, correct design and mechanical assessment under physiological conditions are needed. By evaluating the strength of bone, and thus assessing its nonlinear mechanical properties, implants acting under these physiological environments may be properly evaluated, which may significantly improve their design features and thus their performance.

The finite element method (FEM) is a widely employed numerical technique used to solve partial differential equations (PDE) numerically. This technique is hugely utilised in engineering, but particularly in solid mechanics, with bone mechanics being a subfield of solid mechanics in which FEM is widely used to evaluate the behaviour of bone and bone-implant systems. At the macroscopic level, finite element (FE) simulations have been used in a vast range of applications, from prediction of bone fracture (Schileo et al., 2008; Ural and Vashishth, 2007), hip arthroplasty (Phillips et al., 2006; Terrier et al., 2014), total knee replacement (Au et al., 2005; Conlisk et al., 2015), limb fracture fixation (Donaldson et al., 2012; Watson et al., 2007), or pure constitutive modelling of nonlinear phenomena (Garcia et al., 2009; Wolfram et al., 2012). Homogenised FE models have the potential to include the microstructural information in macroscopic models and thus account for all known bone strength affecting factors, and can improve bone strength assessment over traditional BMD-based methods (Dall'Ara et al., 2013, 2012).

At the microscopic level, micro-FE (μFE) simulations have been primarily used to assess the macroscopic stiffness tensor of bone (Donaldson et al., 2011; van Rietbergen et al., 1996, 1995) and, more recently, to assess the macroscopic yield surface (Bayraktar et al., 2004a; Rincón-Kohli and Zysset, 2009; Sanyal et al., 2015; Wolfram et al., 2012). These μFE models are created by converting each voxel from a set of micro-computed tomography (μCT) scans to a trilinear hexahedron element.

The technique used in these μFE simulations to upscale properties from the micro- to the macroscale is homogenisation (de Souza Neto and Feijóo, 2008; Hill, 1972; Perić et al., 2011; Wang et al., 2009; Wolfram et al., 2012). This technique relies

on the averaging of stresses and strains over a representative volume element (RVE) to represent the continuum material properties. This RVE has a characteristic length which is much smaller than the characteristic length of the continuum, which in this study would be bone at the organ level, but at the same time much larger than the size of the microstructural features (Wang et al., 2009), which in this study would be trabeculae and pores[1]. Hill (1963) stated that the RVE is structurally entirely typical of the whole mixture on average, and contains a sufficient number of inclusions for the apparent overall moduli to be effectively independent of the surface values of traction and displacement, as long as these values are "macroscopically uniform". Due to the considerable size of the features present in the microstructure of trabecular bone, and since the macroscopic level is not much larger than the scale at which trabeculae become discernible, the material sample window of trabecular bone is smaller than a proper RVE and thus, from now onwards, it will be called a volume element (VE), which can be used to obtain *apparent* properties, instead of *effective* properties. These apparent properties are dependent on the size of the considered specimen and also on the boundary conditions used (Wang et al., 2009).

Needless to say, the results of any FE system are strongly dependant upon the modelling assumptions: geometry, material properties and (natural and essential) boundary conditions (BC). Due to the limitations in acquiring experimental data from biological systems, robust data regarding any of these features can be extremely challenging to obtain. At the microscale, the problem of obtaining appropriate geometry has been almost completely solved since μCT scans can obtain a precise description of the microstructure of trabecular bone and the only remaining problem is the lack of objectivity of the binarisation procedure, which is the process of converting a gray-scale image to a black-and-white image, so that only solid and void phases are represented. Most of the binarisation approaches are not fully automatic as they require some interaction with the user (Gómez et al., 2013). BCs at the microscale are usually considered within the framework of homogenisation-based multiscale analysis. Several studies have defined the effects of different BCs on the macroscopic stiffness tensor (Pahr and Zysset, 2008; Wang et al., 2009) and one has studied their effect on the macroscopic yield surface (Panyasantisuk et al., 2015b).

The focus of this study is on material properties, specifically on the constitutive model of trabecular bone at the macroscale. As previously mentioned, homogenised trabecular bone models can improve the assessment of bone strength (Dall'Ara et al., 2013, 2012) but since the outcome of a FE system considerably depends on the material

[1] A more thorough description of the characteristic lengths of the scales involved in this study is given in Section 3.1 of Chapter 3.

properties, these need to be adequately defined. Due to the hierarchical nature of bone (Fratzl and Weinkamer, 2007; Wang and Gupta, 2011), the mechanical properties at each of its scales are interlinked and therefore multiscale analyses should be considered if precise material properties at the macroscale need to be defined. An important consideration to take into account is the relatively limited experimental data on the mechanical behaviour of the solid phase of trabecular bone, i.e. at the microscopic level. Only a few studies describe the mechanical behaviour of the solid phase, and these mostly comprise of nanoindentation studies (Carnelli et al., 2010; Tai et al., 2006). More recently, experiments at the extracellular level (Luczynski et al., 2015; Schwiedrzik et al., 2014), which is a scale below the microscopic scale, have also been conducted; however, these studies provide limited information about the multiaxial behaviour of the solid phase of trabecular bone.

The solid phase is modelled in this study by using a phenomenological approximation at the microscale, i.e. based on the mechanical response in an average sense (de Souza Neto et al., 2008), without taking into account the effects of mechanisms at lower scales. Since it is recognised that the macroscopic anisotropy of trabecular bone is largely a consequence of its anisotropic microstructure, a micromechanical approach is considered at the macroscale, i.e. the macroscopic effect of this microstructure is studied by means of homogenisation techniques (de Souza Neto et al., 2008; Perić et al., 2011).

While macroscopic elastic properties of trabecular bone have been extensively assessed using homogenisation in previous studies (Donaldson et al., 2011; Pahr and Zysset, 2008; van Rietbergen et al., 1996, 1995; Wang et al., 2009; Zysset, 2003), only a few studies have assessed its macroscopic yield and post-yield behaviour by means of homogenisation techniques (Bayraktar et al., 2004a; Panyasantisuk et al., 2015b; Sanyal et al., 2015; Wolfram et al., 2012). These previous studies either used simplified models for the solid phase, e.g. by employing an asymmetric strength criterion in principal strain space (Bayraktar et al., 2004a; Sanyal et al., 2015; Wolfram et al., 2012), and/or considered only a few load cases to represent the whole six-dimensional multiaxial description of the yield surface (Panyasantisuk et al., 2015b; Wolfram et al., 2012) (if the considered sample is described in a three-dimensional Euclidean space, taking into account the symmetry of the considered stress or strain second-order tensor implies that the tensor space is six-dimensional; the corresponding yield surface is a five-dimensional hypersurface in such a space). Furthermore, the macroscopic multiaxial post-yield behaviour of trabecular bone has not yet been assessed in the context of homogenisation-based multiscale modelling. This means that none of the previous

studies considered the assessment of damage or hardening at the macroscale by using this multiscale technique.

1.1 Structure of the thesis

This dissertation is divided into eight chapters and a brief description of the content of each of the remaining chapters is as follows.

Chapter 2 reviews the literature that is relevant to this topic. It focuses on the morphology and mechanical behaviour of trabecular bone at the microscale and macroscale. The mechanical behaviour in the elastic and post-elastic regimes is discussed, with a special emphasis on plasticity and damage applied to trabecular bone.

Chapter 3 considers multiscale modelling and concepts of computational plasticity and damage. The multiscale method presented here is homogenisation. Numerical algorithms for integration of evolution equations for damage and plasticity are then developed and compared.

Chapter 4 discusses FEM and high performance computing (HPC). The FEM is described in both infinitesimal and finite strain regimes and its computer implementation is explained. Key topics associated with HPC are discussed, including the software used (ParaFEM), a brief introduction to the hardware, and the developed driver program for finite strain elastoplasticity.

Chapter 5 describes the study of the effect of the solid phase yield surface on the macroscopic behaviour of trabecular bone. Several load cases are investigated and conclusions are drawn by separating these load cases into specific sets.

Chapter 6 describes the study of the macroscopic yield surface of trabecular bone. A similar set of load cases to those employed in Chapter 5 is used, and a minimisation procedure is employed to find a closed-form expression which minimises a fitting error. Several symmetry cases (isotropy, orthotropy and full anisotropy) are investigated.

Chapter 7 describes the study of the post-yield behaviour of trabecular bone. A full set of uniaxial cases (three tensile, three compressive and three shear) is used to investigate the hardening and damage behaviour at the macroscale, starting from an assumption of a solid phase constitutive law, for a small range of plastic strains.

Chapter 8 outlines the conclusions which can be drawn from this study, with a special emphasis on the macroscopic mechanical behaviour of trabecular bone. Then the future work which could be performed in near and distant futures is also outlined.

Chapter 2

Literature review

This Chapter reviews the relevant literature on trabecular bone. Its description from a morphological point of view and its mechanical behaviour are discussed. The literature on mechanical properties is discussed at both scales studied: microscale (scale where the trabecular structure can be described in detail) and macroscale (continuum). In the following sections and chapters, trabecular bone at the microscopic level is referred to as *solid phase* or *tissue*, and the mechanical behaviour of trabecular bone at the macroscopic level as *macroscopic* or *apparent*.

2.1 Morphological description of bone

Bone is a hierarchical composite material. At the nanoscale it consists of type I collagen molecules which are periodically reinforced with nanocrystal platelets of hydroxyapatite. This basic unit is periodically arranged within an extra-fibrillar mineral matrix to form mineralised collagen fibrils. These fibrils are then hierarchically organised into lamellae, which are planar layers of bone tissue, with a thickness of around 5 μm. Lamellae are arranged like a rotated plywood structure, where the fibre direction rotates around the axis perpendicular to the layers; this is true for both cortical and trabecular bone (Fratzl and Weinkamer, 2007; Gupta et al., 2005; Hellmich and Ulm, 2002)

The composition of bone at the microscale depends on what macroscopic morphology is being considered, cortical or trabecular. Around 80% of the skeletal mass is cortical, or compact, bone which is mainly found in the shaft of long bones. Trabecular, or cancellous/porous, bone comprises the remaining 20% of the skeletal mass and is typically found in the ends of long bones. This distinction is made because of their macroscopic appearance, with cortical bone resembling a continuum and trabecular bone resembling an open-cell foam. They have different porosities and anisotropies, and in general, different material properties.

Cortical bone is a very dense material, containing porosity of the order of 6% mostly due to the presence of blood vessels (Fratzl and Weinkamer, 2007). These blood vessels are concentrically surrounded by multiple lamellae, forming an osteon, which is the basic building block of cortical bone. These osteons are mainly arranged in parallel arrays following the axial direction of the bone. Trabecular bone, which has a porosity with an average value of around 80%, consists of a large lattice of plates and rods known as trabeculae. The porous space between trabeculae is filled with marrow and living cells. Trabeculae are composed of the same material as cortical bone, but its arrangement is not in osteons, but in bone packets with different mineral content. They contain some microporosity due to the presence of osteocyte (bone cells) lacunae, which are channels thinner than the blood vessels in osteons; these lacunae are linked between them and to the exterior by even thinner channels, called canaliculi (Fratzl and Weinkamer, 2007; Weiner and Wagner, 1998). At the nanoscopic level, collagen fibrils and mineral particles forming trabecula closely follow their orientation (Cowin, 2001; Jaschouz et al., 2003; Roschger et al., 2001).

The microstructure, or microarchitecture, of trabecular bone has been studied at an approximate resolution of 20 μm (Cowin, 2001; Sanyal et al., 2015). This microstructure is not random as it is linked to mechanical usage by adaptation through Wolff's law (Wolff, 1870), targeting its optimum functioning as a load carrying system. There is a wide variety of methods to quantify the microstructure of trabecular bone, including 2D histomorphometric methods or 3D reconstruction methods. This study will focus on bone volume over total volume fraction (BV/TV) and fabric assessed through the mean intercept length (MIL) fabric tensor, as these are the two most common parameters used to formulate closed-form expressions of the macroscopic mechanical behaviour of trabecular bone (Cowin, 1986; Harrigan and Mann, 1984; Odgaard et al., 1997; Turner et al., 1990; Wolfram et al., 2012; Zysset, 2003). BV/TV is probably the most basic quantifier of trabecular bone and it is a term which is often used to represent density, although it has no units. It is defined as the fraction between the volume occupied by the solid phase over the volume occupied by the solid phase plus marrow (Cowin, 2001). MIL is a measure of the anisotropy of the microstructure and is usually expressed as a symmetric second-order tensor, i.e. the fabric tensor (Harrigan and Mann, 1984; Kanatani, 1984; Whitehouse, 1974). MIL is not the only method used to calculate the fabric tensor; two additional widely used methods are the star volume distribution (Cruz-Orive et al., 1992) and the star length distribution (Smit et al., 1998). Note that regardless of the definition of fabric tensor, its principal directions and the macroscopic principal mechanical directions of trabecular bone are closely related (Odgaard et al., 1997).

2.2 Mechanical behaviour of bone

A better understanding of the mechanical properties of trabecular bone improves the assessment of bone strength as fractures frequently occur in regions of trabecular bone (Fratzl and Weinkamer, 2007). Additionally, homogenised FE models may improve the assessment of bone strength (Dall'Ara et al., 2013, 2012) and implant stability prediction (Steiner et al., 2015). For these homogenised models to succeed, they require an accurate description of the microscopic elastic and post-elastic properties of trabecular bone. Note that trabecular bone actually behaves as a visco-elastoplastic material (Gupta et al., 2007; Gupta and Zioupos, 2008; Manda et al., 2016). These viscous contributions originate from the viscosity of the marrow in the voids between trabeculae and also due to the viscous properties of bone tissue itself. However, some studies have suggested that the use of rate-independent models is adequate if strain rates are within the range of physiological strain rates (Cowin, 2001; Garcia et al., 2010), which are around $1\% - 3\%$ per second (Schaffler et al., 1989). Some studies have also suggested that rate-independent models are appropriate if strain rates are around 0.5% per second (Kopperdahl and Keaveny, 1998; Morgan and Keaveny, 2001). In these cases, rate-dependent effects can be safely ignored and several studies involving homogenisation have assumed this (Bayraktar et al., 2004a; Panyasantisuk et al., 2015b; Wolfram et al., 2012).

The solid phase of trabecular bone is usually assumed to be isotropic (Bayraktar et al., 2004a; Kabel et al., 1999; Sanyal et al., 2015; Wolfram et al., 2012) although as discussed in Section 2.1, the solid phase actually behaves as an anisotropic material. However, as Cowin (1997) pointed out, there is little to no error in assuming tissue isotropy: trabeculae are composed of laminated material about their axes, implying transverse isotropy or orthotropy, and since the loading axis is the same as the axis of the trabecula, a beam made of orthotropic material can be reduced to a beam made of isotropic material.

Another common assumption at the solid phase level is homogeneity, i.e. the spatial distribution of properties in the solid phase is constant (Hambli, 2013; van Rietbergen et al., 1995; Verhulp et al., 2008). However, it is well-known that the solid phase of trabecular bone is heterogeneous in mineral content (Blanchard et al., 2013; Fratzl and Weinkamer, 2007; Renders et al., 2008). Although the effect of mineral content on the stiffness has been widely studied in linear μFE models (Bourne and van der Meulen, 2004; Gross et al., 2012; Kaynia et al., 2014), its effect on models including geometrical and material nonlinearities is still unknown.

2.2.1 Elastic behaviour

Physiological strains in bone are usually below 0.3% (Schaffler et al., 1989). When trabecular bone is subjected to macroscopic strains of such magnitude, the mechanical behaviour can be approximated as linear, and bone is considered to remain in the elastic regime (Bayraktar and Keaveny, 2004; Morgan and Keaveny, 2001). Nonetheless, it is important to differentiate between the elastic regimes at the microscale and at the macroscale, as they both have different properties and limits (i.e. yield stresses or strains). These limits are discussed in Section 2.2.2.

As mentioned earlier, the solid phase is commonly described as an isotropic homogeneous material, which can also be considered as linear elastic when the strains are sufficiently low. This isotropy is mainly due to the axis of the material being very close to the loading/trabecular axis (Jaschouz et al., 2003; Roschger et al., 2001). The assumption of solid phase homogeneity is also widely used (Bayraktar and Keaveny, 2004; Donaldson et al., 2011; Sanyal et al., 2012) and it has been shown that its effect on the macroscopic elastic properties is minor (Gross et al., 2012; Kaynia et al., 2014). The effect of tissue mineral density (TMD) is included in μFE models by assessing attenuation values from μCT or synchrotron-radiation μCT (SRμCT) scans and then using a hydroxyapatite calibration phantom to convert these attenuation values to density units (Easley et al., 2010; Kaynia et al., 2014). Density values are then typically converted to Young's modulus (E_μ) through a power law and then assigned to each element in the μFE system depending on the element's density (Easley et al., 2010). Although homogeneous μCT-based μFE models have been shown to considerably overestimate the macroscopic stiffness when compared to heterogeneous μCT-based μFE models (Jaasma et al., 2002; Mulder et al., 2007; Renders et al., 2008), it has been recently shown that these heterogeneous models also underestimate the macroscopic stiffness when compared to heterogeneous SRμCT-based μFE models, with the latter ones being considered the gold standard in assessing TMD variation in trabecular bone (Kaynia et al., 2014). The assumption of ignoring TMD heterogeneity at the tissue level is then justified when assessing the macroscopic elastic properties as TMD heterogeneity has a minor effect (Gross et al., 2012; Kaynia et al., 2014).

E_μ has been accurately assessed through nanoindentation experiments, which require the assumption of isotropy and typically assume a Poisson's ratio of 0.3 (Hengsberger et al., 2002; Rho et al., 1997). Hengsberger et al. (2002) provides E_μ for individual human bone lamellae under physiological conditions, ranging from 7.4$\pm$0.45 GPa to 18.5$\pm$4.9 GPa. Wolfram et al. (2010a,b) reported E_μ values of around 12 GPa under wet conditions. Bayraktar et al. (2004a,b) used a combined experimental and numerical approach to calculate specimen-specific E_μ, which consists of finding which

is the macroscopic on-axis (related to the principal axis) elastic modulus (E_0) through a simple compression experiment and through a μFE simulation with an arbitrary E_μ. Then this E_μ is scaled by the factor E_0/E_μ. They reported E_μ of 18.0±2.8 GPa, with a range from 12.1 to 22.2 GPa. It is apparent that there is a considerably broad range of values of E_μ in the literature, with variations arising due to testing methods and conditions.

The macroscopic elastic stiffness of trabecular bone is usually considered orthotropic (Fratzl and Weinkamer, 2007; Odgaard et al., 1997; Ulrich et al., 1998; van Rietbergen et al., 1996), with nine independent parameters. The on-axis E_0 for human bone ranges from 0.3 to 3,000 MPa, spanning four orders of magnitude. It has been reported that BV/TV can explain up to 87% of the variability of the elastic constants, with relative errors ranging from 31% to 71%; adding fabric to the model improves the adjusted coefficients of determination (R^2_{adj}) of the regression by 0.03 to 0.25 and decreases the relative errors by 5% to 27% (Zysset, 2003). Some experimental techniques have been used to evaluate the orthotropic elastic constants of trabecular bone; these include mechanical testing and ultrasonic techniques (Reilly and Burstein, 1975; Snyder and Hayes, 1990; van Buskirk et al., 1981; Yahia et al., 1988). Mechanical experiments have been successful in determining some of the orthotropic elastic constants. Some studies reported orthotropic elastic moduli using multiple uniaxial compression experiments (Goulet et al., 1994; Hodgskinson and Currey, 1990b; Snyder and Hayes, 1990). Ultrasonic methods have a significant advantage over traditional mechanical testing (Ashman et al., 1989; Rho, 1996): smaller and more simply shaped specimens can be used. However, ultrasonic methods require the specification of a mean TMD to evaluate the macroscopic elastic properties, which is a source of limitation since, as previously mentioned, the solid phase is heterogeneous in mineral content (Cowin, 2001).

μFE models have been widely used for evaluating the macroscopic orthotropic stiffness of trabecular bone as they naturally overcome some of the limitations associated with experimental techniques (Ulrich et al., 1998; van Rietbergen et al., 1996, 1995). The procedure to create μFE models is to binarise μCT scans, i.e. to determine what is solid and what is void through image analysis techniques (Gómez et al., 2013) and then assign a hexahedron to every solid voxel. The resulting FE mesh is then subjected to six different strain or stress states: three tensile or compressive load scenarios in directions 1, 2 and 3, and three pure shear load scenarios in planes 12, 13 and 23 (Hollister and Kikuchi, 1992). These tests permit evaluation of the macroscopic stiffness tensor using standard mechanics methodologies for a given set of boundary conditions[1] (Hollister and Kikuchi, 1992; van Rietbergen et al., 1996). Kinematic uniform BCs (KUBC)

[1] Boundary conditions for homogenisation-based multiscale methods are reviewed in Chapter 3.

represent an upper bound while static uniform BCs (SUBC) represent a lower bound (Kanit et al., 2003). The use of periodic BCs (PBC) results in the macroscopic stiffness tensor lying in between these bounds and provides the most realistic prediction (Hollister and Kikuchi, 1992; Kanit et al., 2003; Zysset, 2003). The macroscopic stiffness tensor can be calculated as

$$\mathbb{D}_0^e = \frac{1}{V}\int \mathbb{D}_\mu^e : \mathbb{M}_\mu \, dV, \tag{2.1}$$

where V is the total volume of the considered sample and $\mathbb{D}_\mu^e$ is the tissue elastic stiffness tensor. $\mathbb{M}_\mu$ is the local structure tensor (Hollister and Kikuchi, 1992; Suquet, 1985; van Rietbergen et al., 1996), which relates the strain at each integration point ($\boldsymbol{\varepsilon}_\mu$) of the μFE mesh to the homogeneous strain ($\boldsymbol{\varepsilon}_0$), such that $\boldsymbol{\varepsilon}_\mu = \mathbb{M}_\mu : \boldsymbol{\varepsilon}_0$. A detailed discussion on the structural tensor is included in Section 3.1 of Chapter 3. A matrix representation of the macroscopic orthotropic stiffness tensor can be considered by taking advantage of its symmetries, and thus reducing the number of components from 81 to 36, and further to 21 if the matrix symmetry is considered, such that

$$\begin{aligned}[\mathbb{D}_0^e] &= \begin{bmatrix} \mathbb{D}_{1111} & \mathbb{D}_{1122} & \mathbb{D}_{1133} & \mathbb{D}_{1112} & \mathbb{D}_{1113} & \mathbb{D}_{1123} \\ \mathbb{D}_{2211} & \mathbb{D}_{2222} & \mathbb{D}_{2233} & \mathbb{D}_{2212} & \mathbb{D}_{2213} & \mathbb{D}_{2223} \\ \mathbb{D}_{3311} & \mathbb{D}_{3322} & \mathbb{D}_{3333} & \mathbb{D}_{3312} & \mathbb{D}_{3313} & \mathbb{D}_{3323} \\ \mathbb{D}_{1211} & \mathbb{D}_{1222} & \mathbb{D}_{1233} & \mathbb{D}_{1212} & \mathbb{D}_{1213} & \mathbb{D}_{1223} \\ \mathbb{D}_{1311} & \mathbb{D}_{1322} & \mathbb{D}_{1333} & \mathbb{D}_{1312} & \mathbb{D}_{1313} & \mathbb{D}_{1323} \\ \mathbb{D}_{2311} & \mathbb{D}_{2322} & \mathbb{D}_{2333} & \mathbb{D}_{2312} & \mathbb{D}_{2313} & \mathbb{D}_{2323} \end{bmatrix} \\ &= \begin{bmatrix} e_{11} & e_{12} & e_{13} & \delta_{14} & \delta_{15} & \delta_{16} \\ e_{21} & e_{22} & e_{23} & \delta_{24} & \delta_{25} & \delta_{26} \\ e_{31} & e_{32} & e_{33} & \delta_{34} & \delta_{35} & \delta_{36} \\ \delta_{41} & \delta_{42} & \delta_{43} & e_{44} & \delta_{45} & \delta_{46} \\ \delta_{51} & \delta_{52} & \delta_{53} & \delta_{54} & e_{55} & \delta_{56} \\ \delta_{61} & \delta_{62} & \delta_{63} & \delta_{64} & \delta_{65} & e_{66} \end{bmatrix}, \end{aligned} \tag{2.2}$$

where e_{ij} are the orthotropic coefficients and δ_{ij} are the non-orthotropic coefficients. Each applied $\boldsymbol{\varepsilon}_0$ enables the evaluation of one column of $\mathbb{M}_\mu$ at each integration point, so that $[\mathbb{M}_\mu]_{ij} = \{\boldsymbol{\varepsilon}_\mu\}_i / \{\boldsymbol{\varepsilon}_0\}_j$. If the axes of the considered VE are not aligned with the orthotropic axes, a minimisation procedure needs to be used to rotate the sample to the axes which best represent orthotropy. van Rietbergen et al. (1996) used a function representing the ratio of the squared non-orthotropic coefficients to the squared orthotropic coefficients,

$$Obj = \frac{\sum_{i,j=1}^{6} \delta_{ij}^2}{\sum_{i,j=1}^{6} e_{ij}^2}. \tag{2.3}$$

Note that in a material such as trabecular bone, which is not purely orthotropic, the assumption of orthotropy implies a certain error as the non-orthotropic coefficients are generally non-zero. van Rietbergen et al. (1996) calculated the error associated with this assumption as

$$Error_{ORT} = \|[\mathbb{I}] - [\mathbb{D}_0^e]^{-1}[\mathbb{D}_0^e]\|, \tag{2.4}$$

where $\|(\cdot)\|$ denotes the Euclidean norm of the corresponding matrix, $[\mathbb{I}]$ is the matrix representation of the fourth-order unit tensor defined as $\mathbb{I}_{ijkl} = \delta_{ik}\delta_{jl}$ and δ is the Kronecker Delta.

Some theoretical models have been proposed to describe the relationship between the microstructure of trabecular bone and its macroscopic elastic properties. Zysset (2003) describes one isotropic and four anisotropic models. The isotropic model relates the macroscopic stiffness and macroscopic compliance tensors of the corresponding cellular material with BV/TV (Gibson, 1985). The four anisotropic models add the effect of fabric on the elastic properties (Cowin, 1985; Yang et al., 1998; Zysset, 2003; Zysset et al., 1998). These models typically establish relationships between the μFE-obtained elastic properties of trabecular bone samples, BV/TV and fabric tensors in order to obtain closed-form expressions of the macroscopic stiffness tensor. As an example, $\mathbb{D}_0^e$ obtained through Zysset's model (Zysset et al., 1998) is defined as

$$\begin{aligned}\mathbb{D}_0^e(\rho,\mathbf{M}) = &\sum_{i=1}^{3}(\lambda_0+2\mu_0)\rho^k\, m_i^{2l}\,\mathbf{M}_i\otimes\mathbf{M}_i \\ &+\sum_{\substack{i,j=1\\ i\neq j}}^{3}\lambda_0'\,\rho^k\, m_i^l\, m_j^l\,\mathbf{M}_i\otimes\mathbf{M}_j + \sum_{\substack{i,j=1\\ i\neq j}}^{3}2\mu_0\,\rho^k\, m_i^l\, m_j^l\,\mathbf{M}_i\,\overline{\otimes}\,\mathbf{M}_j\,,\end{aligned} \tag{2.5}$$

where the fabric tensor is defined as $\mathbf{M} = \sum_{i=1}^{3} m_i\,\mathbf{M}_i = \sum_{i=1}^{3} m_i\,(\mathbf{m}_i\otimes\mathbf{m}_i)$, m_i are the strictly positive fabric tensor eigenvalues, $\mathbf{M}_i$ are the normalised fabric eigentensors, $\mathbf{m}_i$ are the normalised fabric eigenvectors, λ_0 and μ_0 are the Lamé constants if $\rho = 1$ and the material was isotropic ($\mathbf{M} = \mathbf{I}$), ρ is BV/TV and λ_0' would be equal to λ_0 if the material was isotropic.

2.2.2 Post-elastic behaviour

Bone shows two main mechanisms of energy dissipation after yield, plastic deformation and damage (Schwiedrzik and Zysset, 2013). Plastic deformation implies that irrecoverable deformation is present in the material and damage implies stiffness degradation (Garcia et al., 2009). This happens for both cortical and trabecular bone (Fondrk et al., 1999; Keaveny et al., 1999); however, in trabecular bone, excessive compressive loads

lead to damage progression, as in microcrack propagation, and further leading to the complete fracture and collapse of trabecula, which may lead to a softening behaviour (Hambli, 2013; Schwiedrzik and Zysset, 2013; Yeh and Keaveny, 2001) and eventual densification (i.e. hardening at very large strains, e.g. larger than 40%) (Hosseini et al., 2012), produced by the contact between collapsing trabecula.

Plastic behaviour

The plastic behaviour of the solid phase of trabecular bone presents strength asymmetry, i.e. a greater strength in compression than in tension (Carnelli et al., 2010; Lucchini et al., 2011; Tai et al., 2006). Tai et al. (2006) suggested that this increased strength in compression can be explained by nanogranular friction between mineral particles. This indicates that bone at the nanoscale behaves as a cohesive-frictional material and that this behaviour could be modelled with a pressure-sensitive yield surface. Tai et al. (2006) suggested that a Mohr-Coulomb yield surface is able to capture some features from nanoindentation experiments on bone. They assessed a yield stress from the fitted pressure-sensitive yield surface of 260 MPa; they also performed macroscopic compression tests in which they reported yield values for cortical bone of 178 MPa. Strength asymmetry at the nanoscale is likely to be upscaled, but these differences in yield stresses have been reported to be caused by heterogeneities and defects, which may weaken the mechanical properties at higher scales. Carnelli et al. (2010) and Lucchini et al. (2011) suggested the use of a Drucker-Prager yield surface instead. They respectively reported uniaxial compressive yield stresses of 182 MPa and 150 MPa. Bayraktar et al. (2004b) calculated the yield strains for the solid phase by using a combined numerical-experimental approach in which μFE simulations and macro-level mechanical testing were used; the resulting yield strains were 0.41% in tension and 0.83% in compression; these values for the yield strains have been used in many recent μFE studies (Panyasantisuk et al., 2015b; Sanyal et al., 2015; Wolfram et al., 2012). Maghous et al. (2009) showed that an isotropic porous material with a Drucker-Prager yield surface for the solid phase reduces to an eccentric-ellipsoid macroscopic yield surface when upscaled, with reduced uniaxial yield values. Consequently, and due to porosity present at every hierarchical scale of bone (Smith et al., 2008), Schwiedrzik and Zysset (2013) suggested that an eccentric-ellipsoid could model the yield surface of bone at different scales.

The macroscopic yield surface of trabecular bone has been modelled in the past by using a wide range of yield surfaces: anisotropic eccentric-ellipsoid, or Tsai-Wu, in stress space (Cowin, 1986; Schwiedrzik et al., 2013; Wolfram et al., 2012); isotropic superellipsoid in principal strain space (Bayraktar et al., 2004a), anisotropic yield

surface in stress space based on Kelvin modes (Arramon et al., 2000), anisotropic halfspace-wise generalised Hill criterion in stress space (Rincón-Kohli and Zysset, 2009), an anisotropic quartic in strain space (Sanyal et al., 2015), and a cuboid in strain space (Pankaj and Donaldson, 2013). Except for the yield criteria defined by Arramon et al. (2000), Bayraktar et al. (2004a), Sanyal et al. (2015), and Pankaj and Donaldson (2013), the remaining are fabric-based. Macroscopic yield surfaces for trabecular bone in strain space have a weak dependency on BV/TV and fabric, as reported by Panyasantisuk et al. (2015b). Matsuura et al. (2008) found that yield strains decrease with increasing fabric eigenvalues in samples with good alignment, and suggested that a high value of fabric in a given direction means that there are long trabeculae along this direction, which are prone to buckling, and therefore yield at earlier strains. Wolfram et al. (2012) suggested that even an isotropic criterion in strain space is not able to reflect the yield behaviour completely as there is still some anisotropy in yield strain values. They also reported that BV/TV can have some effect on yield strains due to the reported p-values, but the slope of the linear regression with respect to density is much smaller than that with respect to fabric, and thus density dependence may be neglected. Pankaj and Donaldson (2013) assumed isotropy and developed an asymmetric multisurface yield criterion in strain space. As an example of one of the most commonly used yield surfaces to represent the macroscopic yield behaviour of trabecular bone, an orthotropic Tsai-Wu yield surface in stress space (Wolfram et al., 2012) is defined as

$$f(\boldsymbol{\sigma}_0) = \boldsymbol{\sigma}_0 : \mathbb{F} : \boldsymbol{\sigma}_0 + \mathbf{F} : \boldsymbol{\sigma}_0 - 1, \tag{2.6}$$

where

$$\mathbf{F} = \sum_{i=1}^{3} \left(\frac{1}{\sigma_{ii}^{+}} - \frac{1}{\sigma_{ii}^{-}} \right) \mathbf{M}_i, \tag{2.7}$$

and

$$\mathbb{F} = \sum_{i=1}^{3} \frac{1}{\sigma_{ii}^{-}\sigma_{ii}^{+}} \mathbf{M}_i \otimes \mathbf{M}_i - \sum_{\substack{i,j=1 \\ i \neq j}}^{3} \frac{\chi_{ij}}{\sigma_{ii}^{-}\sigma_{ii}^{+}} \mathbf{M}_i \otimes \mathbf{M}_j + \sum_{\substack{i,j=1 \\ i \neq j}}^{3} \frac{1}{2\tau_{ij}^{2}} \mathbf{M}_i \overline{\otimes} \mathbf{M}_j, \tag{2.8}$$

where f is the yield surface in stress space, σ_{ii}^{+} are the uniaxial tensile (+) and compressive (-) yield stresses along the axis $\mathbf{e}_i$ $(i = 1,2,3)$, τ_{ij} are the shear stresses in the plane $\mathbf{e}_i\,\mathbf{e}_j$ $(i,j = 1,2,3;\ i \neq j)$, and χ_{ij} are the stress interaction coefficients.

Homogenisation-based multiscale techniques have also been used to assess the macroscopic multiaxial yield behaviour of trabecular bone. However, in the nonlinear regime, more than six simulations per sample are needed to approximate the whole yield envelope. Strain interactions are expected, such as interactions between normal

components or the cellular solid-like behaviour in combined normal and shear cases (Fenech and Keaveny, 1999; Sanyal et al., 2015). Only a few studies have employed this powerful technique to determine the macroscopic yield surface of trabecular bone (Bayraktar et al., 2004a; Panyasantisuk et al., 2015b; Sanyal et al., 2015; Wolfram et al., 2012). Bayraktar et al. (2004a), Sanyal et al. (2015) and Wolfram et al. (2012) used 3, 10 and 15 samples respectively, with the first using only high BV/TV (28% to 38%) samples and the latter only covering low BV/TV (6% to 15%) samples. Panyasantisuk et al. (2015b) and Wolfram et al. (2012) used 17 load cases, a number which is much smaller when compared to the 297 and 231 load cases of Bayraktar et al. (2004a) and Sanyal et al. (2015), respectively. All of these studies used the same yield behaviour, a bilinear model (Bayraktar and Keaveny, 2004), except Panyasantisuk et al. (2015b) who used an approximated Drucker-Prager criterion. With respect to BCs, Panyasantisuk et al. (2015b) investigated the effect of BCs on the macroscopic yield behaviour of trabecular bone and found that KUBCs present an upper bound of the yield surface, with this effect being more pronounced when the yield surface is defined in stress space.

Needless to say, the homogenised macroscopic behaviour is likely to depend on the assumptions made at the solid phase level, i.e. different solid phase constitutive laws will reflect different macroscopic behaviours; which is why it is important to define these appropriately. To the author's knowledge, only one study has compared the effect of different solid phase pressure-dependent yield surfaces on the macroscopic behaviour of trabecular bone (Baumann et al., 2016). This study concluded that the macroscopic mechanical behaviour is relatively insensitive to the solid phase yield criterion and inclusion of an appropriate strength asymmetric model is adequate. They also stated that it is unlikely to be able to validate a solid phase constitutive law from macro-level experiments alone due to the reported insensitivity of the results.

Damage behaviour

Jepsen and Davy (1997) and Fondrk et al. (1999) quantified the effect of damage mechanisms on the macroscopic behaviour of cortical bone and Keaveny et al. (1994, 1999) quantified it for trabecular bone. Both types of bone exhibit a degradation in their elastic properties as overloading occurs. Although the lamellar organisation in cortical and trabecular bone is different, they share a similar nanostructure (Garcia et al., 2009; Rho et al., 1998), and therefore it has been suggested that damage originates at the nanoscopic level. There is some experimental evidence of damage mechanisms at the microscale and nanoscale (Gupta et al., 2006; Lucchini et al., 2011; Zhang et al., 2010). Gupta et al. (2006) showed that there is a decohesion between the mineralised collagen fibrils and the interfibrillar matrix, suggesting diminished elastic properties

after yield (Schwiedrzik and Zysset, 2013). Zhang et al. (2010) showed that the decrease in modulus is related to an increasing load and contact area in indentation studies. Some of these experimental findings were successfully recreated with FE simulations using a coupled plastic-damage constitutive model (Lucchini et al., 2011; Zhang et al., 2010). However, it has been suggested that special care must be taken when extracting elasto-plastic properties of a material from a force-displacement indentation curve as materials with significantly different properties may result in very similar curves (Chen et al., 2007). For a more accurate micro-mechanical description, some studies have quantified microscopic damage by using different staining agents which allows for labelling of pre-existing damage and damage caused by an *in vitro* mechanical overloading (Hernandez et al., 2014; Lambers et al., 2014).

Several computational damage models have been proposed for bone at the microscale (Lucchini et al., 2011; Ramtani and Zidi, 2001; Schwiedrzik and Zysset, 2013; Zhang et al., 2010). Ramtani and Zidi (2001) derived a theoretical model to simulate the effect of damage on bone adaptation; however, full experimental validation of all required constants is needed and both damage and adaptation are two processes which are not fully understood yet, even less so their interaction. In both Zhang et al. (2010) and Lucchini et al. (2011), the elastic region is bounded by a Drucker-Prager-like yield surface. In Lucchini et al. (2011), the damage scalar variable is governed by an equivalent plastic strain and in Zhang et al. (2010) the damage variable is governed by equivalent plastic strains in tension and compression, which respectively depend on the maximum and minimum eigenvalues of the plastic strain second-order tensor ($\boldsymbol{\varepsilon}^p$). Schwiedrzik and Zysset (2013) developed a visco-plastic damage constitutive model for bone, which is applicable at several scales, from the nano to the macroscale. However, the small amount of porosity present in some scales may imply that the yield onset is better described with a surface without a yield limit in hydrostatic compression, such as Mohr-Coulomb or Drucker-Prager (Carnelli et al., 2010; Tai et al., 2006).

Apparent damage behaviour has been modelled in only a few studies (Garcia et al., 2009; Schwiedrzik and Zysset, 2013; Zysset and Curnier, 1996). Zysset and Curnier (1996) described a continuum damage model with fabric-based elasticity. The model features isotropic hardening and the yield criterion has the same symmetry as the elastic space. Garcia et al. (2009) created a macroscopic damage constitutive model which is applicable to both cortical and trabecular bone. It features a halfspacewise Hill criterion damage onset, an anisotropic ellipsoid yield surface and isotropic hardening. Schwiedrzik and Zysset (2013) used an eccentric-ellipsoid to define yield and damage onsets, with nonlinear isotropic hardening. All these studies feature a scalar damage variable, implying isotropic damage behaviour.

2.2.3 Bovine vs. human trabecular bone

The biomechanical properties of bone tissue varies considerably between species, even amongst mammalians, and are strongly related to the size of the considered animal. For instance, mice do not have osteons (Carriero et al., 2014). In this study, bovine trabecular bone was used due to its easy accessibility. One might argue that bovine trabecular bone is not as relevant as human trabecular bone, especially since one of the aims of this study is to establish predictive criteria for load scenarios such as implant loosening and bone strength; situations which are relevant almost exclusively for humans.

However, Poumarat and Squire (1993) evaluated the stress-strain curves from bovine and human trabecular bone samples, and they found that the stress-strain curves and ultimate strengths did not differ significantly between species. Only differences in Young's modulus were found. Hodgskinson and Currey (1990a,b) found that up to 94% of the observed variation in the measured apparent Young's modulus of bovine and human trabecular bone could be explained by a composite measure of BV/TV, trabecular orientation, and ratio of anisotropy. These results suggest that the elastic and failure properties of both bovine and human trabecular bone may be studied solely on the base of BV/TV and fabric, and that trabecular bone of both species indeed have comparable mechanical properties.

Chapter 3

Multiscale modelling and plasticity

This Chapter introduces the concepts of homogenisation-based multiscale modelling, plasticity and damage. These form the basis for the following chapters.

3.1 Homogenisation-based multiscale modelling

This Section briefly describes homogenisation-based multiscale theory and largely follows the work and notation of de Souza Neto and Feijóo (2006), Perić et al. (2011), and Nguyen et al. (2012). The theory outlined in this Section is based on linear kinematics, and thus the infinitesimal stress-strain conjugate pair is used. However, a finite strain extension can be implemented as discussed in de Souza Neto and Feijóo (2008).

This theory will be discussed in a general sense with a further progressive refinement to specifically deal with the material studied in this thesis, trabecular bone, and the assumptions made. Quasi-static approach is used in this study, and body forces and viscous effects are neglected as an approximation. Trabecular bone is a biphasic material, with solid and void phases. Marrow is contained in the void phase, and is a soft compressible material; thus the assumption that the marrow does not exert any traction force upon the solid phase through the solid-void interface is taken into account (Lacroix and Prendergast, 2002).

Every point $\mathbf{x}$ in the macroscopic continuum is associated to a local RVE with a domain Ω_μ and a boundary $\partial\Omega_\mu$ (Fig. 3.1). The size of the microscopic domain (l_μ) is much smaller than the characteristic length (l) of the macroscopic continuum; this difference in length in general engineering materials ranges from three to five orders of magnitude, typically. However, in the case of trabecular bone this separation in scales is much smaller, of around two orders of magnitude (from tens to hundreds of micrometres in the microscale to a few millimetres in the macroscale), and this is why

the macroscopic response is usually largely dependent on both the boundary conditions used for the RVE (thus a trabecular bone RVE becomes a VE) and the size of the considered VE, as it is discussed in Section 3.1.4 and Wang et al. (2009). The domain Ω_μ of the RVE consists of solid (Ω_μ^s) and void (Ω_μ^v) parts, such that

$$\Omega_\mu = \Omega_\mu^s \cup \Omega_\mu^v. \tag{3.1}$$

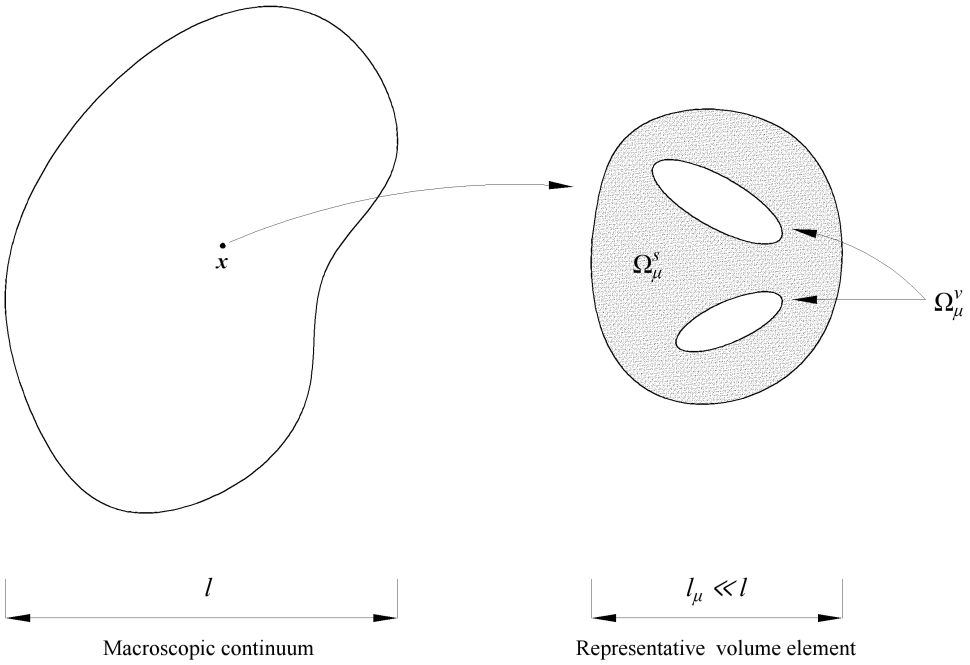

Fig. 3.1 Macroscopic continuum with the associated local microstructure.

The external boundaries are defined as

$$\partial\Omega_\mu = \partial\Omega_\mu^{s\,ext} \cup \partial\Omega_\mu^{v\,ext}, \tag{3.2}$$

where $\partial\Omega_\mu^{s\,ext}$ and $\partial\Omega_\mu^{v\,ext}$ are respectively $\partial\Omega_\mu \cap \partial\Omega_\mu^s$ and $\partial\Omega_\mu \cap \partial\Omega_\mu^v$, i.e. the external boundaries for the solid and void phases. With respect to the internal boundaries, the following relationships can be defined:

$$\begin{aligned} \partial\Omega_\mu^s &= \partial\Omega_\mu^{s\,ext} \cup \partial\Omega_\mu^{s\,int}, \\ \partial\Omega_\mu^v &= \partial\Omega_\mu^{v\,ext} \cup \partial\Omega_\mu^{v\,int}, \end{aligned} \tag{3.3}$$

where $\partial\Omega_\mu^{s\,int} = \partial\Omega_\mu^{v\,int}$. This distinction of internal and external boundaries is significant to the material considered in this study. The internal boundaries are in contact with the marrow and appropriate assumptions are made in the following sections with

respect to its mechanical behaviour. The external boundaries are significant when the relevant BCs are considered within a homogenisation-based multiscale setting.

3.1.1 RVE equilibrium

The RVE is in constant equilibrium for each instant t of its deformation history. It is subjected to an external traction field ($\mathbf{t}_\mu^{ext}$) applied to $\partial\Omega_\mu$. The principle of Virtual Work establishes that the RVE is in equilibrium if the following variational equation holds:

$$\int_{\Omega_\mu} \boldsymbol{\sigma}_\mu(\mathbf{y},t) : \nabla^{sym}\boldsymbol{\eta}\, \mathrm{d}V - \int_{\partial\Omega_\mu} \mathbf{t}_\mu^{ext}(\mathbf{y},t)\cdot\boldsymbol{\eta}\, \mathrm{d}A = 0 \quad \forall\boldsymbol{\eta}\in\mathscr{V}, \tag{3.4}$$

where $\boldsymbol{\sigma}_\mu$ are the microscopic stresses, $\mathbf{y}$ are the local coordinates of the RVE, t is (pseudo-) time, ":" is the double contraction defined as $\mathbf{A}:\mathbf{B}\rightarrow A_{ij}B_{ij}$, ∇^{sym} is the symmetric gradient operator applied to $(\cdot)$ as in $\nabla^{sym}(\cdot)=\frac{1}{2}[\nabla(\cdot)+\nabla(\cdot)^{\mathrm{T}}]$, $\boldsymbol{\eta}$ are the virtual displacements and $\mathscr{V}$ is an appropriate space of virtual displacements of the RVE. An alternative strong form of Eq. 3.4 can be written as

$$\begin{cases} \operatorname{div}\boldsymbol{\sigma}_\mu(\mathbf{y},t)=0 & \forall\mathbf{y}\in\Omega_\mu \\ \boldsymbol{\sigma}_\mu(\mathbf{y},t)\mathbf{n}=\mathbf{t}_\mu^{ext}(\mathbf{y},t) & \forall\mathbf{y}\in\partial\Omega_\mu \\ [\![\boldsymbol{\sigma}_\mu(\mathbf{y},t)\mathbf{n}^{v\,int}]\!]=0 & \forall\mathbf{y}\in\partial\Omega_\mu^{v\,int} \end{cases}, \tag{3.5}$$

where $\mathbf{n}$ is the unit normal vector to $\partial\Omega_\mu$, $\mathbf{n}^{v\,int}$ is the unit normal vector to $\partial\Omega_\mu^{v\,int}$, and $[\![\boldsymbol{\sigma}_\mu(\mathbf{y},t)\mathbf{n}^{v\,int}]\!]$ is the jump equation of the corresponding vector field across $\partial\Omega_\mu^{v\,int}$. Further refinements of Eq. 3.4 can be performed in order to obtain a more thorough decomposition of its terms. For instance, taking into account that pores might be filled with fluid and that these might be pressurised enough to substantially contribute to the mechanical behaviour of the RVE, the following is obtained:

$$\begin{aligned} &\int_{\Omega_\mu^s} \boldsymbol{\sigma}_\mu(\mathbf{y},t) : \nabla^{sym}\boldsymbol{\eta}\, \mathrm{d}V + \int_{\Omega_\mu^v} \boldsymbol{\sigma}_\mu(\mathbf{y},t) : \nabla^{sym}\boldsymbol{\eta}\, \mathrm{d}V \\ &- \int_{\partial\Omega_\mu^{s\,ext}} \mathbf{t}_\mu^{ext}(\mathbf{y},t)\cdot\boldsymbol{\eta}\, \mathrm{d}A - \int_{\partial\Omega_\mu^{v\,ext}} \mathbf{t}_\mu^{ext}(\mathbf{y},t)\cdot\boldsymbol{\eta}\, \mathrm{d}A = 0 \quad \forall\boldsymbol{\eta}\in\mathscr{V}. \end{aligned} \tag{3.6}$$

The voids are also in equilibrium through Eq. 3.4, resulting in the following expression:

$$\int_{\Omega_\mu^v} \boldsymbol{\sigma}_\mu(\mathbf{y},t) : \nabla^{sym}\boldsymbol{\eta}\, \mathrm{d}V - \int_{\partial\Omega_\mu^{v\,int}} \mathbf{t}_\mu^{v}(\mathbf{y},t)\cdot\boldsymbol{\eta}\, \mathrm{d}A - \int_{\partial\Omega_\mu^{v\,ext}} \mathbf{t}_\mu^{ext}(\mathbf{y},t)\cdot\boldsymbol{\eta}\, \mathrm{d}A = 0 \quad \forall\boldsymbol{\eta}\in\mathscr{V}, \tag{3.7}$$

where $\mathbf{t}_\mu^v$ is the void traction field, i.e. the traction exerted by the fluid upon the solid part through the solid-void interface. By substituting Eq. 3.7 into Eq. 3.6, the following

expression is recovered:

$$\begin{aligned}&\int_{\Omega_\mu^s} \boldsymbol{\sigma}_\mu(\mathbf{y},t) : \nabla^{sym}\boldsymbol{\eta}\ \mathrm{d}V - \int_{\partial\Omega_\mu^{s\,ext}} \mathbf{t}_\mu^{ext}(\mathbf{y},t)\cdot\boldsymbol{\eta}\ \mathrm{d}A \\ &+ \int_{\partial\Omega_\mu^{v\,int}} \mathbf{t}_\mu^{v}(\mathbf{y},t)\cdot\boldsymbol{\eta}\ \mathrm{d}A = 0 \quad \forall\boldsymbol{\eta}\in\mathscr{V}.\end{aligned} \tag{3.8}$$

An additional simplification can be considered, which is that the void does not exert traction forces on the solid phase (the marrow is a soft compressible material which would exert minimal forces to the solid phase), which results in

$$\int_{\Omega_\mu^s} \boldsymbol{\sigma}_\mu(\mathbf{y},t) : \nabla^{sym}\boldsymbol{\eta}\ \mathrm{d}V - \int_{\partial\Omega_\mu^{s\,ext}} \mathbf{t}_\mu^{ext}(\mathbf{y},t)\cdot\boldsymbol{\eta}\ \mathrm{d}A = 0 \quad \forall\boldsymbol{\eta}\in\mathscr{V}. \tag{3.9}$$

Equation 3.9 is the final expression of the principle of virtual work at the microscale, which is relevant to trabecular bone due to the considered assumptions.

3.1.2 Averaging of strain and stress

At any instant t, the macroscopic strain ($\boldsymbol{\varepsilon}_0$) and macroscopic stress ($\boldsymbol{\sigma}_0$) tensors at point $\mathbf{x}$ of the macroscopic continuum are respectively defined as the volume averages of the microscopic strain ($\boldsymbol{\varepsilon}_\mu$) and microscopic stress ($\boldsymbol{\sigma}_\mu$) tensor fields over Ω_μ, resulting in

$$\boldsymbol{\varepsilon}_0(t) = \frac{1}{V}\int_{\Omega_\mu} \boldsymbol{\varepsilon}_\mu(\mathbf{y},t)\ \mathrm{d}V \tag{3.10}$$

and

$$\boldsymbol{\sigma}_0(t) = \frac{1}{V}\int_{\Omega_\mu} \boldsymbol{\sigma}_\mu(\mathbf{y},t)\ \mathrm{d}V. \tag{3.11}$$

Equation 3.10 can be further developed by using $\boldsymbol{\varepsilon}_\mu = \nabla^{sym}\mathbf{u}_\mu$ and the divergence theorem, resulting in

$$\begin{aligned}\boldsymbol{\varepsilon}_0(t) &= \frac{1}{V}\int_{\Omega_\mu} \boldsymbol{\varepsilon}_\mu(\mathbf{y},t)\ \mathrm{d}V \\ &= \frac{1}{V}\Big(\int_{\partial\Omega_\mu^{s\,ext}} \mathbf{u}_\mu(\mathbf{y},t)\otimes^{sym}\mathbf{n}\ \mathrm{d}A + \int_{\partial\Omega_\mu^{v\,ext}} \mathbf{u}_\mu(\mathbf{y},t)\otimes^{sym}\mathbf{n}\ \mathrm{d}A \\ &+ \int_{\partial\Omega_\mu^{s}\cap\partial\Omega_\mu^{v}} \mathbf{u}_\mu(\mathbf{y},t)\otimes^{sym}\mathbf{n}^{s\,int}\ \mathrm{d}A + \int_{\partial\Omega_\mu^{v}\cap\partial\Omega_\mu^{s}} \mathbf{u}_\mu(\mathbf{y},t)\otimes^{sym}\mathbf{n}^{v\,int}\ \mathrm{d}A\Big),\end{aligned} \tag{3.12}$$

where $\otimes^{sym}$ is the symmetric tensor product, defined as $\mathbf{u}\otimes^{sym}\mathbf{v} = \frac{1}{2}(\mathbf{u}\otimes\mathbf{v}+\mathbf{v}\otimes\mathbf{u}) \to \frac{1}{2}(u_i v_j + v_i u_j)$, and $\mathbf{n}^{s\,int}$ and $\mathbf{n}^{v\,int}$ are respectively the outward unit normals to $\partial\Omega_\mu^{s\,int}$ and $\partial\Omega_\mu^{v\,int}$. By observing that $\mathbf{n}^{s\,int} = -\mathbf{n}^{v\,int}$ at $\partial\Omega_\mu^s\cap\partial\Omega_\mu^v$, the final expression of

the macroscopic strain can be recovered as (Nguyen et al., 2012)

$$\boldsymbol{\varepsilon}_0(t) = \frac{1}{V}\int_{\partial\Omega_\mu} \mathbf{u}_\mu(\mathbf{y},t) \otimes^{sym} \mathbf{n}\, \mathrm{d}A. \tag{3.13}$$

Equation 3.11 can be further developed by using the tensor relation:

$$\int_\Omega \mathbf{S}(\nabla \mathbf{v})^{\mathrm{T}}\, \mathrm{d}V = \int_{\partial\Omega} (\mathbf{S}\mathbf{n}) \otimes \mathbf{v}\, \mathrm{d}A - \int_\Omega (\operatorname{div} \mathbf{S}) \otimes \mathbf{v}\, \mathrm{d}V. \tag{3.14}$$

By substituting $\mathbf{S}$ for $\boldsymbol{\sigma}_\mu$, $\mathbf{v}$ for $\mathbf{y}$, Ω for Ω_μ, and considering that $\nabla \mathbf{y} = \mathbf{I}$, the following is obtained:

$$\begin{aligned}
\boldsymbol{\sigma}_0(t) &= \frac{1}{V}\int_{\Omega_\mu} \boldsymbol{\sigma}_\mu(\mathbf{y},t)\, \mathrm{d}V \\
&= \frac{1}{V}\Big(\int_{\Omega_\mu^s} \boldsymbol{\sigma}_\mu(\mathbf{y},t)\, \mathrm{d}V + \int_{\Omega_\mu^v} \boldsymbol{\sigma}_\mu(\mathbf{y},t)\, \mathrm{d}V\Big) \\
&= \frac{1}{V}\Big(\int_{\partial\Omega_\mu^{s\,ext}} (\boldsymbol{\sigma}_\mu(\mathbf{y},t)\mathbf{n}^{s\,ext}) \otimes \mathbf{y}\, \mathrm{d}A + \int_{\partial\Omega_\mu^s \cap \partial\Omega_\mu^v} (\boldsymbol{\sigma}_\mu(\mathbf{y},t)\mathbf{n}^{s\,int}) \otimes \mathbf{y}\, \mathrm{d}A \\
&+ \int_{\partial\Omega_\mu^{v\,ext}} (\boldsymbol{\sigma}_\mu(\mathbf{y},t)\mathbf{n}^{v\,ext}) \otimes \mathbf{y}\, \mathrm{d}A + \int_{\partial\Omega_\mu^v \cap \partial\Omega_\mu^s} (\boldsymbol{\sigma}_\mu(\mathbf{y},t)\mathbf{n}^{v\,int}) \otimes \mathbf{y}\, \mathrm{d}A \\
&- \int_{\Omega_\mu^s} (\operatorname{div} \boldsymbol{\sigma}_\mu(\mathbf{y},t)) \otimes \mathbf{y}\, \mathrm{d}V - \int_{\Omega_\mu^v} (\operatorname{div} \boldsymbol{\sigma}_\mu(\mathbf{y},t)) \otimes \mathbf{y}\, \mathrm{d}V \\
&+ \int_{\partial\Omega_\mu^{v\,int}} [\![\boldsymbol{\sigma}_\mu(\mathbf{y},t)\mathbf{n}^{v\,int}]\!] \otimes \mathbf{y}\, \mathrm{d}A\Big).
\end{aligned} \tag{3.15}$$

The last term in Eq. 3.15 is added to ensure traction continuity where the stress field may be discontinuous (e.g. material interfaces). By observing that $\mathbf{n}^{s\,int} = -\mathbf{n}^{v\,int}$ at $\partial\Omega_\mu^s \cap \partial\Omega_\mu^v$ and using Eq. 3.5, the final expression of the macroscopic stress can be recovered:

$$\boldsymbol{\sigma}_0(t) = \frac{1}{V}\int_{\partial\Omega_\mu} (\boldsymbol{\sigma}_\mu(\mathbf{y},t)\mathbf{n}) \otimes \mathbf{y}\, \mathrm{d}A = \frac{1}{V}\int_{\partial\Omega_\mu} \mathbf{t}_\mu^{ext}(\mathbf{y},t) \otimes \mathbf{y}\, \mathrm{d}A. \tag{3.16}$$

From Eq. 3.11, and using the fact that the stress is the linear mapping of the elastic strain through the fourth-order elasticity tensor, and homogeneity of the solid phase properties throughout the RVE and for all time, the following is obtained:

$$\boldsymbol{\sigma}_0(t) = \frac{1}{V}\int_{\Omega_\mu} \boldsymbol{\sigma}_\mu(\mathbf{y},t)\, \mathrm{d}V \rightarrow \mathbb{D}_0^e : \boldsymbol{\varepsilon}_0^e(t) = \frac{1}{V}\int_{\partial\Omega_\mu} \mathbb{D}_\mu^e : \boldsymbol{\varepsilon}_\mu^e(\mathbf{y},t)\, \mathrm{d}V. \tag{3.17}$$

Through the use of the local structure tensor $\mathbb{M}_\mu$, defined as $\boldsymbol{\varepsilon}_\mu(\mathbf{y},t) = \mathbb{M}_\mu(\mathbf{y},t) : \boldsymbol{\varepsilon}_0(t)$ (Hollister and Kikuchi, 1992), on Eq. 3.17, the following is obtained:

$$\mathbb{D}_0^e : \boldsymbol{\varepsilon}_0^e(t) = \frac{1}{V}\int_{\partial\Omega_\mu} \mathbb{D}_\mu^e : \mathbb{M}_\mu(\mathbf{y},t)\, \mathrm{d}V : \boldsymbol{\varepsilon}_0^e(t), \tag{3.18}$$

and therefore $\mathbb{D}_0^e$ is defined as

$$\mathbb{D}_0^e = \frac{1}{V}\int_{\partial\Omega_\mu} \mathbb{D}_\mu^e : \mathbb{M}_\mu(\mathbf{y},t)\, \mathrm{d}V. \tag{3.19}$$

Equation 3.19 is the definition of the elastic stiffness tensor which is used in elastic homogenisation studies to assess the magnitude and symmetries of the elastic mechanical behaviour of trabecular bone at the macroscale (van Rietbergen et al., 1996).

3.1.3 The Hill-Mandel principle of macrohomogeneity

The Hill-Mandel principle of macrohomogeneity (Hill, 1965) establishes that the deformation energy at the microscale and at the macroscale should be equal. It can be stated through

$$\boldsymbol{\sigma}_0(t) : \boldsymbol{\varepsilon}_0(t) = \frac{1}{V}\int_{\Omega_\mu} \boldsymbol{\sigma}_\mu(\mathbf{y},t) : \boldsymbol{\varepsilon}_\mu(\mathbf{y},t)\, \mathrm{d}V. \tag{3.20}$$

The microscopic displacement field ($\mathbf{u}_\mu$) can be decomposed into a mean part ($\mathbf{u}_0$) and a fluctuation with mean equal to zero ($\tilde{\mathbf{u}}_\mu$), resulting in

$$\mathbf{u}_\mu(\mathbf{y},t) = \mathbf{u}_0(\mathbf{y},t) + \tilde{\mathbf{u}}_\mu(\mathbf{y},t) = \boldsymbol{\varepsilon}_0(t)\mathbf{y} + \tilde{\mathbf{u}}_\mu(\mathbf{y},t), \tag{3.21}$$

which results in the corresponding decomposition of strains, in a similar fashion

$$\boldsymbol{\varepsilon}_\mu(\mathbf{y},t) = \boldsymbol{\varepsilon}_0(t) + \tilde{\boldsymbol{\varepsilon}}_\mu(\mathbf{y},t). \tag{3.22}$$

By combining Eq. 3.22 with Eq. 3.20, the following is obtained:

$$\int_{\Omega_\mu} \boldsymbol{\sigma}_\mu(\mathbf{y},t) : \tilde{\boldsymbol{\varepsilon}}_\mu(\mathbf{y},t)\, \mathrm{d}V = 0. \tag{3.23}$$

By using the following two well-known tensorial relationships (Holzapfel, 2000):

$$\begin{aligned} \mathrm{div}\,(\mathbf{A}^{\mathrm{T}}\mathbf{u}) &= (\mathrm{div}\,\mathbf{A})\mathbf{u} + \mathbf{A} : \nabla\mathbf{u}\,, \\ \int_{\partial\Omega} \mathbf{u}\cdot\mathbf{A}\mathbf{n}\, \mathrm{d}A &= \int_{\Omega} \mathrm{div}\,(\mathbf{A}^{\mathrm{T}}\mathbf{u})\, \mathrm{d}V, \end{aligned} \tag{3.24}$$

and Eq. 3.16, a more refined version of the Hill-Mandel principle is obtained as

$$\int_{\partial\Omega_\mu} \mathbf{t}_\mu^{ext}(\mathbf{y},t)\cdot\tilde{\mathbf{u}}_\mu(\mathbf{y},t)\,\mathrm{d}A = 0 \quad \forall\tilde{\mathbf{u}}_\mu \in \mathscr{V}. \tag{3.25}$$

It is important to point out that the displacement fluctuation field $\tilde{\mathbf{u}}_\mu$ and the virtual displacement field $\boldsymbol{\eta}$ coincide (Perić et al., 2011), and thus Eq. 3.9 becomes

$$\int_{\Omega_\mu^s} \boldsymbol{\sigma}_\mu(\mathbf{y},t) : \nabla^{sym}\boldsymbol{\eta}\,\mathrm{d}V = 0 \quad \forall\boldsymbol{\eta} \in \mathscr{V}. \tag{3.26}$$

If Eq. 3.21 is applied to Eq. 3.25, the following is recovered:

$$\boldsymbol{\sigma}_0(t) : \boldsymbol{\varepsilon}_0(t) = \frac{1}{V}\int_{\partial\Omega_\mu} \mathbf{t}_\mu^{ext}(\mathbf{y},t)\cdot\mathbf{u}_\mu(\mathbf{y},t)\,\mathrm{d}A. \tag{3.27}$$

By taking into account Eq. 3.13, Eq. 3.16, the fact that the macroscopic quantities are independent of the RVE coordinates, and $\frac{1}{V}\int_{\partial\Omega_\mu}\mathbf{n}\otimes\mathbf{y}\,\mathrm{d}A = \mathbf{I}$ (Nguyen et al., 2012), the following three equations are obtained:

$$\begin{aligned}
\boldsymbol{\sigma}_0(t) : \boldsymbol{\varepsilon}_0(t) &= \frac{1}{V}\int_{\partial\Omega_\mu} \mathbf{t}_\mu^{ext}(\mathbf{y},t)\cdot(\boldsymbol{\varepsilon}_0(t)\mathbf{y})\,\mathrm{d}A,\\
\boldsymbol{\sigma}_0(t) : \boldsymbol{\varepsilon}_0(t) &= \frac{1}{V}\int_{\partial\Omega_\mu} \mathbf{u}_\mu(\mathbf{y},t)\cdot(\boldsymbol{\sigma}_0(t)\mathbf{n})\,\mathrm{d}A,
\end{aligned} \tag{3.28}$$

and

$$\boldsymbol{\sigma}_0(t) : \boldsymbol{\varepsilon}_0(t) = \frac{1}{V}\int_{\partial\Omega_\mu} (\boldsymbol{\varepsilon}_0(t)\mathbf{n})\cdot(\boldsymbol{\sigma}_0(t)\mathbf{y})\,\mathrm{d}A. \tag{3.29}$$

Equations 3.27 and 3.28 can be combined to yield

$$\begin{aligned}
0 = \frac{1}{V}\int_{\partial\Omega_\mu} \left[\mathbf{t}_\mu^{ext}(\mathbf{y},t)\cdot\mathbf{u}_\mu(\mathbf{y},t) - \mathbf{t}_\mu^{ext}(\mathbf{y},t)\cdot(\boldsymbol{\varepsilon}_0(t)\mathbf{y}) - \mathbf{u}_\mu(\mathbf{y},t)\cdot(\boldsymbol{\sigma}_0(t)\mathbf{n})\right]\mathrm{d}A\\
+ \boldsymbol{\sigma}_0(t) : \boldsymbol{\varepsilon}_0(t).
\end{aligned} \tag{3.30}$$

The last term of the right-hand side can be rewritten by using Eq. 3.29, as

$$\begin{aligned}
0 = \int_{\partial\Omega_\mu} \big[\mathbf{t}_\mu^{ext}(\mathbf{y},t)\cdot\mathbf{u}_\mu(\mathbf{y},t) - \mathbf{t}_\mu^{ext}(\mathbf{y},t)\cdot(\boldsymbol{\varepsilon}_0(t)\mathbf{y}) - \mathbf{u}_\mu(\mathbf{y},t)\cdot(\boldsymbol{\sigma}_0(t)\mathbf{n})\\
+ (\boldsymbol{\varepsilon}_0(t)\mathbf{n})\cdot(\boldsymbol{\sigma}_0(t)\mathbf{y})\big]\,\mathrm{d}A.
\end{aligned} \tag{3.31}$$

Equation 3.31 can be rewritten as

$$\int_{\partial\Omega_\mu} (\mathbf{t}_\mu^{ext}(\mathbf{y},t) - \boldsymbol{\sigma}_0(t)\mathbf{n})\cdot(\mathbf{u}_\mu(\mathbf{y},t) - \boldsymbol{\varepsilon}_0(t)\mathbf{y})\,\mathrm{d}A = 0. \tag{3.32}$$

3.1.4 Boundary conditions of the RVE

Equations 3.25, 3.27 and 3.32 are alternative forms of the Hill-Mandel principle of macrohomogeneity (Eq. 3.20). Equation 3.32 is more convenient for defining the appropriate BCs of the RVE. Needless to say, any chosen set of BCs should satisfy one of these equations in order to be admissible. Three types of BCs are described:

1. *Static uniform boundary conditions (SUBC) or Neumann boundary conditions*
   The external traction field ($\mathbf{t}_\mu^{ext}$) is prescribed on $\partial\Omega_\mu$ in terms of a macroscopic stress, as
   $$\mathbf{t}_\mu^{ext}(\mathbf{y},t) = \boldsymbol{\sigma}_0(t)\mathbf{n} \quad \forall \mathbf{y} \in \partial\Omega_\mu . \tag{3.33}$$

2. *Kinematic uniform boundary conditions (KUBC) or Dirichlet boundary conditions*
   The displacement field ($\mathbf{u}_\mu$) is prescribed on $\partial\Omega_\mu$ in terms of a macroscopic strain, as
   $$\mathbf{u}_\mu(\mathbf{y},t) = \boldsymbol{\varepsilon}_0(t)\mathbf{y} \quad \forall \mathbf{y} \in \partial\Omega_\mu . \tag{3.34}$$

3. *Periodic boundary conditions (PBC)*
   The RVE boundary $\partial\Omega_\mu$ is divided into positive $\partial\Omega_\mu^+$ and negative $\partial\Omega_\mu^-$ parts, with the respective associated normals, $\mathbf{n}^+$ and $\mathbf{n}^-$, so that $\partial\Omega_\mu = \partial\Omega_\mu^+ \cup \partial\Omega_\mu^-$ and $\partial\Omega_\mu^+ \cap \partial\Omega_\mu^- = 0$. For instance, in the case of a cubic RVE, a positive and negative division would be on opposite sides of the cube. The periodicity of displacement fluctuations ($\tilde{\mathbf{u}}_\mu$) and anti-periodicity of external tractions ($\mathbf{t}_\mu^{ext}$) on the RVE boundary are represented as
   $$\begin{aligned} \tilde{\mathbf{u}}_\mu(\mathbf{y}^+,t) &= \tilde{\mathbf{u}}_\mu(\mathbf{y}^-,t) \quad \forall \mathbf{y}^+ \in \partial\Omega_\mu^+ \quad \text{and matching} \quad \mathbf{y}^- \in \partial\Omega_\mu^- , \\ \mathbf{t}_\mu^{ext}(\mathbf{y}^+,t) &= -\mathbf{t}^{ext}(\mathbf{y}^-,t) \quad \forall \mathbf{y}^+ \in \partial\Omega_\mu^+ \quad \text{and matching} \quad \mathbf{y}^- \in \partial\Omega_\mu^- . \end{aligned} \tag{3.35}$$

Using different BCs for the RVE leads to different estimates of the macroscopic response (*apparent* properties vs *effective* properties, with *effective* properties being independent of BCs and size of the RVE). Amongst the described BCs, KUBCs provide the stiffest response (upper bound) and SUBCs provide the most compliant response (lower bound), with the periodic response in between (Wang et al., 2009). Some studies suggest that periodic BCs provide the least biased estimate (Kanit et al., 2003; Terada et al., 2000), in the sense that the macroscopic response is less dependent on BCS and on the size of the RVE.

3.1.5 Microscopic constitutive model

The microscopic constitutive response, ignoring thermal effects, is defined as a relationship between the microscopic stress over the solid domain and the history of the microscopic strain tensor at that point, through a continuum constitutive functional, such as

$$\boldsymbol{\sigma}_\mu(\mathbf{y},t) = \mathscr{F}_y(\boldsymbol{\varepsilon}^t_\mu(\mathbf{y})), \tag{3.36}$$

where the superscript t denotes the history up to instant t, and the subscript y denotes a possible dependency of the constitutive functional on the local coordinates $\mathbf{y}$ of the RVE (i.e. possible heterogeneity of the properties of the solid phase throughout the RVE).

3.1.6 Multiscale constitutive model

The infinitesimal multiscale constitutive model is completely defined by (de Souza Neto and Feijóo, 2010; Perić et al., 2011):

1. Definition of the domain $\Omega_\mu = \Omega^s_\mu \cup \Omega^v_\mu$ and the microscopic constitutive law $\mathscr{F}_y$ (Section 3.1.5).
2. Choice of an appropriate set of BCs for the RVE (Section 3.1.4).
3. Choice of the resulting multiscale constitutive functional:
   (a) Microscopic equilibrium problem, which is defined as
   "Given the history of the macroscopic infinitesimal strain tensor $\boldsymbol{\varepsilon}_0$ find the field $\tilde{\mathbf{u}}_\mu \in \mathscr{V}$ such that, for each t,

$$\int_{\Omega^s_\mu} \mathscr{F}_y\{[\boldsymbol{\varepsilon}_0(t) + \nabla^{sym}\tilde{\mathbf{u}}_\mu(\mathbf{y},t)]^t\} : \nabla^{sym}\boldsymbol{\eta}\, dV = 0 \quad \forall \boldsymbol{\eta} \in \mathscr{V}." \tag{3.37}$$

   (b) Macroscopic stress tensor evaluation

$$\boldsymbol{\sigma}_0(t) = \frac{1}{V}\int_{\Omega^s_\mu} \boldsymbol{\sigma}_\mu(\mathbf{y},t)\, dV = \int_{\Omega^s_\mu} \mathscr{F}_y[(\boldsymbol{\varepsilon}_0(t) + \nabla^{sym}\tilde{\mathbf{u}}_\mu(\mathbf{y},t))]\, dV. \tag{3.38}$$

3.2 Plasticity

This Section briefly describes continuum rate-independent plasticity and its numerical implementation through the closest-point projection method (CPPM). The theory presented here largely follows the description in de Souza Neto et al. (2008), Armero and Pérez-Foguet (2002) and Pérez-Foguet and Armero (2002). The theory outlined in this

Section is based on infinitesimal strains, but a large strain extension in the context of isotropic multiplicative plasticity will be briefly introduced in Chapter 4. Additionally, the plastic constitutive laws described in this Section, and used throughout this study, are associative[1].

3.2.1 Thermodynamics of internal variables

In the context of plasticity it is useful to use an alternative to history functionals (Eq. 3.36), which is based on thermodynamics of internal variables (de Souza Neto et al., 2008). The underlying hypothesis to this theory is that at any instant of a thermodynamic process, the thermodynamic state can be completely determined by knowing the instantaneous value (not the past history) of a finite number of state variables. In the applications contemplated in this study, the thermodynamic state at a point is determined by the following state variables: strain $\boldsymbol{\varepsilon}$, and a finite set of scalar, vectorial, or tensorial strain-like internal variables of cardinality k, $\boldsymbol{\alpha}_k$, associated with dissipative mechanisms.

Following the hypothesis of thermodynamics of internal variables, and by ignoring thermal effects, the free energy of a considered material can be assumed to have the following form:

$$\psi = \psi(\boldsymbol{\varepsilon}, \boldsymbol{\alpha}_k). \tag{3.39}$$

Equation 3.39 is strictly convex with respect to $\boldsymbol{\varepsilon}$ and each $\boldsymbol{\alpha}_k$, and zero-valued at the origin $\{\boldsymbol{\varepsilon}, \boldsymbol{\alpha}_k\} = \{\mathbf{0}, \mathbf{0}\}$. By taking the time derivative of the free energy (Eq. 3.39), the following expression is obtained:

$$\dot{\psi} = \frac{\partial \psi(\boldsymbol{\varepsilon}, \boldsymbol{\alpha}_k)}{\partial \boldsymbol{\varepsilon}} : \dot{\boldsymbol{\varepsilon}} + \sum_{i=1}^{k} \frac{\partial \psi(\boldsymbol{\varepsilon}, \boldsymbol{\alpha}_k)}{\partial \boldsymbol{\alpha}_i} * \dot{\boldsymbol{\alpha}}_i \,, \tag{3.40}$$

where "$*$" denotes the product between $\frac{\partial \psi}{\partial \boldsymbol{\alpha}_i}$ and $\dot{\boldsymbol{\alpha}}_i$ which yields a scalar. By using the Clausius-Duhem inequality

$$\boldsymbol{\sigma} : \dot{\boldsymbol{\varepsilon}} - \dot{\psi} \geq 0, \tag{3.41}$$

the following is obtained:

$$\left(\boldsymbol{\sigma} - \frac{\partial \psi(\boldsymbol{\varepsilon}, \boldsymbol{\alpha}_k)}{\partial \boldsymbol{\varepsilon}} \right) : \dot{\boldsymbol{\varepsilon}} - \sum_{i=1}^{k} \frac{\partial \psi(\boldsymbol{\varepsilon}, \boldsymbol{\alpha}_k)}{\partial \boldsymbol{\alpha}_i} * \dot{\boldsymbol{\alpha}}_i \geq 0. \tag{3.42}$$

[1] This assumption is explained in Section 3.2.3.

Since this equation must hold for any kinetic process $\dot{\boldsymbol{\varepsilon}}$, the following holds:

$$\boldsymbol{\sigma} = \frac{\partial \psi(\boldsymbol{\varepsilon}, \boldsymbol{\alpha}_k)}{\partial \boldsymbol{\varepsilon}}. \tag{3.43}$$

For each plastic internal variable ($\boldsymbol{\alpha}_k$), a corresponding hardening thermodynamic force ($\mathbf{A}_k$), or stress-like internal variable, is defined as

$$\mathbf{A}_k = \frac{\partial \psi(\boldsymbol{\varepsilon}, \boldsymbol{\alpha}_k)}{\partial \boldsymbol{\alpha}_k}. \tag{3.44}$$

Therefore, Eq. 3.42 can be rewritten as

$$-\sum_{i=1}^{k} \mathbf{A}_i * \dot{\boldsymbol{\alpha}}_i \geq 0. \tag{3.45}$$

To completely characterise the constitutive model, additional laws defining the evolution of the plastic internal variables must be defined. These will be defined in the context of *normal dissipativity*. The Clausius-Duhem inequality (Eq. 3.45) must hold for any process and it poses restrictions on the possible expressions of the evolution equations. An effective way of ensuring that this is fulfilled is by postulating the existence of a non-negative dissipation potential

$$\Xi = \Xi(\mathbf{A}_k; \boldsymbol{\varepsilon}, \boldsymbol{\alpha}_k) \geq 0, \tag{3.46}$$

where $\boldsymbol{\varepsilon}$ and $\boldsymbol{\alpha}_k$ appear as parameters. Equation 3.46 is a strictly convex function with respect to each $\mathbf{A}_k$ and zero-valued at the origin $\mathbf{A}_k = \mathbf{0}$. Normal dissipativity means that the evolution of the plastic internal variables is determined by the law

$$\dot{\boldsymbol{\alpha}}_k = -\frac{\partial \Xi(\mathbf{A}_k; \boldsymbol{\varepsilon}, \boldsymbol{\alpha}_k)}{\partial \mathbf{A}_k}. \tag{3.47}$$

If a constitutive model is defined by Eqs. 3.39, 3.43, 3.44 and 3.47, it satisfies *a priori* the dissipation inequality (Eq. 3.45).

3.2.2 Mathematical description of plasticity

This Section describes the continuum rate-independent theory of plasticity from a mathematical perspective. All the necessary ingredients to postulate a three-dimensional general elastoplastic constitutive model are introduced: elastoplastic strain decomposition, elastic law, yield function, evolution of the plastic strain, and evolution of the yield function (hardening/softening).

With the assumption of linear kinematics, the infinitesimal strain tensor ($\boldsymbol{\varepsilon}$) can be decomposed into the sum of an elastic component, or elastic strain tensor ($\boldsymbol{\varepsilon}^e$), and a plastic component, or plastic strain tensor ($\boldsymbol{\varepsilon}^p$), such that

$$\boldsymbol{\varepsilon} = \boldsymbol{\varepsilon}^e + \boldsymbol{\varepsilon}^p. \tag{3.48}$$

Following this assumption, Eq. 3.39 can be assumed to be of the form

$$\psi = \psi(\boldsymbol{\varepsilon}, \boldsymbol{\varepsilon}^p, \boldsymbol{\alpha}_k), \tag{3.49}$$

with the plastic strain tensor taken also as a plastic internal variable. It is usual to assume that this energy function can be additively split as

$$\psi = \psi(\boldsymbol{\varepsilon}, \boldsymbol{\varepsilon}^p, \boldsymbol{\alpha}_k) = \psi^e(\boldsymbol{\varepsilon} - \boldsymbol{\varepsilon}^p) + \psi^p(\boldsymbol{\alpha}_k), \tag{3.50}$$

where ψ^e is the elastic contribution and ψ^p is the plastic contribution of the free energy. Following this decomposition and by taking into account that $\boldsymbol{\sigma} = \frac{\partial \psi^e}{\partial \boldsymbol{\varepsilon}^e}$ and $\mathbf{A}_k = \frac{\partial \psi^p}{\partial \boldsymbol{\alpha}_k}$, Eq. 3.45 can be rewritten as a plastic dissipation function

$$\boldsymbol{\sigma} : \dot{\boldsymbol{\varepsilon}}^p - \mathbf{A}_k * \dot{\boldsymbol{\alpha}}_k \geq 0, \tag{3.51}$$

where $-\boldsymbol{\sigma}$ is the hardening thermodynamic force associated with $\boldsymbol{\varepsilon}^p$. The yield function is a scalar function which remains negative as long as yield is not attained and becomes zero when plastic flow may occur. It can be stated that plastic flow happens when

$$f(\boldsymbol{\sigma}, \mathbf{A}_k) = 0. \tag{3.52}$$

Note that, in this case, the yield function is defined as a hypersurface in stress space. However, it can also be expressed as a hypersurface in strain space. If the stress and strain tensors are symmetric, and thus the corresponding spaces are six-dimensional, the yield function is a five-dimensional manifold in these spaces.

The plastic internal variables considered in this Section are the plastic strain tensor $\boldsymbol{\varepsilon}^p$ and the hardening variables $\boldsymbol{\alpha}_k$. Evolution equations for both of them are needed for a complete characterisation of the constitutive model. These evolution equations are introduced as a plastic flow rule $\dot{\boldsymbol{\varepsilon}}^p$ and a hardening function $\dot{\boldsymbol{\alpha}}_k$, respectively as

$$\dot{\boldsymbol{\varepsilon}}^p = \dot{\gamma}\, \mathbf{N}(\boldsymbol{\sigma}, \mathbf{A}_k) \tag{3.53}$$

and

$$\dot{\boldsymbol{\alpha}}_k = \dot{\gamma}\,\mathbf{H}_k(\boldsymbol{\sigma}, \mathbf{A}_k), \tag{3.54}$$

where $\mathbf{N}$ is the flow vector and $\mathbf{H}_k$ is the hardening modulus. These evolution equations are complemented by the loading/unloading conditions, which define when plastic flow may occur, and are stated as

$$f(\boldsymbol{\sigma}, \mathbf{A}_k) \leq 0; \quad \dot{\gamma} \geq 0; \quad f(\boldsymbol{\sigma}, \mathbf{A}_k)\dot{\gamma} = 0. \tag{3.55}$$

In the case of associative plasticity, the evolution equations (Eqs. 3.53 and 3.54) are defined as

$$\dot{\boldsymbol{\varepsilon}}^p = \dot{\gamma}\,\frac{\partial f(\boldsymbol{\sigma}, \mathbf{A}_k)}{\partial \boldsymbol{\sigma}} \tag{3.56}$$

and

$$\dot{\boldsymbol{\alpha}}_k = -\dot{\gamma}\,\frac{\partial f(\boldsymbol{\sigma}, \mathbf{A}_k)}{\partial \mathbf{A}_k}. \tag{3.57}$$

3.2.3 Numerical implementation through the closest-point projection method

The governing equations of the elastoplastic constitutive initial value problem are the following:

$$\begin{aligned}
&\dot{\boldsymbol{\varepsilon}}^e = \dot{\boldsymbol{\varepsilon}} - \dot{\gamma}\,\mathbf{N}(\boldsymbol{\sigma}, \mathbf{A}_k) \\
&\dot{\boldsymbol{\alpha}} = \dot{\gamma}\,\mathbf{H}(\boldsymbol{\sigma}, \mathbf{A}_k) \\
&f(\boldsymbol{\sigma}, \mathbf{A}_k) \leq 0; \quad \dot{\gamma} \geq 0; \quad f(\boldsymbol{\sigma}, \mathbf{A}_k)\dot{\gamma} = 0 \\
&\boldsymbol{\sigma} = \frac{\partial \psi^e(\boldsymbol{\varepsilon}^e)}{\partial \boldsymbol{\varepsilon}^e}; \quad \mathbf{A}_k = \frac{\partial \psi^p(\boldsymbol{\alpha}_k)}{\partial \boldsymbol{\alpha}_k}.
\end{aligned} \tag{3.58}$$

In this Section, the variational formulation of the closest-point projection method (CPPM) equations is presented, which will then allow the derivation of return-mapping algorithms with global convergence. The name "closest-point projection" gives a hint on the variational structure of the equations, which basically has to do with the minimisation of the distance, in the proper metric, between the trial predictor state and the admissible bounding elastic region, defined through the yield surface.

Equations 3.58 need to be integrated in time in order to be usable from a computational perspective. In the FE context, these equations are integrated locally at each of the Gauss integration points in the FE mesh. These equations follow a strain-driven structure, i.e. given an increment of the total strain, determine the current values of the thermodynamic forces $\boldsymbol{\sigma}$ and $\mathbf{A}_k$, and of the plastic internal variables $\boldsymbol{\varepsilon}^p$ and $\boldsymbol{\alpha}_k$.

The loading/unloading conditions in Eqs. 3.58 define plastic consistency, which needs to be enforced in a particular way, which also means that the solution of the elastoplastic constitutive initial value problem does not directly follow traditional solution procedures for initial value problems. Many of the proposed techniques to solve this elastoplastic constitutive initial value problem follow an operator split strategy, i.e. a two-step algorithm with an initial trial-state step where the stresses are updated elastically and if the activation of the plastic evolution equations is detected, a plastic-corrector step follows, where Eqs. 3.58 are numerically solved. This procedure has also been given the name of predictor/corrector. Of particular interest to solve the plastic-corrector step is the closest-point projection method (Armero and Pérez-Foguet, 2002; Pérez-Foguet and Armero, 2002). It consists of an implicit approximation of Eqs. 3.58, leading to a nonlinear system of algebraic equations in the stresses and stress-like internal variables. The major advantage of using the closest-point projection method as a solution of Eqs. 3.58 is that, under some assumptions mentioned later, some algorithms employing the closest-point projection method equations exhibit global convergence and a unique solution. These are very desirable properties in a HPC framework as the time increment does not need to be restarted when the numerical method used to solve Eqs. 3.58 fails to convergence at some integration point of the mesh; this is because this numerical method always converges.

In some cases, such as a Von-Mises yield surface with linear hardening (or perfect plasticity, i.e. no hardening or softening) or a Drucker-Prager yield surface with the same hardening conditions, the plastic-corrector step has closed-form solutions (de Souza Neto et al., 2008). However, this is not the general case, and in order to solve the nonlinear algebraic equations of the plastic-corrector step, an iterative algorithm needs to be applied. A widely used option is a Newton scheme which, when coupled to the closest-point projection method, gives rise to the Newton-CPPM algorithm (Armero and Pérez-Foguet, 2002). The Newton-CPPM scheme is very attractive since it has a quadratic rate of convergence and the linearised closed-form is readily available, which enormously simplifies the derivation of the consistent tangent operator in implicit FE formulations (Simo, 1985). Nonetheless, Newton-like schemes possess limited (local) convergence properties, in the sense that the solution is assured only for limited radius around the initial estimate. This is due to the possible strong nonlinearities of the elastoplastic constitutive initial value problem, usually associated with regions of high curvature of the yield surface. Note that this can happen even in well-posed continuum models, such as constitutive models defined with a convex yield criterion, associative plasticity, strain hardening and constant stiffness. Problems associated with local convergence of the Newton-CPPM scheme will be tackled by implementing a

primal-CPPM scheme instead, which exhibits global convergence under some limiting assumptions (Pérez-Foguet and Armero, 2002).

The existence of the variational structure of the closest-point projection method equations relies on two major assumptions. The first assumption is the strict convexity of the free energy function. However, a stronger assumption is considered here, which is that the free energy function is twice differentiable, with a positive-definite Hessian. The solid phase of trabecular bone is usually modelled with linear elasticity and linear hardening (Panyasantisuk et al., 2015b; Wolfram et al., 2012), with the corresponding free energy function ($\boldsymbol{\alpha}$ in this case usually denotes a scalar internal variable and $\mathbf{H}$ denotes the corresponding linear hardening scalar modulus),

$$\psi(\boldsymbol{\varepsilon}^e, \boldsymbol{\alpha}) = \psi^e(\boldsymbol{\varepsilon}^e) + \psi^p(\boldsymbol{\alpha}) = \frac{1}{2}\boldsymbol{\varepsilon}^e : \mathbb{D}^e : \boldsymbol{\varepsilon}^e + \frac{1}{2}\boldsymbol{\alpha} * \mathbf{H} * \boldsymbol{\alpha}. \tag{3.59}$$

The Hessian is then obtained as

$$[\nabla^2 \psi] = \begin{bmatrix} \frac{\partial^2 \psi}{\partial (\boldsymbol{\varepsilon}^e)^2} & \frac{\partial^2 \psi}{\partial \boldsymbol{\varepsilon}^e \partial \boldsymbol{\alpha}} \\ \frac{\partial^2 \psi}{\partial \boldsymbol{\alpha} \partial \boldsymbol{\varepsilon}^e} & \frac{\partial^2 \psi}{\partial \boldsymbol{\alpha}^2} \end{bmatrix} = \begin{bmatrix} \mathbb{D}^e & \mathbf{0} \\ \mathbf{0} & \mathbf{H} \end{bmatrix}, \tag{3.60}$$

which is indeed positive-definite as $\mathbb{D}^e$ is positive-definite due to being an elasticity tensor and $\mathbf{H}$ is positive due to the presence of hardening. Note that the positive-definiteness of this Hessian implies strict convexity of ψ.

The second assumption is that the evolution equations are associative for a convex and differentiable yield function. The solid phase of trabecular bone has been modelled with smooth approximations of Drucker-Prager yield surfaces recently (Panyasantisuk et al., 2015b), mainly because of its little porosity, which may lead to a possible lack of yield in hydrostatic compression. This yield surface is defined as (Schwiedrzik et al., 2013)

$$f(\boldsymbol{\sigma}, q) = \sqrt{\boldsymbol{\sigma} : \mathbb{F} : \boldsymbol{\sigma}} + \mathbf{F} : \boldsymbol{\sigma} - (1 + q) = 0, \tag{3.61}$$

where $\mathbb{F}$, $\mathbf{F}$ and q are defined later. The Hessian is then obtained as

$$[\nabla^2 f] = \begin{bmatrix} \frac{\partial^2 f}{\partial \boldsymbol{\sigma}^2} & \frac{\partial^2 f}{\partial \boldsymbol{\sigma} \partial q} \\ \frac{\partial^2 f}{\partial q \partial \boldsymbol{\sigma}} & \frac{\partial^2 f}{\partial q^2} \end{bmatrix} = \begin{bmatrix} \frac{\partial^2 f}{\partial \boldsymbol{\sigma}^2} & \mathbf{0} \\ \mathbf{0} & 0 \end{bmatrix}, \tag{3.62}$$

where

$$\frac{\partial^2 f}{\partial \boldsymbol{\sigma}^2} = \frac{\mathbb{F}}{\sqrt{\boldsymbol{\sigma} : \mathbb{F} : \boldsymbol{\sigma}}} - \frac{(\mathbb{F} : \boldsymbol{\sigma}) \otimes (\boldsymbol{\sigma} : \mathbb{F})}{\sqrt{(\boldsymbol{\sigma} : \mathbb{F} : \boldsymbol{\sigma})^3}}. \tag{3.63}$$

The yield surface (Eq. 3.61) is convex if its Hessian is positive semi-definite, which holds since

$$\begin{aligned}\boldsymbol{\sigma} : \frac{\partial^2 f}{\partial \boldsymbol{\sigma}^2} : \boldsymbol{\sigma} \geq 0 \rightarrow \boldsymbol{\sigma} : \left(\frac{\mathbb{F}}{\sqrt{\boldsymbol{\sigma} : \mathbb{F} : \boldsymbol{\sigma}}} - \frac{(\mathbb{F} : \boldsymbol{\sigma}) \otimes (\boldsymbol{\sigma} : \mathbb{F})}{\sqrt{(\boldsymbol{\sigma} : \mathbb{F} : \boldsymbol{\sigma})^3}} \right) : \boldsymbol{\sigma} \geq 0 \\ \rightarrow \sqrt{\boldsymbol{\sigma} : \mathbb{F} : \boldsymbol{\sigma}} - \sqrt{\boldsymbol{\sigma} : \mathbb{F} : \boldsymbol{\sigma}} \geq 0,\end{aligned} \tag{3.64}$$

which, at the same time, holds if and only if $\mathbb{F}$ is positive semi-definite, which is true for a hyperbolic approximation to a Drucker-Prager yield surface. Equation 3.61 is differentiable because there are no singularities (i.e. there are no points in the corresponding space where the derivative is non-unique or non-existent); it is important to note that it corresponds to a smooth (hyperbolic) approximation to Drucker-Prager, and therefore it does not have the apex singularity which is present in the traditional Drucker-Prager model. Associativity of the evolution equations is usually assumed when modelling the solid phase of trabecular bone, mostly for simplicity since the current state of validation experiments does not allow for a proper study of its hardening.

It is important to note that these assumptions are only needed from a theoretical point of view. Non-associative models and/or strain-softening can still be used, and although global convergence of the return-mapping equations may not hold, an improved numerical convergence has still been shown when using the aforementioned primal-CPPM scheme instead of the Newton-CPPM scheme (Armero and Pérez-Foguet, 2002).

The starting point of the derivation of the closest-point projection method equations from a variational point of view is to define the complementary energy function (χ), which is obtained through a Legendre transform of the free energy function (Eq. 3.50). The differential of the free energy function is defined as

$$\mathrm{d}\psi = \boldsymbol{\sigma} : \mathrm{d}\boldsymbol{\varepsilon}^e + \mathbf{A}_k * \mathrm{d}\boldsymbol{\alpha}_k \,. \tag{3.65}$$

By using the product rule of differentiation on the conjugate pairs, the following is obtained:

$$\begin{aligned}\mathrm{d}(\boldsymbol{\sigma} : \boldsymbol{\varepsilon}^e) &= \mathrm{d}\boldsymbol{\sigma} : \boldsymbol{\varepsilon}^e + \boldsymbol{\sigma} : \mathrm{d}\boldsymbol{\varepsilon}^e \rightarrow \boldsymbol{\sigma} : \mathrm{d}\boldsymbol{\varepsilon}^e = \mathrm{d}(\boldsymbol{\sigma} : \boldsymbol{\varepsilon}^e) - \mathrm{d}\boldsymbol{\sigma} : \boldsymbol{\varepsilon}^e, \\ \mathrm{d}(\mathbf{A}_k * \boldsymbol{\alpha}_k) &= \mathrm{d}\mathbf{A}_k * \boldsymbol{\alpha}_k + \mathbf{A}_k * \mathrm{d}\boldsymbol{\alpha}_k \rightarrow \mathbf{A}_k * \mathrm{d}\boldsymbol{\alpha}_k = \mathrm{d}(\mathbf{A}_k * \boldsymbol{\alpha}_k) - \mathrm{d}\mathbf{A}_k * \boldsymbol{\alpha}_k + \mathbf{A}_k \,,\end{aligned} \tag{3.66}$$

which when applied to Eq. 3.65 yields

$$\mathrm{d}(\boldsymbol{\sigma} : \boldsymbol{\varepsilon}^e + \mathbf{A}_k * \boldsymbol{\alpha}_k - \psi) = \mathrm{d}\chi = \mathrm{d}\boldsymbol{\sigma} : \boldsymbol{\varepsilon}^e + \mathrm{d}\mathbf{A}_k * \boldsymbol{\alpha}_k \,. \tag{3.67}$$

The complementary energy function is strictly convex due to the strict convexity of the free energy function. Since both χ and ψ are convex functions and are Legendre transforms of each others, their first derivatives are inverse functions of each other, such that

$$\frac{\partial \psi}{\partial \boldsymbol{\varepsilon}^e} = \left(\frac{\partial \chi}{\partial \boldsymbol{\sigma}}\right)^{-1}; \quad \frac{\partial \psi}{\partial \boldsymbol{\alpha}_k} = \left(\frac{\partial \chi}{\partial \mathbf{A}_k}\right)^{-1}. \tag{3.68}$$

The elastic strain and the plastic internal variables can be obtained as

$$\frac{\partial \chi(\boldsymbol{\sigma}, \mathbf{A}_k)}{\partial \boldsymbol{\sigma}} = \frac{\partial}{\partial \boldsymbol{\sigma}}(\boldsymbol{\sigma} : \boldsymbol{\varepsilon}^e + \mathbf{A}_k * \boldsymbol{\alpha}_k - \psi) = \boldsymbol{\varepsilon}^e + \boldsymbol{\sigma} : \frac{\partial \boldsymbol{\varepsilon}^e}{\partial \boldsymbol{\sigma}} - \frac{\partial \psi}{\partial \boldsymbol{\varepsilon}^e} : \frac{\partial \boldsymbol{\varepsilon}^e}{\partial \boldsymbol{\sigma}} = \boldsymbol{\varepsilon}^e, \tag{3.69}$$

and

$$\frac{\partial \chi(\boldsymbol{\sigma}, \mathbf{A}_k)}{\partial \mathbf{A}_k} = \frac{\partial}{\partial \mathbf{A}_k}(\boldsymbol{\sigma} : \boldsymbol{\varepsilon}^e + \mathbf{A}_k * \boldsymbol{\alpha}_k - \psi) = \boldsymbol{\alpha}_k + \mathbf{A}_k * \frac{\partial \boldsymbol{\alpha}_k}{\partial \mathbf{A}_k} - \frac{\partial \psi}{\partial \boldsymbol{\alpha}_k} * \frac{\partial \boldsymbol{\alpha}_k}{\partial \mathbf{A}_k} = \boldsymbol{\alpha}_k \,. \tag{3.70}$$

Under the previously stated assumptions, the closest-point projection method equations can be obtained as the first-order necessary conditions of the following unilaterally constrained variational problem:

$$\min_{\substack{\{\boldsymbol{\sigma}, \mathbf{A}_k\} \\ f(\boldsymbol{\sigma}, \mathbf{A}_k) \leq 0}} \{\chi(\boldsymbol{\sigma}, \mathbf{A}_k) - \boldsymbol{\sigma} : \boldsymbol{\varepsilon}^{e\,trial}_{n+1} - \mathbf{A}_k * \boldsymbol{\alpha}^{trial}_{k\,n+1}\}, \tag{3.71}$$

where $\boldsymbol{\varepsilon}^{e\,trial}$ and $\boldsymbol{\alpha}^{trial}$ are the trial values of the elastic strain and the plastic internal variables, and thus the initial guesses of the minimisation problem. They are obtained as

$$\boldsymbol{\varepsilon}^{e\,trial}_{n+1} = \boldsymbol{\varepsilon}^e_n + \Delta\boldsymbol{\varepsilon}; \quad \boldsymbol{\alpha}^{trial}_{k\,n+1} = \boldsymbol{\alpha}_{k\,n}\,, \tag{3.72}$$

where $\boldsymbol{\varepsilon}^e_n$, $\Delta\boldsymbol{\varepsilon}$ and $\boldsymbol{\alpha}_{k\,n}$ are the previous converged elastic strains, the total strain increment (which depends on the time increment dictated by the FE layer) and the previous converged strain-like internal variables (which would be $\mathbf{0}$ if the corresponding integration point has not yielded yet). Furthermore, the solution of Eq. 3.71, if it exists, is unique and is indeed the solution of the closest-point projection method equations.

The Lagrangian associated to the variational problem (Eq. 3.71), for the Lagrange multiplier field $\dot{\gamma}$, is defined as

$$\mathscr{L}(\boldsymbol{\sigma}, \mathbf{A}_k, \dot{\gamma}) = \chi(\boldsymbol{\sigma}, \mathbf{A}_k) - \boldsymbol{\sigma} : \boldsymbol{\varepsilon}^{e\,trial}_{n+1} - \mathbf{A}_k * \boldsymbol{\alpha}^{trial}_{k\,n+1} + \dot{\gamma} f(\boldsymbol{\sigma}, \mathbf{A}_k). \tag{3.73}$$

The first-order necessary conditions for a local minimum of the unilaterally constrained problem (Eq. 3.71) are

$$\begin{aligned}\frac{\partial \mathscr{L}}{\partial \boldsymbol{\sigma}}\Big|_{\{\boldsymbol{\sigma}_{n+1},\mathbf{A}_{k\,n+1},\Delta\gamma\}} &= \frac{\partial \chi(\boldsymbol{\sigma}_{n+1},\mathbf{A}_{k\,n+1})}{\partial \boldsymbol{\sigma}} - \boldsymbol{\varepsilon}^{e\,trial}_{n+1} + \Delta\gamma\frac{\partial f(\boldsymbol{\sigma}_{n+1},\mathbf{A}_{k\,n+1})}{\partial \boldsymbol{\sigma}} \\ &= \boldsymbol{\varepsilon}^{e}_{n+1} - \boldsymbol{\varepsilon}^{e\,trial}_{n+1} + \Delta\gamma\frac{\partial f(\boldsymbol{\sigma}_{n+1},\mathbf{A}_{k\,n+1})}{\partial \boldsymbol{\sigma}} = \mathbf{0},\end{aligned} \tag{3.74}$$

$$\begin{aligned}\frac{\partial \mathscr{L}}{\partial \mathbf{A}_k}\Big|_{\{\boldsymbol{\sigma}_{n+1},\mathbf{A}_{k\,n+1},\Delta\gamma\}} &= \frac{\partial \chi(\boldsymbol{\sigma}_{n+1},\mathbf{A}_{k\,n+1})}{\partial \mathbf{A}_k} - \boldsymbol{\alpha}^{trial}_{k\,n+1} + \Delta\gamma\frac{\partial f(\boldsymbol{\sigma}_{n+1},\mathbf{A}_{k\,n+1})}{\partial \mathbf{A}_k} \\ &= \boldsymbol{\alpha}_{k\,n+1} - \boldsymbol{\alpha}^{trial}_{k\,n+1} + \Delta\gamma\frac{\partial f(\boldsymbol{\sigma}_{n+1},\mathbf{A}_{k\,n+1})}{\partial \mathbf{A}_k} = \mathbf{0}\end{aligned} \tag{3.75}$$

and the Karush-Kuhn-Tucker (or loading-unloading) conditions are

$$f(\boldsymbol{\sigma}_{n+1},\mathbf{A}_{k\,n+1}) \leq 0; \quad \Delta\gamma \geq 0; \quad \Delta\gamma\, f(\boldsymbol{\sigma}_{n+1},\mathbf{A}_{k\,n+1}) = 0. \tag{3.76}$$

Equations 3.74, 3.75 and 3.76 correspond exactly to the closest-point projection method equations. Using the aforementioned assumptions (positive Hessian of the complementary energy and a differentiable convex yield function with associative evolution equations) results in a positive-definite Hessian of the Lagrangian (Eq. 3.73), which is given by

$$\nabla^2 \mathscr{L} = \nabla^2 \chi + \dot{\gamma}\,\nabla^2 f. \tag{3.77}$$

This results in the strict convexity of the Lagrangian, implying that any solution of the first-order necessary conditions (Eqs. 3.74, 3.75 and 3.76) is a unique global minimum. The existence of this global minimum is assured if the expression to be minimised in Eq. 3.71 satisfies the growth condition, which is

$$\chi(\boldsymbol{\sigma},\mathbf{A}_k) \to \infty \quad \forall\, \|\{\boldsymbol{\sigma},\mathbf{A}_k\}\| \to \infty. \tag{3.78}$$

Note that the assumption of a twice differentiable constant positive-definite Hessian of the complementary energy function assures the coerciveness condition, and thus satisfies the growth condition (Pérez-Foguet and Armero, 2002).

The closest-point projection method equations need to be iteratively solved if the trial-state step is not admissible. The trial state is defined as

$$\boldsymbol{\varepsilon}^{e\,trial}_{n+1} = \boldsymbol{\varepsilon}_{n+1} - \boldsymbol{\varepsilon}^{p}_{n}; \quad \boldsymbol{\varepsilon}^{p\,trial}_{n+1} = \boldsymbol{\varepsilon}^{p}_{n}; \quad \boldsymbol{\alpha}^{trial}_{k\,n+1} = \boldsymbol{\alpha}_{k\,n}\,. \tag{3.79}$$

If the trial state is not admissible (i.e. $f_{n+1} > 0$) then the following set of algebraic equations needs to be solved for a solution where $\Delta\gamma > 0$:

$$\left\{ \begin{array}{c} \boldsymbol{\varepsilon}^e_{n+1} - \boldsymbol{\varepsilon}^{e\,trial}_{n+1} + \Delta\gamma\,\mathbf{N}(\boldsymbol{\sigma}_{n+1}, \mathbf{A}_{k\,n+1}) \\ \boldsymbol{\alpha}_{k\,n+1} - \boldsymbol{\alpha}^{trial}_{k\,n+1} - \Delta\gamma\,\mathbf{H}_k(\boldsymbol{\sigma}_{n+1}, \mathbf{A}_{k\,n+1}) \\ f(\boldsymbol{\sigma}_{n+1}, \mathbf{A}_{k\,n+1}) \end{array} \right\} = \left\{ \begin{array}{c} \mathbf{0} \\ \mathbf{0} \\ 0 \end{array} \right\} \tag{3.80}$$

for

$$\boldsymbol{\sigma}_{n+1} = \frac{\partial \psi(\boldsymbol{\varepsilon}^e_{n+1}, \boldsymbol{\alpha}_{k\,n+1})}{\partial \boldsymbol{\varepsilon}^e}; \quad \mathbf{A}_{k\,n+1} = \frac{\partial \psi(\boldsymbol{\varepsilon}^e_{n+1}, \boldsymbol{\alpha}_{k\,n+1})}{\partial \boldsymbol{\alpha}_k} \tag{3.81}$$

and

$$\mathbf{N}(\boldsymbol{\sigma}_{n+1}, \mathbf{A}_{k\,n+1}) = \frac{\partial f(\boldsymbol{\sigma}_{n+1}, \mathbf{A}_{k\,n+1})}{\partial \boldsymbol{\sigma}}; \quad \mathbf{H}_k(\boldsymbol{\sigma}_{n+1}, \mathbf{A}_{k\,n+1}) = -\frac{\partial f(\boldsymbol{\sigma}_{n+1}, \mathbf{A}_{k\,n+1})}{\partial \mathbf{A}_k}. \tag{3.82}$$

As previously mentioned, a common strategy to solve such a nonlinear system of equations is to use a Newton iterative scheme (Newton-CPPM). This scheme converges if the initial estimate is close to the final solution, exhibiting a quadratic rate of convergence in such a scenario. Although a quadratic rate of convergence is a very desirable property, the convergence radius is small (i.e. the convergence is not global), and thus the usability of the Newton-CPPM scheme is somehow limited. To further understand how the closest-point projection method works, a graphical representation is shown in Fig. 3.2.

Newton-CPPM scheme applied to the generic quadric yield surface with linear isotropic hardening

An example of a Newton-CPPM scheme applied to the isotropic generic quadric yield surface described by Schwiedrzik et al. (2013) is developed here, as this yield surface is extensively used throughout this study. Possible dependencies on variables are dropped for notational convenience in this Section.

The free energy equation of the material being examined is assumed to be quadratic due to the presence of a linear elastic regime and linear hardening

$$\psi = \psi^e + \psi^p = \frac{1}{2}\boldsymbol{\varepsilon}^e : \mathbb{D}^e : \boldsymbol{\varepsilon}^e + \frac{1}{2}\overline{H}_{iso}\,\overline{\kappa}^2, \tag{3.83}$$

where $\overline{H}_{iso}$ is the isotropic constant hardening modulus and $\overline{\kappa}$ is an isotropic plastic internal variable. The yield function of the generic quadric reads

$$f = \sqrt{\boldsymbol{\sigma} : \mathbb{F} : \boldsymbol{\sigma}} + \mathbf{F} : \boldsymbol{\sigma} - (1+q) = 0, \tag{3.84}$$

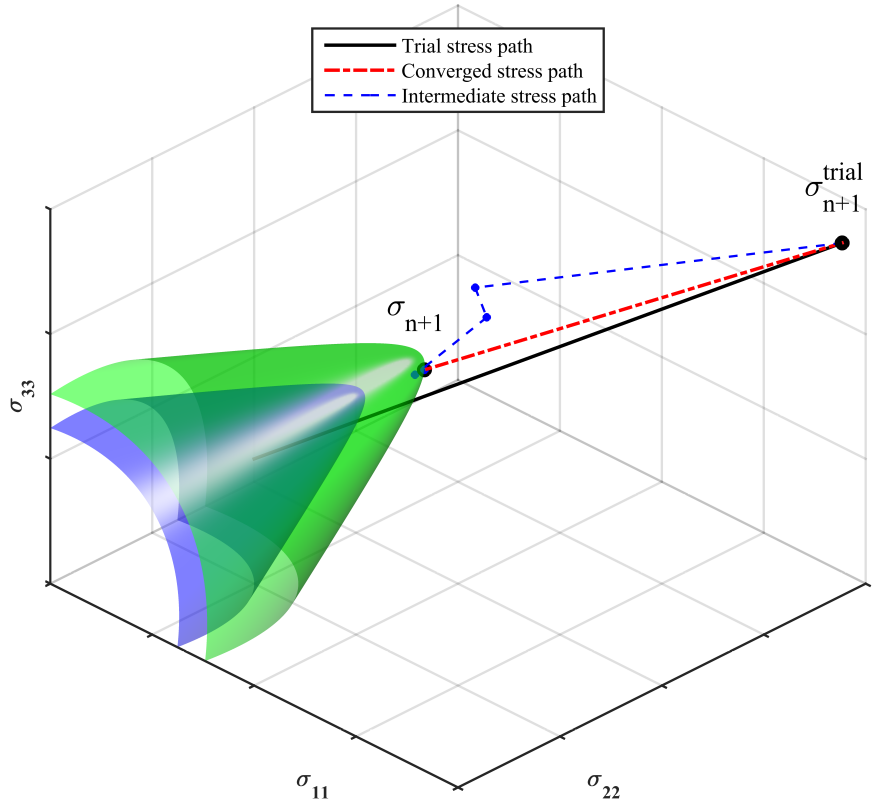

Fig. 3.2 Graphical representation of the closest-point projection method in normal stress space. The blue and green surfaces are respectively the initial (blue) and hardened (green) yield surfaces. The blue dots are the intermediate (i.e. non-converged) stresses.

where $q = \overline{H}_{iso}\overline{\kappa}$ is the conjugate hardening thermodynamic force of $\overline{\kappa}$, the second-order tensor $\mathbf{F}$ is

$$\mathbf{F} = \frac{1}{2}\left(\frac{1}{\sigma_0^+} - \frac{1}{\sigma_0^-}\right)\mathbf{I}, \tag{3.85}$$

the fourth-order tensor $\mathbb{F}$ is

$$\mathbb{F} = -\zeta_0 F_0^2(\mathbf{I}\otimes\mathbf{I}) + (\zeta_0+1)F_0^2(\mathbf{I}\overline{\otimes}\mathbf{I}), \tag{3.86}$$

where

$$F_0 = \frac{\sigma_0^+\sigma_0^-}{2\sigma_0^+\sigma_0^-}, \tag{3.87}$$

and where σ_0^+ and σ_0^- are respectively the uniaxial tension and uniaxial compression yield stresses, and ζ_0 is a parameter which controls the shape of the yield surface.

The system of equations corresponding to the Newton-CPPM applied to this yield surface is written as

$$\left\{\begin{array}{c} \boldsymbol{\varepsilon}^e_{n+1} - \boldsymbol{\varepsilon}^{e\,trial}_{n+1} + \Delta\gamma \mathbf{N}_{n+1} \\ \overline{\kappa}_{n+1} - \overline{\kappa}^{trial}_{n+1} - \Delta\gamma H_{n+1} \\ \sqrt{\boldsymbol{\sigma}_{n+1} : \mathbb{F} : \boldsymbol{\sigma}_{n+1}} + \mathbf{F} : \boldsymbol{\sigma}_{n+1} - (1 + q_{n+1}) \end{array}\right\} = \left\{\begin{array}{c} \mathbf{R}_{\boldsymbol{\varepsilon}^e} \\ R_{\overline{\kappa}} \\ R_f \end{array}\right\} \tag{3.88}$$

where $\mathbf{R}_{\boldsymbol{\varepsilon}^e}$, $R_{\overline{\kappa}}$, and R_f are the residuals of the variables denoted by the corresponding subscripts, and

$$\begin{aligned} \mathbf{N} = \frac{\partial f}{\partial \boldsymbol{\sigma}} = \frac{\mathbb{F} : \boldsymbol{\sigma}}{\sqrt{\boldsymbol{\sigma} : \mathbb{F} : \boldsymbol{\sigma}}} + \mathbf{F}, \\ H = -\frac{\partial f}{\partial q} = 1. \end{aligned} \tag{3.89}$$

Due to the one to one dependency of $\overline{\kappa}$ on $\Delta\gamma$, the second equation of Eqs. 3.88 can be dropped, and therefore they become

$$\left\{\begin{array}{c} \boldsymbol{\varepsilon}^e_{n+1} - \boldsymbol{\varepsilon}^{e\,trial}_{n+1} + \Delta\gamma \mathbf{N}_{n+1} \\ \sqrt{\boldsymbol{\sigma}_{n+1} : \mathbb{F} : \boldsymbol{\sigma}_{n+1}} + \mathbf{F} : \boldsymbol{\sigma}_{n+1} - (1 + q_{n+1}) \end{array}\right\} = \left\{\begin{array}{c} \mathbf{R}_{\boldsymbol{\varepsilon}^e} \\ R_f \end{array}\right\}, \tag{3.90}$$

where $q_{n+1} = \overline{H}_{iso}(\overline{\kappa}^{trial}_{n+1} + \Delta\gamma)$. Equations 3.90 can be linearised with respect to the independent variables, resulting in

$$\left\{\begin{array}{c} \mathrm{d}\boldsymbol{\varepsilon}^e + \Delta\gamma \frac{\partial \mathbf{N}}{\partial \boldsymbol{\varepsilon}^e} : \mathrm{d}\boldsymbol{\varepsilon}^e + \mathrm{d}\Delta\gamma \mathbf{N} \\ \frac{\partial f}{\partial \boldsymbol{\varepsilon}^e} : \mathrm{d}\boldsymbol{\varepsilon}^e + \frac{\partial f}{\partial \Delta\gamma}\mathrm{d}\Delta\gamma \end{array}\right\} = \left\{\begin{array}{c} \mathrm{d}\boldsymbol{\varepsilon}^{e\,trial} \\ 0 \end{array}\right\}. \tag{3.91}$$

The algebraic system of Eqs. 3.91 can be reorganised as

$$[\mathbf{J}_{CPPM}] \left\{\begin{array}{c} \mathrm{d}\boldsymbol{\varepsilon}^e \\ \mathrm{d}\Delta\gamma \end{array}\right\} = \left\{\begin{array}{c} \mathrm{d}\boldsymbol{\varepsilon}^{e\,trial} \\ 0 \end{array}\right\}, \tag{3.92}$$

where $[\mathbf{J}_{CPPM}]$ is the matrix form of the Jacobian of the Newton-CPPM scheme, which is defined as

$$[\mathbf{J}_{CPPM}] = \begin{bmatrix} \mathbb{I} + \Delta\gamma \frac{\partial \mathbf{N}}{\partial \boldsymbol{\varepsilon}^e} & \mathbf{N} \\ \frac{\partial f}{\partial \boldsymbol{\varepsilon}^e} & \frac{\partial f}{\partial \Delta\gamma} \end{bmatrix} = \begin{bmatrix} \mathbb{A}_{11} & \mathbf{A}_{12} \\ \mathbf{A}_{21} & A_{22} \end{bmatrix}, \tag{3.93}$$

where the corresponding coefficients are shown in Table 3.1.
The updated solution at the iteration $k+1$ of the iterative scheme is obtained as

$$\left\{\begin{array}{c} \boldsymbol{\varepsilon}^e \\ \Delta\gamma \end{array}\right\}^{(k+1)} = \left\{\begin{array}{c} \boldsymbol{\varepsilon}^e \\ \Delta\gamma \end{array}\right\}^{(k)} - ([\mathbf{J}_{CPPM}]^{-1})^{(k)} \left\{\begin{array}{c} \mathbf{R}_{\boldsymbol{\varepsilon}^e} \\ R_f \end{array}\right\}^{(k)}. \tag{3.94}$$

Table 3.1 Coefficients of the Jacobian of the closest-point projection method of the generic quadric with isotropic hardening.

Coefficient	Mathematical expression
$\mathbb{A}_{11}$	$\mathbb{I}+\Delta\gamma\frac{\partial \mathbf{N}}{\partial \boldsymbol{\sigma}}:\frac{\partial \boldsymbol{\sigma}}{\partial \boldsymbol{\varepsilon}^e}$
$\mathbf{A}_{12}$	$\mathbf{N}$
$\mathbf{A}_{21}$	$\mathbf{N}:\frac{\partial \boldsymbol{\sigma}}{\partial \boldsymbol{\varepsilon}^e}$
A_{22}	$-\overline{H}_{iso}$
$\frac{\partial \mathbf{N}}{\partial \boldsymbol{\sigma}}$	$\frac{\mathbb{F}}{\sqrt{\boldsymbol{\sigma}:\mathbb{F}:\boldsymbol{\sigma}}}-\frac{(\mathbb{F}:\boldsymbol{\sigma})\otimes(\boldsymbol{\sigma}:\mathbb{F})}{(\sqrt{\boldsymbol{\sigma}:\mathbb{F}:\boldsymbol{\sigma}})^3}$
$\frac{\partial \boldsymbol{\sigma}}{\partial \boldsymbol{\varepsilon}^e}$	$\mathbb{D}^e$

The Newton-CPPM scheme is summarised in Algorithm 1. In this algorithm, n_{CPPM} is the maximum number of Newton-CPPM iterations and tol is the accepted tolerance for the corresponding numerical scheme.

Primal-CPPM scheme applied to the generic quadric yield surface

Global convergence is a very desirable property in an algorithm. It means that all sequences generated by the algorithm converge to a solution of the problem (Luenberger, 2003). In a FE context this property is very important because the non-convergence of the return-mapping equations usually leads to having to reduce the time increment. For problems with relatively few degrees of freedom this may not be critical. However, most of the simulations performed in this study involved large problems and were run on a supercomputer with thousands of cores, and resources, especially on such a platform, are limited.

A simple yet efficient choice for achieving global convergence in the Newton-CPPM scheme is by applying the corresponding line search procedure, leading to the primal-CPPM scheme (Pérez-Foguet and Armero, 2002). This method is chosen over the others because it does not dramatically increase the computational cost of the Newton-CPPM scheme. Moreover, the remaining methods are not fully competitive in terms of computational cost in regions where the primal-CPPM shows no difficulties (Pérez-Foguet and Armero, 2002). In this Section, subscripts within parentheses denote iterations within the Newton scheme while superscripts within parentheses denote iterations within the line search scheme.

A line search is one of the most basic minimisation procedures and can be defined as follows. A general nonlinear unconstrained algebraic system of equations is given by

$$\mathbf{R}(\mathbf{x})=\mathbf{0}, \tag{3.95}$$

Algorithm 1 Newton-CPPM scheme.

1. Define the residual and solution vectors, respectively

$$\begin{Bmatrix} \mathbf{R}_{\boldsymbol{\varepsilon}} \\ R_f \end{Bmatrix} = \begin{Bmatrix} \boldsymbol{\varepsilon}^e_{n+1} - \boldsymbol{\varepsilon}^{e\,trial}_{n+1} + \Delta\gamma \mathbf{N}_{n+1} \\ \sqrt{\boldsymbol{\sigma}_{n+1} : \mathbb{F} : \boldsymbol{\sigma}_{n+1}} + \mathbf{F} : \boldsymbol{\sigma}_{n+1} - (1 + q_{n+1}) \end{Bmatrix}; \; \{\mathbf{x}\} = \begin{Bmatrix} \boldsymbol{\varepsilon}^e_{n+1} \\ \Delta\gamma \end{Bmatrix}$$

where

$$\{\mathbf{R}\}^{(0)} = \begin{Bmatrix} \mathbf{0} \\ \sqrt{\boldsymbol{\sigma}^{trial}_{n+1} : \mathbb{F} : \boldsymbol{\sigma}^{trial}_{n+1}} + \mathbf{F} : \boldsymbol{\sigma}^{trial}_{n+1} - (1 + q^{trial}_{n+1}) \end{Bmatrix}$$

and

$$\{\mathbf{x}\}^{(0)} = \begin{Bmatrix} \boldsymbol{\varepsilon}^{e\,trial}_{n+1} \\ 0 \end{Bmatrix}$$

2. Start a Newton iterative scheme

for $k \leftarrow 0, n_{CPPM}$ **do**

3. Calculate the Jacobian

$$[\mathbf{J}_{CPPM}]^{(k)} = \begin{bmatrix} \mathbb{I} + \Delta\gamma \left(\frac{\mathbb{F}}{\sqrt{\boldsymbol{\sigma} : \mathbb{F} : \boldsymbol{\sigma}}} - \frac{(\mathbb{F} : \boldsymbol{\sigma}) \otimes (\boldsymbol{\sigma} : \mathbb{F})}{\sqrt{(\boldsymbol{\sigma} : \mathbb{F} : \boldsymbol{\sigma})^3}} \right) : \mathbb{D}^e & \frac{\mathbb{F} : \boldsymbol{\sigma}}{\sqrt{\boldsymbol{\sigma} : \mathbb{F} : \boldsymbol{\sigma}}} + \mathbf{F} \\ \left(\frac{\mathbb{F} : \boldsymbol{\sigma}}{\sqrt{\boldsymbol{\sigma} : \mathbb{F} : \boldsymbol{\sigma}}} + \mathbf{F} \right) : \mathbb{D}^e & -\overline{H}_{iso} \end{bmatrix}^{(k)}$$

4. Calculate the new solution vector

$$\begin{Bmatrix} \boldsymbol{\varepsilon}^e_{n+1} \\ \Delta\gamma \end{Bmatrix}^{(k+1)} = \begin{Bmatrix} \boldsymbol{\varepsilon}^e_{n+1} \\ \Delta\gamma \end{Bmatrix}^{(k)} - ([\mathbf{J}_{CPPM}]^{-1})^{(k)} \begin{Bmatrix} \mathbf{R}_{\boldsymbol{\varepsilon}^e} \\ R_f \end{Bmatrix}^{(k)}$$

5. Update $\mathbf{R}^{(k+1)}$ as in Step 1

6. Check for convergence

if $\|\mathbf{R}^{(k+1)}\| \leq tol$ **or** $k = n_{CPPM}$ **then**

SET $(\cdot)_{n+1} = (\cdot)^{(k+1)}_{n+1}$

EXIT

end if

end for

where $\mathbf{R}$ is the vector of residuals and $\mathbf{x} \in \mathbb{R}^{n_\mathbf{x}}$ is the vector of solution variables. Note that this problem is unconstrained in the sense that there are no constraints on any of the components of the solution vector $\mathbf{x}$. Other more sophisticated line search algorithms may take into account the unilateral constrained nature of the plastic multiplier, i.e. being non-negative (Pérez-Foguet and Armero, 2002). However, situations in which the plastic multiplier will be negative cannot be envisaged and thus its non-negative character has not been considered explicitly. In general, Eq. 3.95 corresponds to the first-order necessary conditions of an unconstrained minimisation problem where the continuously differentiable function to be minimised is

$$\varphi(\mathbf{x}) : \mathbb{R}^{n_\mathbf{x}} \rightarrow \mathbb{R}, \tag{3.96}$$

where $\mathbf{R}(\mathbf{x}) = \nabla\varphi(\mathbf{x})$. An iterative scheme is considered in order to solve the minimisation problem

$$\mathbf{x}^{(k+1)} = \mathbf{x}^{(k)} + \alpha^{(k)}\mathbf{d}^{(k)}, \tag{3.97}$$

where α is the line search parameter. Note that the solution update of the Newton-CPPM scheme is recovered if $\alpha = 1$. Since our attention is focused on schemes which exhibit a quadratic rate of convergence, a Newton update direction is considered

$$\mathbf{d}^{(k)} = -(\mathbf{J}^{-1}_{CPPM})^{(k)}\,\mathbf{R}^{(k)}, \tag{3.98}$$

where $\mathbf{J}^{(k)} = \nabla\mathbf{R}^{(k)} \in \mathbb{R}^{n_\mathbf{x}\times n_\mathbf{x}}$ is the Jacobian matrix. The invertibility of this Jacobian matrix is assured in the case where φ is strictly convex (as it is the case for the complementary energy function χ), as the Jacobian would be positive definite.

The classical global convergence theorem (Luenberger, 2003) states that global convergence for bounded sequences $\mathbf{x}^{(k)}$ is acquired if Eq. 3.97 defines a continuous mapping from $\mathbf{x}^{(k)}$ to $\mathbf{x}^{(k+1)}$ and a continuous descent function $M : \mathbb{R}^{n_\mathbf{x}} \rightarrow \mathbb{R}$ exists. This is satisfied provided the line search parameter α is obtained as the minimisation of the following merit function:

$$\hat{M}(\alpha) = M(\mathbf{x}^{(k)} + \alpha^{(k)}\mathbf{d}^{(k)}). \tag{3.99}$$

The direction $\mathbf{d}^{(k)}$ defines a descent direction so that

$$\frac{\partial\hat{M}}{\partial\alpha}\Big|_{\alpha=0} = \frac{\partial M(\mathbf{x}^{(k+1)})}{\partial\mathbf{x}^{(k+1)}}\Big|_{\alpha=0} \cdot \frac{\partial\mathbf{x}^{(k+1)}}{\partial\alpha} = \nabla M(\mathbf{x}^{(k)}) \cdot \mathbf{d}^{(k)} \leq 0. \tag{3.100}$$

Typical line search schemes obtain a numerical solution of the minimisation problem of the merit function (Eq. 3.99). For global convergence to be achieved, the Goldstein's

conditions (Luenberger, 2003) need to be met:

$$M(\mathbf{x}^{(k)}+\alpha^{(k)}\mathbf{d}^{(k)}) \leq M(\mathbf{x}^{(k)})+\beta\alpha^{(k)}\nabla M(\mathbf{x}^{(k)})\cdot\mathbf{d}^{(k)}, \tag{3.101}$$

and

$$M(\mathbf{x}^{(k)}+\alpha^{(k)}\mathbf{d}^{(k)}) \geq M(\mathbf{x}^{(k)})+(1-\beta)\alpha^{(k)}\nabla M(\mathbf{x}^{(k)})\cdot\mathbf{d}^{(k)}, \tag{3.102}$$

where $\beta \in (0,0.5)$. The first Goldstein condition implies the reduction of the merit function at each iteration and bounds $\alpha > 0$ from above. The second Goldstein condition assures that α is away from zero. Note that these are not the only possible conditions to be used in a line search scheme; similar alternative conditions can be found in the literature, e.g. Wolfe (1969). The descent function M can be written with respect to the residual $\mathbf{R}$ as

$$M(\mathbf{x}^{(k)}) = \frac{1}{2}\left[\mathbf{R}(\mathbf{x}^{(k)})\cdot\mathbf{R}(\mathbf{x}^{(k)})\right]. \tag{3.103}$$

The descent direction (Eq. 3.100) can be rewritten by using the Newton update direction (Eq. 3.98) such that

$$\nabla M(\mathbf{x}^{(k)})\cdot\mathbf{d}^{(k)} = -\frac{1}{2}\left[\frac{\partial(\mathbf{R}\cdot\mathbf{R})}{\partial\mathbf{x}}\right]^{(k)}\cdot\left[\left(\frac{\partial\mathbf{R}}{\partial\mathbf{x}}\right)^{-1}\right]^{(k)}\mathbf{R}^{(k)} = -2M(\mathbf{x}^{(k)}) \leq 0. \tag{3.104}$$

Several numerical approximations can be used to construct the line search scheme (Seifert and Schmidt, 2008), such as quadratic or cubic fittings of the merit function $\hat{M}$ through the current and previous values of $\hat{M}$ and $\hat{M}'$, or even pseudo-analytical schemes, where $\hat{M}$ is evaluated at equidistant values of the line search parameter α, and α is chosen where $\hat{M}$ is minimum. In this case, a quadratic fitting of $\hat{M}$ from the values $\hat{M}^{(k)}_{(0)}$, $\hat{M}'^{(k+1)}_{(0)}$, and $\hat{M}^{(k)}_{(j)}$ at $\alpha^{(k)}_{(j)}$ is chosen (Pérez-Foguet and Armero, 2002). The line search parameter of the next line search iteration, $\alpha^{(k)}_{(j+1)}$, is chosen as the minimum of the fitted quadratic curve. The line search iterative scheme is repeated for $j = 0,\ldots,n_{ls}$ until the first Goldstein condition (Eq. 3.101) is met, which now reads

$$\hat{M}(\alpha^{(k)}_{(j)}) = \hat{M}^{(k)}_{(j)} \leq (1-2\beta\alpha^{(k)}_{(j)})\,\hat{M}^{(k)}. \tag{3.105}$$

The second Golstein condition (Eq. 3.102) is considered by imposing $\alpha^{(k)}_{(j+1)} \geq \eta\alpha^{(k)}_{(j)}$ for a fixed value $\eta > 0$. These conditions lead to the "backtracking" line search (i.e. iteratively shrinking α) (Shultz et al., 1985). The values used in this study are $\eta = 0.1$ and $\beta = 10^{-4}$, as suggested by Pérez-Foguet and Armero (2002).

The primal-CPPM scheme is summarised in Algorithm 2. In this, n_{ls} is the maximum number of line search iterations. If the primal-CPPM scheme is compared to the Newton-CPPM scheme, one will notice that the addition of a line search scheme does not lead to

a significant increase in required computational effort in comparison with the traditional Newton-CPPM. This is because only a few additional vector computations are needed as the Jacobian is kept constant during the line search procedure, and the calculation of the Jacobian is more expensive than calculating the residual and solution vectors.

Comparison of the Newton-CPPM and the Primal-CPPM schemes applied to the generic quadric

Both Newton-CPPM and primal-CPPM schemes were applied to the generic quadric (Eq. 3.84) and were implemented in MATLAB (MathWorks, Natick, MA, USA). Their performance and convergence properties were assessed by a single time increment for different imposed trial strain levels.

The set of parameters used in these tests, which need to be defined in Eqs. 3.83, 3.84, 3.85 and 3.86, were $\sigma_0^+ = 50$, $\sigma_0^- = 100$, $\overline{H}_{iso} = 0.05$. The parameter ζ_0 was varied from $\zeta_0 = -1$ to $\zeta_0 = 0.49$. The corresponding shapes of the yield functions defined through these values are shown in Fig. 3.3. The isotropic stiffness tensor is defined as

$$\mathbb{D}^e = 2G\,\mathbb{I}_{sym} + (K - \frac{2}{3}G)\mathbf{I}\otimes\mathbf{I}, \tag{3.106}$$

where G and K are respectively the shear and bulk modulus, defined through a Young's modulus of $E = 10000$ and a Poisson's ratio of $\nu = 0.3$. The fourth-order tensor $\mathbb{I}_{sym}$ is defined as $(\mathbb{I}_{sym})_{ijkl} = \frac{1}{2}(\delta_{ik}\delta_{jl} + \delta_{il}\delta_{jk})$.

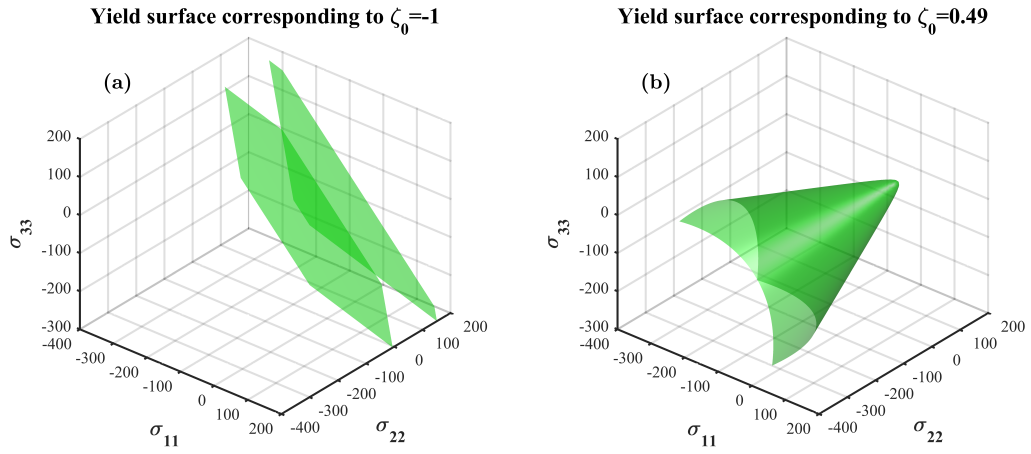

Fig. 3.3 (a) Yield surface corresponding at $\zeta_0 = -1$. **(b)** Yield surface corresponding at $\zeta_0 = 0.49$. Both surfaces are plotted in normal stress space.

As shown in Fig. 3.3a, the yield surface corresponding to $\zeta_0 = -1$ is defined through two parallel planes in normal stress space, which intersect the axes at σ_0^+ and σ_0^-. This implies that the associative flow vector always has the same direction. The yield surface

Algorithm 2 Primal-CPPM scheme.

1. 1. Define the residual and solution vectors, respectively

$$\left\{\begin{matrix}\mathbf{R}_{\boldsymbol{\varepsilon}^e}\\ R_f\end{matrix}\right\} = \left\{\begin{matrix}\boldsymbol{\varepsilon}^e_{n+1} - \boldsymbol{\varepsilon}^{e\,trial}_{n+1} + \Delta\gamma\mathbf{N}_{n+1}\\ \sqrt{\boldsymbol{\sigma}_{n+1} : \mathbb{F} : \boldsymbol{\sigma}_{n+1}} + \mathbf{F} : \boldsymbol{\sigma}_{n+1} - (1+q_{n+1})\end{matrix}\right\};\ \{\mathbf{x}\} = \left\{\begin{matrix}\boldsymbol{\varepsilon}^e_{n+1}\\ \Delta\gamma\end{matrix}\right\}$$

   where

$$\{\mathbf{R}\}^{(0)} = \left\{\begin{matrix}\mathbf{0}\\ \sqrt{\boldsymbol{\sigma}^{trial}_{n+1} : \mathbb{F} : \boldsymbol{\sigma}^{trial}_{n+1}} + \mathbf{F} : \boldsymbol{\sigma}^{trial}_{n+1} - (1+q^{trial}_{n+1})\end{matrix}\right\};\ \{\mathbf{x}\}^{(0)} = \left\{\begin{matrix}\boldsymbol{\varepsilon}^{e\,trial}_{n+1}\\ 0\end{matrix}\right\}$$

2. 2. Start a Newton iterative scheme
   - **for** $k \leftarrow 0, n_{CPPM}$ **do**
     - 3. Calculate the Jacobian $[\mathbf{J}_{CPPM}]^{(k)}$
     - 4. Start a line search scheme for unconstrained problems, with
       $\alpha^{(k)}_{(0)} = 1$; $\hat{M}^{(k)}_{(0)} = \frac{1}{2}(\mathbf{R}^{(k)} \cdot \mathbf{R}^{(k)})$; $\hat{M}'^{(k)}_{(0)} = -2\hat{M}^{(k)}_{(0)}$
       with the appropriate input data $\mathbf{R}^{(k)}_{(0)}$, $\mathbf{x}^{(k)}_{(0)}$, and $\mathbf{d}^{(k)}_{(0)}$
       - **for** $j \leftarrow 0, n_{ls}$ **do**
         - 5. Compute the new residual, solution, and merit function
           $\mathbf{R}^{(k+1)}_{(j)} = \mathbf{R}(\mathbf{x}^{(k+1)}_{(j)})$; $\mathbf{x}^{(k+1)}_{(j)} = \mathbf{x}^{(k)}_{(0)} + \alpha^{(k)}_{(j)}\mathbf{d}^{(k)}_{(0)}$
           $\hat{M}^{(k+1)}_{(j)} = \frac{1}{2}\left(\mathbf{R}^{(k+1)}_{(j)} \cdot \mathbf{R}^{(k+1)}_{(j)}\right)$
         - 6. Check the first Goldstein condition (Eq. 3.101)
           - **if** $\hat{M}^{(k+1)}_{(j)} \leq (1 - 2\beta\alpha^{(k)}_{(j)})\hat{M}^{(k)}$ or $j = n_{ls}$ **then**
             SET $\mathbf{x}^{(k+1)} = \mathbf{x}^{(k+1)}_{(j)}$
             EXIT
           - **else**
             $\alpha^{(k)}_{(j+1)} = \text{MAX}\left(\eta\alpha^{(k)}_{(j)},\ \frac{-\left(\alpha^{(k)}_{(j)}\right)^2 \hat{M}'^{(k)}_{(0)}}{2\left(\hat{M}^{(k+1)}_{(j)} - \hat{M}^{(k)}_{(0)} - \alpha^{(k)}_{(j)}\hat{M}'^{(k)}_{(0)}\right)}\right)$
           - **end if**
         - **end for**
     - 7. Check for convergence
       - **if** $\|\mathbf{R}^{(k+1)}\| \leq tol$ **or** $k = n_{CPPM}$ **then**
         SET $(\cdot)_{n+1} = (\cdot)^{(k+1)}_{n+1}$
         EXIT
       - **end if**
   - **end for**

in Fig. 3.3b corresponds to a hyperbolic approximation of a cone in normal stress space, with the same uniaxial yield stresses as the case where $\zeta_0 = -1$.

Convergence of the algorithm is achieved when $\|\mathbf{R}(\mathbf{x})\| \leq 10^{-8}$. The number of iterations to achieve convergence for both Newton-CPPM and primal-CPPM schemes is shown in Fig. 3.4. The y-axis represents the ζ_0 parameter, which varies from -1 to 0.49, and which changes the general curvature of the yield surface, but especially around the positive hydrostatic region when $\zeta_0 \geq 0.45$ as the yield surface becomes a cone when $\zeta_0 = 0.5$ (Schwiedrzik et al., 2013). The x-axis represents the elastic trial strain with a scalar ε_h defining its magnitude, and ranging from 0 to 10. The colourbar represents the number of iterations needed to achieve convergence, with the maximum number set to 50.

To test that the convergence of the closest-point projection method under difficult situations, stress returns are performed in regions where the yield surface is highly curved. Therefore, the tests include trial strains which have a direction close to the positive hydrostatic direction. The trial strain is defined as

$$\{\boldsymbol{\varepsilon}^{e\,trial}\} = \varepsilon_h \begin{Bmatrix} 1.1 \\ 1 \\ 1 \\ 0 \\ 0 \\ 0 \end{Bmatrix}. \tag{3.107}$$

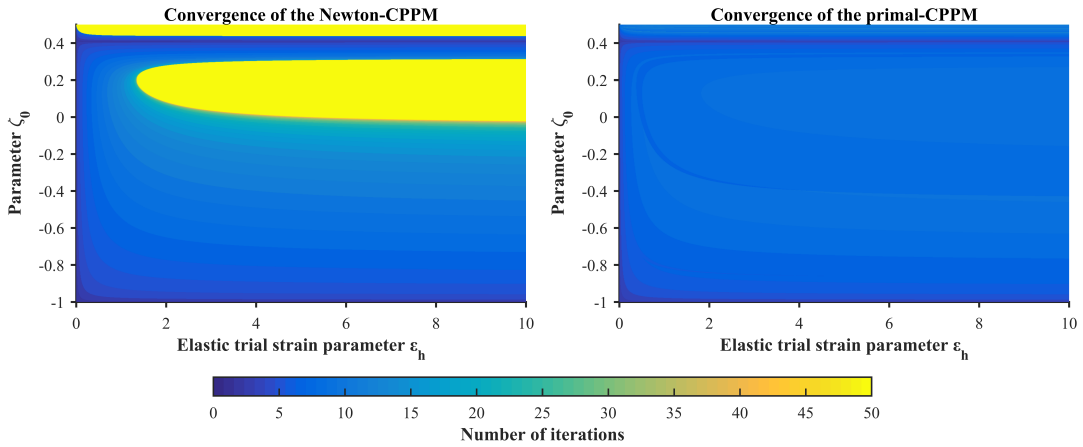

Fig. 3.4 Convergence of the Newton-CPPM **(left)** and of the primal-CPPM **(right)**.

It is observed in Fig. 3.4 that the Newton-CPPM scheme has regions where convergence is not achieved while the primal-CPPM scheme has none. The zones of non-convergence are situated in regions where the curvature of the yield surface is high and where the

trial-state is far away from the final solution. This is expected as the Newton-CPPM may have convergence difficulties in these situations. For both algorithms there is a region of convergence with low number of iterations close to $\zeta_0 = -1$ and $\varepsilon_h = 0$, which is expected as in these cases, the direction of the flow vector does not vary much and the trial-state is close to the final solution.

3.2.4 Mathematical description of damage

This Section describes the continuum rate-independent theory of damage from a physico-mathematical perspective. It is assumed that damage can be modelled as a scalar variable as the current state of validation experiments does not allow for evaluation of possible anisotropic damage at the solid phase level. The description of the theory presented here is based on de Souza Neto et al. (2008) and Murakami (2012).

Following the decomposition of the strain into elastic and plastic components (see Eq. 3.48), the addition of the damage scalar (D) only involves a modification of the elastic component of the free energy function, such that

$$\psi(\boldsymbol{\varepsilon}^e, D, \overline{\kappa}) = \psi^e(\boldsymbol{\varepsilon}^e, D) + \psi^p(\overline{\kappa}) = \frac{1}{2}(1-D)\boldsymbol{\varepsilon}^e : \mathbb{D}^e : \boldsymbol{\varepsilon}^e + \frac{1}{2}\overline{H}_{iso}\,\overline{\kappa}^2. \tag{3.108}$$

Therefore, the stress is now defined as

$$\boldsymbol{\sigma} = \frac{\partial \psi}{\partial \boldsymbol{\varepsilon}^e} = (1-D)\mathbb{D}^e : \boldsymbol{\varepsilon}^e. \tag{3.109}$$

The thermodynamic force associated with the damage variable D is defined as

$$Y = -\frac{\partial \psi}{\partial D} = \frac{1}{2}\boldsymbol{\varepsilon}^e : \mathbb{D}^e : \boldsymbol{\varepsilon}^e. \tag{3.110}$$

A dissipation potential (Eq. 3.46) is then considered as

$$\Xi(\boldsymbol{\sigma}, Y, q) = f(\boldsymbol{\sigma}, q) + F^D(Y). \tag{3.111}$$

The first part of the right-hand side of Eq. 3.111 corresponds to the yield surface and the second part corresponds to the damage dissipation potential. A possible expression for the damage dissipation potential is

$$F^D(Y) = \frac{1}{2}\overline{H}_{dam}Y^2. \tag{3.112}$$

The evolution of the damage variable for a material with associative behaviour is then defined as

$$\dot{D} = \dot{\gamma}\frac{\partial F^D}{\partial Y} = \dot{\gamma}\overline{H}_{dam}Y. \tag{3.113}$$

Newton-CPPM scheme applied to the generic quadric yield surface with damage

The free energy equation of the material being considered is again assumed to be quadratic due to the presence of a linear elastic regime, which now depends on the damage variable, and linear hardening (Eq. 3.108).

The considered yield function is the same as in the undamaged case (see Eq. 3.84), as it is defined in stress space rather than in effective stress space. If the latter was the case, damage would produce softening in the stress-strain curve due to the contraction of the yield surface as damage increases, and therefore would not preserve the desired constant hardening of 5% of the elastic modulus (Schwiedrzik and Zysset, 2015).
The closest-point projection method equations (Eqs. 3.80) for this damaged material read as

$$\begin{Bmatrix} \boldsymbol{\varepsilon}^e_{n+1} - \boldsymbol{\varepsilon}^{e\,trial}_{n+1} + \Delta\gamma\mathbf{N}_{n+1} \\ D_{n+1} - D^{trial}_{n+1} - \Delta\gamma\overline{H}_{dam}Y_{n+1} \\ \overline{\kappa}_{n+1} - \overline{\kappa}^{trial}_{n+1} - \Delta\gamma H_{n+1} \\ \sqrt{\boldsymbol{\sigma}_{n+1} : \mathbb{F} : \boldsymbol{\sigma}_{n+1}} + \mathbf{F} : \boldsymbol{\sigma}_{n+1} - (1 + q_{n+1}) \end{Bmatrix} = \begin{Bmatrix} \mathbf{R}_{\boldsymbol{\varepsilon}^e} \\ R_D \\ R_{\overline{\kappa}} \\ R_f \end{Bmatrix}, \tag{3.114}$$

where again $H = 1$, which means that the equation for the internal variable $\overline{\kappa}$ can be dropped, leading to Eqs. 3.114 becoming

$$\begin{Bmatrix} \boldsymbol{\varepsilon}^e_{n+1} - \boldsymbol{\varepsilon}^{e\,trial}_{n+1} + \Delta\gamma\mathbf{N}_{n+1} \\ D_{n+1} - D^{trial}_{n+1} - \Delta\gamma\overline{H}_{dam}Y_{n+1} \\ \sqrt{\boldsymbol{\sigma}_{n+1} : \mathbb{F} : \boldsymbol{\sigma}_{n+1}} + \mathbf{F} : \boldsymbol{\sigma}_{n+1} - (1 + q_{n+1}) \end{Bmatrix} = \begin{Bmatrix} \mathbf{R}_{\boldsymbol{\varepsilon}^e} \\ R_D \\ R_f \end{Bmatrix}. \tag{3.115}$$

The consistent linearisation of Eqs. 3.115 yields

$$\begin{Bmatrix} \mathrm{d}\boldsymbol{\varepsilon}^e + \mathrm{d}\Delta\gamma\mathbf{N} + \Delta\gamma\frac{\partial\mathbf{N}}{\partial\boldsymbol{\varepsilon}^e} : \mathrm{d}\boldsymbol{\varepsilon}^e \\ \mathrm{d}D - \mathrm{d}\Delta\gamma\overline{H}_{dam}Y_{n+1} - \Delta\gamma\overline{H}_{dam}\frac{\partial Y}{\partial\boldsymbol{\varepsilon}^e} : \mathrm{d}\boldsymbol{\varepsilon}^e \\ \frac{\partial f}{\partial\boldsymbol{\varepsilon}^e} : \mathrm{d}\boldsymbol{\varepsilon}^e + \frac{\partial f}{\partial D}\mathrm{d}D + \frac{\partial f}{\partial\Delta\gamma}\mathrm{d}\Delta\gamma \end{Bmatrix} = \begin{Bmatrix} \mathrm{d}\boldsymbol{\varepsilon}^{e\,trial} \\ 0 \\ 0 \end{Bmatrix}. \tag{3.116}$$

And thus, the Jacobian of the closest-point projection method scheme is now defined as

$$[\mathbf{J}_{CPPM}] = \begin{bmatrix} \mathbb{I} + \Delta\gamma\frac{\partial\mathbf{N}}{\partial\boldsymbol{\varepsilon}^e} & \mathbf{0} & \mathbf{N} \\ -\Delta\gamma\overline{H}_{dam}\frac{\partial Y}{\partial\boldsymbol{\varepsilon}^e} & 1 & -\overline{H}_{dam}Y \\ \frac{\partial f}{\boldsymbol{\varepsilon}^e} & \frac{\partial f}{\partial D} & \frac{\partial f}{\partial\Delta\gamma} \end{bmatrix} = \begin{bmatrix} \mathbb{A}_{11} & \mathbf{A}_{12} & \mathbf{A}_{13} \\ \mathbf{A}_{21} & A_{22} & A_{23} \\ \mathbf{A}_{31} & A_{23} & A_{33} \end{bmatrix}, \tag{3.117}$$

where the corresponding coefficients are given in Table 3.2.

Table 3.2 Coefficients of the Jacobian of the closest-point projection method of the generic quadric with isotropic hardening and isotropic damage.

Coefficient	Mathematical expression
$\mathbb{A}_{11}$	$\mathbb{I}+\Delta\gamma\frac{\partial \mathbf{N}}{\partial \boldsymbol{\sigma}}:\frac{\partial \boldsymbol{\sigma}}{\partial \boldsymbol{\varepsilon}^e}$
$\mathbf{A}_{12}$	$\mathbf{0}$
$\mathbf{A}_{13}$	$\mathbf{N}$
$\mathbf{A}_{21}$	$-\Delta\gamma\overline{H}_{dam}\mathbb{D}^e:\boldsymbol{\varepsilon}^e$
A_{22}	1
A_{23}	$-\overline{H}_{dam}Y$
$\mathbf{A}_{31}$	$\mathbf{N}:\frac{\partial \boldsymbol{\sigma}}{\partial \boldsymbol{\varepsilon}^e}$
A_{32}	$-\mathbf{N}:\mathbb{D}^e:\boldsymbol{\varepsilon}^e$
A_{33}	$-\overline{H}_{iso}$
$\frac{\partial \mathbf{N}}{\partial \boldsymbol{\sigma}}$	$\frac{\mathbb{F}}{\sqrt{\boldsymbol{\sigma}:\mathbb{F}:\boldsymbol{\sigma}}}-\frac{(\mathbb{F}:\boldsymbol{\sigma})\otimes(\boldsymbol{\sigma}:\mathbb{F})}{(\sqrt{\boldsymbol{\sigma}:\mathbb{F}:\boldsymbol{\sigma}})^3}$
$\frac{\partial \boldsymbol{\sigma}}{\partial \boldsymbol{\varepsilon}^e}$	$(1-D)\mathbb{D}^e$

Comparison of the Newton-CPPM and the Primal-CPPM schemes applied to the generic quadric with damage

The performance and convergence properties of the Newton-CPPM and primal-CPPM for the generic quadric with damage are assessed by a single time increment for different strain levels imposed. The set of parameters and settings used in these tests are the same as before, except for the trial strain parameter ε_h, which now ranges from 0 to 0.1. The addition of a damage parameter is needed for this model; an arbitrary value of $\overline{H}_{dam}=0.01$ was used. The convergence is shown in Fig. 3.5.

It can be observed from Fig. 3.5 that both the Newton-CPPM and primal-CPPM have regions of no convergence. This is because, in the case of damage, global convergence may not be guaranteed as the aforementioned assumptions for global convergence are not fulfilled. For instance, the assumption of a twice differentiable positive-definite Hessian of the complementary energy function χ is not fulfilled, and thus global convergence for the primal-CPPM algorithm is not attained. This is easily seen, as

$$\frac{\partial^2 \psi}{\partial D^2}=0. \tag{3.118}$$

However, there are alternative methods to obtain improved convergence when damage is considered. In this study, an improved trial predictor was used (Bićanić and Pearce,

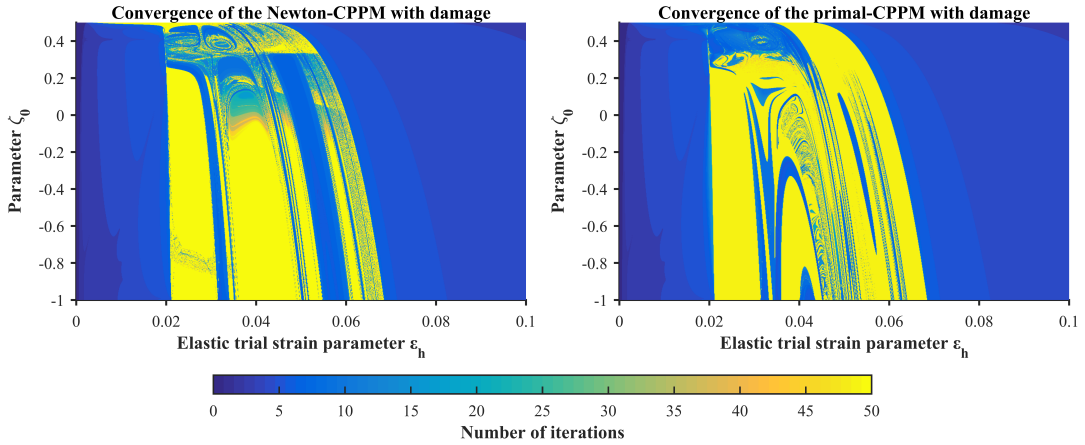

Fig. 3.5 Convergence of the Newton-CPPM **(left)** and of the primal-CPPM **(right)** when considering damage.

1996; de Souza Neto et al., 2008). This consists of performing a Newton-CPPM loop as normal, if convergence is not achieved then the loop is restarted but with the initial guess for stress now being $\boldsymbol{\sigma}^{proj}$, which is defined as the stress returned to the frozen yield surface, i.e. no hardening or damage evolution. Needless to say that, in order to obtain $\boldsymbol{\sigma}^{proj}$, a primal-CPPM scheme with the perfectly plastic material without damage should be used. This scheme is detailed in Algorithm 3. The convergence of this method is compared with the convergence of the Newton-CPPM and shown in Fig. 3.6.

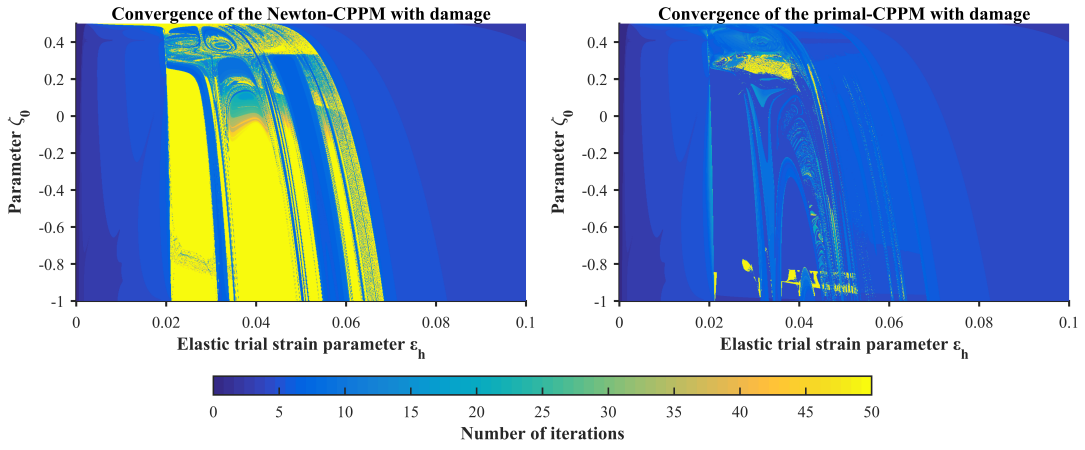

Fig. 3.6 Convergence of the Newton-CPPM **(left)** and of the Newton-CPPM with an improved trial predictor **(right)**.

As shown in Fig. 3.6, the convergence properties of the Newton-CPPM scheme with an improved trial predictor are hugely improved with respect to the traditional

Algorithm 3 Improved initial predictor for a constitutive law with damage.

1. 1. Perform a Newton-CPPM as in Algorithm 1, with the initial guesses
2. $\boldsymbol{\sigma} = \boldsymbol{\sigma}_{n+1}^{trial}; \quad \overline{\kappa} = \overline{\kappa}_{n+1}^{trial}; \quad D = D_{n+1}^{trial}$
3. 2. Check for convergence of the initial Newton-CPPM
4. **if** $\|\mathbf{R}^{(k+1)}\| \leq tol$ **then**
5. SET $(\cdot)_{n+1} = (\cdot)_{n+1}^{(k+1)}$
6. EXIT
7. **else**
8. 3. Perform a primal-CPPM as in Algorithm 2, with the initial guesses
9. $\boldsymbol{\sigma} = \boldsymbol{\sigma}_{n+1}^{trial}; \quad \overline{\kappa} = \overline{\kappa}_{n+1}^{trial}; \quad D = D_{n+1}^{trial}$
10. and with
11. $\overline{H}_{iso} = 0; \quad \overline{H}_{dam} = 0$
12. to obtain $\boldsymbol{\sigma}_{n+1}^{proj}$
13.
14. 4. Perform a Newton-CPPM as in Algorithm 1, with the initial guesses
15. $\boldsymbol{\sigma} = \boldsymbol{\sigma}_{n+1}^{proj}; \quad \overline{\kappa} = \overline{\kappa}_{n+1}^{trial}; \quad D = D_{n+1}^{trial}$
16. **end if**

Newton-CPPM scheme. However, global convergence is not attained, which is expected since the assumptions for it to happen (Eq. 3.118) are not met.

3.2.5 Consistent tangent operator

Consistent tangent operator without incorporation of damage

By rewriting the first row of Eqs. 3.91, the following is obtained:

$$\left(\mathbb{I} + \Delta\gamma \frac{\partial \mathbf{N}}{\partial \boldsymbol{\sigma}} : \mathbb{D}^e\right) : \mathrm{d}\boldsymbol{\varepsilon}^e + \mathrm{d}\Delta\gamma\, \mathbf{N} = \mathrm{d}\boldsymbol{\varepsilon}^{e\,trial}. \tag{3.119}$$

The left-hand side of Eq. 3.119 can be rewritten by using $\mathrm{d}\boldsymbol{\varepsilon}^e = (\mathbb{D}^e)^{-1} : \boldsymbol{\sigma}$, such that

$$\left(\mathbb{I} + \Delta\gamma \frac{\partial \mathbf{N}}{\partial \boldsymbol{\sigma}} : \mathbb{D}^e\right) : \mathrm{d}\boldsymbol{\varepsilon}^e = \left((\mathbb{D}^e)^{-1} + \Delta\gamma \frac{\partial \mathbf{N}}{\partial \boldsymbol{\sigma}}\right) : \mathrm{d}\boldsymbol{\sigma}. \tag{3.120}$$

Using the second row of the system of Eqs. 3.91, the following is obtained:

$$\mathrm{d}\overline{\kappa} = \mathrm{d}\Delta\gamma \rightarrow \mathbf{N} : \mathbb{D}^e : \mathrm{d}\boldsymbol{\varepsilon}^e - \overline{H}_{iso}\overline{\kappa} = 0 \rightarrow \mathrm{d}\Delta\gamma = \frac{1}{\overline{H}_{iso}}(\mathbf{N} : \mathrm{d}\boldsymbol{\sigma}). \tag{3.121}$$

By combining the two previous expressions the following is achieved:

$$\mathrm{d}\Delta\gamma = \frac{1}{\overline{H}_{iso}}(\mathbf{N}:\mathbb{P}:\mathrm{d}\boldsymbol{\varepsilon}^{e\,trial} - \mathrm{d}\Delta\gamma\,\mathbf{N}:\mathbb{P}:\mathbf{N}) \rightarrow \mathrm{d}\Delta\gamma = \frac{\mathbf{N}:\mathbb{P}:\mathrm{d}\boldsymbol{\varepsilon}^{e\,trial}}{\mathbf{N}:\mathbb{P}:\mathbf{N}+\overline{H}_{iso}}, \tag{3.122}$$

where

$$\mathbb{P} = \left((\mathbb{D}^e)^{-1} + \Delta\gamma\,\frac{\partial \mathbf{N}}{\partial \boldsymbol{\sigma}}\right)^{-1}. \tag{3.123}$$

The final expression of the consistent tangent operator is retrieved by using Eq. 3.120 and Eq. 3.122 in Eq. 3.119. This now reads as

$$\mathrm{d}\boldsymbol{\sigma} = \mathbb{P}:\mathrm{d}\boldsymbol{\varepsilon}^{e\,trial} - \frac{\mathbf{N}:\mathbb{P}:\mathrm{d}\boldsymbol{\varepsilon}^{e\,trial}}{\mathbf{N}:\mathbb{P}:\mathbf{N}+\overline{H}_{iso}}\,\mathbb{P}:\mathbf{N} \tag{3.124}$$

and thus leading to the consistent tangent operator $\mathbb{D}^{ep}$

$$\mathbb{D}^{ep} = \frac{\partial \boldsymbol{\sigma}}{\partial \boldsymbol{\varepsilon}^{e\,trial}} = \mathbb{P} - \frac{(\mathbb{P}:\mathbf{N})\otimes(\mathbf{N}:\mathbb{P})}{\mathbf{N}:\mathbb{P}:\mathbf{N}+\overline{H}_{iso}}. \tag{3.125}$$

Consistent tangent operator with damage

Introducing a scalar damage variable in the first row of Eqs. 3.116 gives

$$\left(\mathbb{I} + (1-D)\Delta\gamma\,\frac{\partial \mathbf{N}}{\partial \boldsymbol{\sigma}}:\mathbb{D}^e\right):\mathrm{d}\boldsymbol{\varepsilon}^e + \mathrm{d}\Delta\gamma\,\mathbf{N} = \mathrm{d}\boldsymbol{\varepsilon}^{e\,trial}. \tag{3.126}$$

The left-hand side of Eq. 3.126 can be rewritten by using $\mathrm{d}\boldsymbol{\varepsilon}^e = \frac{1}{1-D}(\mathbb{D}^e)^{-1}:\boldsymbol{\sigma}$, such that

$$\left(\mathbb{I} + (1-D)\Delta\gamma\,\frac{\partial \mathbf{N}}{\partial \boldsymbol{\sigma}}:\mathbb{D}^e\right):\mathrm{d}\boldsymbol{\varepsilon}^e = \left(\frac{1}{1-D}(\mathbb{D}^e)^{-1} + \Delta\gamma\,\frac{\partial \mathbf{N}}{\partial \boldsymbol{\sigma}}\right):\mathrm{d}\boldsymbol{\sigma}. \tag{3.127}$$

Using the second row of the system of Eqs. 3.116, the following is obtained:

$$\mathrm{d}D = \mathrm{d}\Delta\gamma\overline{H}_{dam}Y + \Delta\gamma\overline{H}_{dam}\,(\mathbb{D}^e:\boldsymbol{\varepsilon}^e):\mathrm{d}\boldsymbol{\varepsilon}^e = \mathrm{d}\Delta\gamma\overline{H}_{dam}Y + \Delta\gamma\frac{\overline{H}_{dam}}{1-D}\boldsymbol{\varepsilon}^e:\mathrm{d}\boldsymbol{\sigma}, \tag{3.128}$$

and using the third row of the system of Eqs. 3.116, the following is achieved:

$$(1-D)\mathbf{N}:\mathbb{D}^e:\mathrm{d}\boldsymbol{\varepsilon}^e - \mathbf{N}:\mathbb{D}^e:\boldsymbol{\varepsilon}^e\,\mathrm{d}D - \overline{H}_{iso}\,\mathrm{d}\Delta\gamma = \mathbf{N}:\mathrm{d}\boldsymbol{\sigma} - \mathbf{N}:\mathbb{D}^e:\boldsymbol{\varepsilon}^e\,\mathrm{d}D - \overline{H}_{iso}\,\mathrm{d}\Delta\gamma. \tag{3.129}$$

By combining Eqs. 3.127 - 3.129, the following is obtained:

$$\begin{aligned}
0 &= \mathbf{N} : \mathrm{d}\boldsymbol{\sigma} - \mathrm{d}\Delta\gamma \overline{H}_{dam}\, Y\, (\mathbf{N} : \mathbb{D}^e : \boldsymbol{\varepsilon}^e) - \Delta\gamma \frac{\overline{H}_{dam}}{1-D} (\mathbf{N} : \mathbb{D}^e : \boldsymbol{\varepsilon}^e)(\boldsymbol{\varepsilon}^e : \mathrm{d}\boldsymbol{\sigma}) - \overline{H}_{iso}\, \mathrm{d}\Delta\gamma \\
&\rightarrow \mathrm{d}\Delta\gamma (\overline{H}_{dam}\, Y (\mathbf{N} : \mathbb{D}^e : \boldsymbol{\varepsilon}^e) + \overline{H}_{iso}) \\
&= \left(\mathbf{N} - \Delta\gamma \frac{\overline{H}_{dam}}{1-D} (\mathbf{N} : \mathbb{D}^e : \boldsymbol{\varepsilon}^e) \boldsymbol{\varepsilon}^e \right) : \mathbb{P} : (\mathrm{d}\boldsymbol{\varepsilon}^{e\,trial} - \mathrm{d}\Delta\gamma \mathbf{N}) \\
&\rightarrow \mathrm{d}\Delta\gamma = \frac{\left(\mathbf{N} - \Delta\gamma \frac{\overline{H}_{dam}}{1-D} (\mathbf{N} : \mathbb{D}^e : \boldsymbol{\varepsilon}^e) \boldsymbol{\varepsilon}^e \right) : \mathbb{P} : \mathrm{d}\boldsymbol{\varepsilon}^{e\,trial}}{\overline{H}_{dam}\, Y (\mathbf{N} : \mathbb{D}^e : \boldsymbol{\varepsilon}^e) + \overline{H}_{iso} + \left(\mathbf{N} - \Delta\gamma \frac{\overline{H}_{dam}}{1-D} (\mathbf{N} : \mathbb{D}^e : \boldsymbol{\varepsilon}^e) \boldsymbol{\varepsilon}^e : \right) \mathbb{P} : \mathbf{N}}
\end{aligned} \quad , \tag{3.130}$$

where

$$\mathbb{P} = \left(\frac{1}{1-D} (\mathbb{D}^e)^{-1} + \Delta\gamma \frac{\partial \mathbf{N}}{\partial \boldsymbol{\sigma}} \right)^{-1} . \tag{3.131}$$

The final expression of the consistent tangent operator is retrieved by using Eq. 3.127 and Eq. 3.130 in Eq. 3.126. This now gives

$$\begin{aligned}
\mathrm{d}\boldsymbol{\sigma} &= \mathbb{P} : \mathrm{d}\boldsymbol{\varepsilon}^{e\,trial} \\
&- \frac{\left(\mathbf{N} - \Delta\gamma \frac{\overline{H}_{dam}}{1-D} (\mathbf{N} : \mathbb{D}^e : \boldsymbol{\varepsilon}^e) \boldsymbol{\varepsilon}^e \right) : \mathbb{P} : \mathrm{d}\boldsymbol{\varepsilon}^{e\,trial}}{\overline{H}_{dam}\, Y (\mathbf{N} : \mathbb{D}^e : \boldsymbol{\varepsilon}^e) + \overline{H}_{iso} + \left(\mathbf{N} - \Delta\gamma \frac{\overline{H}_{dam}}{1-D} (\mathbf{N} : \mathbb{D}^e : \boldsymbol{\varepsilon}^e) \boldsymbol{\varepsilon}^e \right) : \mathbb{P} : \mathbf{N}} \mathbb{P} : \mathbf{N}
\end{aligned} \tag{3.132}$$

and thus leading to the, generally unsymmetric, consistent tangent operator $\mathbb{D}^{ep}$

$$\mathbb{D}^{ep} = \mathbb{P} - \frac{(\mathbb{P} : \mathbf{N}) \otimes \left(\left[\mathbf{N} - \Delta\gamma \frac{\overline{H}_{dam}}{1-D} (\mathbf{N} : \mathbb{D}^e : \boldsymbol{\varepsilon}^e) \boldsymbol{\varepsilon}^e \right] : \mathbb{P} \right)}{\overline{H}_{dam}\, Y (\mathbf{N} : \mathbb{D}^e : \boldsymbol{\varepsilon}^e) + \overline{H}_{iso} + \left(\mathbf{N} - \Delta\gamma \frac{\overline{H}_{dam}}{1-D} (\mathbf{N} : \mathbb{D}^e : \boldsymbol{\varepsilon}^e) \boldsymbol{\varepsilon}^e \right) : \mathbb{P} : \mathbf{N}} . \tag{3.133}$$

Chapter 4

The finite element method and high-performance computing

This Chapter introduces the finite element method (FEM) from a mathematical point of view, as it is the main numerical method used in this study to solve the global initial boundary value problem associated to the principle of virtual work, and also because it is crucial to understand some of the following work. Additionally, some high performance computing (HPC) concepts relevant to the simulations conducted are introduced as most of the simulations performed during this study were run on HPC platforms (a Cray XC30 hosted by ARCHER, UK National Supercomputing Centre, EPCC Edinburgh; and a BlueGene/Q hosted by the Hartree Centre, STFC Daresbury).

4.1 The finite element method

In this Section the FEM is briefly described, and it largely follows the description of theory and notation in de Souza Neto et al. (2008) and Belytschko et al. (2000). The theory outlined in this Section is initially described in a linear kinematics setting and then its extension to finite strains is given. A quasi-static approach is used and therefore inertial forces are not considered; also body forces are neglected as an approximation (the weight of the considered trabecular bone specimens is relatively insignificant in comparison to the external forces).

At this point it is worth stating that two main approximations are required in the FE solution of an initial boundary value problem[1].

1. *A time discretisation of the underlying constitutive initial value problem.*
   A numerical integration scheme is used to solve the initial value problem defined

[1] This problem is defined later, in Section 4.1.2.

by the constitutive equations, which relate stresses to the history of deformations (Eqs. 3.43 and 3.47).

2. *A finite element discretisation.*
   A standard FE approximation of the principle of virtual work is considered, where the continuum domain of the body is (approximately) replaced with a finite set of elements of simpler geometry.

With the introduction of these two approximations, the initial boundary value problem is reduced to a set of incremental, generally nonlinear, algebraic FE equations which are solved at each time increment of the considered time interval $[t_0, T]$.

4.1.1 The principle of virtual work

A body occupies a region Ω with a boundary $\partial\Omega$ in its reference (or material) configuration. This body is subjected to surface tractions on $\partial\Omega$. The current (or spatial) description of this body and its boundary respectively corresponds to the region $\boldsymbol{\varphi}(\Omega)$ and the boundary $\boldsymbol{\varphi}(\partial\Omega)$, where $\boldsymbol{\varphi}$ is the mapping of deformations.

The principle of virtual work establishes that a body is in equilibrium if the corresponding variational equation holds. The spatial description of the principle of virtual work reads

$$\int_{\boldsymbol{\varphi}(\Omega)} \boldsymbol{\sigma}(\mathbf{F},t) : \nabla_{\mathbf{x}} \boldsymbol{\eta} \, \mathrm{d}V - \int_{\boldsymbol{\varphi}(\partial\Omega)} \mathbf{t}^{ext}(\mathbf{x},t) \cdot \boldsymbol{\eta} \, \mathrm{d}A = 0, \quad \forall \boldsymbol{\eta} \in \mathscr{V}, \tag{4.1}$$

where $\boldsymbol{\sigma}$ is the Cauchy stress tensor, $\mathbf{F}$ is the deformation gradient tensor, $\mathbf{x}$ are the spatial coordinates, $\mathbf{t}^{ext}$ are the boundary tractions (or external traction field) per unit deformed area, and $\mathscr{V}$ is the space of virtual displacements of the considered body.

If the assumption of linear kinematics is considered, material and spatial configurations coincide, and the principle of virtual work can be rewritten as

$$\int_{\Omega} \boldsymbol{\sigma}(\boldsymbol{\varepsilon},t) : \nabla^{sym}_{\mathbf{X}} \boldsymbol{\eta} \, \mathrm{d}V - \int_{\partial\Omega} \mathbf{t}^{ext}(\mathbf{X},t) \cdot \boldsymbol{\eta} \, \mathrm{d}A = 0, \quad \forall \boldsymbol{\eta} \in \mathscr{V}, \tag{4.2}$$

where in this case $\boldsymbol{\sigma}$ is the infinitesimal stress tensor, $\boldsymbol{\varepsilon}$ is the infinitesimal strain tensor, and $\mathbf{X}$ are the initial (or material) coordinates.

4.1.2 The initial boundary value problem

Coupling together the principle of virtual work (for instance, Eq. 4.2) and the constitutive stress-strain relationships (for instance, an elastoplastic constitutive model as

described in Chapter 3), an initial boundary value problem can be formulated, whose numerical solution is obtained through the FEM.

The boundary of the region occupied by a generic body in the material configuration is decoupled into

$$\partial\Omega = \partial\Omega_u \cup \partial\Omega_t, \tag{4.3}$$

where $\partial\Omega_u$ is the portion of the boundary where the displacements are prescribed and $\partial\Omega_t$ is the portion of the boundary where the tractions are prescribed. This body is subjected to the following BCs:

1. *The natural boundary conditions.*
   The history of surface traction $\mathbf{t}^{ext}(\mathbf{X},t), \quad t \in [t_0,T]$ is prescribed over $\partial\Omega_t$.

2. *The essential boundary conditions.*
   The displacements are prescribed on $\partial\Omega_u$. The set of kinematically admissible displacements of the body is then defined as

$$\mathscr{K} = \{\mathbf{u}(\mathbf{X},t) : \Omega\times\mathbb{R} \to \mathscr{U} \mid \mathbf{u}(\mathbf{X},t) = \overline{\mathbf{u}}(\mathbf{X},t), \quad t\in[t_0,T], \quad \mathbf{X}\in\partial\Omega_u\}, \tag{4.4}$$

   where $\mathbf{u}$ are the displacements, $\mathscr{U}$ is the vector space of dimension equal to the number of considered physical dimensions, and $\overline{\mathbf{u}}$ are the prescribed displacements.

The considered body is made of a material which is assumed to be modelled by a constitutive law based on internal variables. The internal variable field is known at the initial time t_0, which is $\boldsymbol{\alpha}(\mathbf{X},t_0) = \boldsymbol{\alpha}_0(\mathbf{X})$ (usually considered to be $\mathbf{0}$ if the material is not yielded or damaged at t_0).

The initial boundary value problem in spatial configuration is stated as follows:

The spatial quasi-static initial boundary value problem

Find a kinematically admissible displacement function $\boldsymbol{u} \in \mathscr{K}$ *such that, for all* $t \in [t_0, T]$*, the principle of virtual work is satisfied:*

$$\int_{\boldsymbol{\varphi}(\Omega)} \boldsymbol{\sigma}(\mathbf{F},t) : \nabla_{\mathbf{x}} \boldsymbol{\eta} \, \mathrm{d}V - \int_{\boldsymbol{\varphi}(\partial\Omega_t)} \mathbf{t}^{ext}(\mathbf{x},t) \cdot \boldsymbol{\eta} \, \mathrm{d}A = 0, \quad \forall \boldsymbol{\eta} \in \mathscr{V}, \tag{4.5}$$

where

$$\mathscr{V} = \{\boldsymbol{\eta} : \boldsymbol{\varphi}(\Omega,t) \to \mathscr{U} \mid \boldsymbol{\eta} = \mathbf{0} \text{ on } \boldsymbol{\varphi}(\partial\Omega_u,t)\} \tag{4.6}$$

and at each point $\boldsymbol{X}$*,* $\boldsymbol{\sigma}$ *is the solution of* $\boldsymbol{\sigma} = \frac{1}{det\boldsymbol{F}} \frac{\partial \psi(\boldsymbol{F},\boldsymbol{\alpha})}{\partial \boldsymbol{F}} \boldsymbol{F}^T$ *and* $\dot{\boldsymbol{\alpha}} = f(\boldsymbol{F},\boldsymbol{\alpha})$*, with prescribed deformation gradient*

$$\mathbf{F}(\mathbf{X},t) = \nabla_{\mathbf{X}} \boldsymbol{\varphi}(\mathbf{X},t) = \mathbf{I} + \nabla_{\mathbf{X}} \mathbf{u}(\mathbf{X},t). \tag{4.7}$$

The infinitesimal initial boundary value problem is stated as follows:

The infinitesimal quasi-static initial boundary value problem

Find a kinematically admissible displacement function $\boldsymbol{u} \in \mathscr{K}$ *such that, for all* $t \in [t_0, T]$*, the principle of virtual work is satisfied:*

$$\int_{\Omega} \boldsymbol{\sigma}(\boldsymbol{\varepsilon},t) : \nabla^{sym} \boldsymbol{\eta} \, \mathrm{d}V - \int_{\partial\Omega_t} \mathbf{t}^{ext}(\mathbf{X},t) \cdot \boldsymbol{\eta} \, \mathrm{d}A = 0, \quad \forall \boldsymbol{\eta} \in \mathscr{V}, \tag{4.8}$$

where

$$\mathscr{V} = \{\boldsymbol{\eta} : \Omega \to \mathscr{U} \mid \boldsymbol{\eta} = \mathbf{0} \text{ on } \partial\Omega_u\} \tag{4.9}$$

and at each point $\boldsymbol{X}$*,* $\boldsymbol{\sigma}$ *is the solution of the infinitesimal version of Eq. 3.43 and* $\dot{\boldsymbol{\alpha}} = f(\boldsymbol{\varepsilon},\boldsymbol{\alpha})$*, with prescribed infinitesimal strain*

$$\boldsymbol{\varepsilon}(\mathbf{X},t) = \nabla^{sym} \mathbf{u}(\mathbf{X},t). \tag{4.10}$$

4.1.3 Finite element interpolation

The FEM is used to obtain a numerical solution of the previously mentioned initial boundary value problems. This involves replacing $\mathscr{K}$ and $\mathscr{V}$ with discrete subsets $\mathscr{K}^{ip}$ and $\mathscr{V}^{ip}$, respectively, which are generated through a FE discretisation of Ω.

A generic element *el* is defined through a certain number of nodes, with an interpolation (or shape) function $N_i^{el}(\mathbf{X})$ associated to each node i with coordinates $\mathbf{X}^i$. These shape functions are defined so that they have a value of 1 at node i, and 0 at every other

node, so that

$$N_i^{el}(\mathbf{X}^j) = \begin{cases} 1, & \text{for } i = j \\ 0, & \text{for } i \neq j \end{cases} . \tag{4.11}$$

4.1.4 The discretised principle of virtual work

The interpolated sets $\mathscr{K}^{ip}$ and $\mathscr{V}^{ip}$ are respectively

$$\mathscr{K}^{ip} = \{\mathbf{u}^{ip}(\mathbf{X}) = \sum_{i=1}^{n_{nod}} \mathbf{u}(\mathbf{X}^i) N_i^g(\mathbf{X}) \mid \mathbf{u}(\mathbf{X}^i) = \overline{\mathbf{u}}(\mathbf{X}^i), \quad \mathbf{X}^i \in \partial\Omega_u\} \tag{4.12}$$

and

$$\mathscr{V}^{ip} = \{\boldsymbol{\eta}^{ip}(\mathbf{X}) = \sum_{i=1}^{n_{nod}} \boldsymbol{\eta}(\mathbf{X}^i) N_i^g(\mathbf{X}) \mid \boldsymbol{\eta}(\mathbf{X}^i) = \mathbf{0}, \quad \mathbf{X}^i \in \partial\Omega_u\}, \tag{4.13}$$

where n_{nod} stands for the total number of nodes in a FE system. The global interpolation matrix is then defined as

$$\mathbf{N}^g(\mathbf{X}) = [\text{diag}[N_1^g(\mathbf{X})] \quad \text{diag}[N_2^g(\mathbf{X})] \quad ... \quad \text{diag}[N_{gnod}^g(\mathbf{X})]], \tag{4.14}$$

where, in three dimensions, $\text{diag}[N_i^g(\mathbf{X})]$ is defined as (dependency on $\mathbf{X}$ is dropped for convenience from now onwards)

$$\text{diag}[N_i^g] = \begin{bmatrix} N_i^g & 0 & 0 \\ 0 & N_i^g & 0 \\ 0 & 0 & N_i^g \end{bmatrix}. \tag{4.15}$$

The global vector of displacements and the global vector of virtual displacements are respectively defined as

$$\mathbf{u} = \{u_1^1, ..., u_{n_{dim}}^1, ..., u_1^{n_{gnod}}, ..., u_{n_{dim}}^{n_{gnod}}\}^{\mathrm{T}} \tag{4.16}$$

and

$$\boldsymbol{\eta} = \{\eta_1^1, ..., \eta_{n_{dim}}^1, ..., \eta_1^{n_{gnod}}, ..., \eta_{n_{dim}}^{n_{gnod}}\}^{\mathrm{T}}, \tag{4.17}$$

where n_{dim} is the number of spatial dimensions (three dimensions are used throughout this study), and u_i^j is the ith component of the displacement vector at the global node j. Any element $\mathbf{u}^{ip} \in \mathscr{K}^{ip}$ and $\boldsymbol{\eta}^{ip} \in \mathscr{V}^{ip}$ can be respectively represented as

$$\mathbf{u}^{ip} = \mathbf{N}^g \mathbf{u} \tag{4.18}$$

and

$$\boldsymbol{\eta}^{ip} = \mathbf{N}^g \boldsymbol{\eta}. \tag{4.19}$$

The global discrete symmetric gradient in three dimensions is defined as

$$[\mathbf{B}^g] = \begin{bmatrix} N^g_{1,1} & 0 & 0 & N^g_{2,1} & 0 & 0 & \dots & N^g_{n_{gnod},1} & 0 & 0 \\ 0 & N^g_{1,2} & 0 & 0 & N^g_{2,2} & 0 & \dots & 0 & N^g_{n_{gnod},2} & 0 \\ 0 & 0 & N^g_{1,3} & 0 & 0 & N^g_{2,3} & \dots & 0 & 0 & N^g_{n_{gnod},3} \\ N^g_{1,2} & N^g_{1,1} & 0 & N^g_{2,2} & N^g_{2,1} & 0 & \dots & N^g_{n_{gnod},2} & N^g_{n_{gnod},1} & 0 \\ N^g_{1,3} & 0 & N^g_{1,1} & N^g_{2,3} & 0 & N^g_{2,1} & \dots & N^g_{n_{gnod},3} & 0 & N^g_{n_{gnod},1} \\ 0 & N^g_{1,3} & N^g_{1,2} & 0 & N^g_{2,3} & N^g_{2,2} & \dots & 0 & N^g_{n_{gnod},3} & N^g_{n_{gnod},2} \end{bmatrix}, \tag{4.20}$$

where $(\cdot)_{i,j} = \frac{\partial (\cdot)_i}{\partial X_j}$ is the partial derivative of the elements with index i with respect to the elements X of index j. Therefore, the vector representation of the infinitesimal strain is defined as

$$\{\boldsymbol{\varepsilon}\} = [\mathbf{B}^g]\{\mathbf{u}\} = \begin{Bmatrix} u_{1,1} \\ u_{2,2} \\ u_{3,3} \\ u_{1,2} + u_{2,1} \\ u_{1,3} + u_{3,1} \\ u_{2,3} + u_{3,2} \end{Bmatrix} = \begin{Bmatrix} (\nabla^{sym}\mathbf{u})_{11} \\ (\nabla^{sym}\mathbf{u})_{22} \\ (\nabla^{sym}\mathbf{u})_{33} \\ (\nabla^{sym}\mathbf{u})_{12} + (\nabla^{sym}\mathbf{u})_{21} \\ (\nabla^{sym}\mathbf{u})_{13} + (\nabla^{sym}\mathbf{u})_{31} \\ (\nabla^{sym}\mathbf{u})_{23} + (\nabla^{sym}\mathbf{u})_{32} \end{Bmatrix}. \tag{4.21}$$

The vector representation of the infinitesimal stress tensor can be obtained as

$$\{\boldsymbol{\sigma}\}^{\mathrm{T}} = \{\sigma_{11}, \sigma_{22}, \sigma_{33}, \sigma_{12}, \sigma_{13}, \sigma_{23}\}. \tag{4.22}$$

Equation 4.2 can be discretised by using the aforementioned discretisation, resulting in

$$\int_{\Omega^{ip}} (\{\boldsymbol{\sigma}\}^{\mathrm{T}} \cdot [\mathbf{B}^g]\{\boldsymbol{\eta}\})\, \mathrm{d}V - \int_{\partial\Omega^{ip}_t} (\{\mathbf{t}^{ext}\} \cdot [\mathbf{N}^g]\{\boldsymbol{\eta}\})\, \mathrm{d}A = 0, \quad \forall \boldsymbol{\eta} \in \mathcal{V}^{ip}, \tag{4.23}$$

which can be conveniently rearranged as

$$\left(\int_{\Omega^{ip}} ([\mathbf{B}^g]^{\mathrm{T}}\{\boldsymbol{\sigma}\})\, \mathrm{d}V - \int_{\partial\Omega^{ip}_t} ([\mathbf{N}^g]^{\mathrm{T}}\{\mathbf{t}^{ext}\})\, \mathrm{d}A \right) \cdot \{\boldsymbol{\eta}\} = 0, \quad \forall \boldsymbol{\eta} \in \mathcal{V}^{ip}. \tag{4.24}$$

Equation 4.24 is satisfied for all vectors $\{\boldsymbol{\eta}\}$, and therefore $\{\boldsymbol{\eta}\}$ on the left-hand side must vanish. By assuming that the traction forces do not depend on displacements, this equation can be rewritten as

$$\mathbf{f}^{int}(\mathbf{u}) - \mathbf{f}^{ext} = \mathbf{0}, \tag{4.25}$$

where $\mathbf{f}^{int}$ and $\mathbf{f}^{ext}$ are respectively the internal and external forces, defined as

$$\{\mathbf{f}^{int}(\mathbf{u})\} = \int_{\Omega^{ip}} [\mathbf{B}^g]^{\mathrm{T}} \{\boldsymbol{\sigma}(\mathbf{u})\} \, \mathrm{d}V \tag{4.26}$$

and

$$\{\mathbf{f}^{ext}\} = \int_{\partial\Omega_t^{ip}} [\mathbf{N}^g]^{\mathrm{T}} \{\mathbf{t}^{ext}\} \, \mathrm{d}A. \tag{4.27}$$

In view of a linear elastic constitutive law for the stress, $\boldsymbol{\sigma} = \mathbb{D}^e : \boldsymbol{\varepsilon}$ where $\mathbb{D}^e$ is the elastic stiffness tensor, we have that

$$\{\boldsymbol{\sigma}(\mathbf{u})\} = [\mathbb{D}^e][\mathbf{B}^g]\{\mathbf{u}\}, \tag{4.28}$$

which leads to

$$\{\mathbf{f}^{int}(\mathbf{u})\} = \int_{\Omega^{ip}} [\mathbf{B}^g]^{\mathrm{T}} [\mathbb{D}^e][\mathbf{B}^g] \, \mathrm{d}V \{\mathbf{u}\} \tag{4.29}$$

and

$$[\mathbf{K}]\{\mathbf{u}\} = \{\mathbf{f}^{ext}\}, \tag{4.30}$$

where

$$[\mathbf{K}] = \int_{\Omega^{ip}} [\mathbf{B}^g]^{\mathrm{T}} [\mathbb{D}^e][\mathbf{B}^g] \, \mathrm{d}V. \tag{4.31}$$

4.1.5 Path-dependent materials in an infinitesimal strain scenario

In this Section the stress tensor is no longer only a function of the instantaneous value of the strain tensor, but is also dependent on the history of strains to which the solid has been subjected. If plasticity is included, the stress tensor is the solution of a constitutive initial value problem, as in the elastoplastic constitutive initial value problem (Eq. 3.58). After the standard FE discretisation, the problem is reduced to the following:

$$\{\mathbf{R}_{FE}(\mathbf{u}_{n+1})\} = \int_{\Omega^{ip}} [\mathbf{B}^g]^{\mathrm{T}} \{\overline{\boldsymbol{\sigma}}(\boldsymbol{\alpha}_n, \boldsymbol{\varepsilon}(\mathbf{u}_{n+1}))\} \, \mathrm{d}V - \int_{\partial\Omega_t^{ip}} [\mathbf{N}^g]^{\mathrm{T}} \{\mathbf{t}_{n+1}^{ext}\} \, \mathrm{d}A = \{\mathbf{0}\}, \tag{4.32}$$

where $\mathbf{R}_{FE}$ is the residual of the global FE system, and $\overline{\boldsymbol{\sigma}}$ is the stress incremental constitutive function (the stress function with respect to $\boldsymbol{\varepsilon}$ and $\boldsymbol{\alpha}$). This equation is generally nonlinear, and the source of its nonlinearity is the nonlinearity in the stress incremental constitutive function, also called *material nonlinearity*. In this case, the external traction field is assumed to not depend on the displacements, but in some cases such as following forces this would not be a valid assumption.

The incremental behaviour of the system is obtained by assuming proportional loading, which implies that

$$\{\mathbf{f}_{n+1}^{ext}\} = \lambda_{n+1}\{\bar{\mathbf{f}}^{ext}\} = \int_{\partial\Omega_t^{ip}} [\mathbf{N}^g]^{\mathrm{T}}\{\mathbf{t}^{ext}\}\,\mathrm{d}A, \tag{4.33}$$

where λ_{n+1} is the prescribed load factor for the current time increment, and $\bar{\mathbf{f}}^{ext}$ is the time independent external force vector field (or total external force vector).

4.1.6 The Newton-Raphson scheme for the global solution of a finite element system

The Newton-Raphson scheme exhibits a quadratic rate of convergence, which makes it particularly appealing for solutions of systems of nonlinear equations. The linearisation, or first-order Taylor expansion, of Eq. 4.32 can be obtained as

$$\mathbf{0} \approx \mathbf{R}_{FE}\big|_{\mathbf{u}_{n+1}^{(k)}} + \left.\frac{\partial \mathbf{R}_{FE}}{\partial \mathbf{u}_{n+1}}\right|_{\mathbf{u}_{n+1}^{(k)}} (\mathbf{u}_{n+1}^{(k+1)} - \mathbf{u}_{n+1}^{(k)}) = \mathbf{R}_{FE}\big|_{\mathbf{u}_{n+1}^{(k)}} + \left.\frac{\partial \mathbf{R}_{FE}}{\partial \mathbf{u}_{n+1}}\right|_{\mathbf{u}_{n+1}^{(k)}} \delta\mathbf{u}^{(k+1)}, \tag{4.34}$$

where $\delta\mathbf{u}^{(k+1)}$ is the current residual displacement, and

$$\left.\frac{\partial \mathbf{R}_{FE}}{\partial \mathbf{u}_{n+1}}\right|_{\mathbf{u}_{n+1}^{(k)}} = \int_{\Omega^{ip}} [\mathbf{B}^g]^{\mathrm{T}}[\mathbb{D}^{ep}(\boldsymbol{\varepsilon}_{n+1}^{(k)})][\mathbf{B}^g]\,\mathrm{d}V, \tag{4.35}$$

where $\mathbb{D}^{ep}(\boldsymbol{\varepsilon}_{n+1}^{(k)}) = \left.\frac{\partial \overline{\boldsymbol{\sigma}}(\boldsymbol{\alpha}_n, \boldsymbol{\varepsilon}_{n+1})}{\partial \boldsymbol{\varepsilon}_{n+1}}\right|_{\boldsymbol{\varepsilon}_{n+1}^{(k)}}$. After reorganising Eq. 4.34, it can be expressed as

$$\begin{aligned}\int_{\Omega^{ip}} [\mathbf{B}^g]^{\mathrm{T}}[\mathbb{D}^{ep}(\boldsymbol{\varepsilon}_{n+1}^{(k)})][\mathbf{B}^g]\,\mathrm{d}V\,\delta\mathbf{u}^{(k+1)} = &-\Big(\int_{\Omega^{ip}} [\mathbf{B}^g]^{\mathrm{T}}\{\overline{\boldsymbol{\sigma}}(\boldsymbol{\alpha}_n, \boldsymbol{\varepsilon}_{n+1})\}\,\mathrm{d}V \\ &- \int_{\partial\Omega_t^{ip}} [\mathbf{N}^g]^{\mathrm{T}}\{\mathbf{t}_{n+1}^{ext}\}\,\mathrm{d}A\Big)\end{aligned} \tag{4.36}$$

or

$$[\mathbf{K}]^{(k)}\{\delta\mathbf{u}\}^{(k+1)} = -\{\mathbf{R}_{FE}\}^{(k)}. \tag{4.37}$$

It is important to point out that the current displacement field is obtained in terms of the residual displacement field as

$$\mathbf{u}_{n+1}^{(k+1)} = \mathbf{u}_{n+1}^{(k)} + \delta\mathbf{u}^{(k+1)} \tag{4.38}$$

but it can also be obtained in terms of the incremental displacement field as

$$\mathbf{u}_{n+1}^{(k+1)} = \mathbf{u}_n + \Delta\mathbf{u}^{(k+1)}, \tag{4.39}$$

where

$$\Delta \mathbf{u}^{(k+1)} = \Delta \mathbf{u}^{(k)} + \delta \mathbf{u}^{(k+1)}. \tag{4.40}$$

Needless to say, the initial guesses for the displacement fields are

$$\mathbf{u}_0 = \mathbf{0}; \quad \mathbf{u}_{n+1}^{(0)} = \mathbf{u}_n; \quad \Delta \mathbf{u}_{n+1}^{(0)} = \mathbf{0}. \tag{4.41}$$

The Newton-Raphson scheme is depicted graphically in Fig. 4.1.

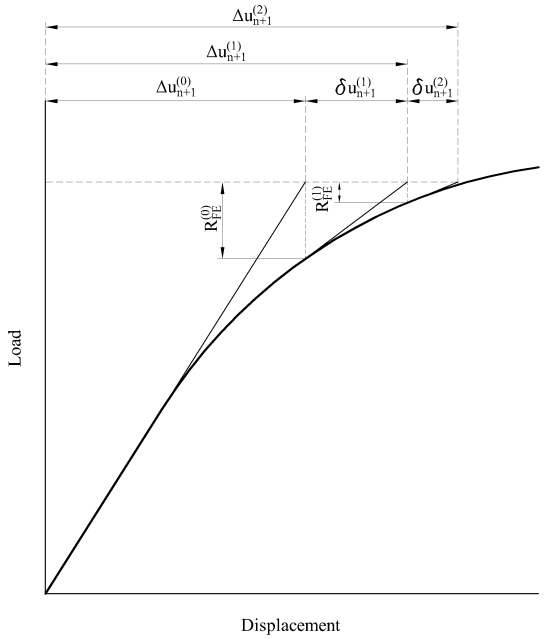

Fig. 4.1 The Newton-Raphson scheme for the solution of nonlinear FE systems.

The algorithm of the Newton-Raphson scheme for an infinitesimal strain setting is summarised in Algorithm 4. In this, $\mathscr{A}$ is the element assembly operator, $\mathbf{J}$ is the Jacobian of the transformation between the continuum and the standard integration domain (or natural coordinates, where the limits of integration are from -1 to 1), n_{el} is the number of elements in the FE system, n_{gauss} is the number of integration points in the element, w_j is the weight corresponding to the jth Gauss integration point, and n_{Newton} is the maximum number of Newton-Raphson iterations.

Alternatives to the Newton-Raphson scheme

The group of schemes discussed in this section are *modified* Newton-Raphson methods. The only difference is in the replacement of the consistent tangential stiffness $\mathbf{K}$ with a suitable approximation. Some traditional methods within this group consist of: using the initial tangent stiffness throughout all time increments, using a constant stiffness

Algorithm 4 The Newton-Raphson scheme for an infinitesimal strain scenario.

1. 1. Compute the initial residual
2. $\mathbf{R}_{FE} = \mathbf{f}^{int}(\mathbf{u}_n) - \lambda_{n+1}\bar{\mathbf{f}}^{ext}$ where $\{\mathbf{f}^{int}(\mathbf{u}_n)\} = \mathscr{A}_{i=1}^{n_{el}}\{\mathbf{f}_i^{int}(\mathbf{u}_n)\}$ and
3. $\{\mathbf{f}_i^{int}(\mathbf{u}_n)\} = \sum_{j=1}^{n_{gauss}} w_j \det \mathbf{J}_j\, [\mathbf{B}_j]^{\mathrm{T}}\{\overline{\boldsymbol{\sigma}}_j(\boldsymbol{\alpha}_n, \boldsymbol{\varepsilon}_n)\}$
4. 2. Initiate the Newton-Raphson iterative scheme
5. **for** $k \leftarrow 0, n_{Newton}$ **do**
6. 3. Compute the global stiffness matrix
7. $\mathbf{K}^{(k)} = \mathscr{A}_{i=1}^{n_{el}} \mathbf{K}_i^{(k)}$
8. where
9. $[\mathbf{K}_i]^{(k)} = \sum_{j=1}^{n_{gauss}} w_j \det \mathbf{J}_j\, [\mathbf{B}_j]^{\mathrm{T}}[\mathbb{D}_j(\boldsymbol{\varepsilon}_{n+1}^{(k)})][\mathbf{B}_j]$
10. and
11. $\mathbb{D}^{ep}(\boldsymbol{\varepsilon}_{n+1}^{(k)}) = \frac{\partial \overline{\boldsymbol{\sigma}}(\boldsymbol{\alpha}_n, \boldsymbol{\varepsilon}_{n+1})}{\partial \boldsymbol{\varepsilon}_{n+1}}\Big|_{\boldsymbol{\varepsilon}_{n+1}^{(k)}}$
12. 4. Solve the linear algebraic system
13. $[\mathbf{K}]^{(k)}\{\delta\mathbf{u}\}^{(k+1)} = -\{\mathbf{R}_{FE}\}^{(k)}$
14. 5. Apply the displacement residual to displacements and update strains
15. $\mathbf{u}_{n+1}^{(k+1)} = \mathbf{u}_{n+1}^{(k)} + \delta\mathbf{u}^{(k+1)}; \quad \{\boldsymbol{\varepsilon}_{n+1}\}^{(k+1)} = [\mathbf{B}^g]\{\mathbf{u}_{n+1}\}^{(k+1)}$
16. 6. Update stresses and dissipative variables
17. $\boldsymbol{\sigma}_{n+1}^{(k+1)} = \overline{\boldsymbol{\sigma}}(\boldsymbol{\alpha}_n, \boldsymbol{\varepsilon}_{n+1}^{(k+1)}); \quad \boldsymbol{\alpha}_{n+1}^{(k+1)} = \overline{\boldsymbol{\alpha}}(\boldsymbol{\alpha}_n, \boldsymbol{\varepsilon}_{n+1}^{(k+1)})$
18. 7. Compute the internal forces $\mathbf{f}^{int}$ and update the residual $\mathbf{R}_{FE}$ as in Step 1
19. 8. Check for convergence
20. **if** $\frac{\{\mathbf{R}_{FE}\}^{(k+1)}\cdot\{\delta\mathbf{u}\}^{(k+1)}}{\{\mathbf{R}_{FE}\}^{(1)}\cdot\{\delta\mathbf{u}\}^{(1)}} \leq tol$ **or** $k = n_{Newton}$ **then**
21. SET $(\cdot)_{n+1} = (\cdot)_{n+1}^{(k)}$
22. EXIT
23. **end if**
24. **end for**

within each time increment, or using a stiffness matrix which is updated after a certain number of iterations within each time increment (de Souza Neto et al., 2008).

Needless to say, the rate of convergence is lower than the quadratic convergence rate of the Newton-Raphson scheme. Although these methods avoid computing the tangent stiffness at each iteration, and thus saving some time in the computation of the consistent tangent operator at each integration point within the FE mesh, they, in general, lead to more iterations needed to achieve convergence. In large problems, solving the linear algebraic systems is the most computationally expensive step; thus, much faster solutions are generally obtained with the Newton-Raphson approach, which is the method considered in this study.

Another widely used alternative for materials with a rapidly changing consistent tangent operator is the use of approximated, or secant, tangent operators. These consist in some approximation to the analytical expression of the consistent tangent operator, and are designed to approximate the terms which rapidly change within iterations of a single time increment.

4.1.7 Finite strain formulation

The stress incremental constitutive function can be expressed as

$$\boldsymbol{\sigma}_{n+1} = \overline{\boldsymbol{\sigma}}(\boldsymbol{\alpha}_n, \mathbf{F}_{n+1}), \tag{4.42}$$

where $\boldsymbol{\sigma}$ is the Cauchy stress tensor, and its dependence upon strain is achieved through the dependence upon the deformation gradient tensor $\mathbf{F}$.

By taking into account Eq. 4.42 and the initial boundary value problem in spatial configuration stated in Section 4.1.2, the following residual can be defined:

$$\mathbf{R}_{FE}(\mathbf{u}_{n+1}) = \mathbf{f}^{int}(\mathbf{u}_{n+1}) - \mathbf{f}^{ext}_{n+1} = \mathbf{0}, \tag{4.43}$$

where

$$\{\mathbf{f}^{int}\} = \int_{\boldsymbol{\varphi}_{n+1}(\Omega^{ip})} [\mathbf{B}^g]^{\mathrm{T}} \{\overline{\boldsymbol{\sigma}}(\boldsymbol{\alpha}_n, \mathbf{F}_{n+1})\} \, \mathrm{d}V \tag{4.44}$$

and

$$\{\mathbf{f}^{ext}\} = \int_{\boldsymbol{\varphi}_{n+1}(\partial\Omega^{ip}_t)} [\mathbf{N}^g]^{\mathrm{T}} \{\mathbf{t}^{ext}_{n+1}\} \, \mathrm{d}A, \tag{4.45}$$

where $\mathbf{B}^g$ and $\mathbf{N}^g$ have the same format as in Eqs. 4.20 and 4.14, respectively. However, the derivatives of the shape functions are spatial derivatives in this case, which means that they are derivatives with respect to the spatial coordinates of the (deformed) FE mesh, instead of with respect to the material coordinates of the (undeformed) FE mesh.

The Newton-Raphson scheme for the large strain formulation in material description can be obtained in an analogous manner to Section 4.1.6 by first considering $\frac{\partial \mathbf{R}_{FE}}{\partial \mathbf{u}_{n+1}}$ in material description as

$$\left[\frac{\partial \mathbf{R}_{FE}(\mathbf{u}_{n+1})}{\partial \mathbf{u}_{n+1}}\right] = \int_{\Omega^{ip}} \left[\frac{\partial \mathbf{N}^g}{\partial \mathbf{X}}\right]^{\mathrm{T}} [\mathbb{A}(\mathbf{F}_{n+1})] \left[\frac{\partial \mathbf{N}^g}{\partial \mathbf{X}}\right] \mathrm{d}V, \tag{4.46}$$

where $\mathbb{A}$ is the consistent material tangent operator. By using the following equivalences:

$$\frac{\partial \mathbf{N}^g}{\partial \mathbf{X}} = \frac{\partial \mathbf{N}^g}{\partial \mathbf{x}}\mathbf{F}; \quad \int_{\boldsymbol{\varphi}(\Omega)} (\cdot) \frac{1}{\det \mathbf{F}} \mathrm{d}V = \int_{\Omega} (\cdot)\, \mathrm{d}V, \tag{4.47}$$

the following is recovered:

$$\begin{aligned} \left[\frac{\partial \mathbf{R}_{FE}(\mathbf{u}_{n+1})}{\partial \mathbf{u}_{n+1}}\right] &= \int_{\Omega^{ip}} \left[\frac{\partial \mathbf{N}^g}{\partial \mathbf{X}}\right]^{\mathrm{T}} [\mathbb{A}(\mathbf{F}_{n+1})] \left[\frac{\partial \mathbf{N}^g}{\partial \mathbf{X}}\right] \mathrm{d}V \\ &= \int_{\boldsymbol{\varphi}(\Omega^{ip})} [\mathbf{G}^g]^{\mathrm{T}} [\mathbb{C}(\mathbf{F}_{n+1})] [\mathbf{G}^g]\, \mathrm{d}V, \end{aligned} \tag{4.48}$$

where $\mathbb{C}$ is the consistent spatial tangent operator, which is defined in indicial notation as

$$\begin{aligned} \mathbb{C}_{ijkl} &= \frac{1}{\det \mathbf{F}} \left(\frac{\partial \mathbf{P}}{\partial \mathbf{F}}\right)_{imkn} F_{jm} F_{ln} = \frac{1}{\det \mathbf{F}} \frac{\partial}{\partial F_{kn}} (\tau_{ip} F^{-1}_{mp}) \\ &= \frac{1}{\det \mathbf{F}} \left(\frac{\partial \tau_{ip}}{\partial F_{kn}} F^{-1}_{mp} F_{jm} F_{ln} + \tau_{ip} \frac{\partial F^{-1}_{mp}}{\partial F_{kn}} F_{jm} F_{ln}\right) = \frac{1}{\det \mathbf{F}} \left(\frac{\partial \tau_{ij}}{\partial F_{km}} F_{lm} - \tau_{il}\delta_{jk}\right) \\ &= \frac{1}{\det \mathbf{F}} \left(\frac{\partial \tau_{ij}}{\partial \varepsilon_{op}} \frac{\partial \varepsilon_{op}}{\partial B_{rs}} \frac{\partial B_{rs}}{\partial F_{km}} F_{lm} - \tau_{il}\delta_{jk}\right), \end{aligned} \tag{4.49}$$

where $\mathbf{P}$ is the Piola-Kirchhoff stress tensor, τ_{ij} are the components of the Kirchhoff stress tensor, ε_{ij} are the components of the logarithmic strain tensor, B_{ij} are the components of the left Cauchy-Green strain tensor and the matrix $\mathbf{G}^g$ is the global discrete

spatial gradient operator, which is described by

$$\left[\frac{\partial \mathbf{N}^g}{\partial \mathbf{x}}\right] = \begin{bmatrix} N^g_{1,1} & 0 & 0 & N^g_{2,1} & 0 & 0 & \dots & N^g_{n_{gnod},1} & 0 & 0 \\ 0 & N^g_{1,1} & 0 & 0 & N^g_{2,1} & 0 & \dots & 0 & N^g_{n_{gnod},1} & 0 \\ 0 & 0 & N^g_{1,1} & 0 & 0 & N^g_{2,1} & \dots & 0 & 0 & N^g_{n_{gnod},1} \\ N^g_{1,2} & 0 & 0 & N^g_{2,2} & 0 & 0 & \dots & N^g_{n_{gnod},2} & 0 & 0 \\ 0 & N^g_{1,2} & 0 & 0 & N^g_{2,2} & 0 & \dots & 0 & N^g_{n_{gnod},2} & 0 \\ 0 & 0 & N^g_{1,2} & 0 & 0 & N^g_{2,2} & \dots & 0 & 0 & N^g_{n_{gnod},2} \\ N^g_{1,3} & 0 & 0 & N^g_{2,3} & 0 & 0 & \dots & N^g_{n_{gnod},3} & 0 & 0 \\ 0 & N^g_{1,3} & 0 & 0 & N^g_{2,3} & 0 & \dots & 0 & N^g_{n_{gnod},3} & 0 \\ 0 & 0 & N^g_{1,3} & 0 & 0 & N^g_{2,3} & \dots & 0 & 0 & N^g_{n_{gnod},3} \end{bmatrix}. \tag{4.50}$$

In Eq. 4.49, the derivatives are defined as (de Souza Neto et al., 2008; Jog, 2008)

$$\begin{aligned} \frac{\partial \varepsilon_{ij}}{\partial B_{kl}} = \frac{1}{2}\frac{\partial [\ln(B)]_{ij}}{\partial B_{kl}} \rightarrow \frac{1}{2}\frac{\partial \ln \mathbf{B}}{\partial \mathbf{B}} &= \frac{1}{2}\Big(\sum_{i=1}^{3}\frac{1}{B_i}\mathbf{E}_i \otimes \mathbf{E}_i + \sum_{\substack{i,j=1 \\ i\neq j}}^{3}\frac{\ln B_i - \ln B_j}{B_i - B_j}\mathbf{E}_i \otimes \mathbf{E}_j\Big) \\ \frac{\partial B_{ij}}{\partial F_{km}}F_{lm} &= \delta_{ik}B_{jl} + \delta_{jk}B_{il}\,, \end{aligned} \tag{4.51}$$

where B_i and $\mathbf{E}_i$ are respectively the eigenvalues and eigentensors of $\mathbf{B}$. $\frac{\partial \tau_{ij}}{\partial \varepsilon_{op}}$ has exactly the same format as the infinitesimal strain counterpart, but it is restricted to isotropic materials due to the objectivity requirements for the Kirchhoff stress tensor. The first part of Eq. 4.49 is the material contribution to the tangent operator while the second part is the geometrical contribution (also called *geometric nonlinearity*).

The whole FE system of equations for the large strain formulation now reads

$$\begin{aligned} &\int_{\boldsymbol{\varphi}^{(k)}(\Omega^{ip})} [\mathbf{G}^g]^{\mathrm{T}}[\mathbb{C}(\mathbf{F}^{(k)}_{n+1})][\mathbf{G}^g]\,\mathrm{d}V\,\delta\mathbf{u}^{(k+1)} \\ &= -\Big(\int_{\boldsymbol{\varphi}^{(k)}(\Omega^{ip})} [\mathbf{B}^g]^{\mathrm{T}}\{\overline{\boldsymbol{\sigma}}(\boldsymbol{\alpha}_n, \mathbf{F}^{(k)}_{n+1})\}\,\mathrm{d}V - \int_{\boldsymbol{\varphi}^{(k)}(\partial\Omega^{ip}_t)} [\mathbf{N}^g]^{\mathrm{T}}\{\mathbf{t}^{ext}_{n+1}\}\,\mathrm{d}A\Big). \end{aligned} \tag{4.52}$$

The algorithm of the Newton-Rapshon scheme for a large strain setting is summarised in Algorithm 5, where $\odot$ is the operator that performs the following operation in indicial notation $\mathbf{A} \odot \mathbf{B} \rightarrow A_{il}B_{jk}$.

Algorithm 5 Newton-Raphson scheme for a large strain scenario.

1. 1. Compute the initial residual
2. $\mathbf{R}_{FE} = \mathbf{f}^{int}(\mathbf{u}_n) - \lambda_{n+1}\bar{\mathbf{f}}^{ext}$ where $\{\mathbf{f}^{int}(\mathbf{u}_n)\} = \mathop{\mathscr{A}}_{i=1}^{n_{el}} \{\mathbf{f}_i^{int}\}$ and
3. $\{\mathbf{f}_i^{int}(\mathbf{u}_n)\} = \sum_{j=1}^{n_{gauss}} w_j \det \mathbf{J}_j \, [\mathbf{B}_j]^{\mathrm{T}} \{\overline{\boldsymbol{\sigma}}_j(\boldsymbol{\alpha}_n, \boldsymbol{\varepsilon}_n)\}$
4.
5. 2. Initiate the Newton-Raphson iterative scheme
6. **for** $k \leftarrow 0, n_{Newton}$ **do**
7. 3. Compute the global stiffness matrix
8. $\mathbf{K}^{(k)} = \mathop{\mathscr{A}}_{i=1}^{n_{el}} \mathbf{K}_i^{(k)}$
9. where
10. $[\mathbf{K}_i]^{(k)} = \sum_{j=1}^{n_{gauss}} w_j \det \mathbf{J}_j \, [\mathbf{G}_j]^{\mathrm{T}} [\mathbb{C}_j(\mathbf{F}_{n+1}^{(k)})] [\mathbf{G}_j]$
11. and
12. $\mathbb{C}(\mathbf{F}_{n+1}^{(k)}) = \frac{1}{\det \mathbf{F}_{n+1}^{(k)}} \left(\mathbb{D}^{ep}(\boldsymbol{\varepsilon}_{n+1}) : \frac{\partial \boldsymbol{\varepsilon}_{n+1}}{\partial \mathbf{B}_{n+1}} : \frac{\partial \mathbf{B}_{n+1}}{\partial \mathbf{F}_{n+1}} \mathbf{F}_{n+1} - \boldsymbol{\tau}_{n+1} \odot \mathbf{I} \right) \Big|_{\mathbf{F}_{n+1}^{(k)}}$
13. 4. Solve the linear algebraic system
14. $[\mathbf{K}]^{(k)} \{\delta \mathbf{u}\}^{(k+1)} = -\{\mathbf{R}_{FE}\}^{(k)}$
15. 5. Apply the displacement residual to displacements and update $\mathbf{F}$
16. $\mathbf{u}_{n+1}^{(k+1)} = \mathbf{u}_{n+1}^{(k)} + \delta \mathbf{u}^{(k+1)}; \quad \mathbf{F}_{n+1}^{(k+1)} = (\mathbf{I} - \nabla_{\mathbf{x}} \mathbf{u}_{n+1}^{(k+1)})$
17. 6. Update stresses and dissipative variables
18. $\boldsymbol{\sigma}_{n+1}^{(k+1)} = \overline{\boldsymbol{\sigma}}(\boldsymbol{\alpha}_n, \mathbf{F}_{n+1}^{(k+1)}); \quad \boldsymbol{\alpha}_{n+1}^{(k+1)} = \overline{\boldsymbol{\alpha}}(\boldsymbol{\alpha}_n, \mathbf{F}_{n+1}^{(k+1)})$
19. 7. Compute the internal forces $\mathbf{f}^{int}$ and update the residual $\mathbf{R}_{FE}$ as in Step 1
20. 8. Check for convergence
21. **if** $\frac{\{\mathbf{R}_{FE}\}^{(k+1)} \cdot \{\delta \mathbf{u}\}^{(k+1)}}{\{\mathbf{R}_{FE}\}^{(1)} \cdot \{\delta \mathbf{u}\}^{(1)}} \leq tol$ **or** $k = n_{Newton}$ **then**
22. SET $(\cdot)_{n+1} = (\cdot)_{n+1}^{(k)}$
23. EXIT
24. **end if**
25. **end for**

4.2 High-performance computing and ParaFEM

This section briefly describes a bit of history about hardware and software trends in modern computers, with a special emphasis on supercomputers. The main parallelisation paradigms and the used software, ParaFEM, are introduced. Most of the information included in this Chapter can be found in Smith et al. (2013) but a thorough description of the developed driver program is given at the end of this Section.

4.2.1 Hardware

Early computers performed operations in a *serial* fashion, which means that operations were carried out sequentially, one after the other; a second operation cannot start until the first one is finished. However, operations are often carried out on arrays of numbers (or vectors), in a manner that operations performed on specific members of two arrays do not affect the operations on other elements of these arrays. In such cases, operations can be performed simultaneously. Computers consisting of such specialised hardware for performing array operations are called *vector* computers. However, special care needs to be taken when writing the code in order to take full advantage of vector processing.

Until around the 2000s, personal computers had a single core central processing unit (CPU), and it was around then when miniaturisation of the circuits reached a physical limit in terms of energy efficiency and overheating. The clock speed of cores of around 3,000 MHz has not changed much since then. These issues were side-stepped by implementing multicore CPUs, which means that each physical chip could have two or more CPUs. This has been the standard for the last ten years. The downside of multicore processors is that the gain in performance directly depends on the design of the application, in terms of how efficiently it can use more than one core at the same time.

Another method for accelerating calculations are coprocessors. These are secondary processors which are designed to work together with the main processor, and which perform specific tasks, such as manipulating graphics in the case of graphical processing units (GPU). These coprocessors usually carry out the task they are designed to perform much faster than the host processors. Very popular coprocessors are GPUs, which are highly specialised processors with hundreds or thousands of cores; they perform single precision operations extremely fast. The downside is that data needs to be transferred back and forth between the main memory and the memory of the GPU, and thus the speed up is directly dependent on minimising data transfer times. As an example, the power of coprocessors can be shown by comparing the most powerful latest generation Intel Core i7-5960X CPU against the most powerful latest GPU of

NVIDIA, the NVIDIA GeForce GTX 1080. The CPU has eight cores and 16 threads of processing at 3,000 MHz, which means that it has up to 16 lines of execution at that clock speed, while the GPU has 2,560 cores at 1,600 MHz. Another example of coprocessors which have become recently popular are Intel Xeon Phi processors. These feature up to a thousand lines of execution, but with the limitation of a modest memory. However, researchers are currently investigating how to optimise the speed of codes in such architectures (Margetts et al., 2016).

4.2.2 High-performance computing

Most modern supercomputers are made of several thousand "standard" cores, divided in nodes, which are linked together by fast communication networks. These nodes are usually further divided in multicore processors, and maybe in several chips per node. An example of a supercomputer is ARCHER, UK National Supercomputing Service, which is a Cray XC30 MPP supercomputer with 118,080 cores, with each node having 64 GB of memory and 24 lines of execution. Another example of a supercomputer, which is currently the fastest in the world (Strohmaier et al., 1993), is the Sunway TaihuLight, a system build with processors designed and made in China, held at the National Supercomputing Center in Wuxi. It has 10,649,600 cores distributed in 40,960 nodes, displaying a peak performance of 93 petaflop/s (93 quadrillions of calculations per second) on a standard benchmark test.

Without taking into account GPU-based programming, there are two main standards in parallel programming: OpenMP and MPI. OpenMP is also sometimes denoted as *shared memory progamming* as its implementation is limited to systems where all lines of execution share the same physical memory. OpenMP consists of a set of directives which parallelise loops whose iterations can be performed independently. Needless to say, for applications which have to be run on thousands of cores, OpenMP is not the proper approach; in this case, Message Passing Interface (MPI) is the paradigm to be used, and it is in fact the supercomputing standard. MPI is also sometimes denoted as *distributed memory programming*, and thus it can be implemented in systems where the lines of execution do not share the same physical memory. It consists of a set of additional subroutines which allow for communication between the several instances, or lines of execution, of the code which is being run. A big difference between these two paradigms is that OpenMP offers almost no control on how the parallelisation is performed, and MPI offers a complete control on how the data is transferred between processes (Smith and Margetts, 2006; The MPI Forum, 1993).

The use of supercomputers is limited to research institutions and some large companies. A popular alternative nowadays is Cloud Computing, which consists of hiring

a system owned by someone else on a "pay as you go" basis. These companies own several clusters with extra capacity to deal with surges in demand, and Cloud Computing offers the perfect way of using this extra capacity to generate additional income.

4.2.3 ParaFEM

ParaFEM is a parallel library for general purpose FE analysis, written in modern FORTRAN, which uses MPI as the parallelisation paradigm (Margetts et al., 2016; Smith et al., 2013). It is supplied as a set of driver programs where each of them solves specific engineering problems. These driver programs are parallel programs that permit researchers and code developers to modify them for their own specific use without having to deal with thousands and thousands of lines of code. The source code of the software is fully documented in Smith et al. (2013).

In traditional FE codes, the linear algebraic system is fully assembled and then solved by some form of Gaussian elimination. However, for very large systems, Gaussian elimination is not feasible as storage requirements become a burden. ParaFEM uses a matrix free, or element by element, approach (Smith and Margetts, 2006), which means that the global stiffness matrix is never assembled and thus it is more memory efficient. Iterative linear algebraic solvers are used in this case, with the preconditioned conjugate gradient (PCG) solver being one of the most popular options for positive-definite systems. In the case of ParaFEM this is the solver of choice.

In some cases, unsymmetric linear algebraic systems arise, such as in the FE discretisation of the Navier-Stokes equations or when damage or non-associative plasticity are used in solid mechanics. In these cases, alternative iterative solvers need to be used. Kelley (2001) and Greenbaum (1997) described variations of iterative solvers which are able to solve such systems; the alternatives are the generalised minimum residual (GMRES), the stabilised bi-conjugate gradient (BiCGStab) and the stabilised hybrid bi-conjugate gradient (BiCGStab(l)).

Verification, validation and sensitivity analysis

ParaFEM has a wide array of choices for element types. In this study, linear hexahedral elements were used, where each hexahedron would correspond to a voxel from a 3D stack of μCT images. This mesh is not technically a Cartesian mesh, as displacements deform these hexahedra, breaking orthogonality, generating differences in the stiffness matrices of the elements, and thus not taking advantage of the main upper hand of traditional Cartesian meshes. Nonetheless, in this Section this mesh is deemed hexahedral in reference to the use of a voxelised mesh with linear hexahedra.

A recent study (Chen et al., 2014) has assessed the verification, or convergence as mesh gets progressively refined, of uniaxial compression simulations of trabecular bone samples with hexahedral meshes, with both linear and nonlinear material behaviours. They assessed the convergence of specific values at the solid phase level: the third principal stress and strain, and the displacement. Different coarsened meshes were compared to the reference model (i.e. the model with the finest mesh, where each hexahedron was of 19.5 μm). They found that all the solid phase values converge for the linear simulations (differences of less than 5%) but that only displacements converge in the nonlinear cases (differences of less than 10%). These results may highlight a possible limitation of voxelised meshes when evaluating the solid phase strains. It is therefore expected that local strain values may differ considerably between hexahedral and traditional (smoothed) FE meshes, especially at the solid-void interfaces. Nonetheless, the advantage of voxel-based meshes is that the meshing procedure requires less computational power in comparison with traditional meshes (such as those created through Delaunay-based methods), meaning that very large hexahedral meshes, of the orders of hundreds of millions of degrees of freedom (DOF), can be created in seconds with a relatively simple algorithm.

The main method of validating solid phase values in trabecular bone is a method called Digital Volume Correlation (DVC) (Bay et al., 1999; Zhu et al., 2016). Chen et al. (2017) recently found that the displacements at the microscopic level are accurately predicted if the BCs of the μFE simulation are well replicated, which means that the BCs are derived from the displacement field measured by the DVC at the top and bottom layers of the specimen. However, when validating strain, the accuracy and precision of current DVC methods for strain measurement at each element (around $10-20$ μm) are still too low (Grassi and Isaksson, 2015; Palanca et al., 2015).

Most input parameters of trabecular bone constitutive models are subjected to some uncertainty, which limits the confidence in the output of such models. Usually an uncertainty analysis precedes a sensitivity analysis, and it is used to assess the uncertainty in the input parameters, evaluating the confidence in their values. A sensitivity analysis evaluates how these input parameters affect the output uncertainty, evaluating the order of strength and relevance of the input parameters in determining variations in the output (Helton et al., 2006; Saltelli, 2008).

A full sensitivity analysis of the effect of these uncertainties on the output is computationally expensive in a HPC environment, especially if a Monte-Carlo method is used, as it could require thousands of runs in order to explore the full input space. An alternative is to use regression analysis to confirm that the response of the model to the

change of input parameters is close to linear. The (standardized) regression coefficients can be then used to assess how input parameters affect the output.

The sensitivity of the uniaxial macroscopic tensile/compressive yield stresses/strains with respect to the input parameters of the solid phase constitutive model of Chapter 5 was performed. Two strain-controlled uniaxial loading cases were considered, ε_{11}^{+} and ε_{11}^{-}. Two input parameters were analysed, the solid phase tensile and compressive yield stresses, σ_0^{+} and σ_0^{-}. ζ_0 was not included as its partial effect, i.e. without interactions, on the output is assessed in Chapter 5, and it was indeed found to be relatively minor. Multilinear regressions of the macroscopic values with respect to these two input parameters were performed; the regression coefficients can be seen in Table 4.1 and the actual data can be seen in Fig. 4.2.

The sensitivity of the uniaxial macroscopic tensile/compressive yield stresses/strains with respect to the solid phase Young's modulus was also performed for completeness. The data values can be seen in Fig. 4.2.

Table 4.1 Regression coefficients of the multilinear fits of macroscopic tensile/compressive yield stresses/strains with respect to solid phase tensile/compressive yield stresses. The multilinear equation is defined as $z = A \times x + B \times y + C$, where x are the solid phase tensile yield stresses and y are the solid phase compressive yield stresses. For the macroscopic yield stresses, A and B have no units while C has MPa as units. For the macroscopic yield strains, A and B have $1/\text{MPa}$ as units while C has no units. All the regressions were statistically significant ($p < 0.05$).

Output	**A**	**B**	**C**	R^2
Tensile stress	0.22	-0.01	0.42	0.99
Compressive stress	-0.36	0.41	6.27	0.95
Tensile strain	7.4E-5	-4.3E-6	2.1E-3	0.99
Compressive strain	1.2E-4	1.4E-4	4.1E-3	0.95

As seen in Table 4.1, all the coefficients of determination are high ($R^2 > 0.9$), which suggests that the output variation with respect to the input parameters is indeed almost linear. The macroscopic yield stresses and strains follow a similar pattern, as the stresses are the strains projected with the elastic slope, which is the same in each of these simulations, and which can be obtained from the appropriate stress-strain curve (Fig. 5.3 in Chapter 5). Macroscopic tensile stresses were found to largely depend on the solid phase tensile yield stress and not on the solid phase compressive yield stress; nonetheless, macroscopic compressive stresses were found to largely depend on both solid phase yield stresses. This is because the sample is largely subjected to a load case which closely follows hydrostatic compression in stress space; if the solid phase tensile yield stress is reduced , the (approximated) Drucker-Prager cone opens, enlarging the elastic regime in the hydrostatic compression area.

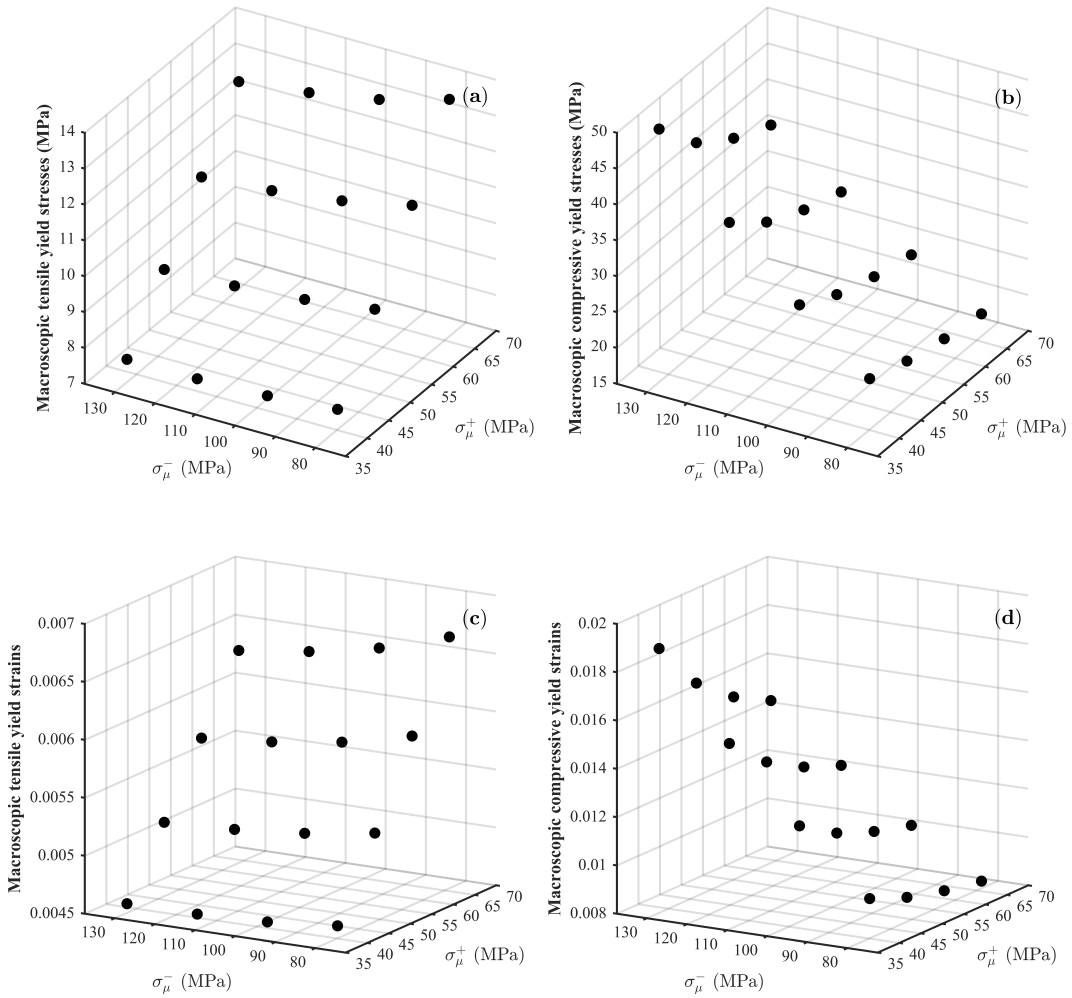

Fig. 4.2 Multilinear fits of macroscopic tensile yield stress (a), macroscopic compressive yield stress (b), macroscopic tensile yield strain (c) and macroscopic compressive yield strain (d) with respect to solid phase tensile/compressive yield stresses.

The variation of macroscopic yield stresses/strains with respect to the solid phase Young's modulus is almost linear, as seen in Fig. 4.3. Macroscopic yield stresses are almost insensitive to solid phase Young's modulus while macroscopic yield strains moderately decrease with increasing elastic modulus. When the solid phase Young's modulus is increased, the slope with intersects the macroscopic stress-strain curve to determine yield increases as well, which effectively reduces the strain intercept.

Linear algebraic systems in FE and ParaFEM

In the context of solid mechanics, the linear algebraic systems which can arise from the FE discretisation of the underlying PDEs can be different, depending on the considered physics (de Souza Neto et al., 2008).

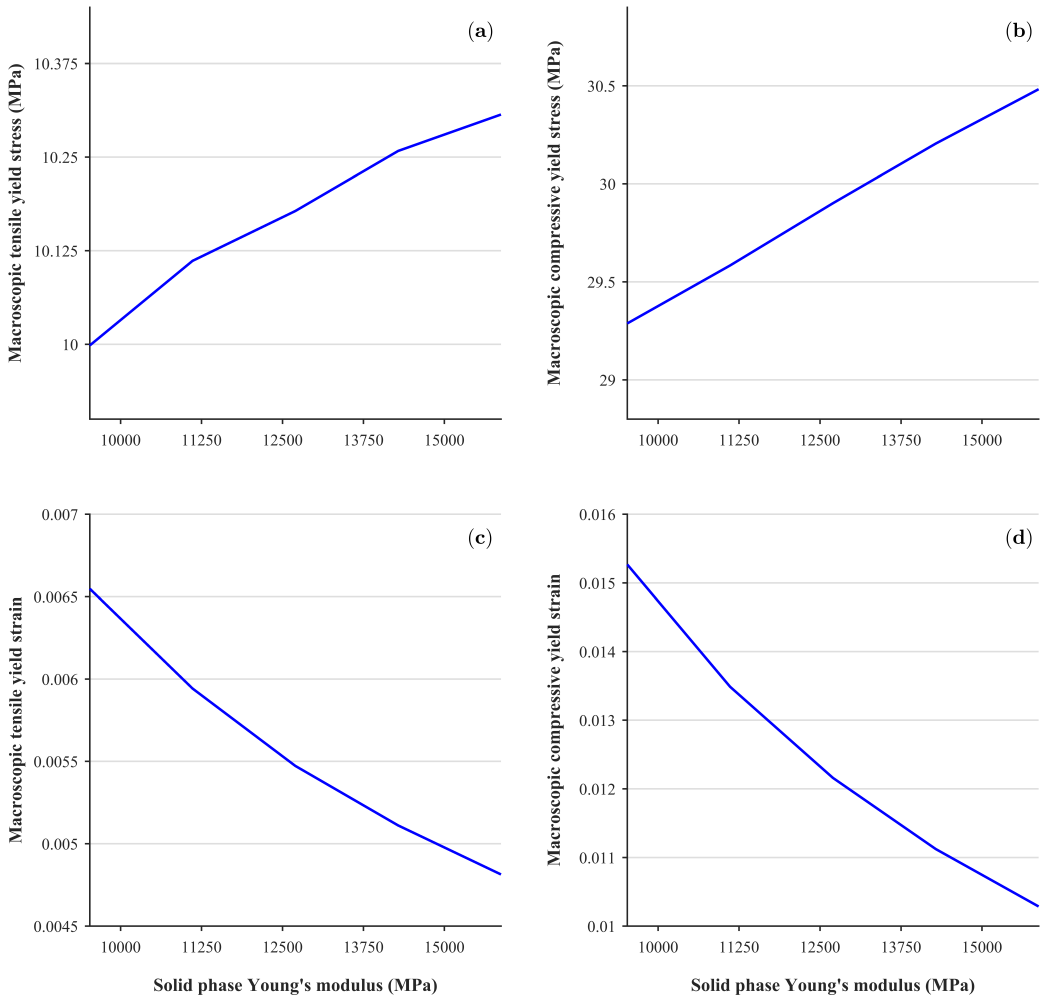

Fig. 4.3 Macroscopic tensile yield stress (a), macroscopic compressive yield stress (b), macroscopic tensile yield strain (c) and macroscopic compressive yield strain (d) with respect to solid phase Young's modulus.

In the finite strain regime, an elastic system will remain positive-definite as long as buckling is not reached. When buckling is reached, one of the eigenvalues of the stiffness matrix will become zero; when the buckling point is surpassed, the system may soften, leading to the stiffness matrix being indefinite. If the linear algebraic system becomes indefinite, a candidate iterative solver is the minimum residual method (MINRES).

If non-associative plasticity and/or damage are considered, the resulting stiffness matrix is unsymmetric, which arises from an unsymmetric consistent tangent operator (e.g. Section 3.2.5 of Chapter 3). If the linear algebraic system becomes unsymmetric, candidates are, as previously mentioned, the BiCGStab(l) or the GMRES.

In ParaFEM only two solvers are implemented, the widely used PCG and the more specialised BiCGSTab(l). To enhance the solving capabilities of ParaFEM, an awarded ongoing embedded CSE (eCSE, ARCHER) project (eCSE06-4, "Implementation of generic solving capabilities in ParaFEM", the author is a co-investigator) aims to implement more generic solving capabilities in the package. This project consists of extending the linear algebraic system solving capabilities of ParaFEM by interfacing ParaFEM with the linear algebraic solver library PETSc (Balay et al., 2016).

Within the wide range of solvers and preconditioners of PETSc, the investigators wanted to include a hybrid iterative/direct approach which is able to solve linear algebraic systems with symmetric (positive-definite and indefinite) and unsymmetric matrices. The architecture of ARCHER, which consists of a large number of very powerful cores within each node, is likely to take advantage of such a hybrid scheme and potentially improve running times for very large systems, since the communication between processes is greatly reduced. In order to achieve faster computing times for small problems (fewer than ~2.5M degrees of freedom), the investigators wanted to include parallel direct solvers for sparse matrices. By doing this and after having implemented the hybrid solver, ParaFEM will be able to effectively deal with problems of any range of DOF.

4.2.4 Developepment of the driver program for finite strain elasto-plasticity

In order to obtain a precise description of trabecular bone, μCT scans should have a resolution of $<$20 μm (Müller et al., 1996). It has been reported that a serious decrease of precision in properties appears at resolutions higher than 20 μm (Christiansen, 2016). The appropriate size of a VE of trabecular bone is around 5 mm (Sanyal et al., 2015; van Rietbergen et al., 1995), and therefore the resulting μFE meshes can have around 10M$-$40M DOF, depending on the BV/TV of the sample. Considering that the mechanical behaviour of trabecular bone is highly nonlinear, and thus the resulting μFE simulations need to be performed in a sequence of steps, the needed computational effort is considerable. For example, if an implicit μFE simulation of 40M DOF is performed in 50 load steps, a linear algebraic system of 40M unknowns needs to be solved 50 times the number of Newton-Raphson iterations per corresponding load step.

Commercial FE packages, such as ANSYS (ANSYS, Canonsburg, USA) or ABAQUS (SIMULIA, Dassault Systèmes, Vélizy-Villacoublay, France) are very valuable tools as they hugely decrease the time needed to set up FE simulations, due to their flexibility and powerful graphical user interface. However, these general purpose FE

codes were started during the seventies, when parallel processing was very limited, or almost non-existent. Although both ANSYS and ABAQUS do possess parallel capabilities (OpenMP, MPI, and GPU), their scalability is limited, and do not take full advantage of the powerful architectures of Tier-1 (national level) and Tier-0 (European level) supercomputers.

Obviously, there is a limit to what can be done on a desktop, due to restricted memory and restricted number of CPUs, amongst others. Therefore, in order to solve large problems in reasonable time frameworks, the use of a cluster or a supercomputer is hugely advantageous. An appropriately designed software which scales well on a large number of processors needs to be used on such platforms, but to the author's knowledge there is no finite strain elastoplasticity software that scales well. Thus, a driver program within the framework of ParaFEM was developed, which preserves its scalability and efficiency. This driver program was tested on high-end HPC platforms, such as ARCHER and Eddie (Edinburgh Compute and Data Facility, Edinburgh, UK).

The developed finite strain elastoplastic driver program was designed based on a *hyperelastic*-based plastic formulation (Simo and Ortiz, 1985; Simo and Taylor, 1985). Early work on the extension of infinitesimal strain elastoplastic models to the finite strain regime was carried out through the use of *hypoelastic*-based constitutive models (Argyris et al., 1978; Argyris and Kleiber, 1977; Mcmeeking and Rice, 1975). In these, the original evolution equations were extended by recasting them in terms of a suitably chosen objective stress rate. However, many controversial issues arise (de Souza Neto et al., 2008), such as the use of different objective stress rates in the formulation of the constitutive equations (Atluri, 1984; Perić, 1992), possible lack of objectivity of incremental constitutive laws (Hughes and Winget, 1980; Rubinstein and Atluri, 1983), observed oscillatory stress response under monotonic loading (Nagtegaal, 1982), and dissipative behaviour within the elastic range (Kojić and Bathe, 1987; Simo and Pister, 1984).

Hyperelastic-based formulations use a multiplicative decomposition of the deformation gradient (Lee and Liu, 1967); they do not exhibit dissipative behaviour under elastic strains and trivially satisfy the requirements of incremental objectivity. Additionally, if the Hencky strain energy function (linear relationship between the Kirchhoff stress tensor and the logarithmic strain tensor) is used, an infinitesimal strain return-mapping stress-update procedure is recovered under some special circumstances (Eterovic and Bathe, 1990; Perić et al., 1992; Simo, 1992; Weber and Anand, 1990).

Hyperelastic-based formulations require the use of an appropriate objective conjugate stress-strain pair, which in this case is the Kirchhoff stress ($\boldsymbol{\tau}$) – logarithmic strain pair ($\boldsymbol{\varepsilon}$). The choice was based on the retrieval of an infinitesimal strain return-mapping

stress-update scheme, as in the example described in Section 3.2.3 of Chapter 3. This permits a straightforward extension from the small strain to the finite strain regimes, by allowing the reuse of infinitesimal strain constitutive laws in finite strain simulations. The only limitation is the restriction of isotropy for both the elastic and plastic regimes, which arises due to the objectivity requirements for the Kirchhoff stress tensor. Due to the use of an updated Lagrangian FE formulation, the updated Cauchy stress and the updated consistent spatial tangent operator (as defined per Eq. 4.49) need to be provided at the end of the time step. A summary of the algorithm is described in Algorithm 6. In this, $\mathbf{F}_{\Delta}$ is the incremental deformation gradient, $\mathbf{F}_{n+1}$ is the current deformation gradient, $\mathbf{F}_n$ is the previous deformation gradient, $\mathbf{B}^e$ is the elastic left Cauchy-Green strain tensor, $\boldsymbol{\varepsilon}^e$ is the elastic logarithmic strain tensor, $\mathbf{B}^{e\,trial}$ is the trial elastic left Cauchy-Green strain tensor, $\boldsymbol{\varepsilon}^{e\,trial}$ is the trial elastic logarithmic strain tensor, $\mathbf{V}^{e\,trial}$ is the trial elastic left stretch tensor, $\boldsymbol{\tau}$ is the Kirchhoff stress, and $\boldsymbol{\sigma}$ is the Cauchy stress tensor.

It is important to point out that any constitutive law within the scope of continuum solid mechanics can be easily implemented in this driver program, with the previously mentioned restrictions. All the mechanical phenomena which can be modelled with this driver program include elasticity, plasticity, visco-elasticity, visco-plasticity, damage, and any possible combination of these. The only modification which needs to be performed in the driver program is to modify the time scale accordingly when using time-dependent effects.

The implemented solution scheme for the global FE system (Eq. 4.52) is a Newton-Raphson scheme (Fig. 4.1). The reasons for making this choice are its ease of implementation and its speed. The major downside of the Newton-Raphson scheme is its inability to deal with buckling points (i.e. points where the stiffness matrix has an eigenvalue of value equal to zero) (de Souza Neto et al., 2008). There are several algorithms which can overcome buckling points, such as displacement control or arc-length methods (Feng et al., 1995, 1996). However, due to its ability of overcoming *snap-back* and *snap-through*, the arc-length method is the most reliable choice. The author is currently implementing this scheme in ParaFEM in order to deal with problems involving large and slender trabecular bone samples.

In order to evaluate the speed and efficiency of the developed driver program within the framework of ParaFEM, a table containing running times on ARCHER for problems of different size is provided in Table 4.2. The systems used for these tests are cuboids which undergo large (5%) confined homogeneous compression in 50 load increments, in the sense that every integration point in the FE mesh is stressed in the same way. The constitutive law applied is an eccentric-ellipsoid. The parameters in Eqs. 3.84−3.87

Algorithm 6 Finite strain return-mapping scheme.

1. 1. Given the incremental displacement $\Delta\mathbf{u}_{n+1}$, calculate the incremental and current deformation gradients, respectively
2. $\quad \mathbf{F}_\Delta = \mathbf{I} + \nabla(\Delta\mathbf{u}_{n+1}); \quad \mathbf{F}_{n+1} = \mathbf{F}_\Delta \mathbf{F}_n$
3. 2. Compute the elastic predictor state
4. $\quad \mathbf{B}^e_n = \mathrm{e}^{2\boldsymbol{\varepsilon}^e_n}$
5. $\quad \mathbf{B}^{e\,trial}_{n+1} = \mathbf{F}_\Delta \mathbf{B}^e_n (\mathbf{F}_\Delta)^{\mathrm{T}}$
6. $\quad \boldsymbol{\varepsilon}^{e\,trial}_{n+1} = \ln(\mathbf{V}^{e\,trial}_{n+1}) = \frac{1}{2}\ln(\mathbf{B}^{e\,trial}_{n+1})$
7. $\quad \boldsymbol{\alpha}^{trial}_{n+1} = \boldsymbol{\alpha}_n$
8. 3. If the elastic predictor state is not admissible, perform the infinitesimal strain return mapping stress-update as in Section 3.2.3 of Chapter 3 (update $\boldsymbol{\tau}$, $\boldsymbol{\varepsilon}^e$, $\boldsymbol{\alpha}$ and obtain $\mathbb{D}^{ep} = \frac{\partial \boldsymbol{\tau}}{\partial \boldsymbol{\varepsilon}}$).
9. 4. Update the Cauchy stress
10. $\quad \boldsymbol{\sigma}_{n+1} = \frac{1}{\det \mathbf{F}_{n+1}} \boldsymbol{\tau}_{n+1}$
11. 5. Update the consistent spatial tangent operator
12. $\quad \mathbb{C}_{n+1} = \frac{1}{\det \mathbf{F}_{n+1}} \left(\mathbb{D}^{ep} : \frac{\partial \boldsymbol{\varepsilon}}{\partial \mathbf{B}} : \frac{\partial \mathbf{B}}{\partial \mathbf{F}} \cdot \mathbf{F} - \boldsymbol{\tau} \odot \mathbf{I} \right) \Big|_{n+1}$

were $\zeta_0 = 0.2$, $\sigma_0^+ = 50$, $\sigma_0^- = 100$, and $\overline{H}_{iso} = 0.001$; the elastic constants were $E = 12,700$ and $\nu = 0.3$. The constitutive law was implemented with a primal-CPPM algorithm (Algorithm 2 in Chapter 3) so that global convergence was achieved in the solution of the return-mapping equations. It is important to note that these tests were designed to overcome any load imbalance issues when solved in parallel. When a real system is run, it is likely that the mesh partition creates an uneven distribution of yielded and unyielded integration points amongst the MPI processes, leading to a load imbalance. This load imbalance is caused by the longer computational effort needed to solve the return-mapping equations. When the load amongst processes is completely balanced, the running times show that the developed driver program scales very well for elastoplastic systems even with a very large number of processes (up to 30,720).

Chen et al. (2014) showed that the use of HPC platforms may be circumvented in some cases. They performed some linear and nonlinear simulations on cylinders of trabecular bone specimens of different numbers of DOFs (0.07M, 0.5M, 3.4M, 22.2M and 158.1M) with ANSYS 14 on one core of an Intel Xeon E5-2670, 2.6 GHz and 256 GB of RAM; the largest nonlinear case was run on 32 cores. They show that even very large nonlinear systems, up to 158M DOF, may be solved in high-end desktop computers with a general purpose commercial FE solver, ANSYS 14, in a reasonable timeframe (105,000 seconds for a 158M DOF simulation).

In another test to evaluate the possible differences in computational effort between constitutive laws, cuboids of 1M DOF were subjected to large (5%) confined compres-

Table 4.2 Running times on ARCHER (UK National Supercomputing Service) for 50 load increments and under 5% apparent homogeneous confined compression.

Degrees of Freedom	Number of MPI processes	Time (s)
10M	960	181.5
	1,920	96.1
	3,840	60.8
	7,680	30.3
	15,360	38.5
50M	960	1,336.5
	1,920	712.0
	3,840	364.9
	7,680	228.0
	15,360	175.8
100M	1,920	1,612.2
	3,840	903.4
	7,680	484.2
	15,360	351.9
	30,720	250.2
190M	1,920	3,636.7
	3,840	1,890.1
	7,680	1,031.1
	15,360	621.4
	30,720	478.1
270M	7,680	1,838.7
	15,360	1,124.9
	30,720	721.3

sion in 50 load increments. The parameters of the constitutive law were the same as in the previous example, except that three different yield surfaces were considered: a fully elastic material (i.e. no yield surface), traditional Drucker-Prager and the previously used eccentric-ellipsoid. It is important to point out that only the eccentric-ellipsoid considers a primal-CPPM (Algorithm 2 in Chapter 3) to solve the return-mapping equations, as in the traditional Drucker-Prager case these equations have a closed-form solution. The corresponding running times on ARCHER are shown in Table 4.3. When the load amongst processes is completely balanced, the running times show that the developed driver program scales well and that the running times increase for systems which undergo yielding. In the plastic cases, traditional Drucker-Prager has a closed-form solution and therefore the running times are generally faster than when using the eccentric-ellipsoid.

Table 4.3 Running times on ARCHER for 50 load increments and under 5% apparent homogeneous confined compression, for different materials.

Material used	Number of MPI processes	Time (s)
Elastic	60	905
	120	511
	240	290
	480	133
	960	123
Drucker-Prager	60	1,218
	120	647
	240	362
	480	237
	960	125
Eccentric-ellipsoid	60	1,271
	120	707
	240	386
	480	222
	960	148

An example of a real system solved with this driver program is depicted in Fig. 4.4, which shows the longitudinal displacement distribution. This simulation consists of a cylinder of trabecular bone of approximately 40M DOF, which was subjected to simple apparent compression of 2.5% in 50 load increments. The constitutive law considered is an eccentric-ellipsoid, with $\zeta_0 = 0.2$, $\sigma_0^+ = 50$ and $\sigma_0^- = 100$, and $\overline{H}_{iso}$ corresponding to 5% of the elastic slope in Eqs. 3.84−3.87; $E = 12,700$ and $\nu = 0.3$. The HPC platform used to perform this simulation was Eddie, Edinburgh Compute and Data Facility, The University of Edinburgh. The simulation took 73,000 seconds by using 256 cores with a relatively slow Ethernet connection between the nodes.

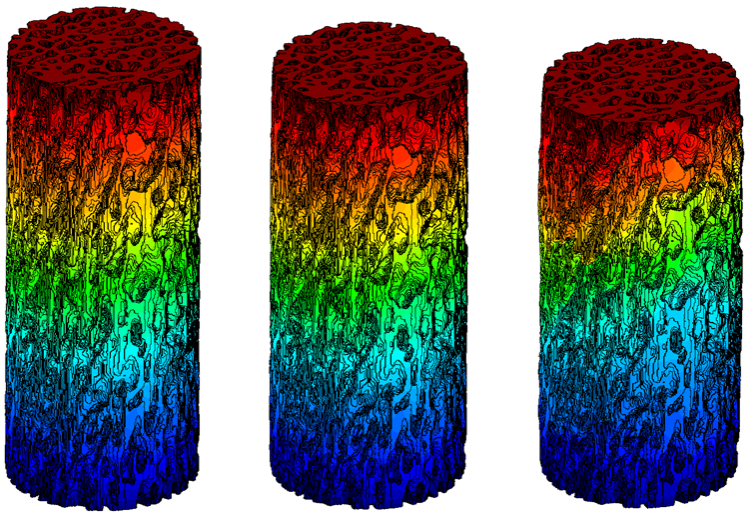

Fig. 4.4 Displacement field of a trabecular bone speciment under simple apparent compression of 2.5%. The deformations have been magnified for visual purposes.

Chapter 5

Effect of the solid phase constitutive law on the macroscopic behaviour

This Chapter evaluates the effect of compressive hydrostatic yield at the solid phase on the macroscopic yield surface of trabecular bone in strain space, by means of a nonlinear homogenisation method derived from multiscale theory. High-resolution FE meshes from three trabecular bone samples of a wide range of BV/TV and directly obtained from μCT images are considered; applying a wide range of macroscopic load cases. This Chapter resulted in the following publication:

- Levrero-Florencio, F., Manda, K., Margetts, L., and Pankaj, P. (2016). Nonlinear homogenisation of trabecular bone: Effect of solid phase constitutive model. *Proceedings of the Institution of Mechanical Engineers, Part H: Journal of Engineering in Medicine*, DOI: 10.1177/0954411916676220.

Porosity is a key feature of bone, which is reported to be present at every hierarchical scale (Smith et al., 2008). Tai et al. (2006) showed that bone behaves like a cohesive-frictional material and that the increased yield properties in compression may be explained by the friction between the mineral components, and that cohesion is provided by the organic matrix. Several computational studies on the nanoindentation behaviour of bone tissue have successfully modelled the mechanical response found in nanoindentation experiments by using a Mohr-Coulomb (Tai et al., 2006) or a Drucker-Prager (Carnelli et al., 2010) yield surfaces. Maghous et al. (2009) showed that an eccentric-ellipsoid is the yield surface of an isotropic porous material the matrix of which is modelled with a Drucker-Prager yield surface. Consequently, Schwiedrzik and Zysset (2013) reported that an eccentric-ellipsoid could effectively approximate the yield behaviour of bone tissue. Data on the post-yield hardening behaviour of the solid phase of bone is not readily available and most of the simulations in nonlinear homogenisation use 5% of the elastic slope as the linear hardening slope (Bayraktar

et al., 2004a; Panyasantisuk et al., 2015b; Sanyal et al., 2015; Wolfram et al., 2012). Some experimental studies have measured the hardening behaviour of the extracellular matrix (Luczynski et al., 2015; Schwiedrzik et al., 2014), but this cannot be directly employed for representing the solid phase of trabecular bone due to the difference in scale.

At the macroscale, high BV/TV bone is prone to tissue yielding, while low BV/TV bone is likely to fail via a mixture of large deformation failure mechanisms and tissue yielding (Bevill et al., 2006; Morgan et al., 2004). At the microscale, total strains can be large and a small strain approximation may be invalid (Stölken and Kinney, 2003). It is important to note that local yielding or buckling may not imply simultaneous yielding, or failure, of the homogenised structure; the latter results from a significantly compromised stress carrying capacity. While all of this is true for macroscopic compression, it is important to mention that bone at the organ level, when submitted to tensile loads, suffers from pure fragile failures (Juszczyk et al., 2013).

Homogenisation techniques to obtain the macroscopic response of bone from its microstructure have been successfully employed for determining bone apparent anisotropic elastic properties (Donaldson et al., 2011; van Rietbergen et al., 1996, 1995). Links have also been established to relate elastic properties with BV/TV and fabric tensors (Cowin, 1985; Turner et al., 1990; Zysset, 2003). However, homogenisation procedures to find yield and post-yield properties of bone are much more computationally expensive since they require evaluation of multiple load cases to assess the multiaxial behaviour appropriately. Additionally, in order to capture nonlinear phenomena, FE meshes need to be finer and each load step may require a number of iterations to obtain a converged solution if an implicit time integration scheme is used. Only few studies have attempted nonlinear homogenisation techniques on trabecular bone (Bayraktar et al., 2004a; Panyasantisuk et al., 2015b; Sanyal et al., 2015; Wolfram et al., 2012). In these studies, only Panyasantisuk et al. (2015b) used a Drucker-Prager criterion, while the others used a simple bilinear criterion to represent the solid phase of bone.

To the knowledge of the author, there is only one previous study that has examined the effect of different solid phase yield criteria on the macroscopic yield response of trabecular bone (Baumann et al., 2016). However, this study only considered two simple load cases, unconfined uniaxial compression and pure shear, and concluded that the differences between macroscopic yield with different solid phase criteria were small and any solid phase criterion with an appropriate strength asymmetry will perform reasonably well. The aim of this Chapter is to evaluate the effect of two different solid phase yield surfaces with the same uniaxial strength asymmetry, Drucker-Prager and eccentric-ellipsoid, on the yield strains at the macroscopic level by using a nonlinear

homogenisation approach, derived from multiscale theory (de Souza Neto et al., 2015; Kruch and Chaboche, 2011), by applying a large range of load cases, including complex normal and shear scenarios.

5.1 Methods

5.1.1 Sample extraction and imaging

Three cylindrical specimens of bovine trabecular bone (young cattle, <2.5 years old) were extracted from bovine femoral greater trochanters, which were obtained from a local abattoir. The extracted specimens had approximate dimensions of 10.7 mm diameter and 30 mm length. Diamond-coated coring tools (Starlite Industries, Rosemont, PA, USA) were used in the extraction of the specimens and the edges were cut with a slow speed saw (Isomet 1000, Buehler, Düsseldordf, Germany) by using a diamond wafering blade specially designed for bone; all these operations were performed under constant irrigation to avoid excessive abrasion and overheating. After coring, the specimens were submerged in phosphate buffered saline and scanned using a μCT device (Skyscan 1172, Bruker, Zaventern, Belgium) with a resolution of 17.22 μm. The scanning parameters were set to 94 kV, 136 mA, and 200 ms integration time; and four scans in 720 equiangular radial positions were used. Binarisation of the grey scale images was performed with an automatic thresholding algorithm (Gómez et al., 2013), with no user intervention required.

Three virtual cubes of 5 mm length were extracted from the aforementioned cylinders; this length is considered appropriate to capture the features of trabecular bone (Harrigan et al., 1988; Sanyal et al., 2015; van Rietbergen et al., 1995). The MIL fabric tensor (Harrigan and Mann, 1984) was evaluated using BoneJ (Doube et al., 2010) and then used to align the coordinate axes of the images with the fabric. This approach has been recently employed by Wolfram et al. (2012) and Panyasantisuk et al. (2015b). After the 5 mm cubes were cropped, the alignment was rechecked to ensure that no misalignment larger than 8° was found (Sanyal et al., 2015; Wolfram et al., 2012). If the cropped cube was misaligned, the process was restarted by cropping a different 5 mm region, which resulted in a trial and error-based iterative process which was repeated until the misalignment was lower than 8°. MIL is known to approximate the macroscopic elastic orthotropy of trabecular bone (Odgaard et al., 1997) and thus the samples can be considered to be aligned with these axes.

The samples can be seen in Fig. 5.1, and the following important morphological indices of these three samples can be seen in Table 5.1: BV/TV, Degree of Anisotropy

(DOA), Structure Model Index (SMI) and Connectivity (Conn). As it can be seen, BV/TV ranges from relatively low (14.8%) to high (30.3%); the SMI ranges accordingly, from a largely rod-like sample (SMI = 1.59) to a largely plate-like sample (SMI = 0.52).

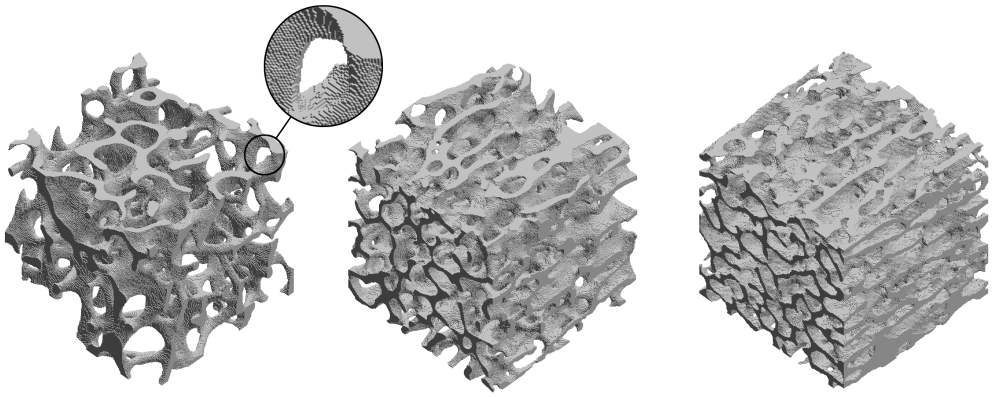

Fig. 5.1 The three specimens used in increasing density from left to right. A detailed zoom of the FE mesh of the most porous sample is shown.

Table 5.1 Morphological indices of the three specimens used.

Morphological index	Porous sample	Medium sample	Dense sample
BV/TV (%)	14.8	23.1	30.3
DOA	2.65	2.09	2.67
SMI	1.59	0.98	0.52
Conn	209	813	1059

5.1.2 Solid phase constitutive model

The solid phase was modelled with a homogeneous isotropic elastoplastic constitutive model, although it is recognised that its mechanical behaviour is actually better modelled with transverse isotropy or orthotropy (Hellmich et al., 2004; Malandrino et al., 2012; Wolfram et al., 2010a). The solid phase is also known to be heterogeneous in mineral density (Blanchard et al., 2013; Renders et al., 2008). However, as Cowin (1997) pointed out, there is little to no error in assuming tissue isotropy and therefore the model with the least number of parameters was chosen. With respect to the solid phase heterogeneity, Gross et al. (2012) stated that the effect of a heterogeneous TMD on the apparent elastic properties of trabecular bone is minor.

The elastic regime of the solid phase was modelled by using Hencky's hyperelastic model, with a Poison's ratio of 0.3 and a Young's modulus of 12,700 MPa (Wolfram

et al., 2012). Nonetheless, the value of Young's modulus for the solid phase typically ranges from around 7 to 25 GPa (Rho et al., 1993; Zysset et al., 1999). However, even if the solid phase Young's modulus or the solid phase yield values are changed, they are not expected to change trends in the comparison as the main difference between the two solid phase yield surfaces used in this study is kept (the presence or not of compressive hydrostatic yielding). A sensitivity analysis assessing the effect of these parameters is included in Section 4.2.3 of Chapter 4.

The yield surface of the solid phase was modelled by using the following yield criterion (Schwiedrzik et al., 2013)

$$f(\boldsymbol{\sigma},q) = \sqrt{\boldsymbol{\sigma} : \mathbb{F} : \boldsymbol{\sigma}} + \mathbf{F} : \boldsymbol{\sigma} - (1 + \overline{H}_{iso}\overline{\kappa}) = 0, \tag{5.1}$$

where $\overline{H}_{iso}$ corresponds to 5% of the elastic slope (Bayraktar and Keaveny, 2004; Sanyal et al., 2012; Wolfram et al., 2012). Equation 5.1 corresponds to a hyperbolic approximation of a Drucker-Prager yield surface (Fig. 5.2b) when $\zeta_0 = 0.49$ in

$$\mathbb{F} = -\zeta_0 F_0^2 (\mathbf{I} \otimes \mathbf{I}) + (\zeta_0 + 1) F_0^2 (\mathbf{I} \underline{\otimes} \mathbf{I}) \tag{5.2}$$

and an arbitrarily chosen $\zeta_0 = 0.2$ was used to define an eccentric-ellipsoid (Fig. 5.2a); both these surfaces are defined in stress space and have the same uniaxial yield values. Uniaxial yield strains of 0.41% in tension (ε_0^+) and 0.83% in compression (ε_0^-) (Bayraktar and Keaveny, 2004) were converted to yield stresses by using following expressions (Schwiedrzik et al., 2015):

$$\sigma_0^+ = E_\mu \, \varepsilon_0^+ \tag{5.3}$$

and

$$\sigma_0^- = E_\mu \, \varepsilon_0^- \, . \tag{5.4}$$

5.1.3 Computational methods

The three cubic specimens were meshed with a voxelised mesh by using trilinear hexahedra, with the largest mesh having around nine million nodes. KUBC were used to constrain the cubic VEs (Wang et al., 2009); the corresponding displacement BCs were applied as

$$\overline{\mathbf{u}} = \boldsymbol{\varepsilon}_0 \mathbf{y} \quad \forall \mathbf{y} \in \partial\Omega_\mu^s . \tag{5.5}$$

Each VE was subjected to 144 strain load cases, as listed in Table 5.2. This number is much higher than the 17 load cases used by Wolfram et al. (2012) and Panyasantisuk et al. (2015b), and is of the same order as the 231 and 297 load cases of Sanyal et al.

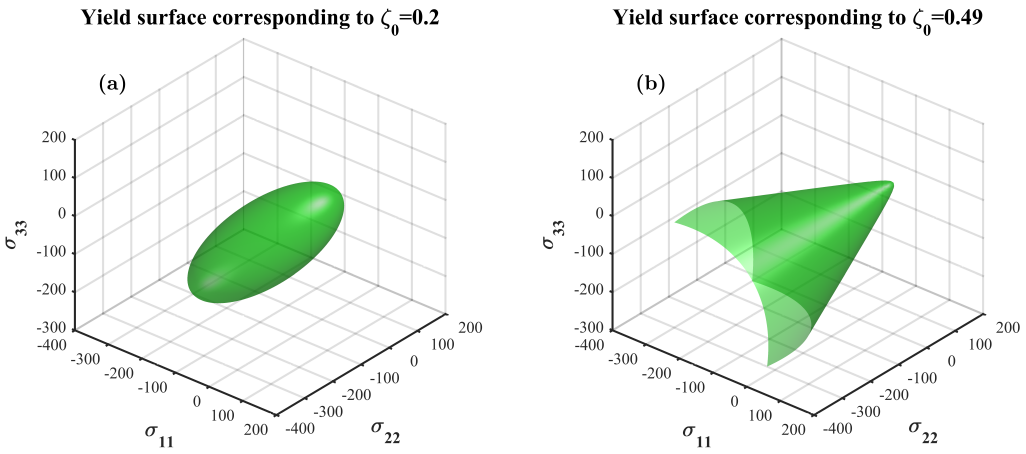

Fig. 5.2 (a) Eccentric-ellipsoid ($\zeta_0 = 0.2$). **(b)** Drucker-Prager ($\zeta_0 = 0.49$). Both surfaces are plotted in normal stress space.

(2015) and Bayraktar et al. (2004a), respectively. This set of load cases was designed to provide a thorough assessment of the yield surface in normal, shear and combined normal and shear strain spaces. The macroscopic behaviour of trabecular bone is relatively unknown in the combined normal and shear strain space, and only few studies have considered it (Fenech and Keaveny, 1999; Sanyal et al., 2015); therefore, this study considered a large number of load cases in this space.

The simulations were performed on a Cray XC30 MPP supercomputer, hosted by ARCHER, UK National Supercomputing Service. The FE analyses were carried out with an *in-house* developed finite strain elastoplasticity parallel implicit FE solver, within the framework of ParaFEM (Section 4.2.4) (Margetts, 2002; Smith et al., 2013). This code uses MPI to perform the parallelisation (Smith and Margetts, 2006; The MPI Forum, 1993) and its high scalability is shown in Section 4.2.4 of Chapter 4. Usage of this driver program permitted the simulation of 144×3 large μFE simulations (from ~10M to ~30M DOF) in a relatively short time, as each simulation took around ~12 minutes on 1,920 cores of ARCHER.

The local integration point-based CPPM equations were solved with the primal-CPPM algorithm (Algorithm 2 in Chapter 3). The initial load increment size corresponded to 0.1% macroscopic strain norm and could decrease to a minimum of 0.001% if global convergence was not achieved. However, no convergence problems occurred in these simulations. The simulation stopped when macroscopic yield, as defined in Section 5.1.4, was achieved.

Table 5.2 Description of the performed load cases. Clockwise and counter-clockwise shear cases are differentiated by the sign of the off-diagonal terms of the macroscopic strain tensor. Biaxial normal-shear cases have normal to shear ratios of 1 to 1, 0.25 to 0.75 and 0.75 to 0.25.

Type of analysis	Description	Number
Uniaxial normal $\varepsilon_{ii} \neq 0;\ \varepsilon_{jj} = \varepsilon_{kk} = 0$ $\varepsilon_{ij} = \varepsilon_{ik} = \varepsilon_{jk} = 0$	3 tensile and 3 compressive	6
Biaxial normal $\varepsilon_{ii} = \varepsilon_{jj} \neq 0;\ \varepsilon_{kk} = 0$ $\varepsilon_{ij} = \varepsilon_{ik} = \varepsilon_{jk} = 0$	1 analysis per quadrant	12
Uniaxial shear $\varepsilon_{ii} = \varepsilon_{jj} = \varepsilon_{kk} = 0$ $\varepsilon_{ij} \neq 0;\ \varepsilon_{ik} = \varepsilon_{jk} = 0$	3 clockwise and 3 counter-clockwise	6
Biaxial shear $\varepsilon_{ii} = \varepsilon_{jj} = \varepsilon_{kk} = 0$ $\varepsilon_{ij} = \varepsilon_{ik} \neq 0;\ \varepsilon_{jk} = 0$	1 analysis per quadrant	12
Biaxial normal-shear $\varepsilon_{ii} \neq 0;\ \varepsilon_{jj} = \varepsilon_{kk} = 0$ $\varepsilon_{lm} \neq 0;\ \varepsilon_{ln} = \varepsilon_{mn} = 0$	3 analysis per quadrant	108
$i, j, k, l, m, n = 1, 2, 3$ $i \neq j \neq k$ $l \neq m \neq n$	Total	144

5.1.4 Definition of macroscopic yield

Although a finite strain formulation needs to be taken into account when performing the simulations involving the microstructure, strains at the macroscopic level can be considered small due to their relatively small norms (Bayraktar et al., 2004a; Sanyal et al., 2015; Wolfram et al., 2012), and thus a linear kinematic formulation could be used as a simplification, and indeed in all our simulations the macroscopic strains never exceeded 1.5%. The macroscopic yield points were described in the plane where the x-axis is the Euclidean norm of the applied macroscopic Green-Lagrange strain tensor and the y-axis is the Euclidean norm of the homogenised Second Piola-Kirchhoff stress, which is described by

$$\boldsymbol{\sigma}_0 = \frac{1}{V} \sum_{i=1}^{n_{el}} \sum_{j=1}^{n_{gauss}} w_i \det\left(\mathbf{J}_{ij}\, \boldsymbol{\sigma}_{\mu\, ij}\right), \tag{5.6}$$

where there is no summation implied over repeated indices. The 0.2% strain rule was used to define the yield points (Panyasantisuk et al., 2015b; Sanyal et al., 2015; Wolfram

et al., 2012), as defined in Fig 5.3. The 0.2% strain rule consists of establishing the yield point where a line parallel to the elastic slope at 0.2% strain crosses the stress-strain curve.

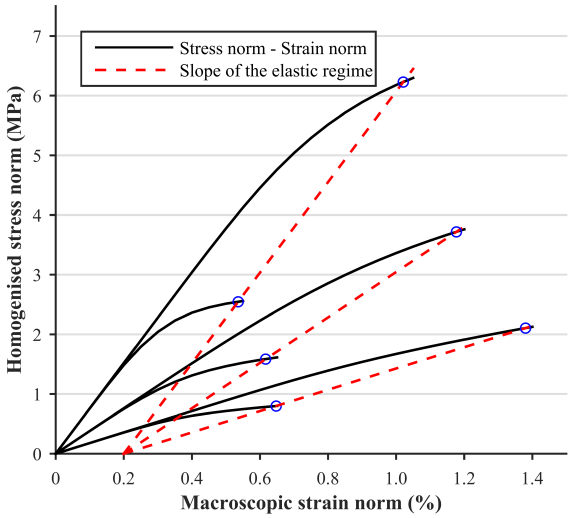

Fig. 5.3 Determination of the macroscopic yield points by using the 0.2% strain criterion for the tensile and compressive uniaxial load cases of one sample. As it can be seen, the tensile and compressive uniaxial cases have the same elastic slope, as expected.

5.2 Results

The samples have been labelled as *Low density*, *Medium density* and *High density* for BV/TV of 14.8%, 23.1% and 30.3%, respectively. The macroscopic yield strains for these three samples for the uniaxial normal and biaxial normal cases (rows 1 and 2 of Table 5.2) are shown in Fig. 5.4. Further, since strain-based yield criteria have been previously shown to be approximately isotropic, yield points in strain space were used.

When considering these two different yield surfaces for the solid face, it can be seen that differences between macroscopic yield strains are not significant in tension-tension quadrants (Fig. 5.4a-c, upper right quadrant) or even in tension-compression quadrants (Fig. 5.4a-c, upper left and lower right quadrants). However, they become distinguishable in compression-compression quadrants (Fig. 5.4a-c, lower left quadrants).

The macroscopic yield strains for these three samples in uniaxial and biaxial shear cases (rows 3 and 4 of Table 5.2) are shown in Fig. 5.5. It can be seen that there are no significant differences in the macroscopic shear yield strains when using these two different yield criteria for the solid phase.

Macroscopic yield strain norms were evaluated separately for load cases with only: normal compressive components; normal tensile components; and shear components,

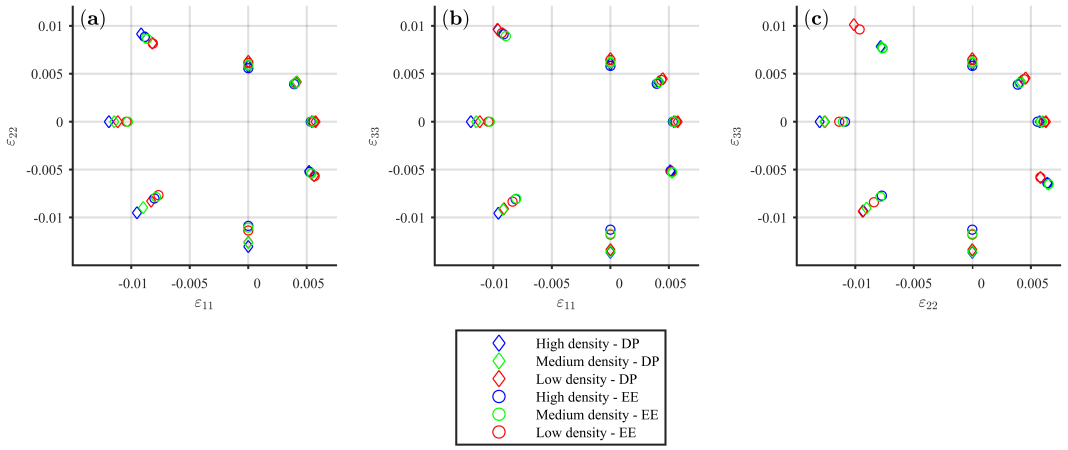

Fig. 5.4 Macroscopic yield strains in normal-normal planes. The axes have been rearranged so that the orthotropic Young's moduli are descending in value $E_{11} > E_{22} > E_{33}$. DP stands for Drucker-Prager and EE stands for eccentric-ellipsoid.

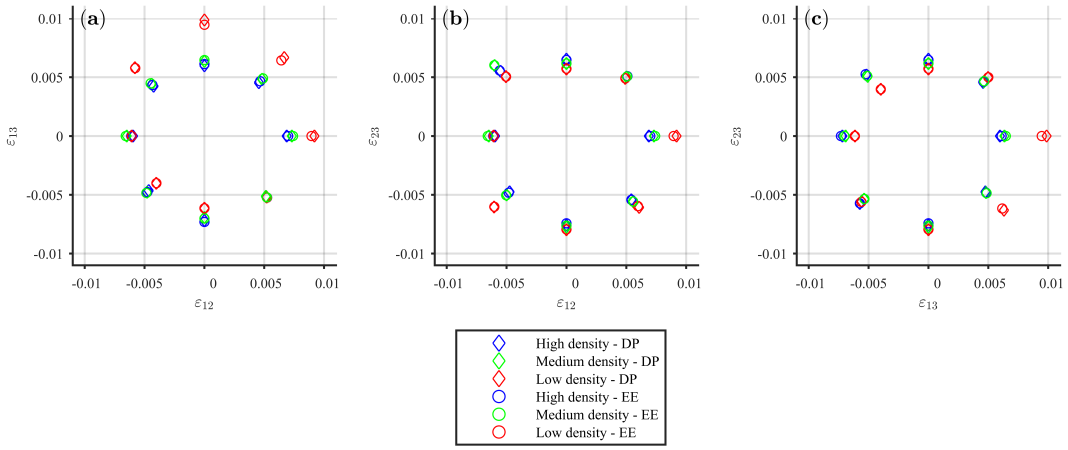

Fig. 5.5 Macroscopic yield strains in shear-shear planes. DP stands for Drucker-Prager and EE stands for eccentric-ellipsoid.

for both material models and all three samples. These are shown in Fig. 5.6. It can be shown that the yield strain norm for tension-only and shear-only load cases is almost the same, but differs by around 13% for compression-only load cases.

Macroscopic yield strains in normal-shear planes are shown in Fig. 5.7 (row 5 of Table 5.2). This figure shows that these yield strains differ for load cases which have compressive components when considering these two different microscopic yield surfaces, and this difference increases as the considered load case becomes more compression-dominated (i.e. the load case has a higher proportion of compression over shear) (Fig. 5.8). Figure 5.8 shows that this effect is also more prominent for the higher density samples. This effect was also found to occur in normal-normal planes (Fig. 5.4).

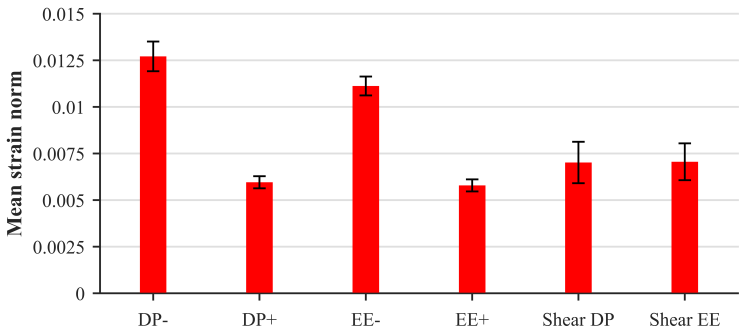

Fig. 5.6 Bar plot showing the average of the macroscopic yield strain norm for load cases that only contain: compressive components, tensile components, and shear components, for both eccentric-ellipsoid and Drucker-Prager (DP stands for Drucker-Prager and EE stands for eccentric-ellipsoid). The error bars are the standard deviation of the macroscopic yield strain norms. The minus sign (-) stands for compressive and the plus sign (+) stands for tensile.

5.3 Discussion

This Chapter shows that the effect of hydrostatic yield in the solid phase constitutive model is significant for compression-dominated load cases and that this effect is larger for high density samples. These findings agree with Baumann et al. (2016) who only considered uniaxial unconfined compression and pure shear load cases and consequently concluded that the solid phase strength asymmetry dominated the macroscopic mechanical response.

Macroscopic yield strains in normal-normal planes (Fig. 5.4) show that the effects of the two solid phase yield surfaces on the macroscopic behaviour is minimum except for cases containing only compressive components (Fig. 5.4a-c, lower left quadrants). When comparing the macroscopic yield strain norms for the two material models, it can be seen that Drucker-Prager results in a norm which is around 13% larger than when using eccentric-ellipsoid for compressive load cases (Fig. 5.6). The highly aligned microstructure of trabecular bone is likely to partially reflect features of the solid phase yield criterion, which in this case is a lack of hydrostatic compression yielding, resulting in an increase of the macroscopic yield strain norms in compression-dominated load cases. Figure 5.4 also shows that tension-dominated load cases are not affected when using different solid phase yield surfaces.

When considering shear load cases, it can be seen that there are no differences in macroscopic yield strains when using these two solid phase yield criteria (Fig. 5.5 and Fig. 5.7). This is consistent with Sanyal et al. (2012) in that tensile microscopic strains predominate in macroscopic shear loading, which results in these load cases being relatively unaffected when using these two solid phase yield surfaces. However, it is important to point out that shear load cases in clockwise and counter-clockwise di-

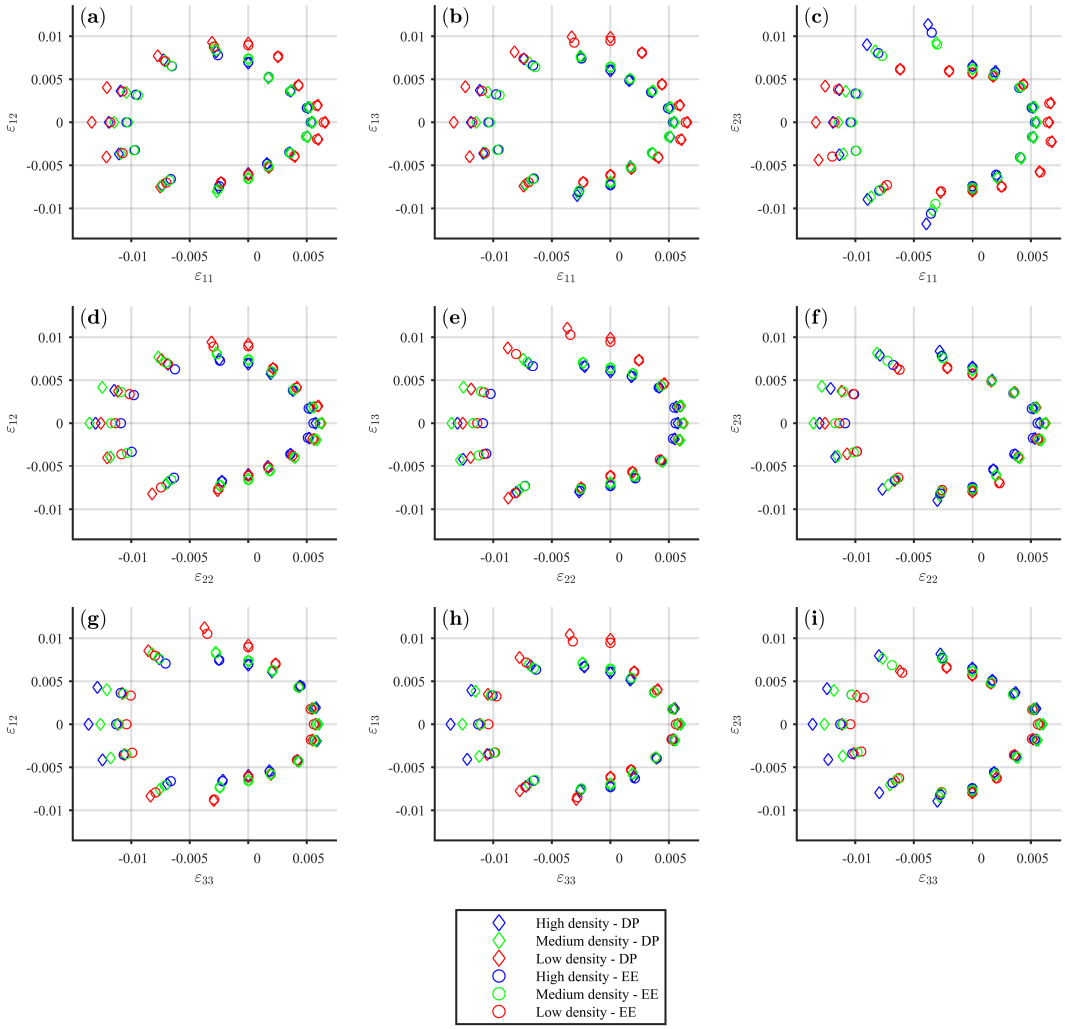

Fig. 5.7 Macroscopic yield strains in normal-shear planes, with the normal component in the x-axis and the shear component in the y-axis. DP stands for Drucker-Prager and EE stands for eccentric-ellipsoid.

rections can have different yield strains, especially in low BV/TV samples, as explained in Chapter 6.

In normal-shear planes (Fig. 5.7a-i, upper and lower left quadrants), the macroscopic yield strains follow a similar pattern to those in normal-normal planes (Fig. 5.4). Specifically, the two solid phase yield criteria result in greater differences as the load case becomes more compression-dominated, which is shown graphically in Fig. 5.8. This figure shows the difference in macroscopic yield strains between the Drucker-Prager and eccentric-ellipsoid in load cases which are pure shear, pure compression or compression-shear. This difference increases as the compression/shear proportion increases and also as the density increases; this means that higher density samples, which are more continuum-like, demonstrate a greater difference between the two

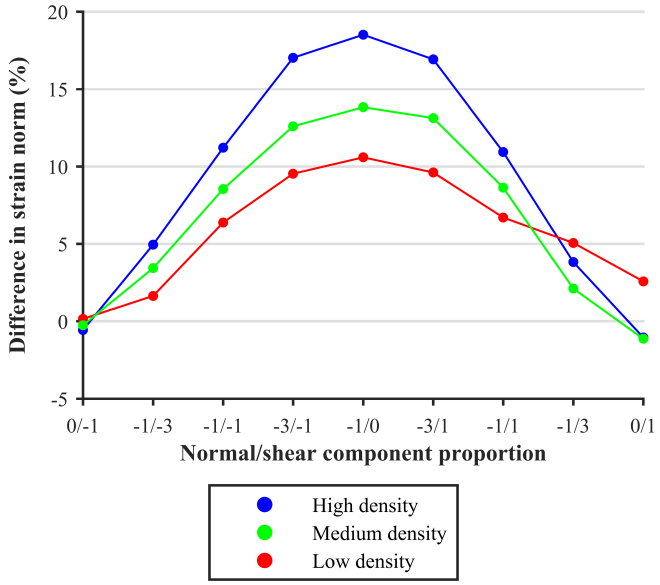

Fig. 5.8 Difference in macroscopic yield strain norm between Drucker-Prager and eccentric-ellipsoid, for cases in normal-shear planes with a compressive component ($\varepsilon_{ii} \leq 0$; $i = 1,2,3$). The first number in the proportion in the x-axis corresponds to the normal component, and the second to the shear component.

solid phase material properties, as these properties are more directly mirrored at the macroscale.

To the authors' best knowledge, only one previous study has assessed the effect of different solid phase yield criteria on the macroscopic yield strains (Baumann et al., 2016). The load cases considered in this study were limited to unconfined compression and shear. As a large number of complex load cases is considered in this Chapter, this should be considered as a possible extension of the above cited study. Although the material properties in this Chapter are different from those in Baumann et al. (2016), and the way of assessing macroscopic yield is also different, it can be shown that shear yield strains are very similar (the shear yield strains here need to be scaled by two to be comparable, because these are shown as tensorial components); compressive yield strains cannot be compared because the uniaxial compressive cases here are confined and theirs are unconfined.

This study has some limitations. Validation for all the macroscopic yield strains is not possible as these are very complex load cases which cannot be tested experimentally and samples tested once cannot be retested. However, there have been some attempts to perform complex load cases, such as multiaxial compression, on trabecular bone samples (Keaveny et al., 1999; Rincón-Kohli and Zysset, 2009). For the solid phase properties, homogeneous tissue properties were considered, which may result in an overestimation of the macroscopic values (Blanchard et al., 2013; Renders et al., 2008).

However, recent results suggest that μCT-based heterogeneous models underestimate the apparent stiffness when compared to SRμCT-based heterogeneous models, which are considered the gold standard in TMD measurement (Kaynia et al., 2014). However, any over or underestimation of properties is likely to be similar for both the solid phase models, and keeping the solid phase properties as homogeneous allows for these results to be compared with the existing literature on the topic; furthermore, the effect of heterogeneities at the solid phase on μFE models of trabecular bone with geometrical nonlinearities is still unclear. The assumption that the solid phase can be modelled with plasticity is also considered, which may not be true as localised tissue strains can cause microcracks, possibly leading to an eventual fracture; these are effects that plasticity models are not readily able to capture (Nawathe et al., 2013; Yeh and Keaveny, 2001). Furthermore, although the meshes considered in this study were extremely detailed, and thus these simulations were computationally expensive, only three samples were considered, which may not deliver statistically conclusive results.

Chapter 6

Macroscopic yield behaviour using nonlinear homogenisation

This Chapter evaluates the macroscopic yield surface of trabecular bone in strain space. It also evaluates the symmetries of this macroscopic yield surface by means of fitted closed-form quadric surfaces. This Chapter resulted in the following publication:
- Levrero-Florencio, F., Margetts, L., Sales, E., Xie, S., Manda, K., and Pankaj, P. (2016). Evaluating the macroscopic yield behaviour of trabecular bone using a nonlinear homogenisation approach. *Journal of the Mechanical Behavior of Biomedical Materials*. DOI: 10.1016/j.jmbbm.2016.04.008.

The macroscopic elastic behaviour of bone has been mostly modelled using isotropic linear elasticity at the organ level. Often, bone macroscopic properties are assumed to be homogeneous with separate elastic properties being assigned to cortical and trabecular bone (Completo et al., 2009; Conlisk et al., 2015). Sometimes, subject specific macroscopic elastic properties are assigned using CT scans, which permit inhomogeneity in the material properties on the basis of CT attenuations (Helgason et al., 2008; Schileo et al., 2008; Tassani et al., 2011). However, it is important to note that even if the constitutive properties are isotropic but heterogeneous, they could lead to an overall structural anisotropy; however, this study is concerned about material symmetries at the constitutive level. That said, the assumption of isotropy for the macroscopic constitutive model is usually made since the reliability of any introduced anisotropy is relatively poor due to the difficulty of measuring fabric anisotropy with standard CT scans. It is, however, well recognised that the macroscopic behaviour of bone is more accurately modelled with transverse isotropic or orthotropic constitutive laws, provided that an accurate measure of fabric can be obtained. For trabecular bone, which resembles open cell foams, the anisotropy is largely a consequence of its anisotropic microarchitecture (Odgaard et al., 1997; Turner et al., 1990). An ultrasonic approach

proposed by van Buskirk et al. (1981) was shown to provide a good approximation of the nine orthotropic elastic constants if a heterogeneity correction was included. In general, experimental mechanical techniques are unable to provide the complete stiffness tensor at the resolution required for modelling (Odgaard et al., 1989).

While modelling bone as an elastic material may be adequate for a few applications, a significant proportion of applications requires evaluation of its post-elastic response, e.g. to evaluate implant loosening resulting in its failure. However, linear elastic analyses may be sufficient for predicting failure in certain loading scenarios, for instance the fragile failure of a whole femur under stance and fall loading configurations (Schileo et al., 2014). Both stress and strain-based criteria have been used to describe the macroscopic yield surface of bone (Keaveny et al., 1994; Keller, 1994; Kopperdahl and Keaveny, 1998). In recent years a consensus appears to be emerging, that strain-based criteria are easier to apply as trabecular bone behaviour in this space is "more isotropic" and density independent than in stress space (Bayraktar et al., 2004a; Chang et al., 1999; Pankaj and Donaldson, 2013). There is also now some evidence to suggest that failure of bone is strain-controlled rather than stress-controlled (Nalla et al., 2003). However, there is little consensus on the yield criterion that may be suitable for this cellular material.

The aim of this Chapter is to characterise the macroscopic yield surface of trabecular bone by using a numerical homogenisation approach, derived from multiscale theory (Kruch and Chaboche, 2011; McDowell, 2010; Nguyen et al., 2012): using high resolution μFE meshes obtained from μCT images; applying a wide range of load cases which adequately describes the multiaxial behaviour of bone at the macroscale (including complex normal and shear load combinations); incorporating both geometrical and material nonlinearities; and with a validated pressure sensitive yield criterion for the solid phase. A wide range of trabecular bone samples with varying BV/TV and the efficacy of quadric surfaces as representatives for its macroscopic yield surface is examined.

6.1 Methods

6.1.1 Sample extraction and imaging

Twenty virtual cubes were extracted, as a larger set, from the cylindrical trabecular bone specimens mentioned in Chapter 5. The extraction and alignment procedures were the same as discussed in Chapter 5. Important morphological indices of these 20 cubes are shown in Table 6.1. As it can be seen, BV/TV ranges from low (13.7%) to

relatively high (30.3%); the range of SMIs is also considerably wide, ranging from a largely rod-like sample (SMI = 1.59) to a largely plate-like sample (SMI = 0.52).

Table 6.1 Morphological indices of the 20 used specimens.

Number of specimen	BV/TV (%)	DOA	SMI	Conn
1	30.3	2.67	0.52	1059
2	25.5	2.20	0.94	1285
3	13.7	2.80	1.56	424
4	14.9	2.91	1.50	233
5	18.1	3.47	1.33	235
6	14.8	2.65	1.59	209
7	19.7	3.86	1.06	561
8	15.5	2.69	1.45	586
9	17.7	2.59	1.40	493
10	16.2	2.30	1.52	570
11	20.1	1.64	1.50	421
12	19.2	1.62	1.39	582
13	17.0	1.79	1.53	680
14	15.3	1.52	1.53	470
15	15.5	1.78	1.48	642
16	17.8	1.58	1.29	910
17	22.2	3.47	0.84	622
18	24.6	2.85	0.88	847
19	20.3	1.61	1.16	1030
20	26.9	2.55	0.79	627

6.1.2 Solid phase constitutive model

The solid phase constitutive law used in Chapter 5 was used in this Chapter as well (with $\zeta_0 = 0.49$), except for its hardening, which in this case was set to perfect plasticity, although a very small hardening modulus ($\overline{H}_{iso} = 0.001$ in $q = \overline{H}_{iso}\overline{\kappa}$ of Eq. 3.84 in Chapter 3) was included to aid in the prevention of a possible loss of ellipticity. Although there have been some experimental studies which have evaluated hardening of the extracellular matrix (Luczynski et al., 2015; Schwiedrzik et al., 2014), there is no clear agreement on the hardening behaviour of the solid phase. Some studies have assumed linear hardening (Bayraktar and Keaveny, 2004; Bevill et al., 2006) and some others assumed perfect plasticity (Carnelli et al., 2010, 2011).

6.1.3 Computational methods

The 20 specimens were meshed using a voxelised mesh, where every voxel corresponds to a trilinear hexahedron. Each of them was then subjected to 160 strain-controlled load cases, as described in Table 6.2. This number is much higher than the 17 load cases used by Wolfram et al. (2012) and Panyasantisuk et al. (2015b), and is of the same order as the 231 and 297 load cases of Sanyal et al. (2015) and Bayraktar et al. (2004a), respectively. This set of load cases was designed to provide a thorough assessment of the yield surface in normal, shear and combined normal and shear strain spaces. Triaxial normal (eight cases) and triaxial shear (eight cases) load cases were added to the set of load cases considered in Chapter 5 in order to have a more thorough description of the yield behaviour in such loading regimes.

The employed boundary conditions were set to KUBC (Wang et al., 2009). All the FE simulations were run on a Cray XC30 MPP supercomputer hosted by ARCHER. The analyses were carried out with an *in-house* finite strain elastoplasticity parallel implicit FE solver, as discussed in Section 4.2.4 of Chapter 4.

At the integration point level, in order to ensure global convergence of the plasticity return-mapping Newton-CPPM scheme, a line search procedure was implemented as in the primal-CPPM scheme developed as Algorithm 2 in Chapter 3. At the global level, a Newton-Raphson scheme was used as the solution tracking method, and a PCG solver was used to solve the resulting linear algebraic systems. Newton-Raphson and PCG are relatively fasts algorithms if compared to possible alternatives, and if there are any convergence problems, they may arise from the same origin, which is the possible loss of positive-definiteness of the global stiffness matrix. However, convergence problems were only encountered in a few of the porous samples (in 20 out of 3,200 simulations), and they can be related to a limit point or large-deformation related failure mechanisms (Bevill et al., 2006; de Souza Neto et al., 2008) as the number of PCG iterations increased as this failure point was being reached. These points were marked with a different marker in figures and included in the fitting procedure as yield (failure) points. The considered initial load increment corresponded to 0.1% macroscopic strain norm and could decrease to a minimum of 0.001% if global convergence was not achieved. The simulations were stopped when macroscopic yield was reached, which was assessed by the 0.2% rule, as described in Fig 5.3 in Chapter 5.

6.1.4 Different symmetries of the macroscopic yield surface

The macroscopic yield surface was examined by fitting a quadric surface (Schwiedrzik et al., 2013) in strain space, through the minimisation procedure described in Section

Table 6.2 Description of the performed load cases. Clockwise and counter-clockwise shear are differentiated by the sign of the off-diagonal terms of the macroscopic strain tensor. Biaxial normal-shear cases have normal to shear ratios of 1 to 1, 0.25 to 0.75 and 0.75 to 0.25.

Type of analysis	**Description**	**Number**
Uniaxial normal $\varepsilon_{ii} \neq 0;\ \varepsilon_{jj} = \varepsilon_{kk} = 0$ $\varepsilon_{ij} = \varepsilon_{ik} = \varepsilon_{jk} = 0$	3 tensile and 3 compressive	6
Biaxial normal $\varepsilon_{ii} = \varepsilon_{jj} \neq 0;\ \varepsilon_{kk} = 0$ $\varepsilon_{ij} = \varepsilon_{ik} = \varepsilon_{jk} = 0$	1 analysis per quadrant	12
Triaxial normal $\varepsilon_{ii} = \varepsilon_{jj} = \varepsilon_{kk} \neq 0$ $\varepsilon_{ij} = \varepsilon_{ik} = \varepsilon_{jk} = 0$	1 analysis per octant	8
Uniaxial shear $\varepsilon_{ii} = \varepsilon_{jj} = \varepsilon_{kk} = 0$ $\varepsilon_{ij} \neq 0;\ \varepsilon_{ik} = \varepsilon_{jk} = 0$	3 clockwise and 3 counter-clockwise	6
Biaxial shear $\varepsilon_{ii} = \varepsilon_{jj} = \varepsilon_{kk} = 0$ $\varepsilon_{ij} = \varepsilon_{ik} \neq 0;\ \varepsilon_{jk} = 0$	1 analysis per quadrant	12
Triaxial shear $\varepsilon_{ii} = \varepsilon_{jj} = \varepsilon_{kk} = 0$ $\varepsilon_{ij} = \varepsilon_{ik} = \varepsilon_{jk} \neq 0$	1 analysis per octant	8
Biaxial normal-shear $\varepsilon_{ii} \neq 0;\ \varepsilon_{jj} = \varepsilon_{kk} = 0$ $\varepsilon_{lm} \neq 0;\ \varepsilon_{ln} = \varepsilon_{mn} = 0$	3 analysis per quadrant	108
$i,j,k,l,m,n = 1,2,3$ $i \neq j \neq k$ $l \neq m \neq n$	Total	160

6.1.5 (Wolfram et al., 2012). This choice was based on the simplicity of the quadric formulation, because it has been previously related to the microstructure of trabecular bone (Cowin, 1986; Wolfram et al., 2012), and because it is a smooth surface and therefore the use of several plastic multipliers is avoided. This quadric surface is described in strain space as

$$g(\boldsymbol{\varepsilon}^e) = \sqrt{\boldsymbol{\varepsilon}^e : \mathbb{G} : \boldsymbol{\varepsilon}^e} + \mathbf{G} : \boldsymbol{\varepsilon}^e - 1 = 0, \tag{6.1}$$

where $\mathbb{G}$ and $\mathbf{G}$ are respectively a fourth-order and a second-order tensor used to define the shape, directionality and eccentricity of the yield surface. The fourth-order tensor

$\mathbb{G}$ has major and minor symmetries ($\mathbb{G}_{ijkl} = \mathbb{G}_{klij}$ and $\mathbb{G}_{ijkl} = \mathbb{G}_{jikl} = \mathbb{G}_{ijlk} = \mathbb{G}_{jilk}$) allowing it to be defined on a symmetric matrix space (Sym^6), by 21 coefficients (Mehrabadi and Cowin, 1990). $\mathbf{G}$ is a symmetric second-order tensor, and therefore is defined by six coefficients. The convexity of the quadric surface, as discussed in Section 3.2.3 of Chapter 3, is ensured if $\mathbb{G}$ is positive-semidefinite (Schwiedrzik et al., 2013), which can be imposed in some cases by establishing some basic restrictions on the coefficients defining $\mathbb{G}$.

Three different symmetries were investigated: isotropy, orthotropy and anisotropy (triclinic symmetry). The yield surface (Eq. 6.1) is said to be isotropic if

$$g(\boldsymbol{\varepsilon}^e) = g(\mathbf{Q}\boldsymbol{\varepsilon}^e\mathbf{Q}), \tag{6.2}$$

where $\mathbf{Q}$ is any orthogonal tensor ($\mathbf{Q} \in \mathrm{Orth}^3$). If $\mathbf{Q}$ is restricted to a proper subset of the orthogonal tensors ($\mathrm{SOrth}^3 \subset \mathrm{Orth}^3$), then Eq. 6.1 no longer represents an isotropic function. If that was the case, Eq. 6.1 would become an orthotropic function if the orthogonal group Orth^3 was restricted to reflections about the three orthogonal planes whose normal define each of the three directions of the material which have different properties. Furthermore, Eq. 6.1 would become fully anisotropic if $\mathbf{Q} = \pm\mathbf{I}$ (Itskov, 2012).

In the isotropic case it is straightforward to observe that the second-order tensor $\mathbf{G}$ in Eq. 6.1 is of the form $g_0\,\mathbf{I}$, where g_0 is a scalar defined as

$$g_0 = \frac{1}{2}\left(\frac{1}{\varepsilon_0^+} - \frac{1}{\varepsilon_0^-}\right), \tag{6.3}$$

where ε_0^+ and ε_0^- are respectively the uniaxial tensile and the uniaxial compressive yield strains. For $\mathbb{G}$ to be isotropic, it must be a linear combination of the fourth-order tensors $\mathbf{I}\otimes\mathbf{I}$ and $\mathbf{I}\underline{\otimes}\mathbf{I}$. Specifically, $\mathbb{G}$ is of the form

$$\mathbb{G} = -\xi_0\, G_0^2(\mathbf{I}\otimes\mathbf{I}) + (\xi_0 + 1)G_0^2(\mathbf{I}\underline{\otimes}\mathbf{I}), \tag{6.4}$$

where

$$G_0 = \frac{\varepsilon_0^+ + \varepsilon_0^-}{2\varepsilon_0^+\varepsilon_0^-} \tag{6.5}$$

and ξ_0 is an interaction parameter. To ensure the positive semi-definiteness of $\mathbb{G}$, the following inequalities must be satisfied:

$$\varepsilon_0^{\pm} \geq 0; \quad -1 \leq \xi_0 \leq 0.5. \tag{6.6}$$

It is important to note that the upper limit on the restrictions imposed on ξ_0 recovers the traditional Drucker-Prager yield surface, provided $\varepsilon_0^- > \varepsilon_0^+$.

In the orthotropic case the yield surface must be invariant under reflections about the orthotropic axes. Representing the orthotropic axes by $\mathbf{m}_i$, $i = 1,2,3$, and corresponding eigentensors by $\mathbf{M}_i = \mathbf{m}_i \otimes \mathbf{m}_i$, for orthotropy $\mathbf{M}_i = \mathbf{Q}\mathbf{M}_i\mathbf{Q}^{\mathrm{T}}$ if $\mathbf{Q} \in \mathrm{SOrth}^3$ and SOrth^3 is the set of orthogonal tensors which comprise of reflections about the orthotropic axes. For example,

$$\mathbf{M}_1 = \begin{bmatrix} 1 & 0 & 0 \\ 0 & 0 & 0 \\ 0 & 0 & 0 \end{bmatrix} = \mathbf{Q}\mathbf{M}_1\mathbf{Q}^{\mathrm{T}} = \begin{bmatrix} -1 & 0 & 0 \\ 0 & 1 & 0 \\ 0 & 0 & 1 \end{bmatrix} \begin{bmatrix} 1 & 0 & 0 \\ 0 & 0 & 0 \\ 0 & 0 & 0 \end{bmatrix} \begin{bmatrix} -1 & 0 & 0 \\ 0 & 1 & 0 \\ 0 & 0 & 1 \end{bmatrix}. \tag{6.7}$$

The specific forms of $\mathbb{G}$ and $\mathbf{G}$ are given by

$$\mathbb{G} = \sum_{i=1}^{3} G_{ii}^2 \mathbf{M}_i \otimes \mathbf{M}_i - \sum_{\substack{i,j=1 \\ i \neq j}}^{3} \xi_{ij} G_{ii} G_{jj} \mathbf{M}_i \otimes \mathbf{M}_j + \sum_{\substack{i,j=1 \\ i \neq j}}^{3} \frac{G_{ij}^2}{2} \mathbf{M}_i \underline{\overline{\otimes}} \mathbf{M}_j \tag{6.8}$$

and

$$\mathbf{G} = \sum_{i=1}^{3} g_i \mathbf{M}_i, \tag{6.9}$$

where

$$G_{ii} = \frac{\varepsilon_{ii}^+ + \varepsilon_{ii}^-}{2\varepsilon_{ii}^+ \varepsilon_{ii}^-}; \quad G_{ij} = \frac{1}{\varepsilon_{ij}}; \quad g_i = \frac{1}{2}\left(\frac{1}{\varepsilon_{ii}^+} - \frac{1}{\varepsilon_{ii}^-}\right); \quad i = 1,2,3 \tag{6.10}$$

and ε_{ii}^+ and ε_{ii}^- are respectively the three uniaxial tensile and three uniaxial compressive yield strains, ε_{ij} are the three shear yield strains and ξ_{ij} are the three interaction parameters. All of the 12 parameters need to be defined for the orthotropic quadric.

Calculating the determinants of 1×1 and 2×2 principal minors of the projection of $\mathbb{G}$ onto Sym^6 permits establishment of basic restrictions on the coefficients to ensure that $\mathbb{G}$ in the orthotropic case is positive-semidefinite, which are

$$\varepsilon_{ii}^{\pm} \geq 0; \quad \varepsilon_{ij} \geq 0; \quad |\xi_{ij}| \leq 1; \quad i,j = 1,2,3. \tag{6.11}$$

The last restriction comes from applying Schur complements to the 3×3 leading principal minor of the projection of $\mathbb{G}$ onto Sym^6, and is given by

$$2G_{11}^2 G_{22}^2 \xi_{12} \xi_{13} \xi_{23} - G_{11}^2 G_{22}^2 \xi_{12}^2 - G_{11}^2 G_{22}^2 \xi_{13}^2 - G_{11}^2 G_{22}^2 \xi_{23}^2 + G_{11}^2 G_{22}^2 \geq 0. \tag{6.12}$$

In the anisotropic case, the yield surface can present shear yield asymmetry (i.e. different yield values in clockwise and counter-clockwise directions). For an anisotropic quadric, normal yield strains are able to interact with shear yield strains and shear yield strains are also able to interact amongst themselves (Theocaris, 1992; Tsai and Wu, 1971). This means that in the triclinic case $\mathbb{G}$ and $\mathbf{G}$ have 21 and six independent coefficients, respectively.

By performing uniaxial strain load cases, several coefficients of $\mathbb{G}$ and all the coefficients of $\mathbf{G}$ can be determined. For $\mathbf{G}$, the coefficients are

$$G_{ij} = \begin{cases} \frac{1}{2}\left(\frac{1}{\varepsilon_{ij}^{+}} - \frac{1}{\varepsilon_{ij}^{-}}\right) & \text{if } i = j \\ \frac{1}{4}\left(\frac{1}{\varepsilon_{ij}^{+}} - \frac{1}{\varepsilon_{ij}^{-}}\right) & \text{if } i \neq j \end{cases} \qquad i,j = 1,2,3. \tag{6.13}$$

In the case of $\mathbb{G}$, the six diagonal coefficients of the projection of $\mathbb{G}$ onto Sym^6 are

$$\mathbb{G}_{ijij} = \begin{cases} \left(\frac{\varepsilon_{ij}^{+}+\varepsilon_{ij}^{-}}{2\varepsilon_{ij}^{+}\varepsilon_{ij}^{-}}\right) & \text{if } i = j \\ \frac{1}{2}\left(\frac{\varepsilon_{ij}^{+}+\varepsilon_{ij}^{-}}{2\varepsilon_{ij}^{+}\varepsilon_{ij}^{-}}\right) & \text{if } i \neq j \end{cases} \qquad i,j = 1,2,3. \tag{6.14}$$

The 15 remaining parameters to be determined correspond to three normal strain interaction parameters, three shear strain interaction parameters and nine normal-shear strain interaction parameters. These have expressions in the coefficients of $\mathbb{G}$ which are related to the previously stated diagonal coefficients, as shown in Table 6.3.

These, together with the six uniaxial normal yield strains and six uniaxial shear yield strains, add up to a total of 27 parameters. Calculating the determinant of 1×1 and 2×2 principal minors of the projection of $\mathbb{G}$ onto Sym^6 allows for establishment of some basic restrictions on some of the coefficients to ensure that $\mathbb{G}$ is positive-semidefinite, which are

$$\varepsilon_{ij}^{\pm} \geq 0; \quad |\xi_{kl}| \leq 1; \quad i,j = 1,2,3; \quad k,l = 1,2,...,6 \tag{6.15}$$

The remaining restrictions on the coefficients are not expressed analytically but checked after the minimisation procedure to ensure positive-semidefiniteness of $\mathbb{G}$. For every considered symmetry and for every considered sample, the eigenvalues of the projection of $\mathbb{G}$ onto Sym^6 were checked to assure they were non-negative.

6.1.5 Minimisation procedure

The macroscopic yield envelope was fitted by using a minimisation procedure in MATLAB. The sum of squares of the difference between the Euclidean norms of a yield strain and the yield strain calculated through FE, for a corresponding macroscopic strain

Table 6.3 Interaction parameters for the anisotropic quadric.

	Coefficients
Normal interaction	$\mathbb{G}_{1122} = \xi_{12}\left(\frac{\varepsilon_{11}^{+}+\varepsilon_{11}^{-}}{2\varepsilon_{11}^{+}\varepsilon_{11}^{-}}\right)\left(\frac{\varepsilon_{22}^{+}+\varepsilon_{22}^{-}}{2\varepsilon_{22}^{+}\varepsilon_{22}^{-}}\right)$
	$\mathbb{G}_{1133} = \xi_{13}\left(\frac{\varepsilon_{11}^{+}+\varepsilon_{11}^{-}}{2\varepsilon_{11}^{+}\varepsilon_{11}^{-}}\right)\left(\frac{\varepsilon_{33}^{+}+\varepsilon_{33}^{-}}{2\varepsilon_{33}^{+}\varepsilon_{33}^{-}}\right)$
	$\mathbb{G}_{2233} = \xi_{23}\left(\frac{\varepsilon_{22}^{+}+\varepsilon_{22}^{-}}{2\varepsilon_{22}^{+}\varepsilon_{22}^{-}}\right)\left(\frac{\varepsilon_{33}^{+}+\varepsilon_{33}^{-}}{2\varepsilon_{33}^{+}\varepsilon_{33}^{-}}\right)$
Shear interaction	$\mathbb{G}_{1213} = \xi_{45}\left(\frac{\varepsilon_{12}^{+}+\varepsilon_{12}^{-}}{2\varepsilon_{12}^{+}\varepsilon_{12}^{-}}\right)\left(\frac{\varepsilon_{13}^{+}+\varepsilon_{13}^{-}}{2\varepsilon_{13}^{+}\varepsilon_{13}^{-}}\right)$
	$\mathbb{G}_{1223} = \xi_{46}\left(\frac{\varepsilon_{12}^{+}+\varepsilon_{12}^{-}}{2\varepsilon_{12}^{+}\varepsilon_{12}^{-}}\right)\left(\frac{\varepsilon_{23}^{+}+\varepsilon_{23}^{-}}{2\varepsilon_{23}^{+}\varepsilon_{23}^{-}}\right)$
	$\mathbb{G}_{1323} = \xi_{56}\left(\frac{\varepsilon_{13}^{+}+\varepsilon_{13}^{-}}{2\varepsilon_{13}^{+}\varepsilon_{13}^{-}}\right)\left(\frac{\varepsilon_{23}^{+}+\varepsilon_{23}^{-}}{2\varepsilon_{23}^{+}\varepsilon_{23}^{-}}\right)$
Normal-shear interaction	$\mathbb{G}_{1112} = \xi_{14}\left(\frac{\varepsilon_{11}^{+}+\varepsilon_{11}^{-}}{2\varepsilon_{11}^{+}\varepsilon_{11}^{-}}\right)\left(\frac{\varepsilon_{12}^{+}+\varepsilon_{12}^{-}}{2\varepsilon_{12}^{+}\varepsilon_{12}^{-}}\right)$
	$\mathbb{G}_{1113} = \xi_{15}\left(\frac{\varepsilon_{11}^{+}+\varepsilon_{11}^{-}}{2\varepsilon_{11}^{+}\varepsilon_{11}^{-}}\right)\left(\frac{\varepsilon_{13}^{+}+\varepsilon_{13}^{-}}{2\varepsilon_{13}^{+}\varepsilon_{13}^{-}}\right)$
	$\mathbb{G}_{1123} = \xi_{16}\left(\frac{\varepsilon_{11}^{+}+\varepsilon_{11}^{-}}{2\varepsilon_{11}^{+}\varepsilon_{11}^{-}}\right)\left(\frac{\varepsilon_{23}^{+}+\varepsilon_{23}^{-}}{2\varepsilon_{23}^{+}\varepsilon_{23}^{-}}\right)$
	$\mathbb{G}_{2212} = \xi_{24}\left(\frac{\varepsilon_{22}^{+}+\varepsilon_{22}^{-}}{2\varepsilon_{22}^{+}\varepsilon_{22}^{-}}\right)\left(\frac{\varepsilon_{12}^{+}+\varepsilon_{12}^{-}}{2\varepsilon_{12}^{+}\varepsilon_{12}^{-}}\right)$
	$\mathbb{G}_{2213} = \xi_{25}\left(\frac{\varepsilon_{22}^{+}+\varepsilon_{22}^{-}}{2\varepsilon_{22}^{+}\varepsilon_{22}^{-}}\right)\left(\frac{\varepsilon_{13}^{+}+\varepsilon_{13}^{-}}{2\varepsilon_{13}^{+}\varepsilon_{13}^{-}}\right)$
	$\mathbb{G}_{2223} = \xi_{26}\left(\frac{\varepsilon_{22}^{+}+\varepsilon_{22}^{-}}{2\varepsilon_{22}^{+}\varepsilon_{22}^{-}}\right)\left(\frac{\varepsilon_{23}^{+}+\varepsilon_{23}^{-}}{2\varepsilon_{23}^{+}\varepsilon_{23}^{-}}\right)$
	$\mathbb{G}_{3312} = \xi_{34}\left(\frac{\varepsilon_{33}^{+}+\varepsilon_{33}^{-}}{2\varepsilon_{33}^{+}\varepsilon_{33}^{-}}\right)\left(\frac{\varepsilon_{12}^{+}+\varepsilon_{12}^{-}}{2\varepsilon_{12}^{+}\varepsilon_{12}^{-}}\right)$
	$\mathbb{G}_{3313} = \xi_{35}\left(\frac{\varepsilon_{33}^{+}+\varepsilon_{33}^{-}}{2\varepsilon_{33}^{+}\varepsilon_{33}^{-}}\right)\left(\frac{\varepsilon_{13}^{+}+\varepsilon_{13}^{-}}{2\varepsilon_{13}^{+}\varepsilon_{13}^{-}}\right)$
	$\mathbb{G}_{3323} = \xi_{36}\left(\frac{\varepsilon_{33}^{+}+\varepsilon_{33}^{-}}{2\varepsilon_{33}^{+}\varepsilon_{33}^{-}}\right)\left(\frac{\varepsilon_{23}^{+}+\varepsilon_{23}^{-}}{2\varepsilon_{23}^{+}\varepsilon_{23}^{-}}\right)$

direction was minimised. The distance to a yield point, d, must satisfy the following equation:

$$d\left(\sqrt{\frac{\boldsymbol{\varepsilon}_{FE}^{e}}{\|\boldsymbol{\varepsilon}_{FE}^{e}\|} : \mathbb{G} : \frac{\boldsymbol{\varepsilon}_{FE}^{e}}{\|\boldsymbol{\varepsilon}_{FE}^{e}\|}} + \mathbf{G} : \frac{\boldsymbol{\varepsilon}_{FE}^{e}}{\|\boldsymbol{\varepsilon}_{FE}^{e}\|}\right) - 1 = 0, \tag{6.16}$$

where $\|(\cdot)\|$ is the Euclidean norm of $(\cdot)$ (defined as $\|(\cdot)\| = \sqrt{(\cdot):(\cdot)}$ for a second-order tensor), $\boldsymbol{\varepsilon}_{FE}^{e}$ is the macroscopic yield strain for each of the load cases described

in Table 6.2. To evaluate the goodness of fit, the fitting error was evaluated as

$$Error_{FIT} = \frac{1}{N}\sum_{i=1}^{N}\frac{\|\boldsymbol{\varepsilon}^{e}_{fitted} - \boldsymbol{\varepsilon}^{e}_{FE}\|_i}{\|\boldsymbol{\varepsilon}^{e}_{FE}\|_i}, \tag{6.17}$$

where N is the cardinality of a specific set of load cases. This error was evaluated for four different sets: for all the load cases; for the load cases which are entirely contained in the normal strain space (rows 1-3 of Table 6.2); for the load cases which are entirely contained in the shear strain space (rows 4-6 of Table 6.2); and for the strain cases which have a component in the normal strain space and a component in the shear strain space (normal-shear strain space, row 7 of Table 6.2).

6.2 Results

6.2.1 Macroscopic yield strains

The macroscopic yield points in strain space for all considered samples in normal-normal and shear-shear planes are shown in Fig. 6.1. These represent 36 of the 160 performed load cases for each sample, which are contained in the sets described in rows 1-6 of Table 6.2; and no projections have been made, i.e. the yield strains shown only contain out-of-plane components equal to zero. These macroscopic yield strains suggest that the macroscopic yield surface of trabecular bone has a higher yield strain in compression than in tension, which is expected due to the characteristics of the solid phase, which are likely to be partially upscaled to the macroscale with a corresponding decrease of the yield values due to the presence of porosity and the corresponding increase in anisotropy due to the presence of an anisotropic microstructure.

It can be noticed that the tensile quadrant displays quasi-uniform macroscopic yield strains across samples (Fig. 6.1a-c, upper right quadrant). The compressive yield strains have some variability across samples, as can be seen from the spread of the yield points in the lower left quadrant of Fig. 6.1a-c. The largest variation in the normal-normal planes is in the tensile-compressive quadrants (Fig. 6.1a-c, upper left and lower right quadrants).

The macroscopic yield strains in shear-shear planes show a large variation of yield strains across samples (Fig. 6.1d-f). It can also be observed that shear yield strains of trabecular bone are generally different in clockwise and counter-clockwise directions, with absolute differences ranging from 0.0034% to 0.4463%. A statistical comparison between these yield strains was performed for all pure uniaxial shear cases with a paired

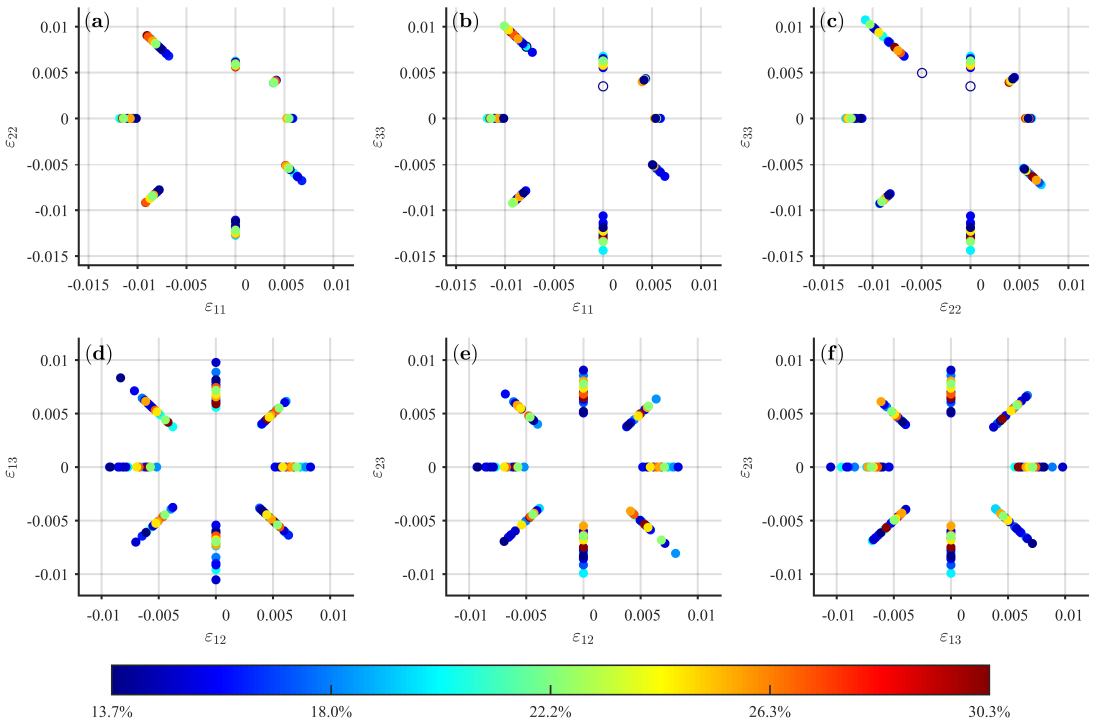

Fig. 6.1 Macroscopic yield points of the 20 samples in normal strain planes (a-c) and in shear strain planes (d-f). The colour coding is on the basis of density and is used as a labelling mechanism. Few of the obtained macroscopic yield points resulted in the loss of positive-definiteness of the stiffness matrix, which are marked with empty circles.

t-test. This test suggests that paired clockwise and counter-clockwise shear yield strains are statistically different ($p < 0.01$).

Macroscopic uniaxial (tensile, compressive and shear) yield strains were related to BV/TV and fabric eigenvalues through multilinear regressions. No relationships between yield strains and BV/TV or between yield strains and fabric eigenvalues were found. Only compressive uniaxial yield strains were mildly related to BV/TV and fabric eigenvalues ($R^2 = 0.44,\ p \to 0$).

In order to examine the macroscopic yield strains in different quadrants (tension-tension, compression-compression and tension-compression), the average of the macroscopic yield strain norms for each of the above three regimes was evaluated, as shown in Fig. 6.2. As expected, the mean of the norms is the lowest for tension-tension, highest for compression-compression and in between for tension-compression. Figure 6.2 also shows the standard deviation of the evaluated norms. It can be seen that the deviation is relatively small for the tension-tension regime, higher for compression-compression regime and the highest for tension-compression regime.

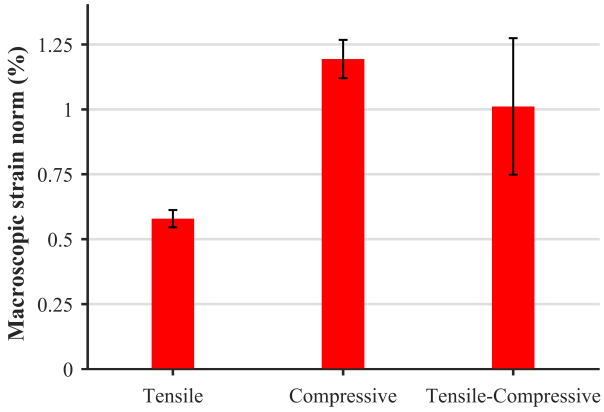

Fig. 6.2 Bar plot of the mean of the macroscopic yield strain norms for tensile cases ($\varepsilon_{ii} \geq 0$; $i = 1,2,3$), compressive cases ($\varepsilon_{ii} \leq 0$; $i = 1,2,3$) and tensile-compressive cases ($\varepsilon_{ii} \leq 0$; $\varepsilon_{jj} \geq 0$; $i,j = 1,2,3$; $i \neq j$). The error bars correspond to the standard deviations of these values.

6.2.2 Solid phase strains

Strains at the microscale, or at the solid phase, were examined. Under uniaxial macroscopic tension more localised strains were found to occur at the solid phase, and there were mostly no compressive solid phase strains anywhere in the specimens. However, under uniaxial macroscopic compression the compressive solid phase strains were more diffused and found to occur throughout the geometry. Further, under uniaxial macroscopic compression large tensile solid phase strains were found to arise due to bending and buckling of trabeculae. Figures 6.3 and 6.4 show this for a slice from one typical porous sample.

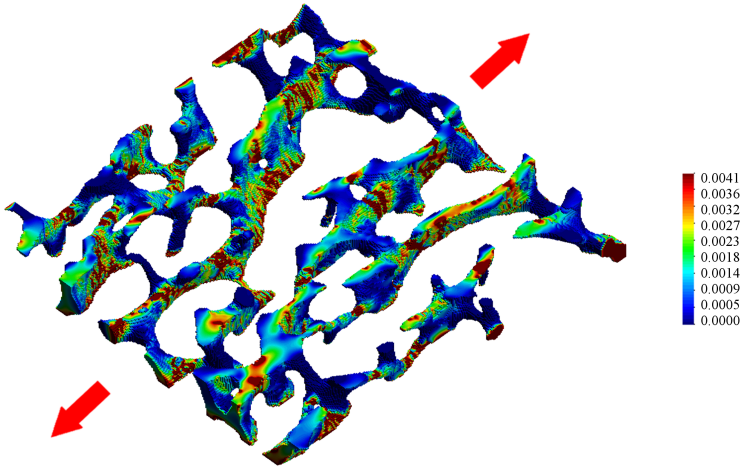

Fig. 6.3 Distribution of the Green-Lagrange solid phase strain component E_{11} for a $0.5 \times 5 \times 5$ mm slice of bone under macroscopic uniaxial tension. Direction 1 is in the direction denoted by the arrows.

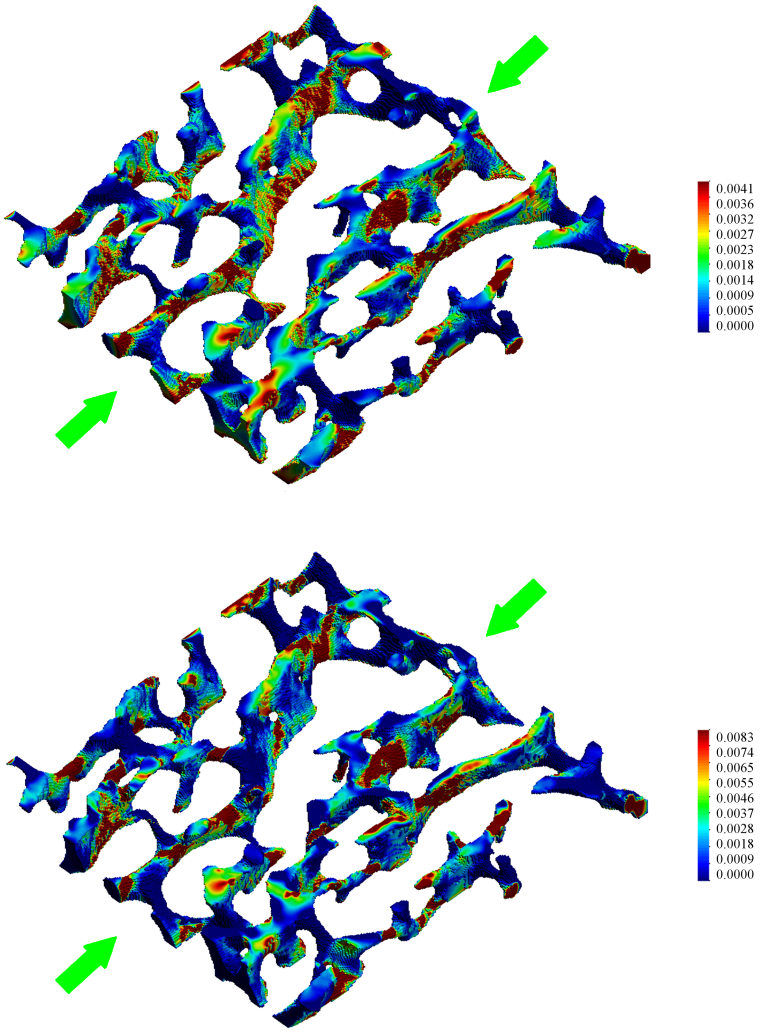

Fig. 6.4 Distribution of the Green-Lagrange solid phase strain under macroscopic uniaxial compression for a $0.5 \times 5 \times 5$ mm slice of bone. **Top** - Tensile component E_{22}. **Bottom** - Compression component E_{11}. Direction 1 is in the direction denoted by the arrows and direction 2 is the orthogonal in-plane direction.

6.2.3 Macroscopic yield surface and fitting errors

A macroscopic yield surface was fitted to each of the 20 samples by using isotropic, orthotropic and fully anisotropic formulations of a quadric yield surface, using all of the 160 load cases. The mean and standard deviation of the fitted parameters for the anisotropic surface are shown in Table 6.4. Plots for the two samples with the highest and lowest densities are shown in Fig. 6.5. The lower density sample shows a higher level of anisotropy in comparison to the higher density sample. Further, if consecutive macroscopic yield points of the porous sample are joined up, the homogenised envelope does not always remain entirely convex in some of the planes (e.g. Fig. 6.5i-k).

Table 6.4 Mean and standard deviation of the parameters of the anisotropic quadric yield surface.

Coefficients	**Value** (mean $\pm$ standard deviation)
$\mathbb{G}_{1111}$	$18,391.8 \pm 5,092.2$
$\mathbb{G}_{1122}$	$7,801.1 \pm 1,059.9$
$\mathbb{G}_{1133}$	$8,492.1 \pm 1,021.2$
$\mathbb{G}_{1112}$	155.5 ± 866.8
$\mathbb{G}_{1113}$	$306.6 \pm 1,883.4$
$\mathbb{G}_{1123}$	150.0 ± 684.1
$\mathbb{G}_{2222}$	$17,510.1 \pm 2,826.5$
$\mathbb{G}_{2233}$	$8,644.4 \pm 1,713.2$
$\mathbb{G}_{2212}$	-83.4 ± 800.1
$\mathbb{G}_{2213}$	84.0 ± 744.1
$\mathbb{G}_{2223}$	$495.5 \pm 1,619.2$
$\mathbb{G}_{3333}$	$20,689.0 \pm 4,299.2$
$\mathbb{G}_{3312}$	12.2 ± 628.9
$\mathbb{G}_{3313}$	$260.1 \pm 1,616.6$
$\mathbb{G}_{3323}$	$538.9 \pm 1,787.2$
$\mathbb{G}_{1212}$	$4,557.3 \pm 688.8$
$\mathbb{G}_{1213}$	228.2 ± 374.2
$\mathbb{G}_{1223}$	287.8 ± 482.6
$\mathbb{G}_{1313}$	$5,016.1 \pm 724.8$
$\mathbb{G}_{1323}$	-3.5 ± 427.7
$\mathbb{G}_{2323}$	$5,200.4 \pm 844.0$
$\mathbf{G}_{11}$	52.6 ± 14.3
$\mathbf{G}_{22}$	52.0 ± 8.2
$\mathbf{G}_{33}$	60.9 ± 12.5
$\mathbf{G}_{12}$	0.4 ± 2.5
$\mathbf{G}_{13}$	0.8 ± 5.1
$\mathbf{G}_{23}$	1.8 ± 4.6

Mean fitting errors considering all samples and all strain cases are shown in Fig. 6.6. It can be seen that the isotropic assumption leads to the highest ($\sim$11%) error, followed by the orthotropic ($\sim$10%) and the anisotropic ($\sim$8%) assumptions. The standard deviation of the fitting errors is also shown in the figure and it can be seen that the error variation across densities with the isotropic assumption is similar to the orthotropic case; the anisotropic assumption produces the smallest variations across samples.

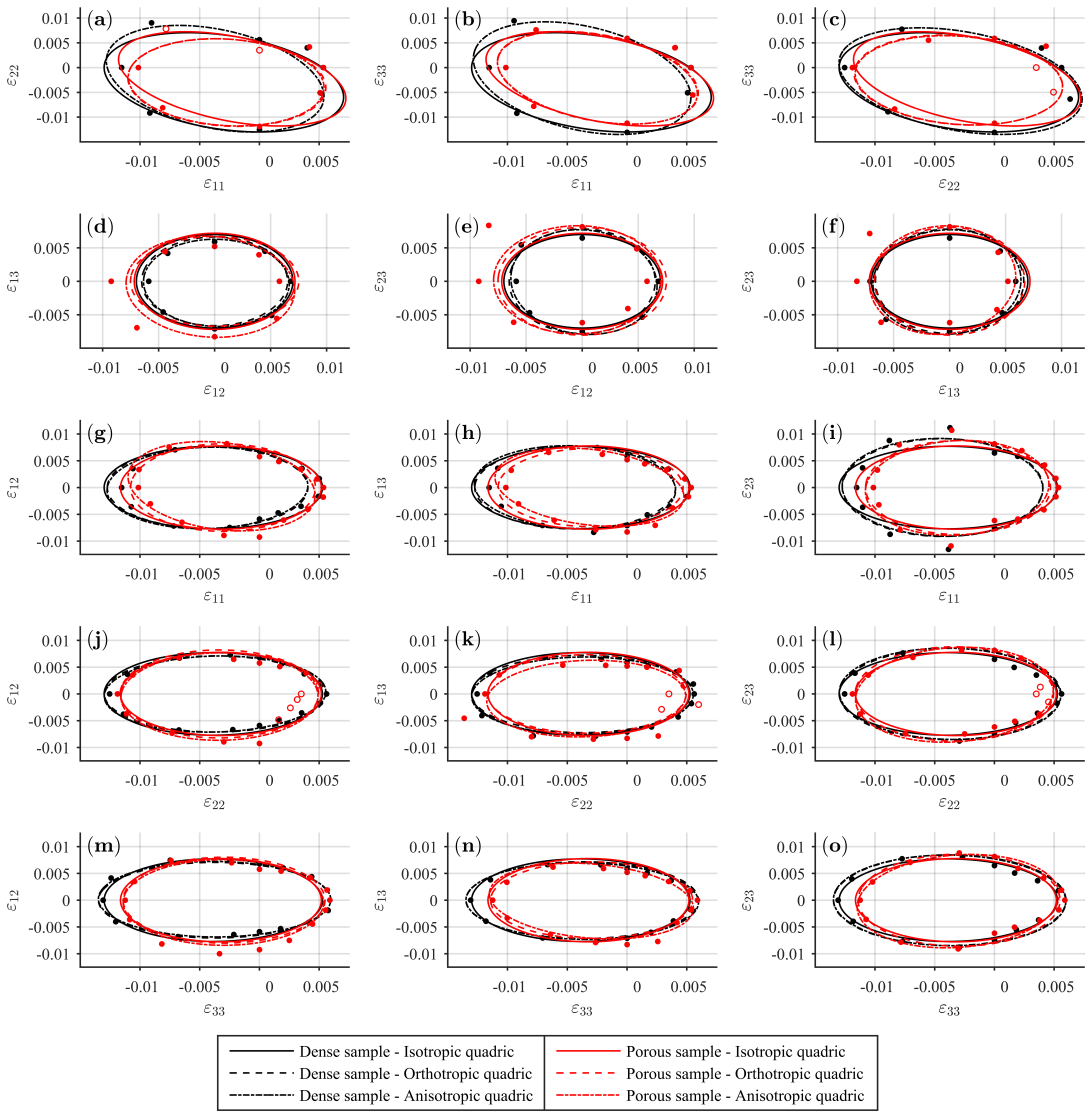

Fig. 6.5 Macroscopic yield points for the densest and most porous samples and their corresponding isotropic, orthotropic and anisotropic fitted quadric surfaces in normal strain planes (a-c), shear strain planes (d-f), and combined normal and shear strain planes (g-o). Few of the obtained macroscopic yield points resulted in the loss of positive-definiteness of the stiffness matrix, which are marked with empty circles.

In general, fitting errors were not found to correlate with BV/TV (Fig. 6.7). In normal strain space (Fig. 6.7a) the assumption of an isotropic quadric led to consistently higher errors, while the orthotropic and anisotropic assumptions resulted in smaller fitting errors. In the shear strain space (Fig. 6.7b), in the combined normal and shear strain space (Fig. 6.7c) and in the general strain space (Fig. 6.7d) the assumption of an anisotropic quadric had the smallest errors. A mild trend of errors decreasing with increasing density was observed for the isotropic and orthotropic assumptions in shear strain space. In the general strain space, the errors and the error differences between assumptions also tend to reduce with increasing density.

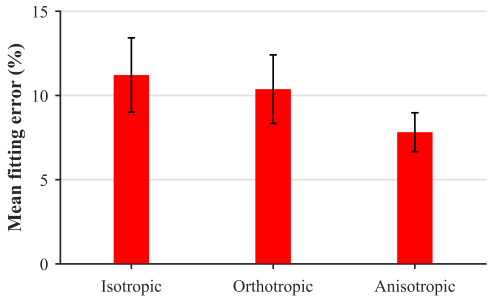

Fig. 6.6 Bar plot of the mean of the fitting errors across all samples for the isotropic, orthotropic and anisotropic quadrics. All the strain cases are taken into account. The error bars correspond to the standard deviations of these values.

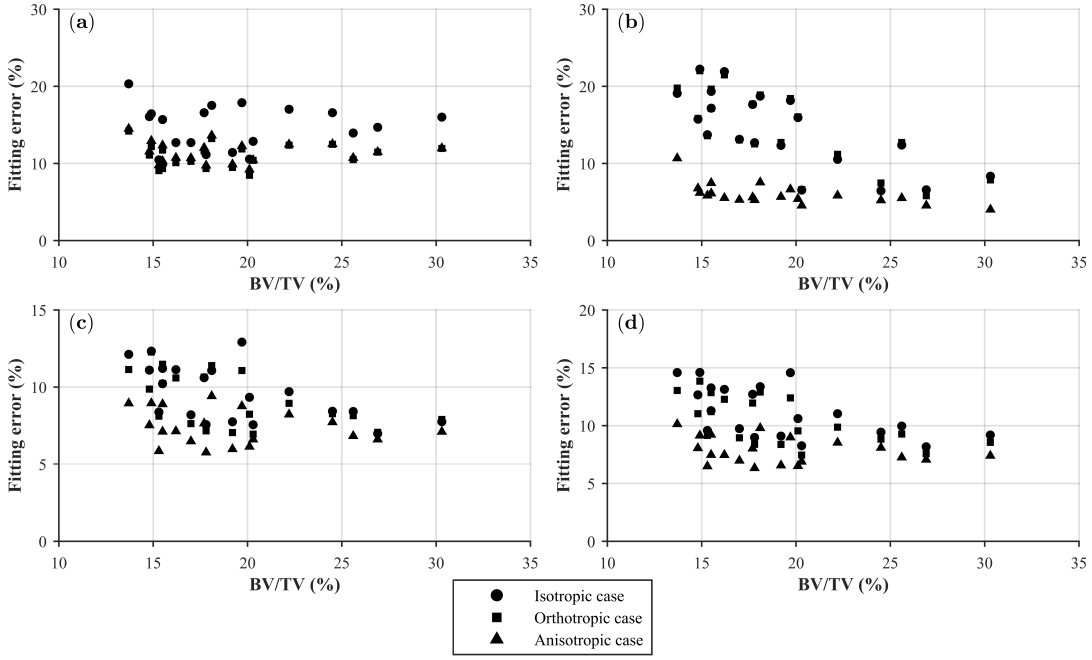

Fig. 6.7 Fitting errors as described in Eq. 6.17 for the normal strain space (a), shear strain space (b), combined normal and shear strain space (c), and in general strain space (d).

6.3 Discussion

This Chapter shows that the macroscopic yield surface of bone in normal strain space is fairly uniform across a wide range of samples; this confirms findings of previous research (Bayraktar et al., 2004a; Lambers et al., 2014; Pankaj and Donaldson, 2013).

The results shown also demonstrate that the full three-dimensional macroscopic yield behaviour of trabecular bone can be reasonably well described using an isotropic quadric yield surface, though orthotropic and anisotropic surfaces lead to smaller errors. This is in agreement with previous studies in which the strain space yield surface was reported to be isotropic (Bayraktar et al., 2004a), and more recently transverse isotropic (Sanyal et al., 2015), and orthotropic (Wolfram et al., 2012). This being said, although

the errors in the macroscopic yield surfaces in strain space with higher symmetries are slightly smaller, the fact that more parameters are added to the constitutive model increases its uncertainty due to the difficulty in measuring these parameters. Also, as will be mentioned later, due to the fact that BV/TV and fabric do not seem to be strongly related to the yield values in strain space, the isotropic yield surface is the obvious and adequate choice as the macroscopic yield surface for trabecular bone in strain space.

Unlike the studies cited in the previous paragraph, the consideration of shear asymmetry as separate loading cases showed that the differences in the two directions are significant. This is probably because trabeculae are not symmetrically aligned with respect to the axes of the material, which in this case were assessed through the eigenvectors of the MIL fabric tensor. It is important to note that the assumption of identical macroscopic yield points in clockwise and counter-clockwise directions restricts the system to orthotropy at best (Theocaris, 1992; Tsai and Wu, 1971). We also observed predominance of tensile solid phase strains in pure macroscopic uniaxial shear, which is consistent with Sanyal et al. (2012).

Multilinear regressions suggest that the macroscopic uniaxial yield strains are not correlated with BV/TV and fabric (Matsuura et al., 2008; Morgan and Keaveny, 2001; Panyasantisuk et al., 2015b). Only a mild dependence was found for the uniaxial compressive yield strains ($R^2 = 0.44,\ p \to 0$), with a positive slope for BV/TV and a negative slope for fabric, which suggests that long trabeculae, i.e. trabeculae associated with a high fabric eigenvalue, have lower macroscopic yield strain, as suggested by Matsuura et al. (2008). This is because these trabeculae are prone to earlier buckling. Since no clear relationship between fabric tensor and macroscopic yield strains was found, use of an isotropic yield surface formulation in strain space is more practical for real applications.

In uniaxial macroscopic tension, solid phase strains are almost exclusively tensile and independent of density (Bayraktar and Keaveny, 2004; Lambers et al., 2014). The highly oriented microstructure of trabecular bone results in yield strains at the solid phase and at the macroscale being very similar in tension. When trabecular bone is loaded in macroscopic compression, yield mechanisms are different: in this case yielding at the solid phase was found to occur both due to tension, arising from bending and buckling of trabeculae, and compression. As expected, considerable tensile strains in trabeculae for low density samples were found, as has been previously reported in the literature (Bevill et al., 2006; Morgan et al., 2004; Stölken and Kinney, 2003). This "density dependence" results in macroscopic yield variation being displayed via a small spread of yield points in compression-compression quadrants (Fig. 6.1a-c), as shown by the mild relationship between compressive uniaxial yield strains and BV/TV

and fabric. This also implies that solid phase uniaxial yield strain asymmetry is not fully maintained at the macroscale and generally reduces with increasing porosity and increasing fabric eigenvalues. These results are consistent with the experimental results of Lambers et al. (2014) in the sense that the number of microscopic yielded sites in macroscopic compression and in macroscopic tension are similar in number, but in macroscopic tension the microscopic yielded zones have more localised strains, which could be related to microcrack initiation and propagation.

Except for Panyasantisuk et al. (2015b), the few previous studies which have evaluated the macroscopic yield surface of trabecular bone from its microstructure have all used a bilinear criterion, with yield strain asymmetry. This constitutive model uses a reduced stiffness beyond defined tissue yield values (Bayraktar et al., 2004a; Sanyal et al., 2015; Wolfram et al., 2012). In this Chapter, the solid phase of trabecular bone was modelled with a Drucker-Prager type criterion (hyperbolic approximation to the cone), which has been validated via previous experimental studies (Carnelli et al., 2010; Tai et al., 2006). This Chapter also considered macroscopic yield strains arising from 160 different load cases, while some recent studies have been limited to 17 load cases (Panyasantisuk et al., 2015b; Wolfram et al., 2012). In order to compare the results obtained here to those in literature, 17 strain cases similar to those in the cited studies were considered, which resulted in errors of 11.4% for the isotropic case and 10.3% for the orthotropic case. The errors for the same sample but taking into account all 160 strain cases were 11.2% for the isotropic case, 10.4% for the orthotropic case, and 7.8% for the anisotropic case. In other words, the 17 strain cases lead to errors of a similar magnitude to those obtained using all 160 strain cases.

In order to further examine the effect of the considered strain cases on the fitting error, a single sample was considered with a different set of strain cases. The fitting errors were evaluated considering all normal strain cases proposed by Wolfram et al. (2012) (14 cases) and all the shear cases used in this study (26 cases). The obtained errors were 18.0%, 16.3% and 7.6% for isotropic, orthotropic and anisotropic assumptions respectively. With the 17 load cases mentioned previously, the errors reduce to 9.8% and 6.5% for isotropic and orthotropic assumptions respectively. With all the 160 load cases the errors were 13.3%, 12.9% and 9.1% for isotropic, orthotropic and anisotropic assumptions respectively. This illustrates that shear cases contribute significantly to anisotropy, and that the fitting errors clearly depend on the considered load cases, which illustrates the importance of examining a large range of complex load cases. With respect to combined normal and shear strain spaces, the shear component of the macroscopic yield strain is often found to increase when there is a compressive normal

component, indicating a typical cellular solid behaviour (Fenech and Keaveny, 1999; Gibson and Ashby, 1999).

There is a certain number of limitations present in this study. A quadric yield surface was chosen because of its simplicity and because it has been used in previous studies. Quadrics require fewer parameters than higher-order criteria and they are smooth surfaces, not requiring the use of several plastic multipliers. Although the primary aim was to examine the effect of material symmetry assumptions on the macroscopic yield surface of trabecular bone, the fitting errors clearly depend on the shape of the chosen surface and on the considered load cases. While full anisotropy was examined with a quadric yield surface, a previous study employed a higher-order polynomial surface (a quartic), but restricted it to transverse isotropy (Sanyal et al., 2015); a restriction which is clearly not supported by the results of this study. Also, hardening was not considered in this study (Carnelli et al., 2010) because there is no agreement on the hardening law at the solid phase level. Nonetheless, previous experimental and theoretical studies, such as Schwiedrzik et al. (2014), Luczynski et al. (2015) and Fritsch et al. (2009) showed that the extracellular matrix of bone has a hardening behaviour; however, the extracellular matrix could be treated as a scale lower than the solid phase considered in these μFE simulations.

Chapter 7

Post-yield macroscopic behaviour

This Chapter evaluates the macroscopic post-yield behaviour of trabecular bone, due to the inclusion of not only hardening but also stiffness degradation at the solid phase level. This chapter resulted in the following submission:
- Levrero-Florencio, F., Manda, K., Margetts, L., and Pankaj, P. (2017). Effect of including damage at the tissue level in the nonlinear homogenisation of trabecular bone. *Biomechanics and Modeling in Mechanobiology* (*under review*).

There is little information on the post-elastic macroscopic response of trabecular bone, and on how it evolves with further loading; hardening is usually assumed to be isotropic in computational models (Garcia et al., 2009; Schwiedrzik and Zysset, 2013). It is not possible to experimentally test different load directions after yield in the same sample since samples tested once cannot be retested as damage in one direction may affect the rest of directions and finding two or more samples with highly resembling microstructure is not possible. This makes it impossible to experimentally obtain the macroscopic multiaxial post-yield behaviour of trabecular bone. The μFE approach again presents an opportunity to understand this via computational means. To evaluate the macroscopic post-yield response, once again, the solid phase constitutive model needs to be provided. Bone shows two main mechanisms of energy dissipation after yield: plastic deformation and elastic stiffness reduction, or damage (Schwiedrzik and Zysset, 2013). With regard to hardening of the solid phase, it has been assumed to be 5% slope of its elastic stiffness in previous homogenisation studies (Bayraktar and Keaveny, 2004; Wolfram et al., 2012). A recent study showed that the hardening of the extracellular matrix, which can be considered to be a scale below the solid phase of trabecular bone, is, however, slightly nonlinear (Luczynski et al., 2015; Schwiedrzik et al., 2014).

Damage behaviour of bone at different scales has been studied and modelled in several studies (Garcia et al., 2009; Keaveny et al., 1999; Schwiedrzik and Zysset,

2013). Garcia et al. (2009) developed a macroscopic constitutive model for bone - a yield surface defined in stress space using the fabric-based elastic compliance tensor and a damage threshold modelled with a halfspacewise generalisation of the Hill criterion (Rincón-Kohli and Zysset, 2009). Schwiedrzik and Zysset (2013) developed a constitutive model for bone which is potentially applicable to different length scales, ranging from the ultrastructural to the macroscopic level. It includes anisotropic elasticity based on a multiscale homogenisation scheme proposed by Reisinger et al. (2010), an eccentric-elliptical surface which describes the onset of yield and damage (Wolfram et al., 2012), and visco-plasticity described by a Perzyna formulation (Ponthot, 1998). The damage variable used in these two above cited studies is scalar and thus describes isotropic damage evolution, i.e. damage equally affects all directions. While this presents a relatively simple model it appears unlikely that damage due to loading in one direction will affect stiffness components, isotropically, in all directions.

The primary aim of this Chapter is to evaluate how assumptions made for the solid phase of trabecular bone affect its macroscopic post-yield behaviour. The Chapter first assesses how the macroscopic stiffness components are affected by the initiation and development of microscopic damage. It then considers how macroscopic damage is related to the macroscopic strain norm and how well it can be predicted for different load cases. Lastly, the Chapter assesses the evolution of the macroscopic yield surface, in both strain and stress space.

7.1 Methods

7.1.1 Sample extraction and imaging

Twelve virtual cubes were extracted, as a larger set, from the cylindrical trabecular bone specimens discussed in Chapter 5. The extraction of the cubes followed the process discussed in Chapter 5. Important morphological indices of these 12 cubes can be found in Table 7.1. As it can be seen, BV/TV ranges from low (14.8%) to relatively high (30.3%); the range of SMIs is also considerably wide, ranging from a largely rod-like sample (SMI = 1.59) to a largely plate-like sample (SMI = 0.52).

7.1.2 Solid phase constitutive model

The solid phase constitutive law used in this Chapter is an approximation to Drucker-Prager as in Chapter 5, with the addition of the following damage law:

$$D = D_c(1 - \mathrm{e}^{-k_p \bar{\varepsilon}^p}), \tag{7.1}$$

Table 7.1 Morphological indices of the 12 used specimens.

Number of specimen	BV/TV (%)	DOA	SMI	Conn
1	30.3	2.67	0.52	1059
2	25.5	2.20	0.94	1285
3	18.1	3.47	1.33	235
4	14.8	2.65	1.59	209
5	16.5	2.13	1.37	740
6	15.5	2.69	1.45	586
7	17.7	2.59	1.40	493
8	22.2	3.47	0.84	622
9	24.6	2.85	0.88	847
10	20.3	1.61	1.16	1030
11	23.1	2.10	0.98	813
12	26.9	2.55	0.79	627

where D_c is the critical damage value, k_p is the damage evolution constant, and $\overline{\varepsilon}^p$ is the accumulated plastic strain (Euclidean norm of the plastic strain tensor).

In effective stress space, damage implies contraction of the yield surface. To prevent that, the yield surface was defined in stress space (Schwiedrzik and Zysset, 2015), which is

$$f(\boldsymbol{\sigma}, q) = \sqrt{\boldsymbol{\sigma} : \mathbb{F} : \boldsymbol{\sigma}} + \mathbf{F} : \boldsymbol{\sigma} - (1 + \overline{H}_{iso}\overline{\varepsilon}^p) = 0 \tag{7.2}$$

and not in effective stress space, i.e.

$$f(\boldsymbol{\sigma}, q) = \frac{\sqrt{\boldsymbol{\sigma} : \mathbb{F} : \boldsymbol{\sigma}} + \mathbf{F} : \boldsymbol{\sigma}}{1 - D} - (1 + \overline{H}_{iso}\overline{\varepsilon}^p) = 0. \tag{7.3}$$

This means that damage will not lead to softening of the yield surface; this assumption is considered so that the desired hardening of 5% is preserved (Bayraktar and Keaveny, 2004).

7.1.3 Derivation and integration of the evolution equations

The residuals of the damaged quadric yield surface are

$$\begin{Bmatrix} \mathbf{R}_{\boldsymbol{\sigma}} \\ R_f \end{Bmatrix} = \begin{Bmatrix} \boldsymbol{\sigma} - (1 - D)\mathbb{D}^e : \left(\boldsymbol{\varepsilon}^{e\,trial} - \Delta\overline{\varepsilon}^p \frac{\mathbf{N}}{\|\mathbf{N}\|}\right) \\ \sqrt{\boldsymbol{\sigma} : \mathbb{F} : \boldsymbol{\sigma}} + \mathbf{F} : \boldsymbol{\sigma} - [1 + \overline{H}_{iso}(\overline{\varepsilon}^{p\,trial} + \Delta\overline{\varepsilon}^p)] \end{Bmatrix}, \tag{7.4}$$

where $\mathbf{N}$ is defined in Eq. 3.89 and $\overline{\varepsilon}^{p\,trial}$ is the trial value of $\overline{\varepsilon}^p$. Note the equivalence between the increment in plastic strain defined in Eq. 3.88 and the increment in plastic

strain defined as

$$\Delta\boldsymbol{\varepsilon}^p = \Delta\gamma\mathbf{N} = \Delta\overline{\varepsilon}^p \frac{\mathbf{N}}{\|\mathbf{N}\|}. \tag{7.5}$$

The residual of stresses in Eqs. 7.4 can be converted to a residual of elastic strains by using $\boldsymbol{\varepsilon}^e = (1-D)^{-1}(\mathbb{D}^e)^{-1} : \boldsymbol{\sigma}$, as

$$\begin{Bmatrix} \mathbf{R}_{\boldsymbol{\varepsilon}^e} \\ R_f \end{Bmatrix} = \begin{Bmatrix} \boldsymbol{\varepsilon}^e - \boldsymbol{\varepsilon}^{e\,trial} + \Delta\overline{\varepsilon}^p \frac{\mathbf{N}}{\|\mathbf{N}\|} \\ \sqrt{\boldsymbol{\sigma} : \mathbb{F} : \boldsymbol{\sigma}} + \mathbf{F} : \boldsymbol{\sigma} - [1 + \overline{H}_{iso}(\overline{\varepsilon}^{p\,trial} + \Delta\overline{\varepsilon}^p)] \end{Bmatrix}. \tag{7.6}$$

Therefore, the solution variables, $\mathbf{x}$, in Eqs. 7.6 are

$$\mathbf{x} = \begin{Bmatrix} \boldsymbol{\varepsilon}^e \\ \Delta\overline{\varepsilon}^p \end{Bmatrix}. \tag{7.7}$$

Equations 7.6 are then linearised as

$$\begin{Bmatrix} \mathrm{d}\boldsymbol{\varepsilon}^{e\,trial} \\ 0 \end{Bmatrix} = \begin{Bmatrix} \left[\mathbb{I} + \Delta\overline{\varepsilon}^p \frac{\partial}{\partial \boldsymbol{\varepsilon}^e}\left(\frac{\mathbf{N}}{\|\mathbf{N}\|}\right)\right] : \mathrm{d}\boldsymbol{\varepsilon}^e + \mathrm{d}\Delta\overline{\varepsilon}^p \left[\frac{\mathbf{N}}{\|\mathbf{N}\|} + \Delta\overline{\varepsilon}^p \frac{\partial}{\partial \Delta\overline{\varepsilon}^p}\left(\frac{\mathbf{N}}{\|\mathbf{N}\|}\right)\right] \\ \mathbf{N} : \left(\frac{\partial \boldsymbol{\sigma}}{\partial \boldsymbol{\varepsilon}^e} : \mathrm{d}\boldsymbol{\varepsilon}^e + \frac{\partial \boldsymbol{\sigma}}{\partial D} D' \mathrm{d}\Delta\overline{\varepsilon}^p\right) - \overline{H}_{iso}\mathrm{d}\Delta\overline{\varepsilon}^p \end{Bmatrix}, \tag{7.8}$$

and therefore the Jacobian of the CPPM becomes

$$[\mathbf{J}_{CPPM}] = \begin{bmatrix} \mathbb{I} + \Delta\gamma \frac{\partial}{\partial \boldsymbol{\varepsilon}^e}\left(\frac{\mathbf{N}}{\|\mathbf{N}\|}\right) & \frac{\mathbf{N}}{\|\mathbf{N}\|} \\ \frac{\partial f}{\partial \boldsymbol{\varepsilon}^e} & \frac{\partial f}{\partial \Delta\gamma} \end{bmatrix} = \begin{bmatrix} \mathbb{A}_{11} & \mathbf{A}_{12} \\ \mathbf{A}_{21} & A_{22} \end{bmatrix}, \tag{7.9}$$

where the corresponding coefficients are shown in Table 7.2.

Table 7.2 Coefficients of the Jacobian of the CPPM of the generic quadric with damage (Schwiedrzik and Zysset, 2013).

Coefficient	Mathematical expression
$\mathbb{A}_{11}$	$\mathbb{I} + \frac{1-D}{\|\mathbf{N}\|}\left(\mathbb{I} - \frac{1}{(\|\mathbf{N}\|)^2}\mathbf{N}\otimes\mathbf{N}\right) : \frac{\partial \mathbf{N}}{\partial \boldsymbol{\sigma}} : \mathbb{D}^e$
$\mathbf{A}_{12}$	$\frac{\mathbf{N}}{\|\mathbf{N}\|}$
$\mathbf{A}_{21}$	$(1-D)\mathbf{N} : \mathbb{D}^e$
A_{22}	$\mathbf{N} : \frac{\partial \boldsymbol{\sigma}}{\partial D} D' - \overline{H}_{iso}$
$\frac{\partial \boldsymbol{\sigma}}{\partial D}$	$-\mathbb{D}^e : \boldsymbol{\varepsilon}^e$
$\frac{\partial \mathbf{N}}{\partial \boldsymbol{\sigma}}$	$\frac{\mathbb{F}}{\sqrt{\boldsymbol{\sigma}:\mathbb{F}:\boldsymbol{\sigma}}} - \frac{(\mathbb{F}:\boldsymbol{\sigma})\otimes(\boldsymbol{\sigma}:\mathbb{F})}{(\sqrt{\boldsymbol{\sigma}:\mathbb{F}:\boldsymbol{\sigma}})^3}$
D'	$D_c\, k_p\, \mathrm{e}^{-k_p(\overline{\varepsilon}^{p\,trial} + \Delta\overline{\varepsilon}^p)}$

Derivation of the consistent tangent operator

From the first row of Eq. 7.8 the following is obtained:

$$\left[\mathbb{I}+\Delta\overline{\varepsilon}^{p}\frac{1-D}{\|\mathbf{N}\|}\left(\mathbb{I}-\frac{1}{(\|\mathbf{N}\|)^{2}}\mathbf{N}\otimes\mathbf{N}\right):\frac{\partial\mathbf{N}}{\partial\boldsymbol{\sigma}}:\mathbb{D}^{e}\right]:\mathrm{d}\boldsymbol{\varepsilon}^{e}+\frac{\mathbf{N}}{\|\mathbf{N}\|}\mathrm{d}\Delta\overline{\varepsilon}^{p}=\mathrm{d}\boldsymbol{\varepsilon}^{e\,trial}. \quad (7.10)$$

The differential of stress can be obtained by using $\mathrm{d}\boldsymbol{\varepsilon}^{e}=\frac{1}{1-D}(\mathbb{D}^{e})^{-1}:\left(\mathrm{d}\boldsymbol{\sigma}-\frac{\partial\boldsymbol{\sigma}}{\partial\Delta\overline{\varepsilon}^{p}}\mathrm{d}\Delta\overline{\varepsilon}^{p}\right)$, as

$$\begin{aligned}&\left[\mathbb{I}+\Delta\overline{\varepsilon}^{p}\frac{1-D}{\|\mathbf{N}\|}\left(\mathbb{I}-\frac{1}{(\|\mathbf{N}\|)^{2}}\mathbf{N}\otimes\mathbf{N}\right):\frac{\partial\mathbf{N}}{\partial\boldsymbol{\sigma}}:\mathbb{D}^{e}\right]:\mathrm{d}\boldsymbol{\varepsilon}^{e}\\&=\left[\frac{1}{1-D}(\mathbb{D}^{e})^{-1}+\Delta\overline{\varepsilon}^{p}\frac{1}{\|\mathbf{N}\|}\left(\mathbb{I}-\frac{1}{(\|\mathbf{N}\|)^{2}}\mathbf{N}\otimes\mathbf{N}\right):\frac{\partial\mathbf{N}}{\partial\boldsymbol{\sigma}}\right]:\left(\mathrm{d}\boldsymbol{\sigma}-\frac{\partial\boldsymbol{\sigma}}{\partial\Delta\overline{\varepsilon}^{p}}\mathrm{d}\Delta\overline{\varepsilon}^{p}\right),\end{aligned} \quad (7.11)$$

which, when applied to Eq. 7.10, becomes

$$\begin{aligned}\mathrm{d}\boldsymbol{\sigma}&=\mathbb{P}:\left(\mathrm{d}\boldsymbol{\varepsilon}^{e\,trial}-\mathrm{d}\Delta\overline{\varepsilon}^{p}\frac{\mathbf{N}}{\|\mathbf{N}\|}\right)+\frac{\partial\boldsymbol{\sigma}}{\partial\Delta\overline{\varepsilon}^{p}}\mathrm{d}\Delta\overline{\varepsilon}^{p}\\&=\mathbb{P}:\mathrm{d}\boldsymbol{\varepsilon}^{e\,trial}+\left(\frac{\partial\boldsymbol{\sigma}}{\partial\Delta\overline{\varepsilon}^{p}}-\mathbb{P}:\frac{\mathbf{N}}{\|\mathbf{N}\|}\right)\mathrm{d}\Delta\overline{\varepsilon}^{p},\end{aligned} \quad (7.12)$$

where the fourth-order tensor $\mathbb{P}$ is defined as

$$\mathbb{P}=\left[\frac{1}{1-D}(\mathbb{D}^{e})^{-1}+\Delta\overline{\varepsilon}^{p}\frac{1}{\|\mathbf{N}\|}\left(\mathbb{I}-\frac{1}{(\|\mathbf{N}\|)^{2}}\mathbf{N}\otimes\mathbf{N}\right):\frac{\partial\mathbf{N}}{\partial\boldsymbol{\sigma}}\right]^{-1}. \quad (7.13)$$

From the second row of Eq. 7.8, the following is obtained:

$$\mathbf{N}:\mathrm{d}\boldsymbol{\sigma}+\left(\mathbf{N}:\frac{\partial\boldsymbol{\sigma}}{\partial D}D'-\overline{H}_{iso}\right)\mathrm{d}\Delta\overline{\varepsilon}^{p}=0. \quad (7.14)$$

By using Eqs. 7.12 and 7.14, we get to

$$\begin{aligned}&\mathbf{N}:\left[\mathbb{P}:\mathrm{d}\boldsymbol{\varepsilon}^{e\,trial}+\mathrm{d}\Delta\overline{\varepsilon}^{p}\left(-\mathbb{P}:\frac{\mathbf{N}}{\|\mathbf{N}\|}+\frac{\partial\boldsymbol{\sigma}}{\partial\Delta\overline{\varepsilon}^{p}}\right)\right]+\left(\mathbf{N}:\frac{\partial\boldsymbol{\sigma}}{\partial\Delta\overline{\varepsilon}^{p}}-\overline{H}_{iso}\right)\mathrm{d}\Delta\overline{\varepsilon}^{p}=0\\&\rightarrow\mathrm{d}\Delta\overline{\varepsilon}^{p}=\frac{\mathbf{N}:\mathbb{P}:\mathrm{d}\boldsymbol{\varepsilon}^{e\,trial}}{\mathbf{N}:\left(\mathbb{P}:\frac{\mathbf{N}}{\|\mathbf{N}\|}-2\frac{\partial\boldsymbol{\sigma}}{\partial\Delta\overline{\varepsilon}^{p}}\right)+\overline{H}_{iso}},\end{aligned} \quad (7.15)$$

which is then inserted into Eq. 7.12 to obtain

$$\mathrm{d}\boldsymbol{\sigma}=\mathbb{P}:\mathrm{d}\boldsymbol{\varepsilon}^{e\,trial}+\frac{\mathbf{N}:\mathbb{P}:\mathrm{d}\boldsymbol{\varepsilon}^{e\,trial}}{\mathbf{N}:\left(\mathbb{P}:\frac{\mathbf{N}}{\|\mathbf{N}\|}-2\frac{\partial\boldsymbol{\sigma}}{\partial\Delta\overline{\varepsilon}^{p}}\right)+\overline{H}_{iso}}\left(\frac{\partial\boldsymbol{\sigma}}{\partial\Delta\overline{\varepsilon}^{p}}-\mathbb{P}:\frac{\mathbf{N}}{\|\mathbf{N}\|}\right). \quad (7.16)$$

The final expression of the, generally unsymmetric, consistent elastoplastic tangent operator, $\mathbb{D}^{ep}$, is obtained by taking into account that $\mathbb{D}^{ep} = \frac{\partial \boldsymbol{\sigma}}{\partial \boldsymbol{\varepsilon}^{e\,trial}}$, as

$$\mathbb{D}^{ep} = \mathbb{P} + \frac{\left(\frac{\partial \boldsymbol{\sigma}}{\partial \Delta \bar{\varepsilon}^p} - \mathbb{P} : \frac{\mathbf{N}}{\|\mathbf{N}\|}\right) \otimes (\mathbf{N} : \mathbb{P})}{\mathbf{N} : \left(\mathbb{P} : \frac{\mathbf{N}}{\|\mathbf{N}\|} - 2\frac{\partial \boldsymbol{\sigma}}{\partial \Delta \bar{\varepsilon}^p}\right) + \overline{H}_{iso}}. \tag{7.17}$$

7.1.4 Computational methods

The set of load cases used in this Chapter was restricted to uniaxial cases, as shown in Table 7.3. The used boundary conditions were KUBC (Wang et al., 2009). As in previous chapters, the FE simulations were run on a Cray XC30 MPP supercomputer hosted by ARCHER, UK National Supercomputing Service, and run with an *in-house* finite strain elastoplasticity parallel implicit FE solver, developed within the framework of ParaFEM. Elastic homogenisation was performed at each time increment of the simulation, as described in Section 2.2.1 of Chapter 2 (van Rietbergen et al., 1996, 1995). This greatly increased the computation time needed for these simulations to finish, as in each time increment, six linear algebraic systems (elastic homogenisation) plus one per each global Newton-Raphson iteration are solved.

To enlarge the region of convergence of the Newton-CPPM scheme, the primal-CPPM scheme was used instead, as developed in Algorithm 2 in Chapter 3; however, this constitutive law does not follow the assumptions for global convergence as stated in Section 3.2.3 of Chapter 3, due to the presence of damage. Therefore, to ensure that a possible convergence fail of the local (integration point-based) CPPM scheme does not influence the results of the global FE simulation, whenever this happens, this information is broadcasted to all MPI processes in order to cut down the time increment to half of its value, and then the time increment is restarted.

7.1.5 Definition of the macroscopic strain points

As in previous chapters, the macroscopic yield points were assessed with the 0.2%, as described in Fig. 5.3 in Chapter 5. However, the slope used to asses these points was calculated from the damaged macroscopic stiffness tensor as described below.

The homogenised macroscopic stiffness tensor was calculated at every time increment and the damage variable at each integration point was used to reduce the solid phase stiffness tensor isotropically. Since the sample was already aligned according to the directions described by the MIL fabric tensor, the resulting elasticity tensor was assumed to be orthotropic and aligned with the MIL axes (Odgaard et al., 1997). Further

Table 7.3 Description of the performed uniaxial load cases.

Type of analysis	Description	Number
$\varepsilon_{11} > 0;\ \varepsilon_{22} = \varepsilon_{33} = 0$ $\varepsilon_{12} = \varepsilon_{13} = \varepsilon_{23} = 0$	Tensile normal	3
$\varepsilon_{22} > 0;\ \varepsilon_{11} = \varepsilon_{33} = 0$ $\varepsilon_{12} = \varepsilon_{13} = \varepsilon_{23} = 0$		
$\varepsilon_{33} > 0;\ \varepsilon_{11} = \varepsilon_{22} = 0$ $\varepsilon_{12} = \varepsilon_{13} = \varepsilon_{23} = 0$		
$\varepsilon_{11} < 0;\ \varepsilon_{22} = \varepsilon_{33} = 0$ $\varepsilon_{12} = \varepsilon_{13} = \varepsilon_{23} = 0$	Compressive normal	3
$\varepsilon_{22} < 0;\ \varepsilon_{11} = \varepsilon_{33} = 0$ $\varepsilon_{12} = \varepsilon_{13} = \varepsilon_{23} = 0$		
$\varepsilon_{33} < 0;\ \varepsilon_{11} = \varepsilon_{22} = 0$ $\varepsilon_{12} = \varepsilon_{13} = \varepsilon_{23} = 0$		
$\varepsilon_{11} = \varepsilon_{22} = \varepsilon_{33} = 0$ $\varepsilon_{12} \neq 0;\ \varepsilon_{13} = \varepsilon_{23} = 0$	Shear	3
$\varepsilon_{22} = \varepsilon_{11} = \varepsilon_{33} = 0$ $\varepsilon_{13} \neq 0;\ \varepsilon_{12} = \varepsilon_{23} = 0$		
$\varepsilon_{33} = \varepsilon_{11} = \varepsilon_{22} = 0$ $\varepsilon_{23} \neq 0;\ \varepsilon_{12} = \varepsilon_{13} = 0$		
	Total	9

macroscopic points were defined at 0.3%, 0.4% and 0.5% macroscopic strain norm by using the procedure described in Fig. 7.1.

The appropriate slope to define the macroscopic strain points is calculated for the corresponding load case at each time increment. Each of these strain points is calculated when the macroscopic strain norm immediately surpasses the corresponding value (0.2%, 0.3%, 0.4% or 0.5%), and then it is linearly interpolated by using the values of the homogenised stress and macroscopic strain norms of the current and previous time increments. An example is presented here for a uniaxial case in direction 1.

In the following, the homogeneous stress is the projection of the macroscopic elastic strain through the damaged macroscopic stiffness tensor; the first subscript denotes a label and the following subscripts denote indices of the tensor. In the case of superscripts, the first superscript denotes a label and the following superscripts denote powers. Consider application of a normal uniaxial strain in direction 1, the elastic

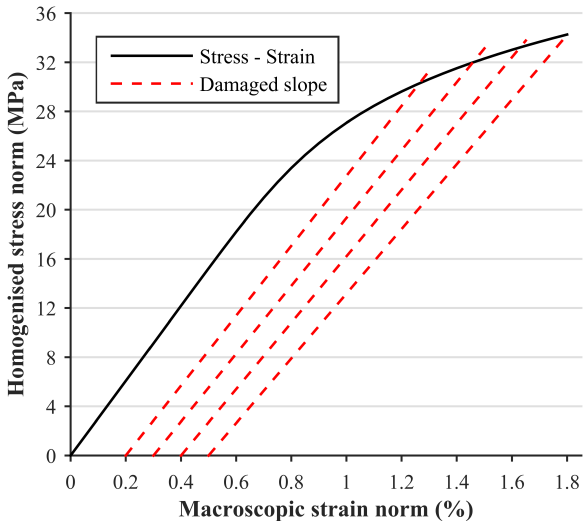

Fig. 7.1 Definition of the macroscopic strain points corresponding to macroscopic strain norms of 0.2%, 0.3%, 0.4% and 0.5% for the compression case in direction 1 of the densest sample (BV/TV=30.3%). The slope at 0.5% macroscopic strain norm is approximately 12% lower than the undamaged slope. The stress and strain used are the Second Piola-Kirchhoff stress tensor and Green-Lagrange strain tensor, respectively.

system can be then written in indicial notation as

$$\sigma_{0\,ij} = \mathbb{D}^{e}_{0\,dam\,ij11}\varepsilon^{e}_{0\,11}\,. \tag{7.18}$$

When the norm of the corresponding homogenised stress is calculated, the following expression can be derived by taking into account the orthotropy of the macroscopic stiffness tensor, such as

$$\|\mathbb{D}^{e}_{0\,dam\,ij11}\varepsilon^{e}_{0\,11}\| = \sqrt{\mathbb{D}^{e\,2}_{0\,dam\,1111}\varepsilon^{e\,2}_{0\,11} + \mathbb{D}^{e\,2}_{0\,dam\,2211}\varepsilon^{e\,2}_{0\,11} + \mathbb{D}^{e\,2}_{0\,dam\,3311}\varepsilon^{e\,2}_{0\,11}}\,, \tag{7.19}$$

and thus the damaged slope K_{dam} used to calculate the macroscopic yield points can be expressed as

$$K_{dam} = \sqrt{\mathbb{D}^{e\,2}_{0\,dam\,1111} + \mathbb{D}^{e\,2}_{0\,dam\,2211} + \mathbb{D}^{e\,2}_{0\,dam\,3311}}\,. \tag{7.20}$$

7.1.6 Young's moduli - density power relationship

In order to check whether the macroscopic orthotropic Young's moduli (E_{11}, E_{22} and E_{33}) may be estimated from BV/TV alone, the macroscopic on-axis Young's moduli was estimated by using a power relationship (Hernandez et al., 2001; Morgan et al., 2003; Yang et al., 1998).

A Young's modulus−ash density power relationship which takes into account the solid phase elastic modulus (Morgan et al., 2003; Yang et al., 1998) was used to estimate the apparent on-axis modulus. This allows for comparison with the orthotropic elastic moduli calculated through elastic homogenisation. This power law reads as

$$E_0 = 1240 E_\mu BV/TV^{1.8}. \tag{7.21}$$

7.2 Results

7.2.1 Macroscopic damage

The damaged orthotropic stiffness components (E_{11}, E_{22}, E_{33}, G_{12}, G_{13} and G_{23}) are obtained from the damaged macroscopic stiffness tensor. These are then normalised by dividing them by the corresponding undamaged orthotropic stiffness and plotted for every sample and for every considered load case (Fig. 7.2).

Figure 7.2 shows that in spite of isotropic damage being assumed at the solid phase level, its effect on the macroscopic level is not isotropic. It can be seen that while all stiffness components reduce in all load cases, the stiffness component corresponding to the load case the sample is subjected to reduces the most. It is also interesting to note that in the case of a uniaxial normal load case, the shear stiffness components corresponding to the shear planes containing the loaded normal component reduce more than the remaining shear component (e.g. if the normal case is in direction 1, G_{12} and G_{13} reduce more than G_{23}).

Stiffness reductions for each of the considered load cases were related to density, corresponding initial orthotropic stiffness and macroscopic strain norm through multilinear regressions. Note that macroscopic strain norm could act as the plastic internal variable defining post-yield evolution. Only relationships with respect to macroscopic strain norms were found to be significant ($p < 0.05$). Therefore, these multilinear regressions were re-evaluated as linear regressions, only with respect to macroscopic strain norms. The coefficients of determination R^2, the intercepts and the slopes of these fits are shown in Table 7.4. Figure 7.3 illustrates these fits along with the actual data points. It can be seen from this figure that damage development under uniaxial tension and uniaxial compression can be reasonably well predicted by a linear relationship with respect to the macroscopic strain norm, but not so well for shear, as the coefficients of determination suggest. It is also important to point out that for the considered range of plastic strains, damage development can be reasonably well approximated with a line although the relationship between damage and accumulated plastic strain at the solid phase is exponential (Eq. 7.1).

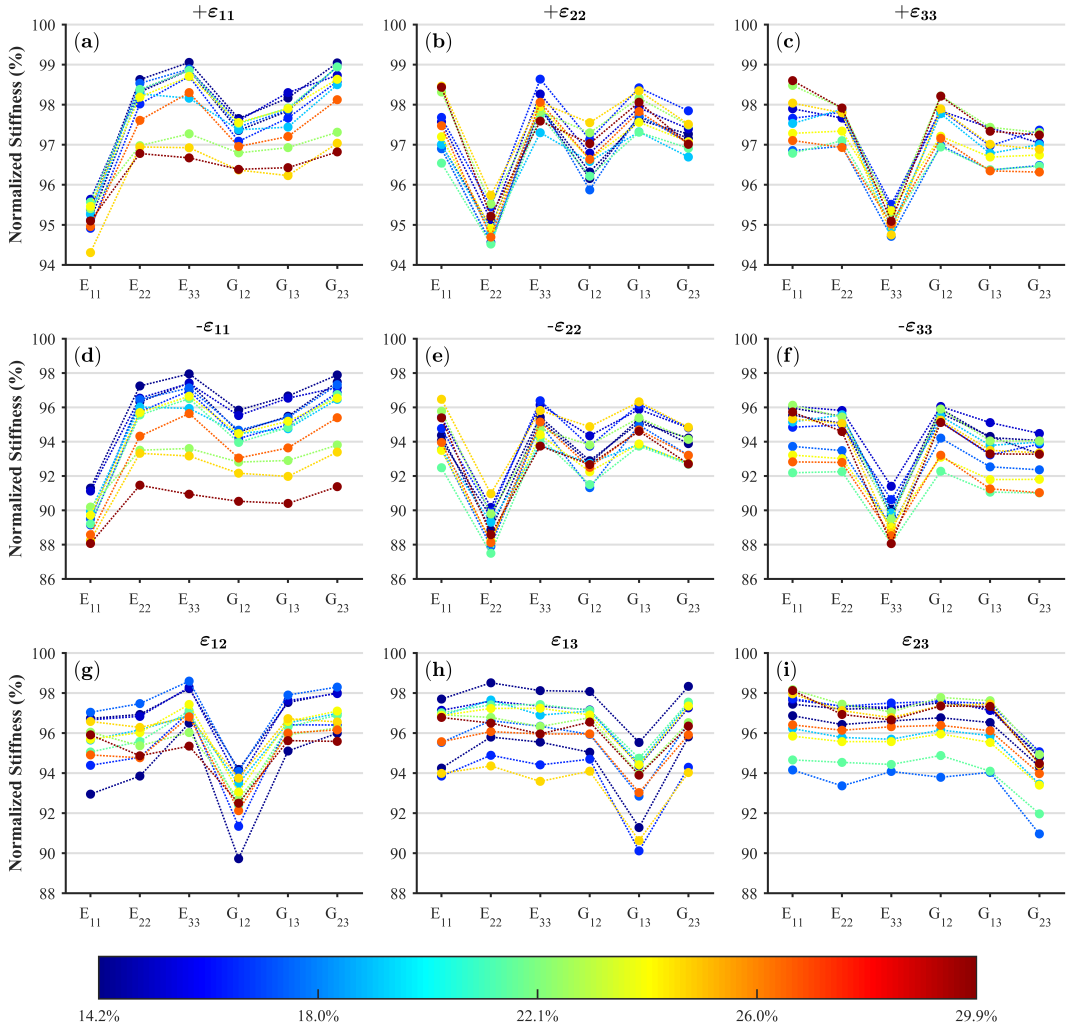

Fig. 7.2 Normalised orthotropic stiffness components for all the samples, and for all the considered load cases: tensile loading in direction 1(a), 2(b) and 3(c) (row 1 of Table 7.3); compressive loading in direction 1(d), 2(e) and 3(f) (row 2 of Table 7.3); and shear loading in plane 1-2(g), 1-3(h), 2-3(i) (row 3 of Table 7.3). The colour coding is on the basis of density and is used as a labelling mechanism. A macroscopic strain norm of 0.5% has been considered here.

Table 7.4 Values of the coefficients of determination R^2, intercepts and slopes for the linear fits between damage and macroscopic strain norm, for all the considered load cases.

Load case	$+\varepsilon_{11}$	$+\varepsilon_{22}$	$+\varepsilon_{33}$	$-\varepsilon_{11}$	$-\varepsilon_{22}$	$-\varepsilon_{33}$	ε_{12}	ε_{13}	ε_{23}
R^2	0.92	0.91	0.95	0.87	0.84	0.85	0.57	0.37	0.60
Intercept (%)	0.66	0.66	0.52	1.96	2.37	1.89	1.22	1.45	0.64
Slope (%)	833	874	880	1718	1727	1758	1211	1062	1102

Figure 7.4 shows the stiffness reduction for the most porous and densest samples, for the load case in which tensile strains are applied in direction 1, for all the considered

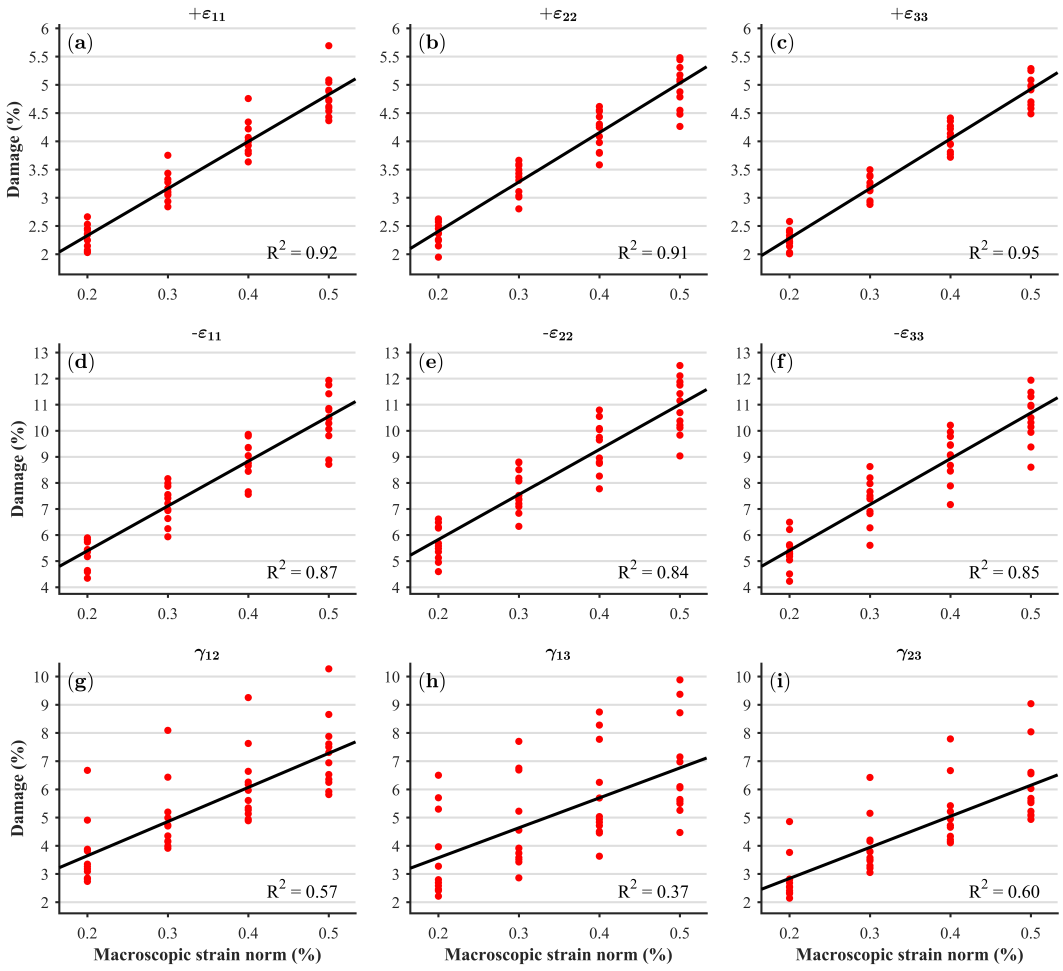

Fig. 7.3 Linear fits between damage and macroscopic strain norm, and the corresponding data points, for each of the considered load cases.

macroscopic strain norm levels. As expected, the decrease in stiffness increases with increasing strain norm. In the case of isotropic damage, it would be expected that all orthotropic stiffness components were equally affected. Notwithstanding, this is not the case; for example, for a tensile case in direction 1, E_{11} is more reduced than the rest, and this effect is different for the two samples compared in Fig. 7.4. In the denser sample, the difference in stiffness reduction between the stiffness component corresponding to the load case the sample is subjected to and the others is smaller than for the porous sample. Therefore, linear regressions between density and the difference between the stiffness reduction in the component corresponding to the load case the sample is subjected to and the average of the rest of the stiffness components were considered. However, poor statistical significance was found ($p > 0.05$), indicating that this was not a general trend.

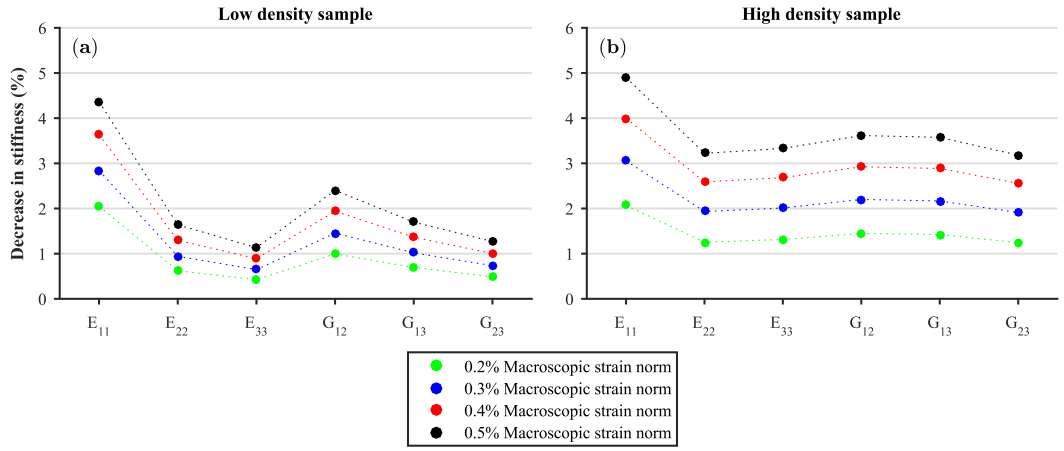

Fig. 7.4 Decrease in stiffness components for the most porous (BV/TV=14.8%) and densest (BV/TV=30.3%) samples due to tensile loading in direction 1, and for all the considered macroscopic strain norm levels.

7.2.2 Macroscopic hardening

Macroscopic yield stresses have been related to fabric and density in previous studies; however, relationships between macroscopic yield strains and these microarchitectural indices are not so clear (Panyasantisuk et al., 2015b; Wolfram et al., 2012). Also, as previously stated, the orthotropic stiffness components have been related to these microarchitectural indices (Odgaard et al., 1997; Zysset, 2003). Therefore, inclusion of orthotropic stiffness in the regression for the macroscopic yield stresses was considered. Macroscopic yield stress norms were related to the corresponding initial orthotropic stiffness and the macroscopic strain norms through multilinear regressions. These fits and the corresponding data points are shown in Fig. 7.5. It can be seen that higher yield stress results from higher initial stiffness and higher macroscopic strain norm, as expected. The coefficients of determination R^2 and slopes of these fits are shown in Tables 7.5 and 7.6. All of these fits were found to be statistically significant ($p < 0.05$).

Table 7.5 Values of the coefficient of determination R^2 and slopes for the linear fits between macroscopic yield stress norm, corresponding initial stiffness and macroscopic strain norm, for all the considered normal load cases. The first slope is with respect to the initial stiffness and the second slope is with respect to the macroscopic strain norm.

Load case	$+\varepsilon_{11}$	$+\varepsilon_{22}$	$+\varepsilon_{33}$	$-\varepsilon_{11}$	$-\varepsilon_{22}$	$-\varepsilon_{33}$
R^2	0.98	0.94	0.89	0.97	0.91	0.81
Slope ($\cdot 10E-3$)	3.73	5.19	3.40	11.31	17.44	10.83
Slope (MPa)	121.9	135.5	175.7	649.0	679.5	687.4

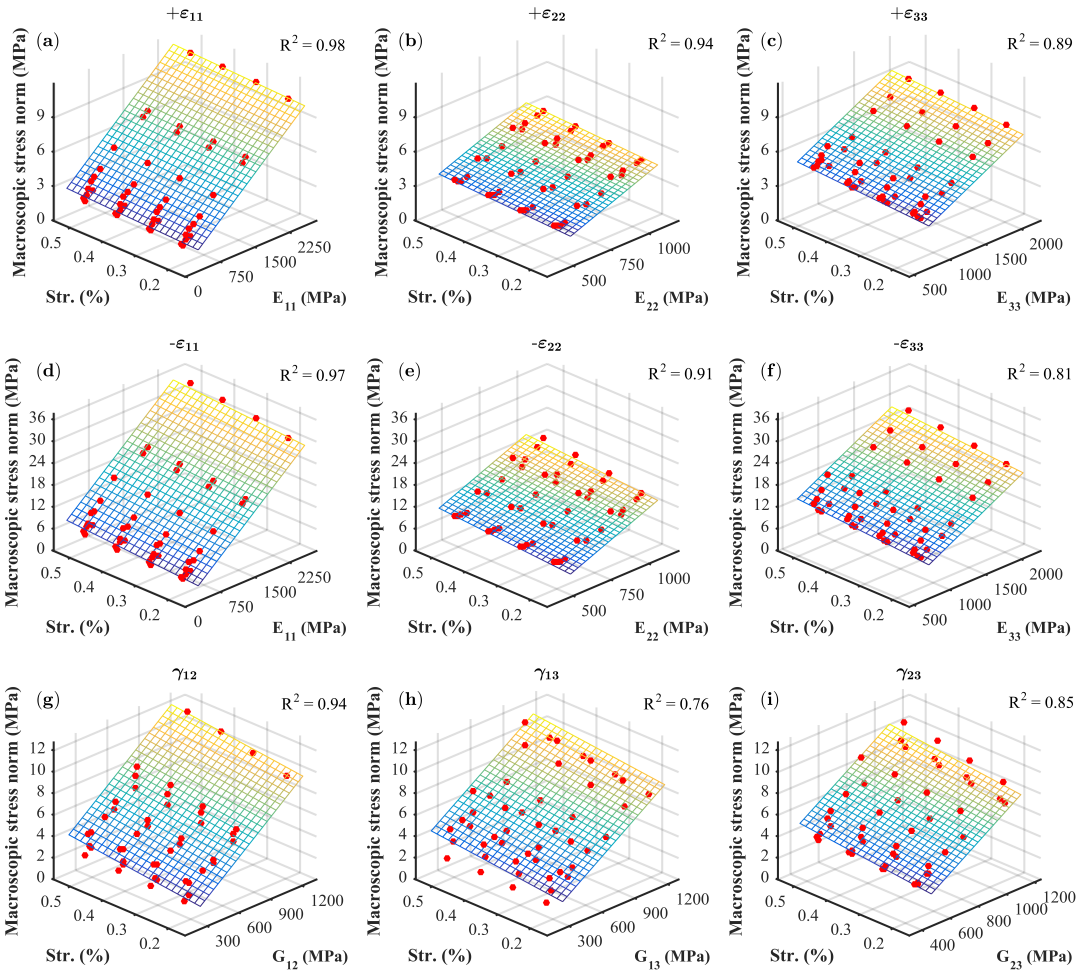

Fig. 7.5 Macroscopic yield stress norms for all the considered samples, for all the considered macroscopic strain norm levels, and for all the considered load cases. Str. stands for macroscopic strain norm.

Table 7.6 Values of the coefficient of determination R^2 and slopes for the linear fits between macroscopic yield stress norm, corresponding initial stiffness and macroscopic strain norm, for all the considered shear load cases. The first slope is with respect to the initial stiffness and the second slope is with respect to the macroscopic strain norm.

Load case	ε_{12}	ε_{13}	ε_{23}
R^2	0.94	0.76	0.85
Slope ($\cdot 10E-3$)	8.29	7.34	8.94
Slope (MPa)	362.6	344.1	339.2

Macroscopic yield strain norms were related to the macroscopic strain norms through linear regressions. These fits and the corresponding data points are shown in Fig. 7.6.

The coefficients of determination R^2 and slopes of these fits are provided in Table 7.7. All of these fits were found to be statistically significant ($p < 0.05$).

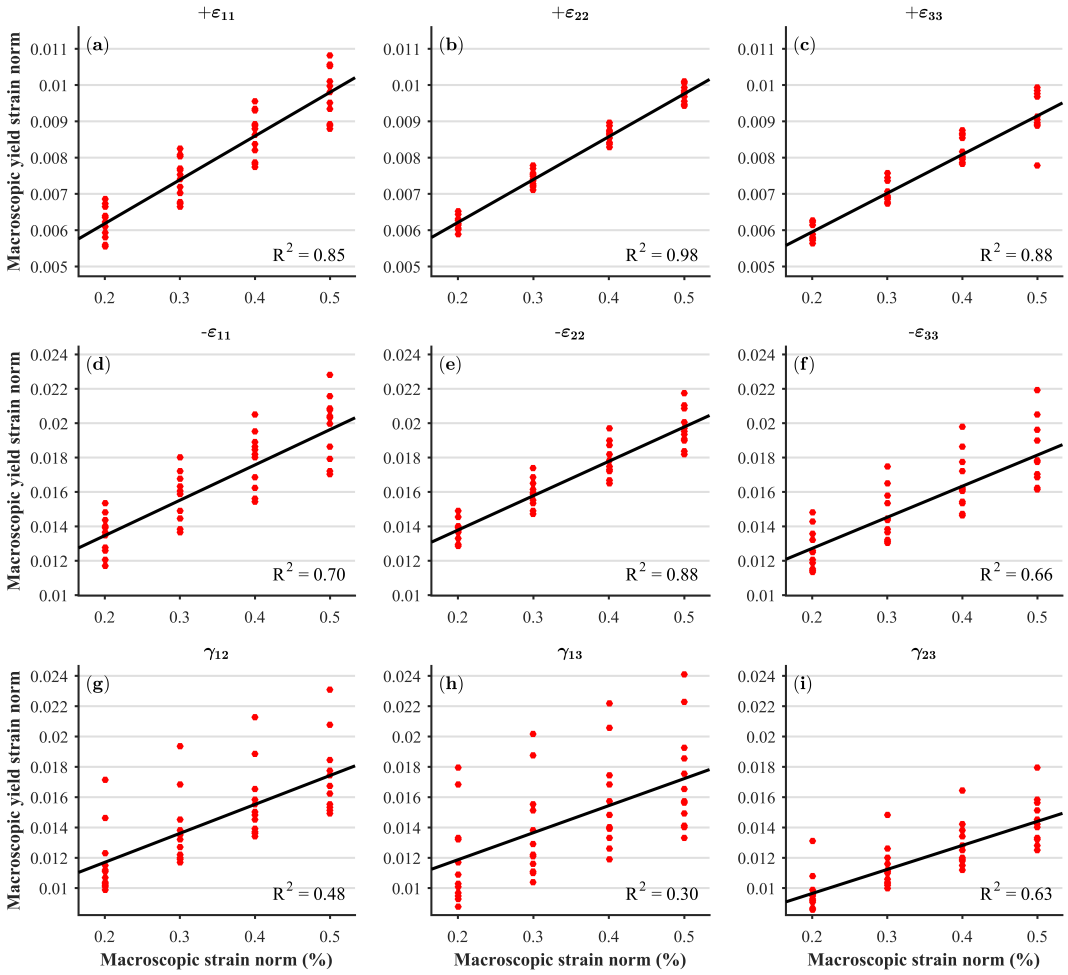

Fig. 7.6 Macroscopic yield strain norms for all the considered macroscopic strain norm levels, for all the considered samples, and for all the considered load cases.

Table 7.7 Values of the coefficient of determination R^2 and slopes for the linear fits between macroscopic yield strain norm and macroscopic strain norm, for all the considered load cases.

Load case	$+\varepsilon_{11}$	$+\varepsilon_{22}$	$+\varepsilon_{33}$	$-\varepsilon_{11}$	$-\varepsilon_{22}$	$-\varepsilon_{33}$	ε_{12}	ε_{13}	ε_{23}
R^2	0.85	0.98	0.88	0.70	0.88	0.66	0.48	0.30	0.63
Slope	1.21	1.18	1.07	2.06	2.00	1.81	1.91	1.79	1.59

7.2.3 Power law relationships

Power relationships between the on-axis elastic modulus of trabecular bone and its ash density have been thoroughly researched in previous studies (Hernandez et al., 2001;

Morgan et al., 2003; Schileo et al., 2007). One of the relevant power law relationships, since it takes into account tissue elastic modulus (Yang et al., 1998), was used to estimate the macroscopic on-axis Young's modulus of the trabecular bone specimens. These estimated values were then compared to the orthotropic Young's moduli obtained from the undamaged macroscopic stiffness tensor from the elastic homogenisation scheme performed at the beginning of the corresponding μFE simulation. The Young's moduli estimates obtained through Eq. 7.21 and the orthotropic Young's moduli obtained through elastic homogenisation are shown in Table 7.8.

Table 7.8 Power law-estimated on-axis Young's modulus (E_0), and orthotropic Young's moduli obtained through elastic homogenisation (E_{11}, E_{22} and E_{33}).

Number of specimen	E_0 (MPa)	E_{11} (MPa)	E_{22} (MPa)	E_{33} (MPa)
1	1,791	2,580	1,058	895
2	1,262	1,656	816	792
3	689	1,249	692	347
4	470	779	482	272
5	537	919	502	461
6	472	822	557	297
7	628	1,125	521	367
8	995	1,542	941	429
9	1,198	1,771	1,024	650
10	805	922	709	512
11	1,069	1,585	743	630
12	1,413	2,025	946	860

As it can be observed in Table 7.8, power law-estimated Young's modulus are generally lower than the largest orthotropic Young's modulus obtained through elastic homogenisation.

7.3 Discussion

The damage behaviour of trabecular bone at the macroscale has been assessed in some previous studies for relatively simple load scenarios (Garcia et al., 2009; Sun et al., 2010; Zioupos et al., 2008). Damage at the microscopic level has also been previously considered (Gupta et al., 2006). This study aims to bridge both scales by investigating the damage behaviour of trabecular bone at the macroscale through a homogenisation-based multiscale approach and the use of multiple uniaxial load cases for trabecular bone samples with very detailed geometry. Twelve μFE meshes of samples covering a wide range of BV/TV and nine uniaxial load cases per sample were investigated, with plasticity and damage included at the solid phase level.

The constitutive behaviour of the solid phase, including its damage behaviour, was considered to be isotropic. In this study, isotropic damage at the microscale was considered, which results in an anisotropic macroscale damage response, which depends on the loading scenario (Fig. 7.2). This means that the orthotropic stiffness component related to the load case the sample is subjected to is more reduced than the rest of components. It is also interesting to note that uniaxial compressive or tensile loading results in damage not only in the direction of loading but also in other normal and shear directions (Fig. 7.2). As an example, if a sample is subjected to tensile loading in direction 1, E_{11} is more affected than E_{22} and E_{33}; with respect to the shear components, G_{12} and G_{13} are more affected than G_{23}. Some previous studies which have modelled damage at the macroscale have assumed an isotropic behaviour (Garcia et al., 2009; Schwiedrzik and Zysset, 2013), which may be an acceptable assumption for proportional loading, but not for changing loads, as would be expected during physiological activities.

Damage can be linearly related to the macroscopic strain norm with high coefficients of determination ($R^2 > 0.84$), except for shear cases ($R^2 < 0.60$) (Fig. 7.3). These results also suggest that the evolution of damage at the macroscale is linear in the range of considered macroscopic strains. Beyond these strain levels other effects, such as cracking and fracture of trabeculae, can lead to structural failure and softening if further loading is applied (Hosseini et al., 2014; Kopperdahl and Keaveny, 1998). These were not considered in this study since it is expected that the relatively low levels of applied macroscopic strain will not trigger these effects.

The values of the slopes of the linear fits are shown in Table 7.4; their values show that damage propagation increases differently for uniaxial tension and compression load cases, with the value for compression cases being around twice the value for tension. This may be due to the fact that under compression, heterogeneous stress distributions occur that include tensile stresses at the solid phase level due to bending and buckling of trabeculae (Bevill et al., 2006; Stölken and Kinney, 2003). Additionally, damage and plasticity in compression are far more diffused than in tension, where they are more localised (Lambers et al., 2014). This leads to larger volumes of bone yielding (and thus being damaged as well) throughout the compression process when compared to tension. This is captured by the homogenisation procedure and expressed as a higher slope for the damage progression during compression. Cracks are more localised and propagate faster in tension than in compression, eventually leading to catastrophic fracture of individual trabeculae. Moreover, it is also likely that cracks under compression exhibit some partial closure since bone is a quasi-brittle material, leading to reduced effects of

damage on the stiffness. Nonetheless, both these effects (fracture and crack closure) have not been included in the solid phase constitutive model.

If individual samples are considered, it can be seen that damage evolves with increasing macroscopic strain norm, and that the low density sample has a considerable difference in damage between the stiffness component corresponding to the load case the sample is subjected to and the rest of stiffness components, an effect which is not observed in the high density sample (Fig. 7.4). However, the expectation that high density, more continuum-like, trabecular bone samples would partially upscale the isotropic damage behaviour of the solid phase was not supported by the statistical analysis as density was not found to be a good predictor of this. Perhaps, more samples with a wider range of densities and microarchitectures could lead to morphological indices being related to damage.

Several previous studies performing nonlinear homogenisation used the 0.2% strain rule to determine the macroscopic yield of trabecular bone (Panyasantisuk et al., 2015b; Wolfram et al., 2012). However, this study shows that if damage is included, it results in a stiffness reduction when the macroscopic strain norm reaches a value of 0.2% (Table 7.4), which is the value considered as macroscopic yield. This implies that a modified elasticity tensor may need to be used once macroscopic yield is reached. This can be done by considering a damaged slope obtained by joining the origin and the yield stress at 0.2% macroscopic strain norm. Previous studies have employed this method with an isotropic reduction of the elastic stiffness (Wolfram et al., 2012), however, this study shows that the macroscopic damage is not isotropic.

With respect to the hardening of trabecular bone at the macroscale, the fits show that yield points described in both stress and strain spaces show linear hardening for this range of macroscopic plastic strains. However, as for damage propagation, the slopes are found to be different for different load cases (Tables 7.5, 7.6 and 7.7); hardening in compression, tension and shear are considerably different. Hardening in compression is considerably larger than for the rest of the cases, which is likely to be due to the fact that Drucker-Prager is used as the solid phase yield criterion, implying that the lack of hydrostatic compression yield may be partially upscaled to the macroscale, resulting in an increased evolution of the stress norm throughout the compression loading process. Although most models of trabecular bone at the macroscale use nonlinear hardening laws (Garcia et al., 2009; Schwiedrzik and Zysset, 2013), the results of this study show a hardening which depends on the considered load case (i.e. tension, compression or shear), and a linear relationship between the macroscopic yield stress/strain norms and the macroscopic strain norm. However, in this study the considered range of plastic strains is small and hardening may become nonlinear if further loading is applied.

When the macroscopic strain norm was assessed, the orthotropic assumption for the macroscopic elastic stiffness was used. The macroscopic strain is readily available since it is directly applied through the considered boundary conditions. Nonetheless, in some shear load cases the homogenised stress presents some non-zero normal components (here non-zero means that a normal stress component is, at most, one order of magnitude lower than the corresponding shear component of the stress tensor). This implies that even for these highly aligned samples, in-plane trabeculae experience normal stresses during macroscopic shear. It was shown by Sanyal et al. (2012) that macroscopic shear load cases are dominated by tensile solid phase stresses in trabeculae which are aligned 45°from the shear in-plane axes. The homogenisation procedure is likely to have captured these tensile stresses when assessing the homogenised stress of the considered VEs. This suggests that at the macroscopic level the normal and shear behaviours do have some interaction, which may outline a possible limit of the orthotropic macroscopic elastic assumption for trabecular bone.

Macroscopic on-axis Young's modulus and macroscopic ash density power relationships have been thoroughly studied in the past (Hernandez et al., 2001; Morgan et al., 2003; Schileo et al., 2007). These estimated values were compared to the orthotropic Young's moduli obtained through elastic homogenisation, and the former were found to be lower, approximately half to three quarters of the values obtained computationally, and are always within the range established by the lowest to largest macroscopic orthotropic Young's moduli. Panyasantisuk et al. (2015a) found that the macroscopic orthotropic components of trabecular bone with KUBCs in elastic homogenisation may lead up to mean errors of 55% in comparison with the components obtained with periodicity-compatible mixed uniform boundary conditions[1], for samples of BV/TV between 11.6% and 20.4%; there is a tendency of decreasing error with increasing BV/TV, up to errors of 19.58% for samples of BV/TV between 32.8% and 40.0%. The overestimation of macroscopic properties due to the use of KUBCs could indeed suffice to explain the differences in the estimated Young's modulus and those obtained from elastic homogenisation (Table 7.8).

This study has a number of limitations. Damage behaviour of bone at the tissue level has been researched in some previous studies (Schwiedrzik and Zysset, 2013, 2015), but the maximum damage value is not known (Schwiedrzik and Zysset, 2015), so it was treated as 90% reduction of the initial stiffness as an approximation and to avoid numerical difficulties related to the complete loss of stress carrying capacity in some part of the model; more research on the damage behaviour at the solid phase is

[1]These boundary conditions yield similar results to PBCs for 5 mm cubes, as mentioned in Pahr and Zysset (2008).

needed. The effect of different maximum damage thresholds at the solid phase level was also checked (including 100% maximum reduction) for one sample and found that the non-isotropic trend in macroscopic damage is maintained and that the difference of macroscopic damage values is relatively small between 90% and 100% maximum reduction. There is plenty of experimental data on uniaxial load cases in literature (Bayraktar and Keaveny, 2004; Keaveny et al., 1997; Manda et al., 2016; Sanyal et al., 2012), but reproducing the uniaxial cases performed in this study is difficult because of the considered boundary conditions. Therefore, validation was performed by comparing macroscopic yield strains to data from similar studies. As in several previous studies (Panyasantisuk et al., 2015b; Wolfram et al., 2012), in this study the solid phase was assumed to be homogeneous. It has previously been shown that trabecular bone tissue has, however, heterogeneous TMD, and thus heterogeneous properties (Blanchard et al., 2013; Renders et al., 2008). Notwithstanding, the effects of these heterogeneities in models with geometrical nonlinearities is still unknown and further research is needed to establish comparisons. For the sake of simplicity, and to be able to compare these results with published data, the solid phase properties were kept as homogeneous. The solid phase was modelled as a damage-plastic material without fracture, which is perhaps appropriate for the level of strains applied; larger strains are likely to cause fracture, an effect which has been neglected in this study. It has been previously shown that ductile solid phase behaviour overestimates the experimental yield properties, especially at low BV/TV (Nawathe et al., 2013). Only uniaxial load cases for a relatively small number of samples were evaluated. In order to describe the full multiaxial behaviour of trabecular bone, more load cases are needed, which remains as future work. However, the computational cost of performing a complete nonlinear simulation with the high resolution used in this study and with damage, plasticity, and an elastic homogenisation at each time increment is very high. It is also important to point out that as damage grows, the stiffness matrix becomes increasingly unsymmetric, which decreases the convergence rate of the used iterative linear algebraic solver (PCG), as this method is only efficient at solving positive-definite linear algebraic systems.

Chapter 8

Conclusions and future work

This study evaluated the macroscopic mechanical behaviour of trabecular bone by means of homogenisation-based multiscale techniques and large scale FE analyses. The macroscopic yield surface of trabecular bone was thoroughly evaluated: the effect of varying yield surfaces at the solid phase level on the macroscopic behaviour was assessed and closed-form expressions of yield surfaces were fitted to the macroscopic yield strains obtained through the μFE simulations. The post-yield macroscopic behaviour was also studied by studying the macroscopic hardening and damage progression, which were both assessed by including damage at the solid phase level and then upscaling its effect to the macroscale.

It is expected that the knowledge of the macroscopic behaviour of trabecular bone gained in this study helps in creating more precise continuum FE models of whole bones to be able to more accurately predict bone failure and/or implant stability. This work is also likely to lead to improved diagnosis of bone quality.

8.1 Conclusions

8.1.1 High-performance computing and nonlinear modelling

The developed driver program was created in order to be able to run large μFE simulations of the nonlinear mechanical behaviour of trabecular bone, which was not possible with the use of commercial packages.

The driver program was successfully incorporated into the parallel layer of ParaFEM, and was found to maintain the high performance and scalability when used in large HPC platforms, such as ARCHER, BlueGene/Q or Eddie. With this driver program, finite strain elastoplasticity (i.e. geometrical and material nonlinearities) were implemented and they were found to be robust and give meaningful results. These results were

compared with the commercial package ABAQUS for the same problems and were found to compare very well, within numerical tolerance of the used iterative methods (iterative linear algebraic solvers were used in ParaFEM, whereas direct solvers were used in ABAQUS; furthermore, the convergence criteria of the Newton-Raphson scheme might have been slightly different).

8.1.2 Effect of the solid phase constitutive law on the macroscopic behaviour

The study examined how yield at the macroscale is influenced by the yield criterion employed for the tissue, or solid phase. The main difference between the two solid phase yield criteria was the presence of compressive hydrostatic yielding, present in one of them. Homogenisation-based multiscale techniques were then used to assess the macroscopic yield strains for the two sets of yield properties and for three samples with very different morphology.

It can be hypothesised that for a porous material like trabecular bone, yielding is likely to be due to yielding of individual trabeculae as beams and struts. Consequently, if the uniaxial tension and compression yield limits are properly set, the choice of yield criterion should not make a large difference.

It was found that this hypothesis holds for porous samples but not for dense samples, especially in compression-dominated load cases. In porous samples, buckling-related effects reduce the strength in compression-dominated load cases and the solid phase is less likely to experience hydrostatic compression. On the other hand, when a Drucker-Prager yield surface is used, the denser, more continuum-like, sample suffers from an overall stress/strain distribution which is closer to a hydrostatic compression. Therefore, the choice of the solid phase yield criterion influences the macroscopic yield of denser samples, particularly in compression-dominated load cases.

8.1.3 Macroscopic yield behaviour using nonlinear homogenisation

Nonlinear homogenisation-based multiscale techniques have been previously used to assess the macroscopic yield surface of trabecular before, but have been limited to either simple constitutive models, or to few load cases. A comprehensive analysis was performed, in which a broad range of load scenarios (160 load cases) was used. Closed-form expressions of quadric yield surfaces of different symmetries (isotropic, orthotropic and anisotropic) were fitted to the set of obtained macroscopic yield strains.

It was found that trabecular bone is reasonably well approximated by an isotropic yield behaviour in strain space, as has been previously reported. The study also shows

that the macroscopic yield strains are largely independent of BV/TV. Evaluation of clockwise and counter-clockwise shear as separate load cases, however, showed for the first time that the shear behaviour in trabecular bone presents some asymmetry even for highly aligned samples, possibly indicating anisotropy higher than orthotropy. However, formulating a non-isotropic yield surface in strain space is difficult due to the weak relationships between fabric and yield strains. The differences in fitting errors between isotropic, orthotropic, and anisotropic assumptions are small. Therefore, an isotropic criterion still presents itself as the most suitable approximation. Nonetheless, for shear and normal-shear load cases, considerable differences between the yield criterion and the actual macroscopic yield strain may arise.

With respect to the yield surface, an eccentric-ellipsoid may adequately represent the macroscopic yield surface of trabecular bone as the fitting errors for all the considered symmetries are reasonably small (from ~8% to ~11%). However, it is important to keep in mind the asymmetry in shear yield strains and that in the normal-shear load cases, the quadric may not be able to represent the macroscopic yield behaviour of trabecular bone well because of the presence of cellular solid behaviour.

8.1.4 Post-yield macroscopic behaviour

Homogenisation-based multiscale techniques were used to study the macroscopic post-elastic behaviour of trabecular bone. Macroscopic damage evolution and hardening were examined by using nine uniaxial load cases for a small range of macroscopic plastic strains.

It was found that macroscopic damage in trabecular bone is non-isotropic and can be linearly related to the macroscopic plastic strain norm with high coefficients of determination, except for shear where the coefficients of determination are smaller. It was also observed that damage in compression evolves faster than in tension, which is likely to be related to the heterogeneity in the solid phase stress distribution under compressive loading. The largest reduction in stiffness is in the component corresponding to the load case the sample is being subjected to. The shear stiffness in shear planes containing the normal direction of the load case the sample is subjected to is also slightly more reduced than the rest of normal stiffness components and remaining shear components.

Macroscopic hardening was also found to be non-isotropic, with macroscopic yield strains found to be linearly related to the macroscopic strain norm with high coefficients of determination. Macroscopic yield stresses are multilinearly related to undamaged orthotropic stiffness and macroscopic strain norm with high coefficients of determination as well. Both the macroscopic yield strains and stresses were found to have smaller coefficients of determination for the shear load cases. It was also observed

that hardening in compression is greater than in tension, which is likely to be related to the lack of compressive hydrostatic yielding in the solid phase yield criterion.

8.2 Future work

Solid phase properties have been considered as homogeneous throughout this study, which could be seen as a potential limitation, but it allows for comparison with existing results in the literature. A possible study which ParaFEM would allow is the study of the effect of TMD heterogeneities at the solid phase on the macroscopic behaviour of trabecular bone in the finite strain regime. TMD heterogeneities are likely to cause strain concentrations in locations where the TMD, and thus the stiffness, is lower. These strain concentrations may cause differences in macroscopic yield values when compared to the case with homogeneous solid phase. A straightforward difficulty and possible limitation is how solid phase yield limits are implemented in such a case – are they properly scaled with the heterogeneous TMD, or are they kept homogeneous (and thus independent of TMD)?

Another important consideration is to further study the sensitivity of macroscopic yield to the solid phase yield criteria. Additional solid phase yield surfaces should be studied, with a special emphasis on the asymmetric criterion in principal strain space (an eccentric cube). This criterion has been widely used in μFE-related literature in the previous 15 years, and it would allow to establish whether μFE simulations require a very precise yield criterion for the solid phase or if only a proper asymmetric yield criterion with uniaxial yield values within an appropriate range is needed.

A limitation which is constantly mentioned in literature is whether the use of ductile plasticity at the solid phase level is appropriate for a material which is actually quasi-brittle. A thorough comparison of fully ductile material models and models where damage and eventually fracture are incorporated should be performed to fully assess the sensitivity of the macroscopic results to these phenomena. Nonetheless, damage and fracture could lead to strain localisations, which may result in mesh-sensitivity of the results, and since these are issues that have not been properly resolved yet, this remains as distant future work. Additionally, these phenomena could also lead to eventual structural softening, which means that a Newton-Raphson scheme for the global FE system will stop working at some point due to structural failure. In this case, an arc-length scheme could be used instead, which would allow for tracking of post-buckling solutions.

This study has provided useful information about the nonlinear behaviour of trabecular bone, including its plastic and damage behaviour. However, all this information

needs to be gathered together and translated into a FE implementation of a macroscopic constitutive law for trabecular bone. This constitutive law should include an appropriate yield envelope, which could be described by an isotropic quadric in strain space, appropriate hardening and damage evolution laws, and an orthotropic elastic stiffness tensor. The evolution of the yield surface would be linear with respect to the macroscopic plastic strain and it would depend on what load case is being considered, i.e. tension, compression or shear. The damage evolution would also be linear with respect to the macroscopic plastic strain, non-isotropic, and it would also be different depending on the considered load case. It is also important to mention that the load case affects differently the on and off-axis stiffness components. This constitutive law should then be tested in an organ-level continuum FE simulation and compared with experimental results to assess its validity.

References

Ammann, P. and Rizzoli, R. (2003). Bone strength and its determinants. *Osteoporosis International*, 14 Suppl 3:S13–8.

Argyris, J., Doltsinis, J., and Kleiber, M. (1978). Incremental formulation in nonlinear mechanics and large strain elasto-plasticity - Natural approach. Part II. *Computer Methods in Applied Mechanics and Engineering*, 14(2):259–294.

Argyris, J. and Kleiber, M. (1977). Incremental formulation in nonlinear mechanics and large strain elasto-plasticity - Natural approach. Part 1. *Computer Methods in Applied Mechanics and Engineering*, 11(2):215–247.

Armero, F. and Pérez-Foguet, A. (2002). On the formulation of closest-point projection algorithms in elastoplasticity - part I: The variational structure. *International Journal for Numerical Methods in Engineering*, 53(2):297–329.

Arramon, Y. P., Mehrabadi, M. M., Martin, D. W., and Cowin, S. C. (2000). A multidimensional anisotropic strength criterion based on Kelvin modes. *International Journal of Solids and Structures*, 37(21):2915–2935.

Ashman, R. B., Rho, J. Y., and Turner, C. H. (1989). Anatomical variation of orthotropic elastic moduli of the proximal human tibia. *Journal of Biomechanics*, 22(8-9):895–900.

Atluri, S. N. (1984). On constitutive relations at finite strain: Hypo-elasticity and elasto-plasticity with isotropic or kinematic hardening. *Computer Methods in Applied Mechanics and Engineering*, 43(2):137–171.

Au, A. G., Liggins, A. B., Raso, V. J., and Amirfazli, A. (2005). A parametric analysis of fixation post shape in tibial knee prostheses. *Medical Engineering & Physics*, 27(2):123–34.

Balay, S., Abhyankar, S., Adams, M. F., Brown, J., Brune, P., Buschelman, K., Dalcin, L., Eijkhout, V., Gropp, W. D., Kaushik, D., Knepley, M. G., McInnes, L. C., Rupp, K., Smith, B. F., Zampini, S., Zhang, H., and Zhang, H. (2016). PETSc Web page. http://www.mcs.anl.gov/petsc.

Baumann, A. P., Shi, X., Roeder, R. K., and Niebur, G. L. (2016). The sensitivity of nonlinear computational models of trabecular bone to tissue level constitutive model. *Computer Methods in Biomechanics and Biomedical Engineering*, 19(5):465–73.

Bay, B. K., Smith, T. S., Fyhrie, D. P., and Saad, M. (1999). Digital volume correlation: Three-dimensional strain mapping using X-ray tomography. *Experimental Mechanics*, 39(3):217–226.

Bayraktar, H. H., Gupta, A., Kwon, R. Y., Papadopoulos, P., and Keaveny, T. M. (2004a). The modified super-ellipsoid yield criterion for human trabecular bone. *Journal of Biomechanical Engineering*, 126(6):677–84.

Bayraktar, H. H. and Keaveny, T. M. (2004). Mechanisms of uniformity of yield strains for trabecular bone. *Journal of Biomechanics*, 37(11):1671–8.

Bayraktar, H. H., Morgan, E. F., Niebur, G. L., Morris, G. E., Wong, E. K., and Keaveny, T. M. (2004b). Comparison of the elastic and yield properties of human femoral trabecular and cortical bone tissue. *Journal of Biomechanics*, 37(1):27–35.

Belytschko, T., Liu, W. K., and Moran, B. (2000). *Nonlinear Finite Elements for Continua and Structures*. Wiley.

Bergot, C., Laval-Jeantet, A. M., Hutchinson, K., Dautraix, I., Caulin, F., and Genant, H. K. (2001). A comparison of spinal quantitative computed tomography with dual energy X-ray absorptiometry in European women with vertebral and nonvertebral fractures. *Calcified Tissue International*, 68(2):74–82.

Bevill, G., Eswaran, S. K., Gupta, A., Papadopoulos, P., and Keaveny, T. M. (2006). Influence of bone volume fraction and architecture on computed large-deformation failure mechanisms in human trabecular bone. *Bone*, 39(6):1218–25.

Bićanić, N. and Pearce, C. J. (1996). Computational aspects of a softening plasticity model for plain concrete. *Mechanics of Cohesive-frictional Materials*, 1(1):75–94.

Blanchard, R., Dejaco, A., Bongaers, E., and Hellmich, C. (2013). Intravoxel bone micromechanics for microCT-based finite element simulations. *Journal of Biomechanics*, 46(15):2710–21.

Boivin, G. Y., Chavassieux, P. M., Santora, A. C., Yates, J., and Meunier, P. J. (2000). Alendronate increases bone strength by increasing the mean degree of mineralization of bone tissue in osteoporotic women. *Bone*, 27(5):687–94.

Bourne, B. C. and van der Meulen, M. C. (2004). Finite element models predict cancellous apparent modulus when tissue modulus is scaled from specimen CT-attenuation. *Journal of Biomechanics*, 37(5):613–621.

Bouxsein, M. L. (2003). Bone quality: where do we go from here? *Osteoporosis International*, 14 Suppl 5:S118–27.

Carnelli, D., Gastaldi, D., Sassi, V., Contro, R., Ortiz, C., and Vena, P. (2010). A finite element model for direction-dependent mechanical response to nanoindentation of cortical bone allowing for anisotropic post-yield behavior of the tissue. *Journal of Biomechanical Engineering*, 132(8):081008.

Carnelli, D., Lucchini, R., Ponzoni, M., Contro, R., and Vena, P. (2011). Nanoindentation testing and finite element simulations of cortical bone allowing for anisotropic elastic and inelastic mechanical response. *Journal of Biomechanics*, 44(10):1852–1858.

Carriero, A., Zimmermann, E. A., Paluszny, A., Tang, S. Y., Bale, H., Busse, B., Alliston, T., Kazakia, G., Ritchie, R. O., and Shefelbine, S. J. (2014). How Tough Is Brittle Bone? Investigating Osteogenesis Imperfecta in Mouse Bone. *Journal of Bone and Mineral Research*, 29(6):1392–1401.

Chang, W. C. W., Christensen, T. M., Pinilla, T. P., and Keaveny, T. M. (1999). Uniaxial yield strains for bovine trabecular bone are isotropic and asymmetric. *Journal of Orthopaedic Research*, 17(4):582–585.

Chen, X., Ogasawara, N., Zhao, M., and Chiba, N. (2007). On the uniqueness of measuring elastoplastic properties from indentation: The indistinguishable mystical materials. *Journal of the Mechanics and Physics of Solids*, 55(8):1618–1660.

Chen, Y., Dall'Ara, E., Sales, E., Manda, K., Wallace, R., Pankaj, P., and Viceconti, M. (2017). Micro-CT based finite element models of cancellous bone predict accurately displacement once the boundary condition is well replicated: A validation study.

Chen, Y., Pani, M., Taddei, F., Mazzà, C., Li, X., and Viceconti, M. (2014). Large-Scale Finite Element Analysis of Human Cancellous Bone Tissue Micro Computer Tomography Data: A Convergence Study. *Journal of Biomechanical Engineering*, 136(10):101013.

Christiansen, B. A. (2016). Effect of micro-computed tomography voxel size and segmentation method on trabecular bone microstructure measures in mice. *Bone Reports*, 5:136–140.

Ciarelli, T. E., Fyhrie, D. P., Schaffler, M. B., and Goldstein, S. A. (2000). Variations in three-dimensional cancellous bone architecture of the proximal femur in female hip fractures and in controls. *Journal of Bone and Mineral Research*, 15(1):32–40.

Completo, A., Simões, J. A., and Fonseca, F. (2009). Revision total knee arthroplasty: the influence of femoral stems in load sharing and stability. *The Knee*, 16(4):275–279.

Conlisk, N., Howie, C. R., and Pankaj, P. (2015). The role of complex clinical scenarios in the failure of modular components following revision total knee arthroplasty: A finite element study. *Journal of Orthopaedic Research*, 33(8):1134–41.

Cowin, S. (1985). The relationship between the elasticity tensor and the fabric tensor. *Mechanics of Materials*, 4(2):137–147.

Cowin, S. (1986). Fabric dependence of an anisotropic strength criterion. *Mechanics of Materials*, 5(3):251–260.

Cowin, S. (1997). Remarks on the paper entitled 'Fabric and elastic principal directions of cancellous bone are closely related'. *Journal of Biomechanics*, 30(11-12):1191–1192.

Cowin, S. (2001). *Bone Mechanics Handbook*. Taylor & Francis, 2 edition.

Cruz-Orive, L. M., Karlsson, L. M., Larsen, S. E., and Wainschtein, F. (1992). Characterizing anisotropy: A new concept. *Micron and Microscopica Acta*, 23(1-2):75–76.

Dall'Ara, E., Luisier, B., Schmidt, R., Kainberger, F., Zysset, P. K., and Pahr, D. (2013). A nonlinear QCT-based finite element model validation study for the human femur tested in two configurations in vitro. *Bone*, 52(1):27–38.

Dall'Ara, E., Pahr, D., Varga, P., Kainberger, F., and Zysset, P. K. (2012). QCT-based finite element models predict human vertebral strength in vitro significantly better than simulated DEXA. *Osteoporosis International*, 23(2):563–72.

de Souza Neto, E., Blanco, P., Sánchez, P., and Feijóo, R. (2015). An RVE-based multiscale theory of solids with micro-scale inertia and body force effects. *Mechanics of Materials*, 80:136–144.

de Souza Neto, E. and Feijóo, R. (2006). Variational foundations of multi-scale constitutive models of solid: small and large strain kinematical formulation. Technical report, National Laboratory for Scientific Computing (LNCC/MCT).

de Souza Neto, E. and Feijóo, R. (2010). *Advanced Computational Materials Modeling: From Classical to Multi-Scale Techniques*. Wiley.

de Souza Neto, E., Peric, D., and Owen, D. (2008). *Computational Methods for Plasticity: Theory and Applications*. Wiley.

de Souza Neto, E. A. and Feijóo, R. A. (2008). On the equivalence between spatial and material volume averaging of stress in large strain multi-scale solid constitutive models. *Mechanics of Materials*, 40(10):803–811.

Donaldson, F. E., Pankaj, P., Cooper, D. M. L., Thomas, C. D. L., Clement, J. G., and Simpson, A. H. R. W. (2011). Relating age and micro-architecture with apparent-level elastic constants: a micro-finite element study of female cortical bone from the anterior femoral midshaft. *Proceedings of the Institution of Mechanical Engineers. Part H, Journal of Engineering in Medicine*, 225(6):585–96.

Donaldson, F. E., Pankaj, P., and Simpson, A. H. R. W. (2012). Investigation of factors affecting loosening of Ilizarov ring-wire external fixator systems at the bone-wire interface. *Journal of Orthopaedic Research*, 30(5):726–32.

Doube, M., Kłosowski, M. M., Arganda-Carreras, I., Cordelières, F. P., Dougherty, R. P., Jackson, J. S., Schmid, B., Hutchinson, J. R., and Shefelbine, S. J. (2010). BoneJ: Free and extensible bone image analysis in ImageJ. *Bone*, 47(6):1076–9.

Easley, S. K., Jekir, M. G., Burghardt, A. J., Li, M., and Keaveny, T. M. (2010). Contribution of the intra-specimen variations in tissue mineralization to PTH- and raloxifene-induced changes in stiffness of rat vertebrae. *Bone*, 46(4):1162–9.

Eterovic, A. L. and Bathe, K. J. (1990). A hyperelastic-based large strain elasto-plastic constitutive formulation with combined isotropic-kinematic hardening using the logarithmic stress and strain measures. *International Journal for Numerical Methods in Engineering*, 30(6):1099–1114.

Fenech, C. M. and Keaveny, T. M. (1999). A Cellular Solid Criterion for Predicting the Axial-Shear Failure Properties of Bovine Trabecular Bone. *Journal of Biomechanical Engineering*, 121(4):414.

Feng, Y. T., Perić, D., and Owen, D. R. J. (1995). Determination of travel directions in path-following methods. *Mathematical and Computer Modelling*, 21(7):43–59.

Feng, Y. T., Perić, D., and Owen, D. R. J. (1996). A new criterion for determination of initial loading parameter in arc-length methods. *Computers {&} Structures*, 58(3):479–485.

Fondrk, M. T., Bahniuk, E. H., and Davy, D. T. (1999). A damage model for nonlinear tensile behavior of cortical bone. *Journal of Biomechanical Engineering*, 121(5):533–41.

Fratzl, P. and Weinkamer, R. (2007). Nature's hierarchical materials. *Progress in Materials Science*, 52(8):1263–1334.

Fritsch, A., Hellmich, C., and Dormieux, L. (2009). Ductile sliding between mineral crystals followed by rupture of collagen crosslinks: Experimentally supported micromechanical explanation of bone strength. *Journal of Theoretical Biology*, 260(2):230–252.

Garcia, D., Zysset, P. K., Charlebois, M., and Curnier, A. (2009). A three-dimensional elastic plastic damage constitutive law for bone tissue. *Biomechanics and Modeling in Mechanobiology*, 8(2):149–65.

Garcia, D., Zysset, P. K., Charlebois, M., and Curnier, A. (2010). A 1D elastic plastic damage constitutive law for bone tissue. *Archive of Applied Mechanics*, 80(5):543–555.

Gibson, L. (1985). The mechanical behaviour of cancellous bone. *Journal of Biomechanics*, 18(5):317–328.

Gibson, L. J. and Ashby, M. F. (1999). *Cellular Solids: Structure and Properties*. Cambridge University Press.

Gómez, W., Sales, E., Lopes, R. T., and Pereira, W. C. A. (2013). A comparative study of automatic thresholding approaches for 3D x-ray microtomography of trabecular bone. *Medical Physics*, 40(9):091903.

Goulet, R., Goldstein, S., Ciarelli, M., Kuhn, J., Brown, M., and Feldkamp, L. (1994). The relationship between the structural and orthogonal compressive properties of trabecular bone. *Journal of Biomechanics*, 27(4):375–389.

Grassi, L. and Isaksson, H. (2015). Extracting accurate strain measurements in bone mechanics: A critical review of current methods. *Journal of the Mechanical Behavior of Biomedical Materials*, 50:43–54.

Greenbaum, A. (1997). *Iterative Methods for Solving Linear Systems*. Society for Industrial and Applied Mathematics.

Gross, T., Pahr, D. H., Peyrin, F., and Zysset, P. K. (2012). Mineral heterogeneity has a minor influence on the apparent elastic properties of human cancellous bone: a SRμCT-based finite element study. *Computer Methods in Biomechanics and Biomedical Engineering*, 15(11):1137–1144.

Gupta, H. S., Fratzl, P., Kerschnitzki, M., Benecke, G., Wagermaier, W., and Kirchner, H. O. K. (2007). Evidence for an elementary process in bone plasticity with an activation enthalpy of 1 eV. *Journal of the Royal Society Interface*, 4(13):277–82.

Gupta, H. S., Wagermaier, W., Zickler, G. A., Hartmann, J., Funari, S. S., Roschger, P., Wagner, H. D., and Fratzl, P. (2006). Fibrillar level fracture in bone beyond the yield point. *International Journal of Fracture*, 139(3-4):425–436.

Gupta, H. S., Wagermaier, W., Zickler, G. A., Raz-Ben Aroush, D., Funari, S. S., Roschger, P., Wagner, H. D., and Fratzl, P. (2005). Nanoscale deformation mechanisms in bone. *Nano Letters*, 5(10):2108–11.

Gupta, H. S. and Zioupos, P. (2008). Fracture of bone tissue: The 'hows' and the 'whys'. *Medical Engineering & Physics*, 30(10):1209–26.

Hambli, R. (2013). Micro-CT finite element model and experimental validation of trabecular bone damage and fracture. *Bone*, 56(2):363–74.

Harrigan, T. P., Jasty, M., Mann, R. W., and Harris, W. H. (1988). Limitations of the continuum assumption in cancellous bone. *Journal of Biomechanics*, 21(4):269–275.

Harrigan, T. P. and Mann, R. W. (1984). Characterization of microstructural anisotropy in orthotropic materials using a second rank tensor. *Journal of Materials Science*, 19(3):761–767.

Helgason, B., Perilli, E., Schileo, E., Taddei, F., Brynjólfsson, S., and Viceconti, M. (2008). Mathematical relationships between bone density and mechanical properties: a literature review. *Clinical Biomechanics*, 23(2):135–46.

Hellmich, C. and Ulm, F. J. (2002). Are mineralized tissues open crystal foams reinforced by crosslinked collagen? Some energy arguments. *Journal of Biomechanics*, 35(9):1199–1212.

Hellmich, C., Ulm, F. J., and Dormieux, L. (2004). Can the diverse elastic properties of trabecular and cortical bone be attributed to only a few tissue-independent phase properties and their interactions? Arguments from a multiscale approach. *Biomechanics and Modeling in Mechanobiology*, 2(4):219–38.

Helton, J., Johnson, J., Sallaberry, C., and Storlie, C. (2006). Survey of sampling-based methods for uncertainty and sensitivity analysis. *Reliability Engineering & System Safety*, 91(10):1175–1209.

Hengsberger, S., Kulik, A., and Zysset, P. K. (2002). Nanoindentation discriminates the elastic properties of individual human bone lamellae under dry and physiological conditions. *Bone*, 30(1):178–84.

Hernandez, C. J., Beaupré, G. S., Keller, T. S., and Carter, D. R. (2001). The influence of bone volume fraction and ash fraction on bone strength and modulus. *Bone*, 29(1):74–78.

Hernandez, C. J., Lambers, F. M., Widjaja, J., Chapa, C., and Rimnac, C. M. (2014). Quantitative relationships between microdamage and cancellous bone strength and stiffness. *Bone*, 66:205–13.

Hill, R. (1963). Elastic properties of reinforced solids: some theoretical considerations. *Journal of the Mechanics and Physics of Solids*, 11:357.

Hill, R. (1965). A self-consistent mechanics of composite materials. *Journal of the Mechanics and Physics of Solids*, 13(4):213–222.

Hill, R. (1972). On Constitutive Macro-Variables for Heterogeneous Solids at Finite Strain. *Proceedings of the Royal Society A: Mathematical, Physical and Engineering Sciences*, 326(1565):131–147.

Hodgskinson, R. and Currey, J. D. (1990a). Effects of structural variation on Young's modulus of non-human cancellous bone. *Proceedings of the Institution of Mechanical Engineers. Part H, Journal of engineering in medicine*, 204(1):43–52.

Hodgskinson, R. and Currey, J. D. (1990b). The effect of variation in structure on the Young's modulus of cancellous bone: a comparison of human and non-human material. *Proceedings of the Institution of Mechanical Engineers. Part H, Journal of Engineering in Medicine*, 204(2):115–21.

Hollister, S. J. and Kikuchi, N. (1992). A comparison of homogenization and standard mechanics analyses for periodic porous composites. *Computational Mechanics*, 10(2):73–95.

Holzapfel, G. (2000). *Nonlinear Solid Mechanics: A Continuum Approach for Enineering: A Continuum Approach for Engineering*. Wiley.

Homminga, J., Van-Rietbergen, B., Lochmüller, E. M., Weinans, H., Eckstein, F., and Huiskes, R. (2004). The osteoporotic vertebral structure is well adapted to the loads of daily life, but not to infrequent "error" loads. *Bone*, 34(3):510–6.

Hosseini, H. S., Clouthier, A. L., and Zysset, P. K. (2014). Experimental validation of finite element analysis of human vertebral collapse under large compressive strains. *Journal of Biomechanical Engineering*, 136(4):041006.

Hosseini, H. S., Pahr, D. H., and Zysset, P. K. (2012). Modeling and experimental validation of trabecular bone damage, softening and densification under large compressive strains. *Journal of the Mechanical Behavior of Biomedical Materials*, 15:93–102.

Hughes, T. J. R. and Winget, J. (1980). Finite rotation effects in numerical integration of rate constitutive equations arising in large-deformation analysis. *International Journal for Numerical Methods in Engineering*, 15(12):1862–1867.

Itskov, M. (2012). *Tensor Algebra and Tensor Analysis for Engineers: With Applications to Continuum Mechanics*. Springer International.

Jaasma, M. J., Bayraktar, H. H., Niebur, G. L., and Keaveny, T. M. (2002). Biomechanical effects of intraspecimen variations in tissue modulus for trabecular bone. *Journal of Biomechanics*, 35(2):237–46.

Jaschouz, D., Paris, O., Roschger, P., Hwang, H. S., and Fratzl, P. (2003). Pole figure analysis of mineral nanoparticle orientation in individual trabecula of human vertebral bone. *Journal of Applied Crystallography*, 36(3):494–498.

Jepsen, K. J. and Davy, D. T. (1997). Comparison of damage accumulation measures in human cortical bone. *Journal of Biomechanics*, 30(9):891–894.

Jog, C. S. (2008). The Explicit Determination of the Logarithm of a Tensor and Its Derivatives. *Journal of Elasticity*, 93(2):141–148.

Johnell, O. (1997). The socioeconomic burden of fractures: today and in the 21st century. *The American Journal of Medicine*, 103(2A):20S–25S; discussion 25S–26S.

Juszczyk, M. M., Cristofolini, L., Salvà, M., Zani, L., Schileo, E., and Viceconti, M. (2013). Accurate in vitro identification of fracture onset in bones: Failure mechanism of the proximal human femur. *Journal of Biomechanics*, 46(1):158–164.

Kabel, J., van Rietbergen, B., Dalstra, M., Odgaard, A., and Huiskes, R. (1999). The role of an effective isotropic tissue modulus in the elastic properties of cancellous bone. *Journal of Biomechanics*, 32(7):673–680.

Kanatani, K. I. (1984). Distribution of directional data and fabric tensors. *International Journal of Engineering Science*, 22(2):149–164.

Kanit, T., Forest, S., Galliet, I., Mounoury, V., and Jeulin, D. (2003). Determination of the size of the representative volume element for random composites: statistical and numerical approach. *International Journal of Solids and Structures*, 40(13-14):3647–3679.

Kaynia, N., Soohoo, E., Keaveny, T. M., and Kazakia, G. J. (2014). Effect of Intraspecimen Spatial Variation in Tissue Mineral Density on the Apparent Stiffness of Trabecular Bone. *Journal of Biomechanical Engineering*, 137(1):011010.

Keaveny, T. M., Pinilla, T. P., Crawford, R. P., Kopperdahl, D. L., and Lou, A. (1997). Systematic and random errors in compression testing of trabecular bone. *Journal of Orthopaedic Research*, 15(1):101–10.

Keaveny, T. M., Wachtel, E. F., Ford, C. M., and Hayes, W. C. (1994). Differences between the tensile and compressive strengths of bovine tibial trabecular bone depend on modulus. *Journal of Biomechanics*, 27(9):1137–1146.

Keaveny, T. M., Wachtel, E. F., and Kopperdahl, D. L. (1999). Mechanical behavior of human trabecular bone after overloading. *Journal of Orthopaedic Research*, 17(3):346–53.

Keller, T. S. (1994). Predicting the compressive mechanical behavior of bone. *Journal of Biomechanics*, 27(9):1159–1168.

Kelley, C. T. (2001). *Iterative Methods for Linear and Nonlinear Equations*. SIAM Press.

Kojić, M. and Bathe, K. J. (1987). Studies of finite element procedures - Stress solution of a closed elastic strain path with stretching and shearing using the updated Lagrangian Jaumann formulation. *Computers & Structures*, 26(1-2):175–179.

Kopperdahl, D. L. and Keaveny, T. M. (1998). Yield strain behavior of trabecular bone. *Journal of Biomechanics*, 31(7):601–608.

Kruch, S. and Chaboche, J.-L. (2011). Multi-scale analysis in elasto-viscoplasticity coupled with damage. *International Journal of Plasticity*, 27(12):2026–2039.

Lacroix, D. and Prendergast, P. (2002). A mechano-regulation model for tissue differentiation during fracture healing: analysis of gap size and loading. *Journal of Biomechanics*, 35(9):1163–1171.

Lambers, F. M., Bouman, A. R., Tkachenko, E. V., Keaveny, T. M., and Hernandez, C. J. (2014). The effects of tensile-compressive loading mode and microarchitecture on microdamage in human vertebral cancellous bone. *Journal of Biomechanics*, 47(15):3605–12.

Lee, E. H. and Liu, D. T. (1967). Finite-Strain Elastic—Plastic Theory with Application to Plane-Wave Analysis. *Journal of Applied Physics*, 38(1):19.

Lucchini, R., Carnelli, D., Ponzoni, M., Bertarelli, E., Gastaldi, D., and Vena, P. (2011). Role of damage mechanics in nanoindentation of lamellar bone at multiple sizes: experiments and numerical modeling. *Journal of the Mechanical Behavior of Biomedical Materials*, 4(8):1852–63.

Luczynski, K. W., Steiger-Thirsfeld, A., Bernardi, J., Eberhardsteiner, J., and Hellmich, C. (2015). Extracellular bone matrix exhibits hardening elastoplasticity and more than double cortical strength: Evidence from homogeneous compression of non-tapered single micron-sized pillars welded to a rigid substrate. *Journal of the Mechanical Behavior of Biomedical Materials*, 52:51–62.

Luenberger, D. G. (2003). *Linear and Nonlinear Programming*. Springer US.

Maghous, S., Dormieux, L., and Barthélémy, J. F. (2009). Micromechanical approach to the strength properties of frictional geomaterials. *European Journal of Mechanics - A/Solids*, 28(1):179–188.

Malandrino, A., Fritsch, A., Lahayne, O., Kropik, K., Redl, H., Noailly, J., Lacroix, D., and Hellmich, C. (2012). Anisotropic tissue elasticity in human lumbar vertebra, by means of a coupled ultrasound-micromechanics approach. *Materials Letters*, 78:154–158.

Manda, K., Xie, S., Wallace, R. J., Levrero-Florencio, F., and Pankaj, P. (2016). Linear viscoelasticity - bone volume fraction relationships of bovine trabecular bone. *Biomechanics and Modeling in Mechanobiology*.

Margetts, L. (2002). *Parallel Finite Element Analysis*. PhD thesis, University of Manchester.

Margetts, L., Arregui-Mena, D., Hewitt, T., and Mason, L. (2016). Parallel finite element analysis on the Intel Xeon Phi. In *Emerging Technology Conference*.

Matsuura, M., Eckstein, F., Lochmüller, E.-M., and Zysset, P. K. (2008). The role of fabric in the quasi-static compressive mechanical properties of human trabecular bone from various anatomical locations. *Biomechanics and Modeling in Mechanobiology*, 7(1):27–42.

McDonnell, P., McHugh, P. E., and O'Mahoney, D. (2007). Vertebral osteoporosis and trabecular bone quality. *Annals of Biomedical Engineering*, 35(2):170–89.

McDowell, D. L. (2010). A perspective on trends in multiscale plasticity. *International Journal of Plasticity*, 26(9):1280–1309.

Mcmeeking, R. M. and Rice, J. R. (1975). Finite-element formulations for problems of large elastic-plastic deformation. *International Journal of Solids and Structures*, 11(5):601–16.

Mehrabadi, M. M. and Cowin, S. C. (1990). Eigentensors of linear anisotropic elastic materials. *The Quarterly Journal of Mechanics and Applied Mathematics*, 43(1):15–41.

Morgan, E. F., Bayraktar, H. H., and Keaveny, T. M. (2003). Trabecular bone modulus–density relationships depend on anatomic site. *Journal of Biomechanics*, 36(7):897–904.

Morgan, E. F., Bayraktar, H. H., Yeh, O. C., Majumdar, S., Burghardt, A., and Keaveny, T. M. (2004). Contribution of inter-site variations in architecture to trabecular bone apparent yield strains. *Journal of Biomechanics*, 37(9):1413–20.

Morgan, E. F. and Keaveny, T. M. (2001). Dependence of yield strain of human trabecular bone on anatomic site. *Journal of Biomechanics*, 34(5):569–77.

Mulder, L., van Ruijven, L. J., Koolstra, J. H., and van Eijden, T. M. G. J. (2007). Biomechanical consequences of developmental changes in trabecular architecture and mineralization of the pig mandibular condyle. *Journal of Biomechanics*, 40(7):1575–82.

Müller, R., Koller, B., Hildebrand, T., Laib, A., Gianolini, S., and Rüegsegger, P. (1996). Resolution dependency of microstructural properties of cancellous bone based on three-dimensional mu-tomography. *Technology and health care : official journal of the European Society for Engineering and Medicine*, 4(1):113–9.

Murakami, S. (2012). *Continuum Damage Mechanics*, volume 185 of *Solid Mechanics and Its Applications*. Springer.

Nagtegaal, J. C. (1982). On the implementation of inelastic constitutive equations with special reference to large deformation problems. *Computer Methods in Applied Mechanics and Engineering*, 33(1-3):469–484.

Nalla, R., Kinney, J., and Ritchie, R. (2003). Mechanistic fracture criteria for the failure of human cortical bone. *Nature Materials*, 2(3):164–168.

Nawathe, S., Juillard, F., and Keaveny, T. M. (2013). Theoretical bounds for the influence of tissue-level ductility on the apparent-level strength of human trabecular bone. *Journal of Biomechanics*, 46(7):1293–9.

Nguyen, V., Béchet, E., Geuzaine, C., and Noels, L. (2012). Imposing periodic boundary condition on arbitrary meshes by polynomial interpolation. *Computational Materials Science*, 55:390–406.

Odgaard, A., Hvid, I., and Linde, F. (1989). Compressive axial strain distributions in cancellous bone specimens. *Journal of Biomechanics*, 22(8):829–835.

Odgaard, A., Kabel, J., van Rietbergen, B., Dalstra, M., and Huiskes, R. (1997). Fabric and elastic principal directions of cancellous bone are closely related. *Journal of Biomechanics*, 30(5):487–95.

Pahr, D. H. and Zysset, P. K. (2008). Influence of boundary conditions on computed apparent elastic properties of cancellous bone. *Biomechanics and Modeling in Mechanobiology*, 7(6):463–76.

Palanca, M., Tozzi, G., Cristofolini, L., Viceconti, M., and Dall'Ara, E. (2015). Three-Dimensional Local Measurements of Bone Strain and Displacement: Comparison of Three Digital Volume Correlation Approaches. *Journal of Biomechanical Engineering*, 137(7):071006.

Pankaj, P. and Donaldson, F. E. (2013). Algorithms for a strain-based plasticity criterion for bone. *International Journal for Numerical Methods in Biomedical Engineering*, 29(1):40–61.

Panyasantisuk, J., Pahr, D. H., Gross, T., and Zysset, P. K. (2015a). Comparison of Mixed and Kinematic Uniform Boundary Conditions in Homogenized Elasticity of Femoral Trabecular Bone Using Microfinite Element Analyses. *Journal of Biomechanical Engineering*, 137(1):11002–11007.

Panyasantisuk, J., Pahr, D. H., and Zysset, P. K. (2015b). Effect of boundary conditions on yield properties of human femoral trabecular bone. *Biomechanics and Modeling in Mechanobiology*.

Pérez-Foguet, A. and Armero, F. (2002). On the formulation of closest-point projection algorithms in elastoplasticity - part II: Globally convergent schemes. *International Journal for Numerical Methods in Engineering*, 53(2):331–374.

Perić, D. (1992). On consistent stress rates in solid mechanics: Computational implications. *International Journal for Numerical Methods in Engineering*, 33(4):799–817.

Perić, D., de Souza Neto, E. A., Feijóo, R. A., Partovi, M., and Molina, A. J. C. (2011). On micro-to-macro transitions for multi-scale analysis of non-linear heterogeneous materials: unified variational basis and finite element implementation. *International Journal for Numerical Methods in Engineering*, 87(1-5):149–170.

Perić, D., Owen, D., and Honnor, M. (1992). A model for finite strain elasto-plasticity based on logarithmic strains: Computational issues. *Computer Methods in Applied Mechanics and Engineering*, 94(1):35–61.

Phillips, A. T. M., Pankaj, P., Howie, C. R., Usmani, A. S., and Simpson, A. H. R. W. (2006). 3D non-linear analysis of the acetabular construct following impaction grafting. *Computer Methods in Biomechanics and Biomedical Engineering*, 9(3):125–33.

Ponthot, J.-P. (1998). An extension of the radial return algorithm to account for rate-dependent effects in frictional contact and visco-plasticity. *Journal of Materials Processing Technology*, 80-81:628–634.

Poumarat, G. and Squire, P. (1993). Comparison of mechanical properties of human, bovine bone and a new processed bone xenograft. *Biomaterials*, 14(5):337–340.

Ramtani, S. and Zidi, M. (2001). A theoretical model of the effect of continuum damage on a bone adaptation model. *Journal of Biomechanics*, 34(4):471–479.

Ray, N. F., Chan, J. K., Thamer, M., and Melton, L. J. (1997). Medical expenditures for the treatment of osteoporotic fractures in the United States in 1995: report from the National Osteoporosis Foundation. *Journal of Bone and Mineral Research*, 12(1):24–35.

Reilly, D. T. and Burstein, A. H. (1975). The elastic and ultimate properties of compact bone tissue. *Journal of Biomechanics*, 8(6):393–405.

Reisinger, A. G., Pahr, D. H., and Zysset, P. K. (2010). Sensitivity analysis and parametric study of elastic properties of an unidirectional mineralized bone fibril-array using mean field methods. *Biomechanics and Modeling in Mechanobiology*, 9(5):499–510.

Renders, G. A. P., Mulder, L., Langenbach, G. E. J., van Ruijven, L. J., and van Eijden, T. M. G. J. (2008). Biomechanical effect of mineral heterogeneity in trabecular bone. *Journal of Biomechanics*, 41(13):2793–8.

Rho, J. Y. (1996). An ultrasonic method for measuring the elastic properties of human tibial cortical and cancellous bone. *Ultrasonics*, 34(8):777–83.

Rho, J. Y., Ashman, R. B., and Turner, C. H. (1993). Young's modulus of trabecular and cortical bone material: ultrasonic and microtensile measurements. *Journal of biomechanics*, 26(2):111–9.

Rho, J. Y., Kuhn-Spearing, L., and Zioupos, P. (1998). Mechanical properties and the hierarchical structure of bone. *Medical Engineering & Physics*, 20(2):92–102.

Rho, J. Y., Tsui, T. Y., and Pharr, G. M. (1997). Elastic properties of human cortical and trabecular lamellar bone measured by nanoindentation. *Biomaterials*, 18(20):1325–30.

Rincón-Kohli, L. and Zysset, P. K. (2009). Multi-axial mechanical properties of human trabecular bone. *Biomechanics and Modeling in Mechanobiology*, 8(3):195–208.

Roschger, P., Grabner, B. M., Rinnerthaler, S., Tesch, W., Kneissel, M., Berzlanovich, A., Klaushofer, K., and Fratzl, P. (2001). Structural development of the mineralized tissue in the human L4 vertebral body. *Journal of Structural Biology*, 136(2):126–36.

Rubinstein, R. and Atluri, S. (1983). Objectivity of incremental constitutive relations over finite time steps in computational finite deformation analyses. *Computer Methods in Applied Mechanics and Engineering*, 36(3):277–290.

Saltelli, A. A. (2008). *Global sensitivity analysis : the primer*. John Wiley.

Sambrook, P. and Cooper, C. (2006). Osteoporosis. *The Lancet*, 367(9527):2010–2018.

Sanyal, A., Gupta, A., Bayraktar, H. H., Kwon, R. Y., and Keaveny, T. M. (2012). Shear strength behavior of human trabecular bone. *Journal of Biomechanics*, 45(15):2513–9.

Sanyal, A., Scheffelin, J., and Keaveny, T. M. (2015). The quartic piecewise-linear criterion for the multiaxial yield behavior of human trabecular bone. *Journal of Biomechanical Engineering*, 137(1).

Schaffler, M., Radin, E., and Burr, D. (1989). Mechanical and morphological effects of strain rate on fatigue of compact bone. *Bone*, 10(3):207–214.

Schileo, E., Balistreri, L., Grassi, L., Cristofolini, L., and Taddei, F. (2014). To what extent can linear finite element models of human femora predict failure under stance and fall loading configurations? *Journal of Biomechanics*, 47(14):3531–3538.

Schileo, E., Dall'ara, E., Taddei, F., Malandrino, A., Schotkamp, T., Baleani, M., and Viceconti, M. (2008). An accurate estimation of bone density improves the accuracy of subject-specific finite element models. *Journal of Biomechanics*, 41(11):2483–91.

Schileo, E., Taddei, F., Malandrino, A., Cristofolini, L., and Viceconti, M. (2007). Subject-specific finite element models can accurately predict strain levels in long bones. *Journal of Biomechanics*, 40(13):2982–2989.

Schwiedrzik, J. J., Gross, T., Bina, M., Pretterklieber, M., Zysset, P. K., and Pahr, D. (2015). Experimental validation of a nonlinear μFE model based on cohesive-frictional plasticity for trabecular bone. *International Journal for Numerical Methods in Biomedical Engineering*.

Schwiedrzik, J. J., Raghavan, R., Bürki, A., LeNader, V., Wolfram, U., Michler, J., and Zysset, P. K. (2014). In situ micropillar compression reveals superior strength and ductility but an absence of damage in lamellar bone. *Nature Materials*, 13(7):740–7.

Schwiedrzik, J. J., Wolfram, U., and Zysset, P. K. (2013). A generalized anisotropic quadric yield criterion and its application to bone tissue at multiple length scales. *Biomechanics and Modeling in Mechanobiology*, 12(6):1155–68.

Schwiedrzik, J. J. and Zysset, P. K. (2013). An anisotropic elastic-viscoplastic damage model for bone tissue. *Biomechanics and Modeling in Mechanobiology*, 12(2):201–13.

Schwiedrzik, J. J. and Zysset, P. K. (2015). The influence of yield surface shape and damage in the depth-dependent response of bone tissue to nanoindentation using spherical and Berkovich indenters. *Computer Methods in Biomechanics and Biomedical Engineering*, 18(5):492–505.

Seifert, T. and Schmidt, I. (2008). Line-search methods in general return mapping algorithms with application to porous plasticity. *International Journal for Numerical Methods in Engineering*, 73(10):1468–1495.

Shultz, G. A., Schnabel, R. B., and Byrd, R. H. (1985). A Family of Trust-Region-Based Algorithms for Unconstrained Minimization with Strong Global Convergence Properties. *SIAM Journal on Numerical Analysis*, 22(1):47–67.

Simo, J. (1985). On the computational significance of the intermediate configuration and hyperelastic stress relations in finite deformation elastoplasticity. *Mechanics of Materials*, 4(3-4):439–451.

Simo, J. (1992). Algorithms for static and dynamic multiplicative plasticity that preserve the classical return mapping schemes of the infinitesimal theory. *Computer Methods in Applied Mechanics and Engineering*, 99(1):61–112.

Simo, J. and Ortiz, M. (1985). A unified approach to finite deformation elastoplastic analysis based on the use of hyperelastic constitutive equations. *Computer Methods in Applied Mechanics and Engineering*, 49(2):221–245.

Simo, J. and Pister, K. (1984). Remarks on rate constitutive equations for finite deformation problems: computational implications. *Computer Methods in Applied Mechanics and Engineering*, 46(2):201–215.

Simo, J. and Taylor, R. (1985). Consistent tangent operators for rate-independent elastoplasticity. *Computer Methods in Applied Mechanics and Engineering*, 48(1):101–118.

Siris, E. S., Chen, Y. T., Abbott, T. A., Barrett-Connor, E., Miller, P. D., Wehren, L. E., and Berger, M. L. (2004). Bone mineral density thresholds for pharmacological intervention to prevent fractures. *Archives of Internal Medicine*, 164(10):1108–12.

Smit, T. H., Schneider, E., and Odgaard, A. (1998). Star length distribution: a volume-based concept for the characterization of structural anisotropy. *Journal of Microscopy*, 191(Pt 3):249–57.

Smith, C. I., Faraldos, M., and Fernández-Jalvo, Y. (2008). The precision of porosity measurements: Effects of sample pre-treatment on porosity measurements of modern and archaeological bone. *Palaeogeography, Palaeoclimatology, Palaeoecology*, 266(3-4):175–182.

Smith, I. M., Griffiths, D. V., and Margetts, L. (2013). *Programming the Finite Element Method*. Wiley.

Smith, I. M. and Margetts, L. (2006). The convergence variability of parallel iterative solvers. *Engineering Computations*, 23(2):154–165.

Snyder, B. and Hayes, W. (1990). Multiaxial structure-property relations in trabecular bone. In Mow, V., Ratcliffe, A., and Woo, S., editors, *Biomechanics of Diarthrodial Joints*, pages 31–59. Springer.

Steiner, J. A., Ferguson, S. J., and van Lenthe, G. H. (2015). Computational analysis of primary implant stability in trabecular bone. *Journal of Biomechanics*, 48(5):807–15.

Stölken, J. S. and Kinney, J. H. (2003). On the importance of geometric nonlinearity in finite-element simulations of trabecular bone failure. *Bone*, 33(4):494–504.

Strohmaier, E., Dongarra, J., Simon, H., and Meuer, M. (1993). TOP500, The List.

Sun, X., Hoon Jeon, J., Blendell, J., and Akkus, O. (2010). Visualization of a phantom post-yield deformation process in cortical bone. *Journal of Biomechanics*, 43(10):1989–96.

Suquet, P. (1985). Elements of homogenization theory for inelastic solid mechanics. In Sanchez-Palencia, E. and Zauoi, A., editors, *Homogenization Techniques for Composite Media*. Springer, Berlin.

Tai, K., Ulm, F. J., and Ortiz, C. (2006). Nanogranular origins of the strength of bone. *Nano Letters*, 6(11):2520–5.

Tassani, S., Ohman, C., Baruffaldi, F., Baleani, M., and Viceconti, M. (2011). Volume to density relation in adult human bone tissue. *Journal of Biomechanics*, 44(1):103–8.

Terada, K., Hori, M., Kyoya, T., and Kikuchi, N. (2000). Simulation of the multi-scale convergence in computational homogenization approaches. *International Journal of Solids and Structures*, 37(16):2285–2311.

Terrier, A., Levrero Florencio, F., and Rüdiger, H. A. (2014). Benefit of cup medialization in total hip arthroplasty is associated with femoral anatomy. *Clinical Orthopaedics and Related Research*, 472(10):3159–65.

The MPI Forum (1993). MPI : A Message Passing Interface. In *Proceedings of the Conference on High Performance Networking and Computing*, pages 878–883.

Theocaris, P. S. (1992). Failure modes of closed-cell polyurethane foams. *International Journal of Fracture*, 56(4):353–375.

Torgerson, D. and Cooper, C. (1998). Osteoporosis as a Candidate for Disease Management. *Disease Management and Health Outcomes*, 3(5):207–214.

Tsai, S. W. and Wu, E. M. (1971). A General Theory of Strength for Anisotropic Materials. *Journal of Composite Materials*, 5(1):58–80.

Turner, C. H., Cowin, S. C., Rho, J. Y., Ashman, R. B., and Rice, J. C. (1990). The fabric dependence of the orthotropic elastic constants of cancellous bone. *Journal of Biomechanics*, 23(6):549–561.

Ulrich, D., van Rietbergen, B., Weinans, H., and Rüegsegger, P. (1998). Finite element analysis of trabecular bone structure: a comparison of image-based meshing techniques. *Journal of Biomechanics*, 31(12):1187–1192.

Ural, A. and Vashishth, D. (2007). Effects of intracortical porosity on fracture toughness in aging human bone: a microCT-based cohesive finite element study. *Journal of Biomechanical Engineering*, 129(5):625–31.

van Buskirk, W. C., Cowin, S. C., and Ward, R. N. (1981). Ultrasonic measurement of orthotropic elastic constants of bovine femoral bone. *Journal of biomechanical engineering*, 103(2):67–72.

van Rietbergen, B., Odgaard, A., Kabel, J., and Huiskes, R. (1996). Direct mechanics assessment of elastic symmetries and properties of trabecular bone architecture. *Journal of Biomechanics*, 29(12):1653–1657.

van Rietbergen, B., Weinans, H., Huiskes, R., and Odgaard, A. (1995). A new method to determine trabecular bone elastic properties and loading using micromechanical finite-element models. *Journal of Biomechanics*, 28(1):69–81.

Verhulp, E., Van Rietbergen, B., Muller, R., and Huiskes, R. (2008). Micro-finite element simulation of trabecular-bone post-yield behaviour–effects of material model, element size and type. *Computer Methods in Biomechanics and Biomedical Engineering*, 11(4):389–95.

Wang, C., Feng, L., and Jasiuk, I. (2009). Scale and boundary conditions effects on the apparent elastic moduli of trabecular bone modeled as a periodic cellular solid. *Journal of Biomechanical Engineering*, 131(12):121008.

Wang, R. and Gupta, H. S. (2011). Deformation and Fracture Mechanisms of Bone and Nacre. *Annual Review of Materials Research*, 41(1):41–73.

Watson, M., Mathias, K. J., Maffulli, N., Hukins, D. W. L., and Shepherd, D. E. T. (2007). Finite element modelling of the Ilizarov external fixation system. *Proceedings of the Institution of Mechanical Engineers. Part H, Journal of Engineering in Medicine*, 221(8):863–71.

Weber, G. and Anand, L. (1990). Finite deformation constitutive equations and a time integration procedure for isotropic, hyperelastic-viscoplastic solids. *Computer Methods in Applied Mechanics and Engineering*, 79(2):173–202.

Weiner, S. and Wagner, H. D. (1998). THE MATERIAL BONE: Structure-Mechanical Function Relations. *Annual Review of Materials Science*, 28(1):271–298.

Wenzel, T. E., Schaffler, M. B., and Fyhrie, D. P. (1996). In vivo trabecular microcracks in human vertebral bone. *Bone*, 19(2):89–95.

Whitehouse, W. J. (1974). The quantitative morphology of anisotropic trabecular bone. *Journal of Microscopy*, 101(Pt 2):153–68.

Wolfe, P. (1969). Convergence Conditions for Ascent Methods. *SIAM Review*, 11(2):226–235.

Wolff, J. (1870). Ueber die innere Architectur der Knochen und ihre Bedeutung für die Frage vom Knochenwachsthum. *Archiv für Pathologische Anatomie und Physiologie und für Klinische Medicin*, 50(3):389–450.

Wolfram, U., Gross, T., Pahr, D. H., Schwiedrzik, J., Wilke, H. J., and Zysset, P. K. (2012). Fabric-based Tsai-Wu yield criteria for vertebral trabecular bone in stress and strain space. *Journal of the Mechanical Behavior of Biomedical Materials*, 15:218–28.

Wolfram, U., Wilke, H. J., and Zysset, P. K. (2010a). Rehydration of vertebral trabecular bone: influences on its anisotropy, its stiffness and the indentation work with a view to age, gender and vertebral level. *Bone*, 46(2):348–54.

Wolfram, U., Wilke, H. J., and Zysset, P. K. (2010b). Valid micro finite element models of vertebral trabecular bone can be obtained using tissue properties measured with nanoindentation under wet conditions. *Journal of Biomechanics*, 43(9):1731–7.

World Health Organisation (2003). Prevention and management of osteoporosis. *World Health Organization Technical Report Series*, 921:1–164, back cover.

Yahia, L. H., Drouin, G., and Duval, P. (1988). A methodology for mechanical measurements of technical constants of trabecular bone. *Engineering in Medicine*, 17(4):169–73.

Yang, G., Kabel, J., Rietbergen, B. V., Odgaard, A., Huiskes, R., and Cown, S. C. (1998). The Anisotropic Hooke's Law for Cancellous Bone and Wood. *Journal of Elasticity*, 53(2):125–146.

Yeh, O. C. and Keaveny, T. M. (2001). Relative roles of microdamage and microfracture in the mechanical behavior of trabecular bone. *Journal of Orthopaedic Research*, 19(6):1001–7.

Zhang, J., Michalenko, M. M., Kuhl, E., and Ovaert, T. C. (2010). Characterization of indentation response and stiffness reduction of bone using a continuum damage model. *Journal of the Mechanical Behavior of Biomedical Materials*, 3(2):189–202.

Zhu, M. L., Zhang, Q. H., Lupton, C., and Tong, J. (2016). Spatial resolution and measurement uncertainty of strains in bone and bone–cement interface using digital volume correlation. *Journal of the Mechanical Behavior of Biomedical Materials*, 57:269–279.

Zioupos, P., Hansen, U., and Currey, J. D. (2008). Microcracking damage and the fracture process in relation to strain rate in human cortical bone tensile failure. *Journal of Biomechanics*, 41(14):2932–9.

Zysset, P. K. (2003). A review of morphology–elasticity relationships in human trabecular bone: theories and experiments. *Journal of Biomechanics*, 36(10):1469–1485.

Zysset, P. K. and Curnier, A. (1996). An implicit projection algorithm for simultaneous flow of plasticity and damage in standard generalized materials. *International Journal for Numerical Methods in Engineering*, 39(18):3065–3082.

Zysset, P. K., Goulet, R. W., and Hollister, S. J. (1998). A global relationship between trabecular bone morphology and homogenized elastic properties. *Journal of Biomechanical Engineering*, 120(5):640–6.

Zysset, P. K., Guo, X. E., Hoffler, C. E., Moore, K. E., and Goldstein, S. A. (1999). Elastic modulus and hardness of cortical and trabecular bone lamellae measured by nanoindentation in the human femur. *Journal of biomechanics*, 32(10):1005–12.

Appendix A

Scientific production

This appendix states the different presented conference posters and oral presentations, as well as the peer-reviewed journal papers related to the work pursued in this PhD thesis.

A.1 Conference posters and podium presentations

- **Levrero-Florencio, F.**, Sales, E., Srivastava, P., Jenkins, P., Mahajan, P., Pankaj, P (2014). An algorithm to map elastic constants in the human femur. *7th World Congress of Biomechanics*, Boston, USA. Poster presentation.

- Margetts, L., Arregui-Mena, J.D., Mummery, P.M., Evans, L.M., Shterenlikht, A., **Levrero-Florencio, F.**, Pankaj, P. (2015). Recent progress in the massively parallel solution of implicit problems. *NAFEMS World Congress 2015*, San Diego, USA. Podium presentation.

- **Levrero-Florencio, F.**, Margetts, L., Manda, K., Pankaj, P. (2015). Massively parallel simulations of the nonlinear mechanical behaviour of trabecular bone. *21st Congress of the European Society of Biomechanics*, Prague, Czech Republic. Podium presentation.

- Manda, K., Wallace, R., Sales, E., **Levrero-Florencio, F.**, Pankaj, P. (2015). Implementation and validation of nonlinear anisotropic viscoelastic model for trabecular bone. *21st Congress of the European Society of Biomechanics*, Prague, Czech Republic. Podium presentation.

- Manda, K., Wallace, R., Sales, E., **Levrero-Florencio, F.**, Pankaj, P. (2015). A combined nonlinear viscoelastic-viscoplastic model for trabecular bone. *21st*

Congress of the European Society of Biomechanics, Prague, Czech Republic. Podium presentation.

- Manda, K., Wallace, R., Sales, E., **Levrero-Florencio, F.**, Pankaj, P. (2015). Anisotropic nonlinear viscoelastic modelling of trabecular bone. *15th Congress of the International Society of Biomechanics*, Glasgow, UK. Podium presentation.

- Xie, S., Manda, K., Wallace, R., Sales, E., **Levrero-Florencio, F.**, Pankaj, P. (2015). Experimental investigation of creep-recovery behaviour of bovine trabecular bone. *British Orthopaedic Research Society 2015 Annual Meeting*, Liverpool, United Kingdom. Podium presentation.

- Sales, E., Wallace, R., Gómez, W., **Levrero-Florencio, F.**, Manda, K., Pankaj, P. (2015). Strain distribution in the trabecular microstructure under compression. *British Orthopaedic Research Society 2015 Annual Meeting*, Liverpool, United Kingdom. Podium presentation.

- **Levrero-Florencio, F.**, Margetts, L., Sales, E., Manda, K., Pankaj, P. (2015). Comparison of constitutive models for finite strain plasticity when applied to the microstructural modelling of trabecular bone. *6th International Conference on Computational Bioengineering*, Barcelona, Spain. Podium presentation.

- **Levrero-Florencio, F.**, Margetts, L., Manda, K., Pankaj, P (2016). Effect of hydrostatic compressive yielding on the macroscale behaviour of trabecular bone. *22nd Congress of the European Society of Biomechanics*, Lyon, France. Podium presentation.

A.2 Peer-reviewed journal papers

- **Levrero-Florencio, F.**, Margetts, L., Sales, E., Xie, S., Manda, K., Pankaj, P. (2016). Evaluating the macroscopic yield behaviour of trabecular bone using a nonlinear homogenisation approach. *Journal of the Mechanical Behavior of Biomedical Materials*. DOI: 10.1016/j.jmbbm.2016.04.008.

- Manda, K., Xie, S., Wallace, R., **Levrero-Florencio, F.**, Pankaj, P. (2016). Linear viscoelasticity - bone volume fraction relationships of bovine trabecular bone. *Biomechanics and Modeling in Mechanobiology*. DOI: 10.1007/s10237-016-0787-0.

- Manda, K., Wallace, R., Xie, S., **Levrero-Florencio, F.**, Pankaj, P. (2016). Nonlinear viscoelastic characterization of bovine trabecular bone. *Biomechanics and Modeling in Mechanobiology*. DOI: 10.1007/s10237-016-0809-y.

- **Levrero-Florencio, F.**, Manda, K., Margetts, L., Pankaj, P. (2016). Nonlinear homogenisation of trabecular bone: effect of solid phase constitutive model. *Proceedings of the Institution of Mechanical Engineers, Part H: Journal of Engineering in Medicine*. DOI: 10.1177/0954411916676220.

- Xie, S., Manda, K., Wallace, R., **Levrero-Florencio, F.**, Simpson, H., Pankaj, P. (2017). Time dependent behaviour of trabecular bone at multiple load levels. *Annals of Biomedical Engineering*. DOI: 10.1007/s10439-017-1800-1.

- **Levrero-Florencio, F.**, Manda, K., Margetts, L., Pankaj, P. (2017). Effect of including damage at the tissue level in the nonlinear homogenisation of trabecular bone. *Biomechanics and Modeling in Mechanobiology* (*under review*).

- Manda, K., **Levrero-Florencio, F.**, Xie, S., Wallace, R., Pankaj, P. (2017). Nonlinear viscoelastic-viscoplastic constitutive modelling of bovine trabecular bone. *Biomechanics and Modeling in Mechanobiology* (*under review*).